

Telma Joana Jesus Ferreira

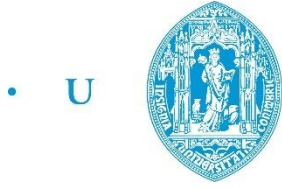
# MICROINJECTION MOULDING OF AUSTENITIC STAINLESS STEEL REINFORCED WITH CARBON NANOTUBES

Doctoral Thesis in Mechanical Engineering, Nanomaterials and Microfabrication, supervised by Professor Maria Teresa Freire Vieira, submitted to the Department of Mechanical Engineering, Faculty of Sciences and Technology of the University of Coimbra.

Fevereiro de 2018



UNIVERSIDADE DE COIMBRA



C •

FCTUC FACULDADE DE CIÊNCIAS  
E TECNOLOGIA  
UNIVERSIDADE DE COIMBRA

# **MICROINJECTION MOULDING OF AUSTENITIC STAINLESS STEEL REINFORCED WITH CARBON NANOTUBES**

**Telma Joana Jesus Ferreira**

A thesis presented for the degree of Doctor in Mechanical Engineering, Nanomaterials  
and Micromanufacturing

**Supervisor**

Professor Maria Teresa Freire Vieira

Department of Mechanical Engineering

Faculty of Science and Technology

University of Coimbra, Portugal

August 2017

**Technical sheet:**

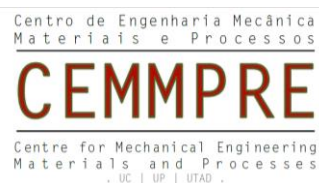
**Title:** Microinjection moulding of austenitic stainless steel reinforced with carbon nanotubes

**Author:** Telma Joana Jesus Ferreira

**Editor:** Department of Mechanical Engineering, Faculty of Science and Technology of the University of Coimbra

**Cover:** SS 316L with 0.9 wt% of MWCNT after debinding step (100 000x)

PhD scholarship (SFRH/BD/86216/2012) financed by:







*“Discovery consists of seeing what everybody has  
seen, and thinking what nobody has thought”*

*“A descoberta consiste em ver o que todos viram  
e em pensar no que ninguém pensou”*

*A. Szent-Gyorgyi*

*(1893 – 1986)*

*To my little princess, Benedita...*

# Acknowledgements

## **I am grateful to:**

Teresa Vieira by the teachings and inspiration words in difficult times;

CEMMPRE group by help along the last years;

IPN/LED&MAT group by the help of all kinds, by the words of encouragement and unconditional help, especially to the boys of microfabrication and Carlos, Eng. Vítor, António and Nelson;

Bruno Abreu and Gil Gonçalves from UA, as well as the whole group, for the kindness while doing the injections;

Rui Rocha from CEMUP, by patience in endless hours of SEM;

Alessandro Benedetti from the CACTI (Vigo University) for preparation of the material for HRTEM studies;

Raquel, Júlia, Rita, João, Sónia, Sami and Jorge by unconditional support;

Marisa for understanding how difficult this is;

MY FAMILY for helping to complete this step and for infinite patience;

BENEDITA for everything...

LIFE, for the great lesson that gave me.

**Thank you!**

# Abstract

In the last decades, the metal powder injection moulding (MIM), in its different version –  $\mu$ MIM technology, is a manufacturing process consolidated as an effective and competitive alternative to produce metallic parts in large series production of small and complex geometry with high quality and reproducibility. The remarkable expansion of  $\mu$ MIM in different industrial sectors obliges to use new materials with new functionalities, like nanocomposites.

This thesis focuses on the viability of processing SS 316L powders nanoreinforced with multiwall carbon nanotube (MWCNT) after  $\mu$ MIM processing. The aim is to study the evolution of MWCNT content during the different steps of processing (from mixing and injection, to debinding and sintering). Different challenges must be overcome such as: to guarantee a homogeneous distribution of MWCNTs in the matrix; to produce nanocomposites feedstocks with suitable rheological characteristics (to guarantee injection moulding) and to maintain the MWCNTs in the matrix after debinding and sintering steps. Afterward, the mechanical properties of SS 316L nanocomposites will be the demonstration of the effectiveness of the procedure.

Firstly, the optimization of the feedstocks as well all the conditions used to the SS 316L matrix (without nanoreinforcement addition) called master feedstocks (MF) are accomplished. The thermal debinding and sintering cycles of SS 316L and commercial binder ( $M_1$ ) feedstocks have been optimized. SS 316L feedstock had always a lower torque value than feedstock with other metallic powders (copper) with similar 3S's (particle size, particle size distribution and shape). The best sintering thermal cycle selected was 1250 °C as sintering temperature, heating rate = 10 °C/min; holding time = 60 minutes; cooling rate = 40 °C/min; Ar+H<sub>2</sub> atmosphere, they are unique to ensure the best compromise between structure, density, geometrical performance and mechanical properties. The addition of different nanoreinforcement contents always increases the torque value of feedstocks, whatever the matrix and the nanoreinforcement type (MWCNT or other nanoparticles). Bearing in mind the high torque values, a milling pre-treatment and addition of stearic acid proved to be essential for dropping torque values and to make possible the injection moulding of the feedstocks. After debinding and sintering cycles, the shrinkage of different sintered nanocomposites varied from 10 to 16 % and the porosity was less than 3 %.

From the analyse of the MWCNTs evolution during thermal processing, it is clear that after debinding step there are some carbon coming from MWCNTs that reacts with the chromium in solid solution in the austenitic matrix and gives rise to Cr<sub>23</sub>C<sub>6</sub> that evolves to Cr<sub>7</sub>C<sub>3</sub>, as the MWCNT (0 to 0.9 wt%). For the highest content of MWCNTs in matrix studied, can achieve a loss of carbon for the formation of carbides, which implies a reduction of carbon from nanotubes below to 50 %, as demonstrated by XRD and EDS, and evidenced by SEM and HRTEM analyses. The role of the atmosphere in carbon supply from nanotubes to matrix,

during thermal processes, was highlighted by coating “brown parts” with different contents of MWCNTs by a compact and uniform thin film of nickel (after being submitted to a vacuum ( $10^{-4}$  Pa) for 48 hours). After sintering, the content of carbon available to form carbides is lower than in the uncoated ones (~ 25%) that means lower MWCNTs degraded.

Nevertheless, the addition of more than 0.2 wt% seems to be efficient to the increment of the mechanical properties. The addition of MWCNTs to 316L stainless steel induces an improvement in hardness, yield strength (YS) and ultimate tensile strength (UTS). For the highest addition feasible (0.9 wt%) a maximum improvement of about 40 % of ultramicrohardness, 55 % of YS and 70 % of UTS having as standard the no reinforced, but submitted to the same methodology of processing, were attained.

**Keywords:** Stainless Steel 316L, MWCNT, Nanocomposites, Torque rheometry, Sintering atmosphere, Mechanical properties

# Resumo

Nas últimas décadas, a moldação por injeção de pós metálicos (MIM), na sua variante –  $\mu$ MIM, é um processo de fabrico consolidado e uma alternativa competitiva para a produção de pequenas peças metálicas de geometria complexa e em grandes séries, com elevada qualidade e reprodutibilidade. A notável expansão do  $\mu$ MIM em diferentes setores industriais obriga à utilização de novos materiais, com novas funcionalidades, como os nanocompósitos.

Esta tese visa estudar a viabilidade do processamento de pós SS 316L nanorreforçados com nanotubos de carbono de parede múltipla (MWCNT), após o processamento por  $\mu$ MIM. O objetivo é estudar a evolução do teor de MWCNTs durante as diferentes etapas de processamento (desde a mistura e injeção, até à eliminação do ligante e sinterização). Diferentes desafios devem ser superados, tais como: garantir uma distribuição homogénea dos MWCNTs na matriz; produzir matérias-primas nanocompósitas com características reológicas adequadas (para garantir a moldação por injeção) e não danificar os MWCNTs na matriz após as etapas de eliminação do ligante e sinterização. Posteriormente, as propriedades mecânicas dos nanocompósitos de SS 316L serão a demonstração da eficácia da tecnologia adotada (técnica, metodologia e conhecimento).

Em primeiro lugar, foi realizada a caracterização reológica da matéria-prima com os pós SS 316L e o ligante comercial ( $M_1$ ), (sem adição de nanorreforços), denominada matéria-prima primordial (MF). Os ciclos térmicos de eliminação do ligante e de sinterização das matérias-primas (*feedstocks*) de matriz SS 316L foram otimizados e serviu de base a todo o processamento. O valor de binário dos *feedstocks* de matriz de SS 316L foi sempre menor do que outras matérias-primas de outros pós metálicos (p.ex. cobre) com semelhante 3S's (tamanho de partícula, distribuição de tamanho de partícula e forma). O melhor ciclo térmico de sinterização selecionado foi de 1250 °C como temperatura de sinterização, taxa de aquecimento = 10 °C/min; tempo de sinterização à temperatura máxima = 60 minutos; taxa de arrefecimento = 40 °C/min; atmosfera de Ar+H<sub>2</sub>. Este ciclo é o único que assegura o melhor compromisso entre estrutura, densidade, desempenho geométrico e propriedades mecânicas. A adição de diferentes teores de nanorreforços aumenta sempre o valor do binário em relação ao da matéria-prima primordial, qualquer que seja a matriz e o tipo de nanorreforço (MWCNT ou outras nanopartículas). O aumento do valor de binário com o teor de nanorreforço, obriga a um pré-tratamento da mistura e adição de ácido esteárico. Após os ciclos de eliminação de ligante e sinterização, a contração do nanocompósito variou de 10 a 16 % e a porosidade final foi inferior a 3 %.

A partir da análise da evolução do teor de MWCNTs durante o processamento térmico, é evidente que, após o ciclo térmico de eliminação do ligante há carbono proveniente dos MWCNTs que reage com o crómio em solução sólida, presente na matriz

austenítica e produz  $\text{Cr}_{23}\text{C}_6$  que evolui para  $\text{Cr}_7\text{C}_3$ , com o aumento de carbono na matriz proveniente dos MWCNTs (0 a 0,9 % em peso). Para os valores mais elevados de MWCNTs na matriz, pode atingir uma perda de carbono para formação de carbonetos que implica uma diminuição de carbono dos nanotubos abaixo para 50 %, como demonstrado pelas técnicas de XRD e EDS, e evidenciado por análises SEM e HRTEM. O papel da atmosfera no fornecimento de carbono dos nanotubos para a matriz, durante os processos térmicos, foi evidenciado pelo revestimento dos denominados "castanhos" (componente após eliminação do ligante) com diferentes teores de MWCNTs, por um filme fino compacto de níquel (depois de ser submetido a vácuo ( $10^{-4}$  Pa) durante 48 horas). Após a sinterização ficou claro que a quantidade de carbono disponível para formar carbonetos é menor do que quando não revestidos (~ 25 %), o que significa que existem menos MWCNTs degradados.

A adição de mais de 0,2 % em peso de MWCNTs parece ser eficiente para o incremento das propriedades mecânicas. A adição de MWCNTs ao aço inoxidável 316L induz uma melhoria da dureza, do limite de elasticidade ( $R_{p0.2}$ ) e de resistência à tração ( $R_m$ ). Para a maior adição possível (0,9 % em peso), foi atingido um aumento de cerca de 40 % para a ultramicrodureza, 55 % do  $R_{p0.2}$  e 70 % da  $R_m$  comparativamente ao padrão não reforçado, mas submetido à mesma metodologia de processamento.

**Palavras-chave:** Aço inoxidável 316L, MWCNT, Nanocompósitos, Reometria de binário, Atmosfera de Sinterização, Propriedades mecânicas

# Abbreviations and symbols

## Abbreviations

AISI – American Iron and Steel Institute

BET – Brunauer, Emmett and Teller

BPR – Ball Powder Ratio

CCVD – Catalytic Carbon Vapour Deposition

CIP – Cold Isostatic Pressing

CMC – Ceramic Matrix Composites

CNT – Carbon Nanotube

CPVC – Critical Powder Volume Concentration

DTA – Differential Thermal Analysis

CVD – Chemical Vapour Deposition

E – Modulus of Elasticity or Young's modulus

EBSD – Electron Backscattered Diffraction

EDS – Energy Dispersive Spectroscopy

EVA – Ethylene Vinyl Acetate

FIB – Focused Ion Beam

FTIR – Fourier Transform Infrared

HDPE – High Density Polyethylene

HIP – Hot Isostatic Pressing

HRTEM – High Resolution Transmission Electron Microscopy

ICDD – International Centre for Diffraction Data

IUPAC – International Union of Pure and Applied Chemistry

IR – Infrared

LDS – Laser Diffraction Spectrometry

LDPE – Low Density Polyethylene

MF – Master Feedstock

MEMS – Micro Electro Mechanical Systems



MIM – Metal Injection Moulding

MMC – Metal Matrix Composites

MWCNT – Multiwall or Multiwalled, Multi-Wall, or Multi-Walled Carbon Nanotube

μMIM – Micro Metal Injection Moulding

PAN – Polyacrylonitrile

PE – Polyethylene

PIM – Powder Injection Moulding

PM – Powder Metallurgy

PP – Polypropylene

PSD – Particle Size Distribution

PVD – Physical Vapour Deposition

PW – Paraffin Wax

rpm – rotation per minute

SA – Stearic Acid

SEM – Scanning Electron Microscopy

SLM – Selective Laser Melting

SPS – Spark Plasma Sintering

SS – Stainless Steel

SWCNT – Single-wall or Single-walled Carbon Nanotubes

TGA – Thermal Gravimetric Analysis

UTS – Ultimate Tensile Strength

XRD – X-Ray Diffraction

YS – Yield Strength

## Symbols

$\text{Al}_2\text{O}_3$  – Aluminium oxide or alumina

$d_{hkl}$  – Interplanar distance

K – Constant of Hall-Petch equation

$L_c$  – Commercial binder

$M_1$  – Commercial binder  
 $S_m$  – Specific surface area  
 $S_w$  – Width particle size distribution  
 $T_g$  – Glass transition temperature  
 $T_m$  – Melting temperature  
vol% – Volume percentage  
wt% – Weight percentage  
 $\rho_w$  – Water density  
 $\varepsilon$  – Deformation  
 $\lambda$  – Wavelength  
 $\sigma_0$  – Strength  
 $\sigma_y$  – Yield Strength (Hall-Petch equation)  
 $\theta$  – Bragg angle

# List of figures

Figure 1 – The number of scientific journal articles published about CNT nanocomposites with different types of matrices from 2000 to May 2017(source: Science Direct)	3
Figure 2 – Classification of the different manufacturing processes of CNT reinforced MMCs [1]	4
Figure 1.1 – Schematic representation of the relation between nanotubes and graphene [34]	11
Figure 1.2 – Schema of ball milling process [3]	15
Figure 1.3 – Roadmap of PM, MIM and $\mu$ MIM processes [52]	21
Figure 1.4 – Flowchart of MIM process (adapt. by [58])	22
Figure 1.5 – Atomization processes [60]	23
Figure 1.6 – Distribution of binder a) excessive binder, b) optimal powder:binder and c) insufficient binder [86], [87]	27
Figure 1.7 – Thermal debinding steps [86]	31
Figure 1.8 – Schematic evolution during the solid state diffusion sintering stage [86], [87]	32
Figure 2.1 – Design of moulds for tensile and flexure specimens	40
Figure 2.2 – MiniJet Pro Piston Injection Moulding System a) machine, b) cylinder and c) cylinder inside machine	41
Figure 2.3 – Debinding cycle	41
Figure 2.4 – Sintering cycle	42
Figure 2.5 – Magnetron sputtering equipment	43
Figure 2.6 – FIB-SEM	47
Figure 2.7 – Gage length ( $L_0$ ) of tensile specimen	49
Figure 3.1 – Particle size distribution of SS 316L	51
Figure 3.2 – Particle shape of SS 316L a) 10000x, b) 25000x	52
Figure 3.3 – X-ray diffractogram of pristine SS 316L powders (as received)	52
Figure 3.4 – TGA of pristine SS 316L powders (as-received)	53
Figure 3.5 – Nanotubes shape of MWCNTs at different magnifications (TEM)	54
Figure 3.6 – TGA of MWCNTs in air and Ar+H <sub>2</sub> (5 %) atmospheres	55
Figure 3.7 – TGA of MWCNTs in atmosphere a) air, b) argon, for different heating rates [50]	56
Figure 3.8 – TGA of binder M <sub>1</sub>	57
Figure 3.9 – TGA of SA	57
Figure 3.10 – TGA of binder M <sub>1</sub> with SA (3:1 vol%)	58
Figure 3.11 – SS 316L feedstock optimization versus a) time and b) SS 316L powders (vol%)	60
Figure 3.12 – SS 316L feedstocks with 40 vol% of M <sub>1</sub> binder	60
Figure 3.13 – Morphological analysis of SS 316L feedstock, at different magnifications a) 10000x and b) 25000x	61
Figure 3.14 – TGA of SS 316L:M <sub>1</sub> feedstock 60:40 vol%	61
Figure 3.15 – Mixing procedure (route 1)	62

Figure 3.16 – SS 316L and M <sub>1</sub> composites feedstock nanoreinforced with a) MWCNT and b) nanoalumina (route 1a))	63
Figure 3.17 – SS 316L feedstocks with 0, 5 and 10 vol% of SA	64
Figure 3.18 – Morphological analysis of SS 316L:binder (60:(30+10) vol%) a) 10000x and b) 25000x	65
Figure 3.19 – TGA of SS 316L+(M <sub>1</sub> +SA) feedstock	65
Figure 3.20 – SS 316L composites feedstock (M <sub>1</sub> +SA) nanoreinforced with a) MWCNT and b) nanoalumina	67
Figure 3.21 – Morphological analysis of SS 316L nanocomposites feedstocks with MWCNT (left) and nanoalumina (right)	69
Figure 3.22 – Schema of feedstock preparation (route 2)	70
Figure 3.23 – Morphological analysis of pre-mixture a), b) 5 minutes, c), d) 15 minutes, e), f) 30 minutes 10000x (left) and 50000x (right)	71
Figure 3.24 – SS 316L nanoreinforced composite feedstock with MWCNT (pre-mixture) (route 2)	72
Figure 3.25 – Morphological analysis of nanocomposites feedstocks with different contents a), b) 0.0, c), d) 0.8, e), f) 1.7, g), h) 2.5, i), j) 3.3 of MWCNTs (vol%) 10000x (left) and 25000x (right)	74
Figure 3.26 – TGA of SS 316L MF with 3.3 vol% (0.8 wt%) MWCNT	74
Figure 3.27 – Design of specimen	75
Figure 3.28 – a) Unfilled mould cavity – T <sub>mould</sub> = 80 °C and b) fulfilled mould cavity – T <sub>mould</sub> = 82 °C	75
Figure 3.29 – Unfilled mould cavity with T <sub>mould</sub> = 82 °C a) 2.5 vol%, b) 3.3 vol% MWCNT	76
Figure 3.30 –SS 316L “green microspecimen”	76
Figure 3.31 – Morphological analysis of SS 316L nanocomposites with a) 0.0, b) 0.5 and c) 0.9 of MWCNT (wt%)	78
Figure 3.32 – Morphological analysis of SS 316L brown nanocomposites reinforced with 0.9 of MWCNT (wt%)	78
Figure 3.33 – X-ray diffractogram of SS 316L “brown part” (without MWCNT addition and milling pre-treatment)	79
Figure 3.34 – TGA of SS 316L “brown parts” with or without milling pre-treatment and MWCNTs additions	79
Figure 3.35 – Dimensions of green, brown and final specimens (T <sub>sint.</sub> = 1250 °C)	80
Figure 3.36 – Shrinkage and porosity versus sintering temperature	81
Figure 3.37 – Optical micrographs of polished sintered surface parts at a), b) 1150 °C, c), d) 1200 °C, e), f) 1250 °C, g), h) 1250 °C (milling) and i), j) 1300 °C	83
Figure 3.38 – Optical micrographs after etching of sintered surface parts at a), b) 1150 °C, c), d) 1200 °C, e), f) 1250 °C, g), h) 1250 °C (milling) and i), j) 1300 °C	84
Figure 3.39 – X-ray diffractogram of sintered parts at different temperatures (zoom)	85
Figure 3.40 – Solid solubility of carbon in austenitic SS [59]	85
Figure 3.41 – Hardness values of sintered parts (MIM* is from Powder Injection Moulding Journal – tensile properties of representative MIM alloys [106])	87
Figure 3.42 – Young’s modulus values of sintered parts	87
Figure 3.43 – Stress-strain curves for sintered parts at a) 1150 °C, b) 1200 °C, c) 1250 °C, d) 1250 °C (milling) and e) 1300 °C	89
Figure 3.44 – Fracture surface of sintered a) without defect, b), c) and d) with defect	89

Figure 3.45 – $\epsilon$ , YS and UTS (MIM* is from Powder Injection Moulding Journal – tensile properties of representative MIM alloys [106])	90
Figure 3.46 – Shrinkage and porosity of nanoreinforced composite specimens	91
Figure 3.47 – Optical micrographs of polished sintered surface parts with a), b) 0.0, c), d) 0.2, e), f) 0.5, g), h) 0.7 and i), j) 0.9 of MWCNTs (wt%)	93
Figure 3.48 – Optical micrographs of etched sintered surface parts with a), b) 0.0, c), d) 0.2, e), f) 0.5, g), h) 0.7 and i), j) 0.9 of MWCNTs (wt%)	95
Figure 3.49 – X-ray diffractogram of nanoreinforced composites sintered with different contents of MWCNTs (0.0, 0.2, 0.5, 0.7 and 0.9 wt%)	96
Figure 3.50 – Hardness versus MWCNTs (wt%)	97
Figure 3.51 – Young's modulus versus MWCNT (wt%)	97
Figure 3.52 – Stress-strain curves of a) 0.0, b) 0.2, c) 0.5, d) 0.7 and e) 0.9 of MWCNTs (wt%)	98
Figure 3.53 – Fracture surface of sintered nanocomposites a) without defect, b), c) and d) with defects	99
Figure 3.54 – Morphological analyses of fracture surface of sintered nanoreinforced steel: a) 0.0 wt%, b) EDS - Z1, c), d), e) 0.5 wt%, f), g) and h) 0.9 wt%	100
Figure 3.55 – Sintered composite with: a), b) 0.0 wt%, c), d) 0.5 wt%, e), f) 0.9 wt% (left: fracture surface and right: X-ray map of iron (green) and chromium (red))	101
Figure 3.56 – TGA of sintered SS 316L specimens with 0.0, 0.5 and 0.9 of MWCNTs (wt%)	102
Figure 3.57 – SEM of sintered nanocomposite reinforced with 0.9 of MWCNTs (wt%)	103
Figure 3.58 – FIB/HRTEM images of sintered composites with 0.9 of MWCNTs (wt%)	104
Figure 3.59 – $\epsilon$ , YS and UTS	105
Figure 3.60 – Morphological analysis of fracture surface of coated sintered nanocomposites with a), b) 0.5 wt%, c), d) 0.9 wt% of MWCNTs	107
Figure 3.61 – Coated sintered composite a), b) 0.5 wt% and c), d) 0.9 wt% of MWCNTs (left: fracture surface and right X-ray map of iron (green) and chromium (red) elements)	108
Figure 3.62 – TGA of sintered SS 316L parts with 0.0, 0.5 and 0.9 of MWCNT (wt%) coated	109
Figure 3.63 – Fracture surface of coated composites with 0.9 of MWCNTs (wt%)	110
Figure 3.64 – FIB/HRTEM images of coated composite with 0.9 of MWCNTs (wt%)	111

## APPENDIX/ANNEX

Figure A.1 – IR spectra of M <sub>1</sub> and SA binders	127
Figure A.2 – Particle size distribution of copper powders	129
Figure A.3 – Particle shape of copper powders: a) 10000x b) 25000x	129
Figure A.4 – X-ray diffraction of copper powders (as received)	130
Figure A.5 – Copper feedstock optimization versus a) time and b) copper powders (vol%)	131
Figure A.6 – Copper feedstock with 40 vol% of M <sub>1</sub> binder	132
Figure A.7 – Morphological analysis of copper feedstock with 40 vol% of M <sub>1</sub> , at different magnifications a) 10000x and b) 25000x	132
Figure A.8 – Copper and M <sub>1</sub> composites feedstock nanoreinforced with a) MWCNT and b) nanoalumina	133
Figure A.9 – Copper feedstocks with 0, 5 and 10 vol% SA	134

Figure A.10 – Morphological analysis of SS 316L:binder (60:(30+10) vol%) a) 10000x and b) 25000x	135
Figure A.11 – Copper composites feedstock (M <sub>1</sub> +SA) nanoreinforced with a) MWCNT and b) nanoalumina	136
Figure A.12 – Morphological analysis of copper nanocomposites feedstocks with MWCNT (left) and nanoalumina (right)	137
Figure A.13 – Morphological analysis of pre-mixture a) b) 5 minutes, c) d) 30 minutes	138
Figure A.14 – Copper nanoreinforced composite feedstock with MWCNT (pre-mixture) (route 2)	139
Figure A.15 – Morphological analysis of nanocomposites feedstocks different contents a), b) 0.0, c), d) 0.7, e), f) 1.8, g), h) 2.5, i), j) 3.3 of MWCNTs (vol%) 10000x (left) and 25000x (right)	141

## List of tables

Table 1.1 – Applications of MMC with carbon nanotubes [36]	12
Table 1.2 – Comparison of electric arc discharge, laser ablation and CVD methods [35], [37]	13
Table 1.3 – Purification methods	13
Table 1.4 – Mechanical milling parameters	17
Table 1.5 – MMC processing parameters	18
Table 1.6 – Characteristics of SS 316L powders used in $\mu$ MIM	23
Table 1.7 – Characteristics of ideal binder system by $\mu$ MIM process [55]	25
Table 1.8 – Different binders combinations used	25
Table 1.9 – Feedstock composition and mixing parameters by $\mu$ MIM	27
Table 1.10 – Different nanocomposites feedstock composition and mixing parameters for MIM	28
Table 1.11 – Injection moulding parameters by $\mu$ MIM	29
Table 1.12 – Injection moulding conditions for nanocomposites feedstocks	30
Table 1.13 – Thermal debinding parameters by $\mu$ MIM	31
Table 1.14 – Thermal debinding parameters	32
Table 1.15 – Sintering parameters for SS 316L by $\mu$ MIM	33
Table 1.16 – Sintering parameters of MMC-MWCNT (by MIM)	34
Table 1.17 – MMC-MWCNT produced by MIM	35
Table 2.1 – Standard chemical composition of SS 316L [59], [60], [91]	37
Table 2.2 – Chemical composition of SS 316L	37
Table 2.3 – MWCNT characteristics	38
Table 3.1 – SS 316L powders characteristics	53
Table 3.2 – Torque values of SS 316L composites feedstocks nanoreinforced with MWCNT or nanoalumina	63
Table 3.3 – Torque values of SS 316L composites feedstocks nanoreinforced with MWCNT and nanoalumina	67
Table 3.4 – Torque values of SS 316L composites feedstocks nanoreinforced with MWCNT (route 2)	72
Table 3.5 – Injection parameters	76
Table 3.6 – Apparent density of sintered at different temperatures	81
Table 3.7 – Properties of “brown parts” sintered at different temperatures and bulk material	90
Table 3.8 – Apparent density of nanoreinforced composite specimens	91
Table 3.9 – Mean grain size versus $\sigma_y$ for different additions of MWCNTs (wt%)	94
Table 3.10 – Resume of all the properties of nanoreinforced composites sintered at 1250 °C	106
APPENDIX/ANNEX	
Table A.1 – Copper powders characteristics	130

Table A.2 –Torque values of copper composites feedstocks nanoreinforced with MWCNT or nanoalumina	134
Table A.3 – Torque values of copper composites feedstocks nanoreinforced with MWCNT and nanoalumina	136
Table A.4 – Torque values of copper composites feedstocks nanoreinforced with MWCNT	139
Table A.5 – Volume percentage of different elements	143
Table A.6 – Weight percentage of different elements	143
Table A.7 – MWCNTs contents in matrix	143
Table A.8 – Properties of SS 316L annealed plate	151



# CONTENT

INTRODUCTION.....	1
CHAPTER I.....	6
State of the art.....	6
1.1 Carbon Nanotubes.....	10
1.2 Preparation of nanocomposite powder mixture.....	14
1.3 Manufacturing.....	17
CHAPTER II.....	36
2.1 Materials.....	37
2.2 Processing methodologies.....	38
2.3 Characterization techniques.....	43
CHAPTER III.....	50
3.1 Materials.....	51
a) SS 316L powders.....	51
b) MWCNTs.....	54
c) Binder.....	56
3.2 Feedstocks nanocomposite powders for $\mu$ MIM.....	59
a) Optimization of SS 316L powders.....	59
b) Feedstocks of composites.....	62
3.3 Injection Moulding.....	75
3.4 Debinding.....	77
3.5 Sintering.....	80
a) Selection of sintering temperatures.....	80
b) Role of nanoreinforcement content.....	91
c) New approach.....	106
CONCLUSIONS.....	112
BIBLIOGRAPHY.....	116
APPENDIX I.....	126
APPENDIX II.....	128
APPENDIX III.....	142
ANNEX I.....	144
ANNEX II.....	150



# INTRODUCTION

---

For sustained and sustainable world, it is required to increase the demand of high strength in small parts/devices with similar functionality to high conventional weight, particularly in what concern to structural properties. Thus, new materials must be developed in order to accomplish this plan. Composites of conventional materials reinforced by the addition of nanometric particles (nanocomposites) and new replicative processes can be the solution. In the new microworld, it is essential to answer to the new current requests, in a fast, efficient and economical way. For energy efficiency and decreasing of natural resources, metallic matrix nanocomposites (MMC) should have characteristics such as lightweight, high mechanical strength and thermal conductivity, low coefficient of thermal expansion, suitable for microparts to be used in automobile, aerospace, and electronic applications [1].

The nanoreinforcements had a fast-emerging success due to a vast potential to create new materials with unique properties and suitable for numerous applications. Engineers, scientists, and researchers are working to develop techniques where devices and structures with microfeatures could be manufactured at large scale and reasonable cost. Nanocomposite is a material with at least one of their constituents being less than 100 nm [2].

The most widespread reinforcement materials used in commercial application are  $\text{Al}_2\text{O}_3$ , TiC, SiC,  $\text{B}_4\text{C}$ , BeO, Mo, NbC, TaC, TiB,  $\text{TiB}_2$ , W and WC and allotropes of carbon, which enhancing the overall properties of composite material [2]–[5]. In recent years, carbon nanotubes, single-wall and multiwall (SWCNT, MWCNTs) have opened new challenges, due to the possibility to improve enormously the structural and functional properties of conventional materials. The carbon nanotubes (CNTs) has been actively researched due to outstanding properties and aiming at wide variety of potential applications [1]. The predicted physical properties of MMCs are only reached if the CNTs have not defects in the lattice, no contaminants or agglomeration [3].

In two last decennia, a number of publications by year on nanocomposites of CNTs in polymer, metallic, and ceramic matrices are increasing (figure 1). However, the main research works concern to the development of polymer nanocomposites, due the low pressures and temperatures used in their processing in relation to metallic and ceramic matrices [3], [6]. Moreover, for high temperatures of processing it is necessary to protect the CNTs from the atmosphere to avoid their degradation [1]. The processing conditions have a significant role on the CNTs degradation, mainly attributed to the reaction of carbon with oxygen in environmental atmosphere ( $> 700\text{ }^\circ\text{C}$ ) (cf. figure 3.6). Some of these aspects have restricted the interest in CNTs as reinforcement in metallic matrices, particularly for those that have high melting temperatures. The outstanding properties of CNTs if associated to metallic matrices (like aluminium, nickel, copper, magnesium, titanium or iron alloys) can led to an high impact on developing new generation of metallic nanocomposites with enhanced

functionality and structural properties [1], [3], [7]. Nevertheless, few studies have been yet published when iron alloys are the based matrix, compared to the other ones.

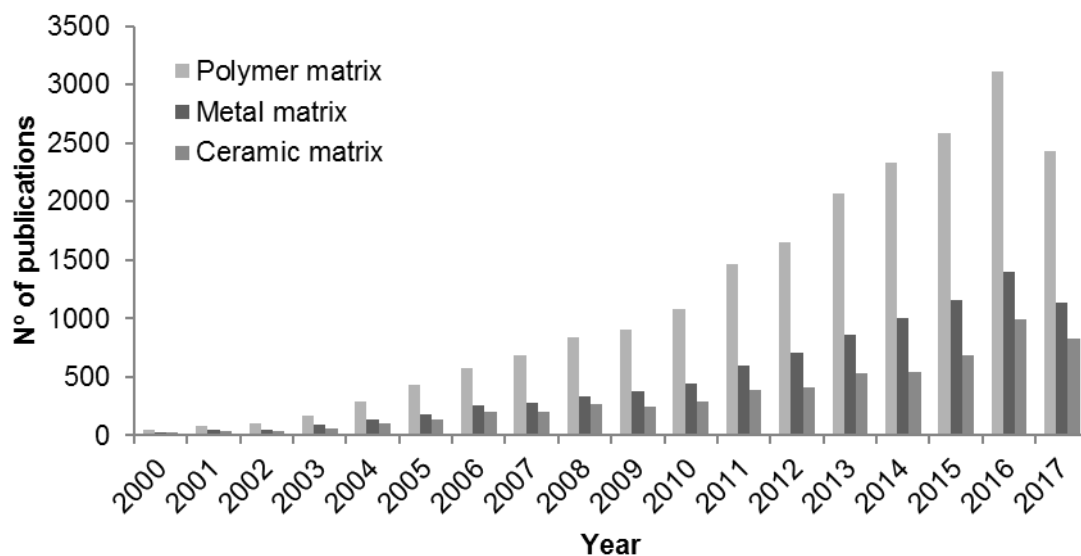


Figure 1 – The number of scientific journal articles published about CNT nanocomposites with different types of matrices from 2000 to May 2017(source: Science Direct)

Besides the processing conditions, one of the most important challenge in manufacturing nanocomposites is how to achieve homogeneous dispersion of CNTs into a metallic matrix. Owing to their enormous surface area, CNTs tend to agglomerate or aggregate in metallic matrix during processing. The critical volume fraction and the agglomeration of nanotubes can lead to composites having toughness, strength and other physical properties lower than expected [4]. Nanocomposites based on CNTs can be manufactured by melting, thermal spraying, electrochemistry, powder metallurgy or other techniques (novel) [1], [2], [4] (figure 2). Of the commercial processes, liquid metal routes such as stir casting and infiltration account for the largest volume in primary production (67 %), however powder metallurgy (PM) represents more and more important role in the market [5]. Whatever the selected process, must assure the minimal damage of CNTs due to temperature, stress and oxidation. Depending on the selected process, temperature and stress may lead to solid solution of carbon in the matrix and chemical reactions, which can give rise to carbide formation ( $Al_4C_3$  and  $Ni_3C$ ) in the interfaces nanotubes/matrix, as detected in nanocomposites of aluminium and nickel [3]. Consequently, depending on size, particle size distribution and chemical composition, the carbides may affect the properties of the nanocomposites favourable or adversely [1].

For acceptable production of metallic nanocomposites based on CNTs, much more research work is need in different aspects (figure 2). Until now, in what concerns the processing of these nanocomposites there are a large gap that needs a rapid solution.

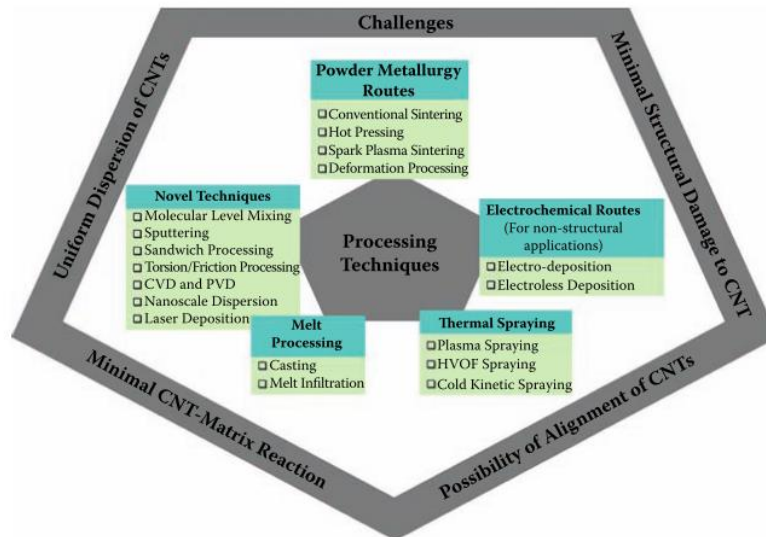


Figure 2 – Classification of the different manufacturing processes of CNT reinforced MMCs [1]

In spite of micromanufacturing processes for metallic materials have attained maturity, responding to current requests to produce parts/devices with reduced size, there are not yet enough competences in what concern the MMC – CNT feedstocks. There are many studies concerning the more popular processes of micromanufacturing – metallic powder injection moulding (MIM and  $\mu$ MIM), however the number of publications is not significant regarding metallic matrix with CNTs. Nevertheless, the largest part of nanocomposites are about CNTs in aluminium, copper, nickel/Inconel, titanium, magnesium, cobalt and others. However, the publications concerning other metallic matrix (e.g. stainless steel) nanoreinforced composites are almost inexistent. The justification is related to sintering temperatures to be high enough that contributes to the degradation and decreasing of CNTs content, being the oxygen the fundamental element that contributes to metal or oxygen reactions [1].

Thus, one of the most exciting features of micro-replicative processes will be to become possible the manufacturing of nanocomposites, where the reinforcement is CNTs and the matrix materials are not compatible in molten state [8].  $\mu$ MIM is a micromanufacturing replicative technique suitable to produce parts/devices with quality and complex geometry, dimensional accuracy and replication reliability when compared with other processes. The main five steps of  $\mu$ MIM that can have significant role on quality of CNTs nanocomposites are, as follows: powders characterization, mixing, injection, debinding, and sintering. Firstly, the 4S's of powders matrix (particle size, particle size distribution, shape and structure) have the most significant role in the process [9]. The second step is composed and optimized – in accord to the rule of critical powder volume concentration (CPVC) [10], the feedstock (mixture of powder, nanoreinforcement and binder (different polymers with other organic materials).

The injection moulding of the feedstock allows attaining the parts/devices with the selected shape (green parts) (3<sup>rd</sup> step). In the debinding step – 4<sup>th</sup> step, the binder should be removed without introducing defects in parts/devices and assuring the stability of nanoparticles in the “brown parts”. Finally, the powder particles, without vestiges of carbon from binder, are consolidated by sintering (5<sup>th</sup> step). The last one is the most critical step, particular in nanocomposite powders based on CNTs, due to their degradation, which determine the final properties.

The thesis motivation is to improve  $\mu$ MIM applications particularly for processing microparts/devices based on nanocomposites, whatever sintering temperature of metallic matrix, always with carbon nanotubes as reinforcement. This target obliges to a deep study in all the steps of process in order to understand the role of CNTs. The study starts by the selection of the matrix – stainless steel 316L (SS 316L) metallic powders, and multiwall carbon nanotubes (MWCNT) as nanoreinforcement. Different percentages from 0.8 to 3.3 (vol%) of MWCNT were tested. In order to understand the effect of nanoreinforcement content, the properties of the green, brown and final parts/devices oblige to a physical and mechanical characterization.

The big challenges are as follows:

- how to disperse the MWCNTs in powders without damaging the nanotubes;
- how to attain a feedstock with a homogeneous distribution of MWCNTs;
- how to promote a nanocomposite feedstock injectable;
- how to optimize the thermal cycles during debinding and sintering, that induce the minimal damage of MWCNTs;

in order to understand the role of MWCNTs during  $\mu$ MIM processes in iron metallic alloys, where carbon content is not significant.

The thesis has three different chapters. After the present introduction, the chapter I starts with a description of the state of the art about the metallic matrix composites nanoreinforced and the powder technology – powder injection moulding. Chapter II focus on the materials selected for the study, the processing methodology and characterization techniques used along this work (in different steps of processing), such as the processing tools, parameters and procedure details. The chapter III exhibits the results and discussion concerning the role of the multiwall carbon nanotubes in 316L stainless steel matrix, during all the stages of processing by  $\mu$ MIM, from mixing up to sintering. The thesis finish highlighting the main conclusions and point to the future work.

# CHAPTER I

## State of the art

---

Metallic matrix nanocomposite and powder technology



In last century, the composite materials have assumed a significant role to improve the properties (i.e. stiffness, toughness, mechanical, thermal and electrical resistance) whatever materials matrix. At XXI century, nanoreinforcement has been helping to reach unexpected limits for engineering properties [11].

For metallic matrix, the nanoreinforcement can have great impact, particularly in applications for aerospace, automotive and sports industries, where small parts/devices must have the highest stiffness and strength to support the same mechanical requests of conventional ones [1], [12]. Moreover, density and homogeneity of MMC are a very important factors because they contribute directly or indirectly (pores) to mechanical and physical properties [13]. Properties like coefficient of thermal conductivity, mechanical strength and elastic modulus also depend on the volume fraction of CNTs inside matrix [1]. The mechanical performance of MMC nanoreinforced can be relatively scarce due to difficulties in achieving homogeneous dispersion of nanoreinforcement in metallic matrices, especially when the reinforcement content is high, and due to a lack of suitable synthesis methodologies [14].

Powder technology approach become easy to reinforce matrices with nanoparticles, including carbon nanotubes with several contents. The decrease of nanoparticle size has a significant role due to the highest ratio of surface area: volume, becoming surface properties the dominant factor [15]. Carbon nanotubes has only one dimension lower than 100 nm, normally depending on the number of layers this is < 30 nm [11]. However, this allotrope of carbon has been demonstrating a unique set of mechanical, chemical and electrical properties which make them very promising reinforcement of materials used in several areas [3], [14].

However, more important than processing methods is the strengthening of CNTs in MMCs, usually complex due to multiple potential mechanisms. The possible mechanisms include [6], [16], [17]:

- load transfer from matrix to CNTs;
- grain refinement caused by CNTs (Hall-Petch relation, Orowan bowing mechanism, Taylor relationship and several other models);
- solid solution strengthening by carbon atoms from CNTs diffused into metallic matrices;
- particle strengthening induced by the precipitated carbide from the reaction between the matrix and CNTs;
- work hardening of the matrix due to dislocation multiplication due to thermal mismatch between the matrix and CNTs at the interfaces;

- strengthening by impurities introduced when mixing CNTs into matrices.

Different research works show that some mechanical properties like wear strength, yield strength and hardness increase by CNTs addition. Aluminium ( $2700 \text{ kg/m}^3$ ), titanium ( $4550 \text{ kg/m}^3$ ), Inconel ( $8300 \text{ kg/m}^3$ ), nickel ( $8910 \text{ kg/m}^3$ ) and copper ( $8930 \text{ kg/m}^3$ ) matrices have been nanoreinforced with CNTs. The last two matrices have similar density, but quite distinct melting points ( $1425 \text{ }^\circ\text{C}$ ,  $1452 \text{ }^\circ\text{C}$ , and  $1080 \text{ }^\circ\text{C}$  respectively).

*S. M. Uddin et al.* [18] show an improvement in hardness (47 %) of the nanocomposite by addition of MWCNTs (0.5 vol%) in a pure copper matrix. However, for higher contents (up to 2 vol%) of MWCNTs is detected a slight decreasing of this property. *V. T. Pham et al.* [19] tested different sintering temperatures and detected that at  $900 \text{ }^\circ\text{C}$  was attained the best effect of the reinforcement material and measured an improve in hardness (18 %) with addition of 13 vol% of MWCNTs in copper. *A. K. Shukla et al.* [14] detected an increasing of hardness in copper after 10 vol% of SWCNTs addition, attributed to the strengthening effect of the CNTs in nanocomposite. However, the hardness decreased for the same content of MWCNTs, attributed by the authors to the possibility of a high MWCNTs content in the grain boundaries. Nevertheless, the experimental support presented is not clear about the justification; it must be highlight that the magnification used in both cases (SWCNT and MWCNT) is not suitable for the envisaged proposes. *G. N. Kim et al.* [20] measured an hardness improvement (200 %) in relation to pure copper when the reinforcement assumes very high content (20 vol% of MWCNTs). *A. A. Sahraei et al.* [21] evaluated the microhardness of nanocomposites and shown to be 1.7 to 2.1 times higher than unreinforced copper, depending on different functionalized MWCNTs with same content (4 vol%). *A. S. Muhsan et al.* [22] assessed an increasing of Young's modulus (48%) after addition of MWCNTs (5 vol%) compared with unreinforced copper matrix, but when MWCNTs contents exceeds 5 vol% up to 10 vol% there are an opposite effect. Others authors assessed an increasing in microhardness (16.8 %) by addition of 4 vol% MWCNTs to copper matrix over the monolithic material, due to a uniform distribution of the nanoreinforcement [23]. *H. Deng et al.* [24] detected that the aggregation of MWCNTs increases with the increasing volume fraction of carbon nanotubes, and the best dispersion was reach in copper with 0.5 vol% of MWCNTs. This nanocomposite reached the best ultimate tensile strength (UTS) (80 %) over the unreinforced copper matrix and the fractured surface present the MWCNTs bridging broken [24]. *H. Wang et al.* [25] show that copper composite containing 0.5 vol% of MWCNTs has a maximum hardness of 1.3 GPa and highest yield strength (YS) of 142 MPa (increase by 150 % compared with pure copper). In this study, the experimental support presented shows a continually decreases of copper grain size with an increase in MWCNTs addition [25].

*J. Liao and M. J. Tan* [26] measured an enhancement of tensile strength and hardness about 24 and 21 %, respectively, though the small addition of 0.65 vol% of MWCNTs to aluminium matrix. *Y. Wu and G. Y. Kim* [27] detected an improvement of hardness, between 51 and 69 % (depending of sintering temperature), with addition of 1.3 vol% of MWCNT to aluminium matrix. These authors attributed this strengthening due to excessive formation of carbide –  $Al_4C_3$ , at elevated temperature [27]. *B. Chen et al.* [28] evaluated an increase in UTS of 180 and 192 MPa for addition of 0.65 and 1.3 vol% of MWCNT (respectively) to aluminium matrix, over the pure aluminium (157 MPa) processed by same way. The nanocomposite had a good plasticity with elongation about 20 %, the aluminium matrix could be strengthened by MWCNTs in possible mechanisms of grain refining and load transfer strengthening [28]. In other work, the authors refereed a significant strengthening effect in the aluminium matrix caused by substantial reduction size due the addition of 1.3 vol% of MWCNT (high milling time – 48 h), where YS and UTS were about 312 MPa and 368 MPa (compared to 118 MPa and 133 MPa for pure aluminium) [6]. However, some of the significant strengthening it is due to the presence of  $Al_4C_3$  carbides and reduction of average grain size [29].

*S. Suárez et al.* [30] showed a strong dependence between MWCNTs addition and the grain size. A large grain size was observed for pure nickel and the addition of 6.5 vol% of MWCNTs induces abnormal grain growth, whereas for 12, 18 and 27 vol% a significant change in grain size was observed, where grain size was much more refined [30]. However, *S. Simões et al.* [29] and *I. Carneiro* [31] observed an increasing of hardness values (about 50 %) with addition of MWCNTs (1 vol%) to nickel matrix, over the non-reinforced nickel. However, the total of MWCNTs do not contribute to the strengthening, since some of MWCNTs clusters were observed in the grain junctions are not bonded to the matrix and cannot assure the load transfer [29]. The increase of % MWCNTs (above 1 vol%) leads to the formation of larger clusters, increasing the heterogeneous distribution of MWCNTs [29].

*P. Wang et al.* [32] produced Inconel 625 composite reinforced with 0.65 vol% MWCNTs by the way similar to MIM process, but instead of injection moulding, made pressing. These authors performed the sintering under different atmospheres (argon, vacuum and hydrogen) and measured the highest densities for parts sintered in argon atmosphere. Also presented differences between the Inconel 625 powders with and without milling, where the density of the sintered milled powders was lower than the as-received powder. In what concerns to Inconel 625 nanocomposite reinforced with MWCNTs, the authors showed further improvement in hardness (96 %), when sintered under argon atmosphere at 1325 °C. This is due to the pinning effect of MWCNTs during the movement of dislocation of grains [32]. In other work, the same composite was produced by selective laser melting (SLM), with an improvement in UTS by 14 % and YS by 30 %. However, the elongation of composite was significantly reduced due to crack initiation from the matrix-

MWCNT interface under high stress loading [33]. These last references showed the ability of MWCNT to “survive” at high temperatures and "aggressive" manufacturing processes, like SLM.

Different aspects must be highlighted from the characteristics of carbon nanotubes to the effect of mixing and processing, including shaping and sintering. Because all of them have significant effect in the final characteristics and properties of the nanocomposite parts/devices.

## 1.1 Carbon Nanotubes

The hybridization of the carbon atomic orbital in the forms of  $sp^1$ ,  $sp^2$  and  $sp^3$  produces different allotropes, from diamond to nanotubes. Carbon in the form of diamond exhibits a  $sp^3$  type tetrahedral covalent bonding. The bonding in graphite is  $sp^2$ , with each atom joined to three neighbours (covalently bonded) in a trigonal planar arrangement to form sheets of hexagonal rings [2], [34], [35]. The graphene is single carbon of layer (s) of graphite structure (IUPAC). The CNTs results from rolling a layer of graphene into hollow cylinders, where nanometric dimension is the diameter. The CNTs were discovered in 1991 by Iijima as a minor sub-product of fullerene synthesis [1], [11], [34]. The characteristics of CNTs can be different depending on graphene sheet has been rolled up to form the tube [1], [34], [35]. Conceptually, the graphene sheets can be rolled into different structures: zig-zag, armchair and chiral (figure 1.1). Two of them correspond to high symmetry CNTs; in “zigzag” tubes (top), some of the C–C bonds lie parallel to the cylinder axis, while in “armchair” tubes (bottom left), some bonds are perpendicular to the axis. The nanotube structure can be described by a chiral vector ( $\vec{C}_h$ ) defined by the following equation [2], [35]:

$$\vec{C}_h = n\vec{a}_1 + m\vec{a}_2 \quad (\text{Eq. 1})$$

where  $\vec{a}_1$  and  $\vec{a}_2$  are unit vectors in a two-dimensional hexagonal lattice. The n and m define the tube: diameter, chirality, metal versus semiconducting nature, and band gap, if semiconducting.

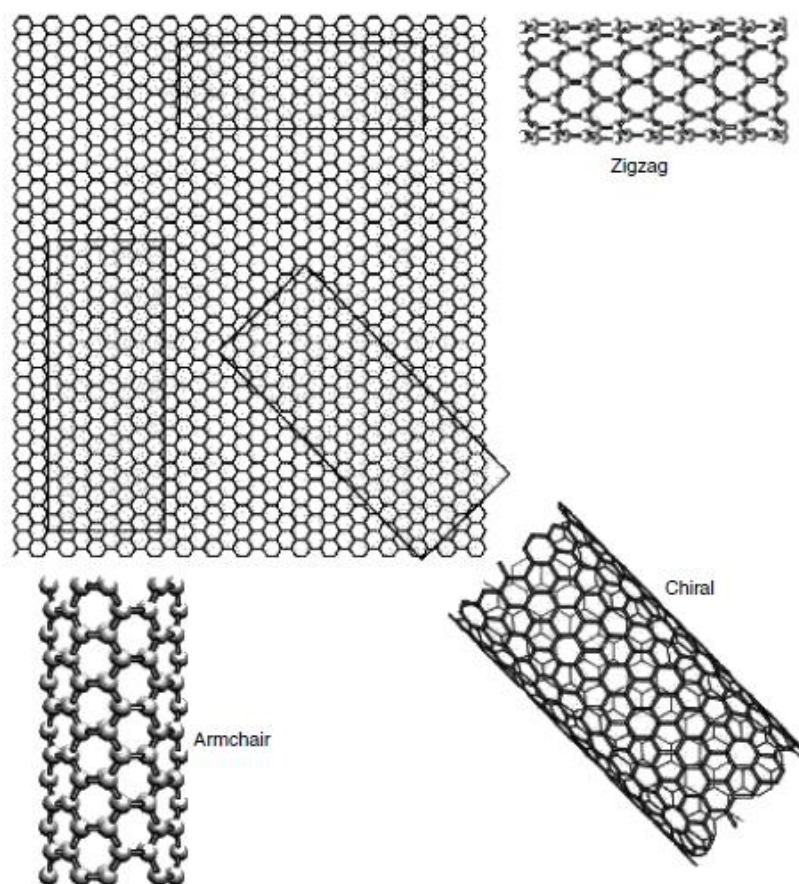


Figure 1.1 – Schematic representation of the relation between nanotubes and graphene [34]

More and more, the CNT are changing to MWCNT comprise coaxial cylinders with an interlayer spacing of 0.34 nm [11], [35], mainly due to toxicological problems resulting for their inhalation. The diameter of MWCNTs usually ranges from 4 to 30 nm [2], [35]. The individual sheets are bonded to one another by secondary bond of Van der Waals forces. Moreover, CNTs tend to agglomerate and form CNTs clusters [1], [34]. For instance, the excellent mechanical and physical properties such as, super high elastic modulus between 0.5 – 2 TPa, large ultimate tensile strength of 20 – 150 GPa, high flexibility and low density show the high level of these nanomaterials [3], [18], [35]. The extraordinary properties of carbon nanotubes are responsible by high impact on developing new generation of nanoreinforced composites, where it is necessary to overcome the new challenges in wide range of applications, for a sustainable society (table 1.1).

Table 1.1 – Applications of MMC with carbon nanotubes [36]

Industry	Application	Property
Automobile industry	Break shoes, cylinder liners, piston rings, gears	High mechanical strength, wear resistance and thermal conductivity, low density
Aerospace industry	Aircraft brakes, landing gears	High wear resistance and thermal conductivity, low density
Space applications	High gain antenna boom, structural radiators	High mechanical strength and electrical conductivity, low coefficient of thermal expansion and density
Sports industry	Light weight bicycles, tennis and badminton rackets	High elastic modulus and mechanical strength
Electronic packaging	Heat sinks for thermal management, solders	High mechanical strength and thermal conductivity, low coefficient of thermal expansion
MEMS and sensors	Micro-beams, micro-gears	High elastic modulus and surface area
Battery and energy storage	Anodes and anode coatings, hydrogen storage materials	Large surface area, high current density, reduced response times, increased H <sub>2</sub> adsorption–desorption rate

Several techniques have been developed to produce CNTs, although only three methods: electric arc discharge, laser ablation and chemical vapour deposition (CVD) are widely implemented [35], [37]. Actually, due to low temperature, the CVD is the most popular method to produce carbon nanotubes. In the low temperature CVD can be accurately controlled the nanotube length, diameter, alignment, purity, density, and orientation [35]. The production of carbon nanotubes by CVD or CCVD (Catalytic Chemical Vapour Deposition) technology that commands the largest market share of the overall carbon nanotubes market [35], [38], due its relative simplicity of operation, process control, energy efficiency, raw material used, high yield and purity. Comparison of different techniques according to the yield rate, cost, synthesis temperature, nanotube type, advantage and disadvantage is summarized in table 1.2.

Table 1.2 – Comparison of electric arc discharge, laser ablation and CVD methods [35], [37]

Method	Arc discharge	Laser ablation	CVD
CNTs Yield rate (%)	< 30	≈ 70	95 – 99
Per unit design cost	High	High	Low
Reaction temperature (°C)	3000 – 4000	3000	500 – 1100
SWNT or MWNT	Both	Both	Both
Advantage	High quality nanotubes	Continuous production	Uncomplicated and flexible technology, large-scale production, aligned growth possible
Disadvantage	Tangled nanotubes, energy extensive	Method limited to the lab-scale	Synthesized CNTs are usually MWNTs, defects

In addition, these materials are available in different forms such as: as-received, purified, functionalized (e.g. COOH, OH) [22], coated (e.g. with Cu, Ni, SS 316L) [39]–[41] and heat treated (2000 – 3000 °C) [39]. Regarding the purification, functionalization and subsequent CNTs examination are costly and time consuming [2]. Consequently, these steps are not always considered in order make the process more expensive and the CNTs are used as-received [40].

None of the techniques mentioned can produce pure CNTs. In order to make use of CNTs it is often necessary to purify them. Depending on CNTs synthesis way, there are many different methods for purification. Therefore, existence of methods with single step processes and unaffected on properties of CNT is essential for producing clean nanotubes and should be targeted in the future [35]. Some scientist prefers to use sonication of nanotube in different media and afterward thermal oxidation of CNT material (at 470°C), as well as acid treatments (table 1.3) [35].

Table 1.3 – Purification methods

Purification	Ref.
Concentrated acid solution H <sub>2</sub> SO <sub>4</sub> :HNO <sub>3</sub> (3:1) under ultrasonic treatment	[19], [20], [22], [25], [32], [33], [42], [43]
HNO <sub>3</sub> , under ultrasonic treatment	[21], [25], [44], [45]
Non	[6], [12]–[14], [18], [23], [24], [26]–[31], [46]–[49]

The temperature and atmosphere which nanotubes are subject can compromise their performance. When the environment atmosphere is air, the thermal stability above 400 °C of MWCNTs is lost, and at 900 °C the degradation is maximum. However, under an inert atmosphere and for high heating rates, the MWCNTs can be stable up to 1300 °C, with very low oxidation ( $\approx 25\%$ ) [50]. In metallic matrix composite, the nanotubes have different behaviour in what concern temperature, due to the active role of the elements present.

The matrix has the main role in the quality of the composite reinforced by CNTs, to obtain a desirable microstructure and to improve the mechanical properties, it is essential a homogeneous distribution of carbon nanotubes in the matrix [6], [14], [17], [28], [34], [36]. Thus, the dispersions of nanoreinforcement in MMC is one of the most significant challenges in the fabrication of nanocomposites. Many researchers have measured low strength, high porosity, and discontinuities due to the clustering phenomena, that leads to the decreasing of mechanical properties [36]. The main factors for heterogeneity are as follows:

- incompatibility between metallic matrix and nanoreinforcement;
- large difference in density;
- poor wettability, resulting in CNTs aggregation;
- bundling and tangling phenomena of CNTs due to the high surface area of CNTs associated with Van der Waal forces between individual CNTs;
- and unsuitable mixing during the preparation of feedstocks [18], [21], [26], [28].

## 1.2 Preparation of nanocomposite powder mixture

One important challenge is to ensure the structural and chemical stability of the CNTs in the metallic matrix. Therefore, several techniques have been proposed to improve the dispersion of CNTs in metallic matrix, which have their own advantages and disadvantages [43]. Techniques such as [39]:

- coatings of CNTs (molecular level mixing, PVD (Physical Vapour Deposition) and CVD);
- dispersion in solvents and surfactant/ultrasonic support;
- dispersion in acids (chemical oxidation);
- and mechanical dispersion.

The powders coating with carbon nanotubes can promote a better dispersion of the nanoreinforcement in matrix. For example, the stainless steel – CNT nanocomposite powder was synthesized by CVD method, where CNT grown in situ [36], [40], [41]. Other authors performed a uniform copper layer (coating) on the surface of carbon nanotubes [25].



*J. Liao, and M. J. Tan* [26] performed a pre-mixture between CNT and polymeric material (i.e. polyethylene glycol) and heated under the melting point temperature of polymer, following the mixture with aluminium powders. This polymer is a non-ionic surfactant with the ability to decrease the agglomeration and improve the dispersion of CNTs [26]. The last one method named as polymer binder assisted. Some of the solvents based on amides are used for dispersion of CNTs or other possibility is to disperse CNTs in water by using surfactants. In this case, the CNTs are covered by the surfactants and help to form a stable colloidal dispersion. The surfactant acts as a coupling agent and may introduce repulsive forces between individual CNTs. These repulsive forces are larger than the Van der Waals attractive forces between the surfaces of CNTs [11], [28], [39].

The chemical oxidation of CNTs surfaces with acids can introduce oxygen containing functional groups onto the surface. During this process, open ends are formed in the oxidizing environment, which result in a well dispersed, electrostatically stabilised colloid in liquids, such as ethanol, isopropanol, ethylene glycol or acids [30], [32], [33], [39]. The efficiency of these last strategy depends on the liquid selected, energy and time ultrasound.

Milling is the most sustainable process to achieve mechanical bonding. In mechanical milling, the metallic powders with nanoreinforcement are mixed into a rotating jar with hardened metallic/ceramic balls (figure 1.2). This disperse method it is the most popular because it is simple, easy to control, and applicable to almost all metallic matrices [6].

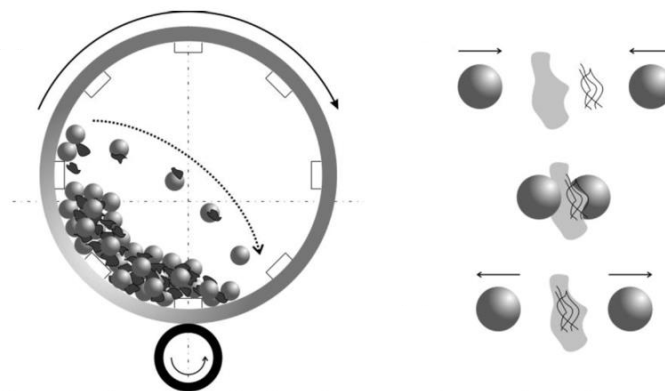


Figure 1.2 – Schema of ball milling process [3]

During milling, the impact of particles against balls and jars leads to their deformation, welding and re-welding or fracturing depending on metallic powders characteristics (ductile and brittle). In the case of ductile metallic powders, the initial impact of the balls causes flatted powders that helps CNTs to be embedded in them [21]. Moreover, in the nanocomposites based on CNTs, the milling induces to their entrapment in metallic powder particles [18], [27]. Milling process must be handled in order to retain the C chemical bonding of the CNTs, since damages of the CNTs materials can be occurred frequently [36]. *M. J. Yu et al.* [47] studied

the influence of balls/powder weight ratio (BPR) on nanocomposite materials and showed that when BPR was 5:1, the balls are not enough to crush powders. Consequently, the CNTs twist around the metallic powders (copper), which is harmful in bonding CNTs with metallic powders. When the BPR was 10:1, the CNTs were distributed homogeneously, ensuring the uniformity of impact and friction on powders. During ball milling, flaky powders (Al, Cu or Fe) were gradually produced under the impact between balls, that is favourable to CNTs entrapment [14], [26], [28], [45]. Although the milling process contributes for homogeneous dispersion, some authors detected the damaging and the reduction length of CNTs with the milling time [6], [17], [18], [26], [28], [36]. The increasing milling time, yields CNTs will progressively lose its tubular structure and after long milling time (50 h), the tubular structure would completely disappear [26].

The milling step between matrix powder and CNTs can be performed with addition of external elements and is named solution ball milling [28]. These elements can be solids (surfactants or stearic acid) in jar, under gaseous atmosphere to protect the metallic powder from excessive oxidation during milling or under solution (i.e. isopropanol). Some authors introduce stearic acid or other polymeric material to assist in the dispersion step, which obliges to an intermediate heat treatment to remove it (like debinding step) [6], [32].

Moreover, interfacial bonding of metallic matrix and nanoreinforcements could be weak or strong depending on mutual solubility and/or wettability, which may induce low density, high porosity, or segregation of the reinforcements [13], [26]. The milling step is important, not only to disperse the nanoreinforcement, but also to create a physical bonding between the powders and MWCNTs, saving the structure of last one. Table 1.4 shows the parameters of milling used by some authors for distinct matrix/MWCNTs.

After preparation of pre-mixture, where the suitable distribution of CNTs is the target, the production of parts/devices with different configurations, it is the next goal. The processing most used are powder pressing (uniaxial, cold isostatic pressure (CIP) or hot isostatic pressure (HIP)), spark plasma sintering (SPS), selective laser melting or metal injection moulding, depending the geometry and the number of components. Generally, the MMC manufacturing by powder technology involves typical three main steps: mixing (matrix powders with MWCNT nanoreinforcement), shaping and sintering [1], [36].

Table 1.4 – Mechanical milling parameters

Material	Time (h)	Speed (rpm)	Atmosphere	BPR	Ref
Cu-MWCNT	1	200	Argon	10:1	[18]
	2	700 – 900	Argon and stearic acid (2.7 vol%)	5:1 10:1 15:1 20:1	[47]
	3	250	Argon	10:1	[21]
	3	200	Argon	10:1	[23]
	5	500	Ethanol	-	[20]
	6	300	Acetone	-	[19]
	9	300	Argon	5:1	[24]
	20	200	Argon	5:1	[14]
Al-MWCNT	1	200	-	-	[28]
	1, 2 and 3	-	Air	-	[27]
	1	200	Isopropanol and surfactants	5:1	[6]
	2 to 48	200	Argon gas and stearic acid (2.7 vol%)		
	2 and 4	200	Stearic acid (5.4 vol%)	5:1	[26]
Inconel 625-MWCNT	6	400	Isopropanol	5:1	[32]
	-	-		-	[33]
Ni-MWCNT	1/4	20800	Isopropanol		[29], [31]
Fe-MWCNT	4	-	Surfactant	-	[45]

### 1.3 Manufacturing

Whatever the manufacturing process selected, it must ensure minimal damage of the nanoreinforcement, particularly on CNTs structure resulting from pressure, heat or chemical reaction with the matrix material, encouraging defects on CNTs, loss of carbon and/or carbide formation which affect the properties of the composites [1]. In all the process steps, besides

the goal be to achieve a homogeneous dispersion of CNTs in the metallic matrix, the focus is also to reach a good bonding at the metal/CNT interface.

In summary, the challenges in processing metallic/CNTs nanocomposites are [36]:

- homogeneous dispersion of CNTs in the metallic matrix;
- interfacial bond strength between CNTs and metallic matrix;
- chemical and structural stability of CNTs.

The research is still incomplete in the description and understanding of the thermal behaviour of CNTs, particularly when the “environment” is a metallic matrix with elements with or without affinity to carbon.

The MMC processing is similar to the processes used for powders depending on geometry and number of parts/devices, like pressing/sintering, powder injection moulding (PIM), additive manufacturing, etc. The parameters as a function of selected matrix by different authors are exhaustively summarized in table 1.5 (considering firstly the process and the CNT content).

Table 1.5 – MMC processing parameters

Material	Process	CNT (vol%)	Parameters	Ref
Cu-MWCNT	Pressing and sintering	0; 0.5; 2; 4; 8 and 16	Hot pressing: 40 MPa Sintering: 750 °C, Argon atmosphere	[18]
		0; 1 and 2	Mixing: 60 min Pressing: 80 kN Sintering: 5 °C/min to 900 °C; holding time: 45, 60 and 90 min; Argon atmosphere	[13]
		0; 2 and 4	Uniaxial pressing: 31 MPa Sintering: 820 °C	[21]
		0 – 15	Cold uniaxial pressing Sintering: 850, 900, 950 °C; holding time: 2h, Argon atmosphere	[19]
		0.2; 5 and 10	Hot uniaxial pressing: 30 MPa Sintering: 700 °C, 30 min, vacuum	[14]
		4	Hot pressing: 150 MPa Sintering: 700 °C; holding time: 30 min; Argon atmosphere	[23]

Cu-MWCNT	Hot extrusion and sintering	21	Extrusion: 950 MPa Sintering: 850 – 880 °C	[20]
	SPS	0; 0.1; 0.3; 0.5 and 1	Uniaxial pressing: 50 MPa Sintering: 100 °C/min (heating rate); 700 °C, holding time: 5 min	[25]
		0; 0.5; 1; 1.5; 2; 3; 5; and 10	Uniaxial pressing: 50 MPa Sintering: 50 °C/min (heating rate); 550 °C, holding time: 1 min	[42]
		0; 5; 10 and 15	Pressing: 50 MPa Sintering: 100 °C/min (heating rate); 600 °C; holding time: 5 min	[44]
		0.3; 0.5; 1; and 2	Pressing: 40 MPa Sintering: 50 °C/min (heating rate); 800 °C, holding time: 30 min	[24]
Al-MWCNT	Pressing and sintering	0.5; 0.75; 1.0; 1.5 and 2.0	Pressing: 300 MPa Sintering: 640 °C, holding time 90 min; vacuum	[29]
		1.3	Pressing: 55 MPa Sintering: 600 – 640 °C; holding time 30 min	[27]
	SPS	0.65	Pressing: 30 MPa Sintering: 500 °C; holding time: 20 min, vacuum	[26]
		1	Pressing: 30 MPa Sintering: 600 °C; holding time: 30 min, vacuum	[28]
		1.3	Sintering: 20 °C/min (heating rate); 600 °C; holding time: 60 min	[6]
Ni-MWCNT	Pressing and sintering	0.5; 0.75 and 1	Pressing: 900 MPa Sintering: 950 °C, holding time 90 min; vacuum	[31]
		0.5; 0.75; 1.0; 1.5 and 2.0	Pressing: 900 MPa Sintering: 950 °C, holding time 120 min; vacuum	[29]
		6.5; 12; 18 and 27	Pressing: 990 MPa Sintering: 950 °C, holding time 150 min; vacuum	[30]

Inconel 625-MWCNT	Pressing and sintering	2.0	Pressing: 637 MPa Debinding: 5 °C/min (heating rate); 700 °C, holding time 60 min; Argon atmosphere Sintering: 5 °C/min (heating rate); 1050 °C, holding time: 60 min; and 5 °C/min (heating rate); 1325 °C, holding time: 60 min; Argon, vacuum and hydrogen atmospheres	[32]
	SLM	2.0	Laser melting: laser power of 360 W; laser scan speed of 400 mm/s; layer thickness of 50 µm	[33]
Ti-MWCNT	Pressing and sintering	1.8	Hot pressing: 30 MPa Sintering: 10 °C/min (heating rate), 900, 1100 and 1300 °C; holding time: 60 min; Vacuum atmosphere Heat treatment: 1100, 1200, 1300 and 1400 °C, holding time: 60 min; Vacuum atmosphere	[7]

During last decennia, there are an increasing number of publications about manufacturing of nanocomposites based on Al, Ni and Cu alloys with MWCNTs, mixture by ball milling, followed of pressing and sintering. However, there is a lack of studies concerning nanocomposites based on stainless steel nanoreinforced with MWCNTs using other manufacturing processes, more dedicated to complex shape and high series of parts/devices. The MIM route has enabled the fabrication of MMCs containing materials that are not compatible in molten state and difficult to fabricate by conventional routes [8], [39]. However, it is necessary to guarantee three important factors:

- suitable nanoreinforcement content in the feedstock;
- ensure feedstock with suitable flowability for injection step;
- and stability of nanoreinforcement in matrix along all the processes steps.

The metallic powder injection moulding, due to its applicability to several materials, such as steels (highest), copper, titanium, aluminium, composites materials and enlarging the utilization to hard and refractory metals, allowing the manufacturing of complex structures [51]–[53]. They specially are successful in delivering higher strength than resulting from die casting, improving tolerances (dimensional accuracy), reproducibility and high number production. Last but not least, it reduces significantly the finishing processes when compared

with the most consolidation methods, capability to reduce wastes materials and increasing economic efficiency [54], [55].

Some authors prepared the composites feedstocks directly in mixer [49], [56], while others use a pre-mixture of powders and CNTs mainly through ball milling and only after it, mixed with binder in order to produce a composite feedstock for MIM [45]. The addition of CNTs into the mixture increases significantly the torque value or the feedstock viscosity, as shown *L. Shuquan et al* [45]. In some studies, the percentage of CNTs added to nanocomposite using MIM compared to other processing techniques is low. On the other, when the content of carbon nanotubes added is high, the feedstock produced has a very high viscosity and consequently can be difficult or impossible to be injected. Moreover, the inhomogeneity after injection moulding of the “green parts/devices” may be a new source of defects that obliges to pay attention. However, the most of research work with access does not emphasize the mixing step (with binder), or its ability for the injection step.

Nevertheless, the “sustainability of new times” needs a significant decrease of parts/devices weight, in the most cases, the solution it is a reduction of dimensions. This requires a new manufacturing processes – micromanufacturing. These processes are similar to the conventional ones, but oblige new equipment and new procedures [55]. Generally, the micro parts/devices from  $\mu$ MIM process have sizes of several micrometres up to millimetres with three-dimensional microstructures located on one or more surface areas [57]. Figure 1.3 shows the situation of different processes in a roadmap on processing of macro/micro/nano parts/devices, until 2030.  $\mu$ MIM is one the most promised technologies to overcome the needs of XXI century.

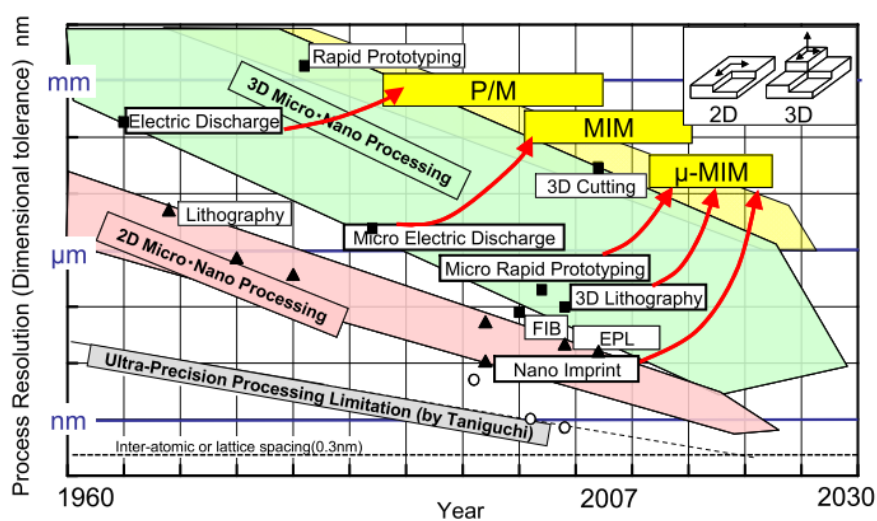


Figure 1.3 – Roadmap of PM, MIM and  $\mu$ MIM processes [52]

## a) $\mu$ MIM

The figure 1.4 shows the flowchart of  $\mu$ MIM process adapted to nanocomposite production. As referred, the feedstock is the mixture of powders, CNTs and binders and the component obtained after injection moulding designated by “green part”. The “brown part” is the specimen after debinding and sintering that means “final part”.

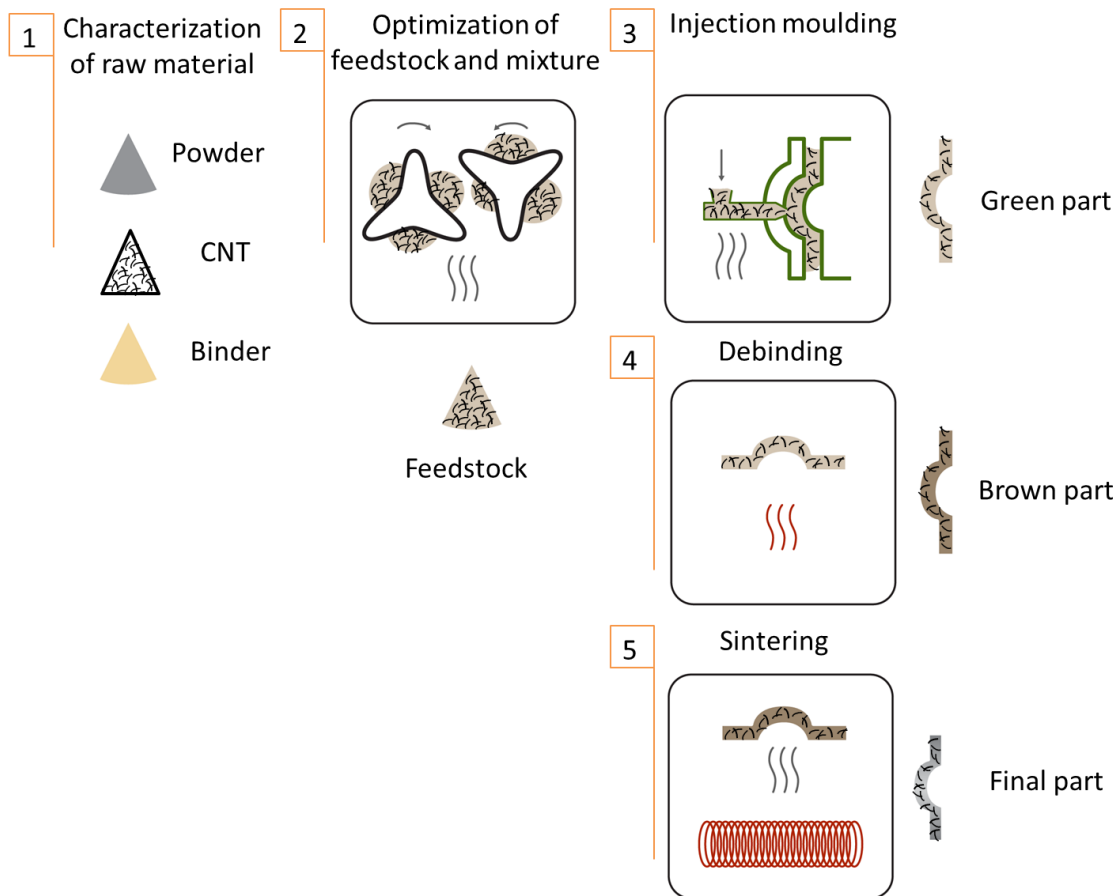


Figure 1.4 – Flowchart of MIM process (adapt. by [58])

## *Metallic Powders*

The powders characteristics (4S's) assumes always a relevant role whatever the process selected. However, this is crucial in micromanufacturing processes, as  $\mu$ MIM [9]. Atomization is the dominant mode of powders production because high production rates, favour economy of scale and pre-alloyed powders can only be produced by atomization [59]. The powder selected for the present study – SS 316L manufactured by water, gas or centrifugal atomization (figure 1.5). Even though the principle methods to be the same, the shape and surface characteristics of the powder particles are different. The atomization methods, such as gas or water are more than 95 % of powder atomization production [60].



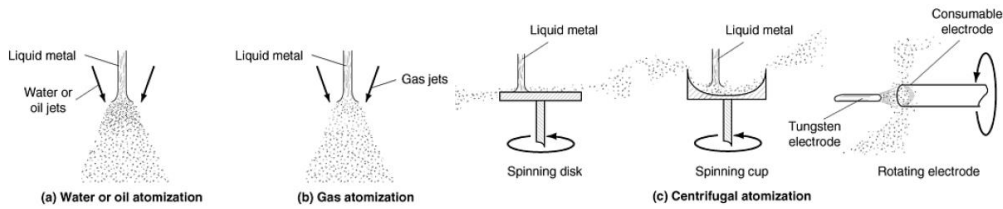


Figure 1.5 – Atomization processes [60]

The water atomization tends to produce non-spherical particles with a rough surface, while gas atomization yields spherical and smooth particles [55]. The reason is that in water atomization the solidification of the metallic particles occurs very quickly, freezing the turbulent structure of the metal droplets attained during impact. On the other hand, in gas atomization the cooling rate allows spherical particle formation. When possible by the chemical composition of particles, water atomization is possible and contributes to low-cost production [55], [60]. Moreover, the temperature of water-cooling can allow attaining a shape factor close to 1, as in the powders furnished by ATMIX® Company, used in the present study. The spherical powder shape in  $\mu$ MIM led to a high packing density (more solids loading) and less shrinkage than for other shapes [55].

For  $\mu$ MIM, due to a significant effect of powder size on final dimensional precision, small particle sizes (less than 5  $\mu\text{m}$ ) have advantages to structural micro features, having atomization also a significant role [54], [55], [61]–[63]. However, as the powder size decreases, other processing challenges must be overcome. For example, the increasing of solids content in the feedstock leads to an increasing viscosity, until it becomes too viscous to be injected into a mould [64]. Fine powders lead to difficulties in attaining a high packing density because of particle agglomeration, in spite of increasing the sintering success [52], [54], [55]. In addition, powders with a broad particle size distribution may be favoured, due to higher packing density as compared to a close distribution [55], [57]. Surface area of powders is the driving force for the sintering process [54]. In table 1.6 are summarized some characteristics of powders for  $\mu$ MIM.

Table 1.6 – Characteristics of SS 316L powders used in  $\mu$ MIM

Powders	Production	Shape	Size $d_{10}/d_{50}/d_{90}$ ( $\mu\text{m}$ )	Ref.
SS 316L	Gas	Spherical	-7/10	[9], [65]
			1.8/3.4/6.0	[57], [66]
			2.5/6.3/9.7	[67]
			3.1/6.3/19.9	[64]
			3.2/5.1/8.1	

SS 316L	Water	spherical	1.4/3/5.2	[68]
			1.8/4.4/7.6	[69]
	Water	irregular	-/4/-	[70]
			-/3/-	[71], [72]
			1.1/3.4/8.3	[73]
			1.2/2.4/4.0	[74]
			2.1/4.0/7.3	[75]
	Water	-	-/3/-	[53]
			-/4/-	[76]
			1.2/2.4/4.0	[62]
			2.1/4/6.7	[77]
			3.2/7.3/10.4	[78]
	-	spherical	1.8/3.4/6.0	[79]

### *Binder*

Besides the main role of powder characteristics in  $\mu$ MIM, it is also important the binder used to prepare the feedstock to be injected. The binder let to the metallic particles be together and to provide suitable fluidity to feedstock [55]. Typically, the binder consists on a primary component (called back bone) that is solid at ambient temperature and viscous at feedstock processing temperature [51], [80]. Moreover, some additives can be in polymer mixture to improve the flow properties of the feedstock and to increase the interaction among metallic powder and binder. The additives include dispersants, stabilizers and plasticizers. Dispersants increases wettability of powder and reduces the surface energy. Stabilizers, prevent particle agglomeration of powder particles and the plasticizers increase the flow behaviour [55]. Thus, binder is a mixture of several polymers and other additives in order to accomplish three functions – homogeneity, low viscosity of the feedstock and suitable debinding (different numerical molecular weight of polymers) keeping the shape of the “green part” [54].

Therefore, the binder should be a temporary vehicle for shaping. During debinding, the shape of the metallic part (brown) must be unchangeable. The properties of binder have influence on the metallic powder distribution, shaping process, dimensions of parts, and the final properties of the sintered (table 1.7).

**Table 1.7 – Characteristics of ideal binder system by  $\mu$ MIM process [55]**

	<b>Desirable characteristics</b>
Binder	Easily available and inexpensive Durability Safe and environment friendly Not degradation due to cyclic heating High strength and stiffness Low thermal expansion coefficient
Powder interaction	Low contact angle Good adhesion with powder Capillary attraction of powder particles Inertness to powder
Flow characteristics	Low viscosity at the moulding temperature Low viscosity changes during moulding Increasing viscosity during cooling
Debinding	Degradation temperature above of mixing and injection temperatures  Multiple different organic polymers that led a progressive debinding, function the methodology selected to debinding  Low residual carbon content after debinding Non-corrosive and non-toxic after debinding

A homogeneous distribution of powder particles in binder is important to obtain a isotropic shrinkage, after debinding and sintering [66]. Avoiding segregation of feedstock components is necessary to prevent visual defects, excessive porosity, warpage and cracks in the sintered part [51]. Table 1.8 shows several binder combinations used in  $\mu$ MIM.

**Table 1.8 – Different binders combinations used**

<b>Binder system</b>	<b>Ref.</b>
PAN 250 + HDPE + EVA	[76]
PAN 250 + LDPE	[53], [74], [77]
LDPE + PW + PP + SA	[66], [79]

LDPE + PW	[57], [61]
LDPE + PW + EVA	[68], [72]
HDPE + PW	[64]
HDPE + PW + EVA	[78]
PP + PW + SA	[69]
Agar based and commercial binder	[9]
Commercial binder ( $L_c$ )	[58], [65], [67], [73]
Commercial binder ( $M_1$ )	[58], [67], [81]–[84]
Polyacetal-based binder	[70]
Wax based binder	[62]

### *Preparation of Feedstocks*

The mixing is a critical step in feedstocks quality, since an inhomogeneous feedstock induces defects that is not possible to overcome in the following steps.

The torque rheometry, is useful in determining maximum and optimum solids loading and the homogeneity of feedstocks as result of a mixing process (last one was used in this work) [10]. On the other, capillary rheometry is also common used because its usefulness in measuring viscosity [12], [64], [68], [78]. However, in last decennia different authors adopted the first one as the technique suitable to characterize the feedstocks to be injected with success [10], [63], [65], [67], [73], [83]–[85].

In feedstocks, CPVC (Critical Powder Volume Concentration) is the maximum volume of powder, suitable to became it injectable [10], [63]. This methodology let to evaluate with high precision the optimum content of binder. High powder content in feedstock with fluidity (4 N.m) results in the best shape preservation enhances sintering process and minimizes shrinkage (figure 1.6). When the fraction of fine powder increases, the viscosity values are higher, moreover when the particle size decreases, the feedstock behaviour becomes more pseudo-flux [64].

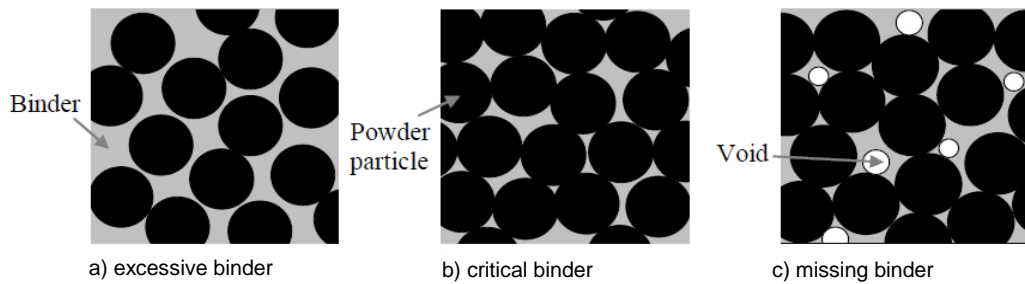


Figure 1.6 – Distribution of binder a) excessive binder, b) optimal powder:binder and c) insufficient binder [86], [87]

Table 1.9 shows the several volume concentrations of powder in different feedstocks as well as the mixing parameters, used in  $\mu$ MIM.

Table 1.9 – Feedstock composition and mixing parameters by  $\mu$ MIM

Powder (vol%)	Equipment/ parameters	Ref.
50, 55, 60, 65	Haake Rheocord 252p/ 170 °C, 45 min, 40 rpm	[64]
55, 58, 61	Haake Rheocord 90/ 140 °C, 30 min	[74]
57, 62	Brabender Plastograph W 50/ 150 °C, 20 min, 60 rpm	[9]
58	Herman Linden Z-blade/ 140 °C, 30 min	[62]
59	Z-blade /-	[61]
60	Brabender Plastograph W 50 / 160 °C, 30 rpm	[79], [82]– [84]
	Z-blade/ 160 °C	[66]
	Herman Linden Z-blade/ 150 °C, 40 rpm	[68], [72]
	Haake Rheocord / 30 min, 30 rpm	[78]
	Haake Rheocord / -	[77]
60, 62, 65	Brabender Plastograph W 50/ 160 °C, 30 rpm	[67]
60, 62, 64, 66	Brabender twin-screw W 50 EHT/ 160 °C, 30 rpm	[57]
60, 65, 67, 69, 71	Herman Linder Z-Blade/ 180 °C, 90 min, 60 rpm	[69]

61	Brabender Plastograph W 50, 20 min, 150 °C, 60 rpm	[73]
61.7, 66.2, 71.2	Haake Rheocord, 140 °C, 60 rpm, 30 min	[88]
62	Brabender Plastograph W 50, 20 min, 160 °C	[65]

The feedstocks are thermally characterized using DTA (Differential Thermal Analysis) for measuring of the glass ( $T_g$ ) and melting ( $T_m$ ) temperatures. TGA (Thermal Gravimetric Analysis) let to evaluate the thermal stability temperature for each component of binder and percentage of weight lost function of temperature. After it is possible to stablish the thermal cycle of debinding [54], [78], [89].

In the production of nanocomposite feedstocks, the introduction of the reinforcement is performed in mixing step. As referred, there are some studies that report the increase in torque value with the addition of nanotubes [45], [48]. The time to attend the permanent regime of the torque for a mixture is an indicator of homogeneity. There are not found bibliography concerning the nanocomposites feedstocks produced by  $\mu$ MIM, and relative to MIM the information is few and are compiled in table 1.10.

Table 1.10 – Different nanocomposites feedstock composition and mixing parameters for MIM

Matrix	MWCNT (vol%)	Equipment/ parameters	Ref.
Cu	0; 1; 2; 5; 7.5 and 10	Haake Rheomix 600/ 165 °C, 30 rpm, under 30 min;	[43]
	0; 1; 2; 5; 7.5 and 10	Co-rotation twin screw/ 59 vol% Cu + MWCNT + PW + HDPE + SA, mixing temperature =160 °C	[48]
	0; 1; 5 and 10	Z blade/ 59 vol% Cu + MWCNT+ HDPE + SA; mixing temperature =160 °C	[22]
	2.5	Z blade/ 59 vol% Cu + MWCNT +PW + HDPE + SA; mixing temperature =160 °C	[12]
Fe	0; 0.7; 1.8; 3 and 4	XSH–60/ 46 – 62 vol% Fe + MWCNT + PW, HDPE + EVA + DVP; mixing temperature 150 °C, under 2h, 47 rpm	[45]
	4 – 22	Sigma mixer/ 160 °C	[49], [56]

## *Injection moulding*

After characterization of the optimized feedstock, it was introduced in an injection moulding suitable for  $\mu$ MIM. The injection moulding is an exciting step in  $\mu$ MIM, since the quality of produced “green parts” has a significant effect on final quality parts/devices concerning accuracy and defects [54].

The process parameters is usually attained by adjusting the pressures and temperatures and/or speeds of melt flow during the filling the thinnest cavities in mould [54], [60], [77]. After cooling the moulding, the parts/devices are extracted and the cycle repeated. Table 1.11 summarizes the injection moulding parameters applied by different authors that processed by  $\mu$ MIM of SS 316L feedstocks.

Microsized parts/devices can be injected using conventional moulding machines and specifically designed for components of this size scale, [55]. The injection moulding conditions of MIM have to be modified/adapted for  $\mu$ MIM, particularly in what concerns mould temperature (high) and ejection speed (low) [61], [77]. This way is to guarantee the complete filling into a narrow cavity and to extract fragile “green parts”. A careful handling is also required in the debinding and sintering processes.

Table 1.11 – Injection moulding parameters by  $\mu$ MIM

<b>Equipment/ parameters</b>	<b>Ref.</b>
-/ $T_{\text{mould}} = 55 \text{ }^{\circ}\text{C}$ ; $T_{\text{inj}} = 180 \text{ }^{\circ}\text{C}$	[61]
-/ $T_{\text{mould}} = 60 \text{ }^{\circ}\text{C}$ ; $T_{\text{inj}} = 170 \text{ }^{\circ}\text{C}$	[77]
Battenfeld 250CDC/ 8 MPa; $T_{\text{mould}} = 40 \text{ }^{\circ}\text{C}$ ; $T_{\text{inj}} = 160 \text{ }^{\circ}\text{C}$	[53], [62]
Battenfeld 250CDC/ 10 MPa; $T_{\text{mould}} = 60 \text{ }^{\circ}\text{C}$ ; $T_{\text{inj}} = 180 \text{ }^{\circ}\text{C}$	[68], [72]
Arburg 220-S/ 100 MPa; $T_{\text{inj}} = 180 \text{ }^{\circ}\text{C}$	[57]
Arburg 220-S/ 100 MPa; $T_{\text{mould}} = 65 \text{ }^{\circ}\text{C}$ ; $T_{\text{inj}} = 190 \text{ }^{\circ}\text{C}$	[66], [79]
Arburg 220-S/ 150 MPa; $T_{\text{mould}} = 65 \text{ }^{\circ}\text{C}$ ; $T_{\text{inj}} = 140 - 160 \text{ }^{\circ}\text{C}$	[65], [67], [73]
Arburg 270-C/ 10 MPa; $T_{\text{mould}} = 60 \text{ }^{\circ}\text{C}$ ; $T_{\text{inj}} = 150 \text{ }^{\circ}\text{C}$	[83], [84]

Nanocomposites feedstocks produced by  $\mu$ MIM are not bibliography supported. However, it was found nanocomposites feedstocks for MIM (table 1.12).

Table 1.12 – Injection moulding conditions for nanocomposites feedstocks

Feedstock composite	Equipment/ parameters	Ref.
Cu-MWCNT	0.4 MPa, $T_{\text{mould}} = 30 - 40 \text{ }^{\circ}\text{C}$ , $T_{\text{inj}}=160 \text{ }^{\circ}\text{C}$	[12], [48]
	0.7 MPa	[15]
	70 MPa; Barrel temperature =165 – 190 $^{\circ}\text{C}$ ; $T_{\text{mould}} = 25 \text{ }^{\circ}\text{C}$ ; 55 rpm;	[43]

### *Debinding*

The composition of binder and its possible interaction with metallic powders determines the debinding procedure. The success of this step depends on binder system and section thickness [90]. Usually the binder, which provides bonding, is removed from the “green part”, gradually increasing the susceptibility of the “green part” to formation of defects, prior to sinter densification [55]. The debinding is the most expensive step due to the long time and temperature [57].

For the same material, the binders can be removed by different ways, more effectively and causing less damage. A wide array of options exists for binder removal: thermal, solvent, catalytic and supercritical debinding. In this study was used thermal debinding process, one of the most common in  $\mu\text{MIM}$  of SS 316L (table 1.13). Binders have multiple components, which undertake degradation at different temperatures, under vacuum or controlled atmosphere, in two stages (figure 1.7). In the first stage, the constituents of the binder removed contributes to the creation of open porosity. During this stage, the remaining constituents of binder system will provide support to metallic powders, keeping the part geometry, and removed gradually during the second stage of the debinding step. The binder should also have the characteristic of total degradation, without carbonaceous residue [59]. Nevertheless, the carbon contamination from the binder is an inherent problem in the  $\mu\text{MIM}$  and MIM processes. Its influence has a strong impact on sintering process, microstructure and mechanical properties [55]. The control of carbonaceous residue is very important and the carbon content in SS 316L must be kept very low for not react with alloy elements (and minimize the presence of precipitates of chromium carbide, chromium nitride and silicon oxide in the microstructure), in order to ensure maximum corrosion resistance [55], [59]. The most used atmospheres are hydrogen, nitrogen, argon or a combination [59]. The interaction between the atmosphere and the powder could produce unpredictable results. Although the presence of hydrogen should lead to the reduction of the residual carbon in standard conditions, if the powder has oxides, the hydrogen contributes to their reduction. The carbonaceous content in “brown parts” under inert atmosphere could be low, which is especially relevant for metallic powders



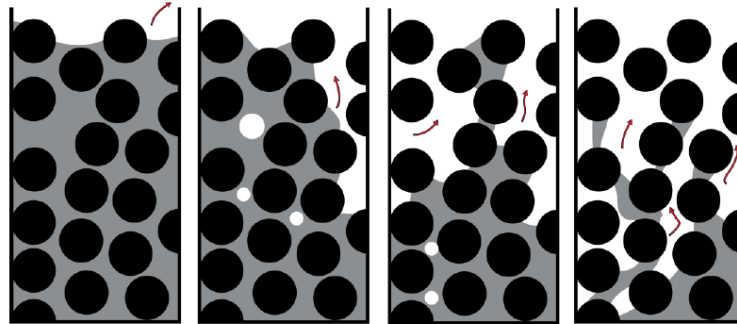


Figure 1.7 – Thermal debinding steps [86]

Table 1.13 – Thermal debinding parameters by  $\mu$ MIM

Cycle parameters	Ref.
1 °C/min (heating rate); 130 °C; 0.1 °C/min (heating rate); 220 °C; Air	[66], [79]
1 °C/min (heating rate); 600 °C; Ar/H <sub>2</sub> atmosphere	[67], [82], [84]
20 °C/h (heating rate); 90 °C, holding time: 1.5 h; 140 °C; holding time: 0.5 h; 200 °C; holding time: 1.5 h; 10 °C/h (heating rate); 370 °C; holding time: 1.25 h; 450 °C; holding time: 1.25 h; 30 °C/h (heating rate); 650 °C; holding time: 1.25 h; Ar/H <sub>2</sub> atmosphere	[77]
20 °C/h (heating rate); 280 °C; holding time: 3h; Ar/H <sub>2</sub> atmosphere	[73]
55 °C/min (heating rate); 130 °C and 4.5 °C/min (heating rate); 220 °C; Argon atmosphere	[57]
200 °C; holding time: 10h and 600 °C; holding time: 17h; Ar/H <sub>2</sub> atmosphere	[65]
475 °C; holding time: 20 h; N <sub>2</sub> atmosphere	[75]
600 °C; Ar/H <sub>2</sub> atmosphere	[68], [72], [78]
Ar/H <sub>2</sub> atmosphere	[61], [62]

The presence of MWCNT in “metallic green parts” could oblige to modify the process of debinding. However, in studies already carried out, they show a mixed methodology to remove the binder (1<sup>st</sup> solvent followed by thermal debinding) (table 1.14).

Table 1.14 – Thermal debinding parameters

Feedstock composite	Cycle parameters	Ref.
Cu-MWCNT	Solvent debinding: heptane, 60 °C, holding time: 5h Thermal debinding: 1°C/min (heating rate); 0 – 450 °C; holding time: 1h	[12]
	Solvent debinding: heptane, 60 °C; holding time: 2h	[15]
	Solvent debinding: heptane Thermal debinding	[22]
	Solvent debinding: heptane; 60 °C; holding time: 5h Thermal debinding: 1 °C/min; 0 – 450 °C; holding time: 1h	[43]
	Solvent debinding: heptane, 60 °C, 5h Thermal debinding: 1 °C/min, 0 – 450 °C, 1h	[48]
Fe-MWCNT	Solvent and thermal debinding	[49], [56]

## Sintering

The last step is sintering and is the process by which “brown parts” are transformed them into dense solids at temperatures below their melting point, between 2/3 to 4/5 of the melting temperature [63]. The driving force behind these sintering phenomena is minimization of the surface free energy. During sintering, the powder particles are bonded together by diffusion and other atomic transport mechanisms, and resulting in a dense solid body, with a variable porosity but achieving mechanical strength (figure 1.8). Usually sintering shrinkage is uniform and isotropic, so the design must oversized the dimensions of parts having in mind the process of manufacturing [51], [63].

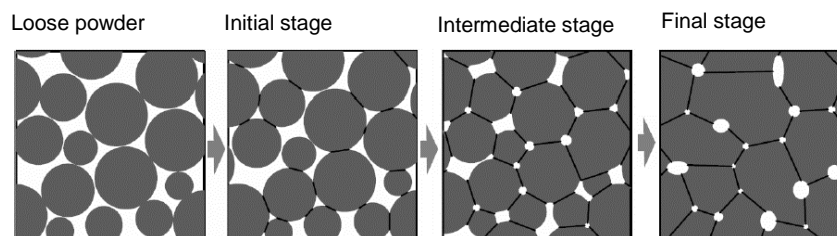


Figure 1.8 – Schematic evolution during the solid state diffusion sintering stage [86], [87]

The properties of the final parts are sensitive to several factors in the sintering process, like furnace atmosphere, thermal cycle, as well as other conditions, like support plate to hold the components [51], [54], [57]. For SS 316L “brown parts” different publications describe several sintering conditions (table 1.15).

Table 1.15 – Sintering parameters for SS 316L by  $\mu$ MIM

Cycle parameters	Ref.
5 °C/min (heating rate); 1000, 1050, 1100, 1200, 1300, and 1350 °C; holding time: 60 min; Argon atmosphere	[75]
5, 10 and 15 °C/min (heating rate); 1200 °C; holding time: 120 min; Argon atmosphere	[57]
5 °C/min (heating rate); 1250 °C; holding time: 60 min; H <sub>2</sub> atmosphere	[61]
5 °C/min (heating rate); 1300 °C; holding time: 30 min; Vacuum or H <sub>2</sub>	[68], [72]
5 °C/min (heating rate); 1300 °C; holding time: 30 min; Vacuum	[70]
5, 8, 10, 12 °C/min (heating rate); 1360 °C; holding time: 120 min	[66]
7 °C/min (heating rate); 1000 °C; 5 °C/min (heating rate); 1200 °C, 1250 °C and 1320 °C; holding time: 10, 30, 60, 90 and 120 min; H <sub>2</sub> atmosphere	[62]
7 °C/min (heating rate); 1250 °C; holding time: 60 min; H <sub>2</sub> atmosphere	[77]
10 °C/min (heating rate); 500 °C; holding time: 35 min; 10 °C/min (heating rate); 900 °C; holding time: 25 min; 10 °C/min (heating rate); 1320 °C; holding time: 60 min; Ar/H <sub>2</sub> atmosphere	[65], [67]
10 °C/min (heating rate), 1250 °C, 60 min; Ar/H <sub>2</sub> atmosphere	[82]–[84]
10 °C/min (heating rate); 1280 °C; holding time: 30 min; N <sub>2</sub> atmosphere	[76]
10 °C/min (heating rate); 1350 °C; holding time: 30 min; N <sub>2</sub> atmosphere	[78]
10 °C/min (heating rate); 1360 °C; holding time: 120 min; Vacuum atmosphere	[79]
10h, 600 °C; 2h, 800 °C; 5h, 1360 °C; holding time: 1h, 1360 °C; Ar/H <sub>2</sub> atmosphere (cooling in vacuum)	[73]

In what concern to metallic composites nanoreinforced with MWCNT, for the same matrix material, some differences in sintering parameters are discernible in different publications (table 1.16).

Table 1.16 – Sintering parameters of MMC-MWCNT (by MIM)

Feedstock composite	Cycle parameters	Ref.
Cu-MWCNT	450 – 900 °C; holding time: 60 min; argon atmosphere (heating rate: 3 °C/min)	[12], [43], [48]
	950, 1000, 1050 °C; holding time: 60, 90, 120 min; argon atmosphere	[22]
	1150 °C, holding time: 50 min; argon atmosphere	[15]
Fe-MWCNT	900 – 1200 °C; holding time: 30 – 120 min, inert atmosphere	[49], [56]

In general, after sintering, parts/devices have excellent strength, with properties near or even superior to those available from other processing routes [60].

Dimensional control is particularly important in “green parts” and after sintering for  $\mu$ MIM parts/devices. The consolidation process is the most important step for dimensional variation, which is between 10 – 22 % [51], [54], [55].

Sintered parts/devices produced by  $\mu$ MIM achieve densities more or less close to the theoretical ones, depending on thermal cycle selected. *A. Bose et al.* [75] measured 91 – 97 % of density and about 623 MPa of UTS. *F. M. Barreiros et. al* [73] assessed about 95 % of density and 16 % of shrinkage. *A. R. Farinha et al.* [65] measured a shrinkage between 11 – 20 % and a microhardness of 1.6 GPa. *J. Meng et al.* [72] referred the presence of chromium carbides ( $M_{23}C_6$ ) when the sintering is conducted under vacuum, whereas only austenite phase was found in hydrogen atmosphere. Consequently, the sintering atmosphere influenced the hardness values, for hydrogen and vacuum were 1.5 GPa and 1.7 GPa (or  $156.3 \pm 6.5$  HV and  $176.3 \pm 8.2$  HV), respectively [72]. *C. Quinard et al.* [66] had 89; 92; 93 and 96% of densification and shrinkages of 7.8; 8.2; 9.3 and 12.0 % function of the heating rates from 5; 8; 10 and 12 °C/min. However, UTS maximum value of 800 MPa was measured when the parts/devices were sintered with 10 °C/min (heating rate) over 710 MPa to heating rate of 12 °C/min [66]. *T. Ferreira* [67] measured 95.7 % of theoretical density, a shrinkage between 15 – 20 % and microhardness about 1.96 GPa. *X. Kong* [57] showed that large shrinkages (11.5 – 13.2 %) are measured in parts/devices with high CVCPs and final density (91.3 – 95.1 %) using low heating rate (5 °C/min).

The results of MMC – MWCNT produced by MIM (table 1.17) are almost imprecise and unsupported. For example, some authors refer the existence of nanotubes based on images with inadequate magnifications.

Table 1.17 – MMC-MWCNT produced by MIM

Composite	Results	Ref.
Cu-MWCNT	Shrinkage about 21 % and referred few MWCNT agglomeration in fractured surface	[12]
	Parts/devices not homogeneous with distortion due to inadequate sintering time or temperature	[15]
	The sintered copper nanocomposites have a relative density about 94.8, 93.5, 90.6 and 89%, 0, 1, 5 and 10 vol% of MWCNTs, respectively. The addition of 10 vol% of MWCNTs increases of Young's modulus (48 %) compared to unreinforced Cu matrix.	[22]
	Isotropic shrinkage between 17 and 21 %	[48]
Fe-MWCNT	Referred improvements in hardness despite few agglomerates in sintered	[49], [56]

# CHAPTER II

---

Materials, processing methodology and characterization  
techniques

## 2.1 Materials

The selected metallic powder used as matrix was the stainless steel 316L (AISI), and as nanoreinforcement multiwall carbon nanotubes (MWCNT). A commercial available binder (M<sub>1</sub>) with addition of stearic acid (SA) were the additives to improve the rheology of powders to be injected.

### a) Powder

Austenitic stainless steels (SS) have a wide range of alloys based on elements like iron, chromium and nickel, which gives corrosion resistance to the steel, in most common corrosive environments. Moreover, austenitic SS exhibits satisfactory resistance to oxidation at high temperatures (900 °C) [59].

Austenitic SS 316L is widely used in aerospace, automotive, sports and medical industries due to its mechanical properties and corrosion resistance [51], [59], [60], [69]. In some cases, SS 316L may contain several additional elements allowing it to have certain properties. The table 2.1 resumes the standard chemical composition for SS 316L powders

Table 2.1 – Standard chemical composition of SS 316L [59], [60], [91]

	<b>Fe</b>	<b>Ni</b>	<b>Cr</b>	<b>Mo</b>	<b>Mn</b>	<b>Si</b>	<b>C</b>	<b>S</b>	<b>P</b>	<b>N</b>	<b>O (ppm)</b>
wt%	Bal.	10-14	16-18	2-3	0-2	0-1	0-0.03	0-0.03	0-0.045	0-0.03	1-2.5

In the present study, stainless steel 316L powders acquired to ATMIX® Company had a specific chemical composition summarized in table 2.2.

Table 2.2 – Chemical composition of SS 316L

	<b>Fe</b>	<b>Ni</b>	<b>Cr</b>	<b>Mo</b>	<b>Mn</b>	<b>Si</b>	<b>C</b>	<b>S</b>	<b>P</b>	<b>O (ppm)</b>
wt%	Bal.	12.31	17.71	2.11	0.06	0.34	0.022	0.005	0.015	3.800

### b) Nanoreinforcement

Carbon nanotube is one of the most promising nanomaterial, presents outstanding physical properties, such as low specific gravity, large aspect ratio, improved mechanical strength, thermal stability, electrical and thermal conductivities, which make them suitable for applications as reinforcement in MMC [1], [22], [28].

The selected nanotubes were multiwall (MWCNT), supplied by Nanocyl and were produced via CVD process. Table 2.3 summarizes the characterization provided by the supplier and length and diameter evaluated by TEM and surface area via BET.

Table 2.3 – MWCNT characteristics

Characteristics	MWCNT
Length, $\mu\text{m}$	1.5
Diameter, nm	9.5
Specific surface area, $\text{m}^2/\text{kg}$	250 000 - 300 000
Purity, %	90

### c) Binder

The binder plays a very crucial role in processing of microcomponents. Since it allows ease moulding of the powders into desired shape. In general, binders are composed by a mixture of several polymers and organic compounds, the main component, a thermoplastic, provides support to the moulded part and the “secondary” component, usually waxes, acid stearic and oleic for improve the feedstock flowability [55]. The stearic acid (IUPAC: octadecanoic acid) is a carboxylic acid with a long unbranched aliphatic chain, without any double bonds or other functional groups like any saturated fatty acids. Stearic acid (SA) is used as an agent to increase the wettability of the polymeric binder, to reduce the melt viscosity (enabling a better flowability of the feedstock) and to promote high fractions in compounds [55]. This is only possible due to a reduced particle-particle interaction. This lubricant has a much lower molecular weight than the polymers. The SA ( $\text{C}_{18}\text{H}_{36}\text{O}_2$ ) was supplied by Acros Organics® Company, as a 97 % pure lubricant.

The binder was supplied by Atect® Company, under the name of M<sub>1</sub>, and is composed by polyolefin waxes and ethylenic polymers with numerical molecular weight. According to the supplier, the density was  $969 \text{ kg/m}^3$ , and thermal process up to  $600 \text{ }^\circ\text{C}$  is enabled to remove it completely.

## 2.2 Processing methodologies

The methodologies and conditions of several steps of process used to produce the sintered parts are following described.

### a) Milling process



Milling processes could be in dry or wet conditions. With the use of cooling milling mediums such as tumbler, vibratory, and/or attrition ball. In most ball milling, particles are subjected to both impact and attrition forces and, if very high energy is available, welding may occur between powder particles, powder and balls, and powder and jar mill walls. Moreover, even in mildly condition, milling metallic powders can change external shape, texture and internal structure. The extent of these changes is determined by milling parameters, milling environment, and physical -chemical properties of the metal or alloy to be milled. These changes in turn affect the physical properties of the metal processing, resulting in consolidated products. Often, a compromise must be made in the selection of ball size and material, as well as milling conditions [60].

In order to attain a better dispersion of MWCNTs in matrix, a pre-mixture in a ball milling of SS 316L and MWCNT, prior to the transfer to the mixer equipment. The milling occurred in a planetary ball-milling machine (Fritsch) under Ar+H<sub>2</sub> (5 %) atmosphere, during 5, 15 and 30 minutes with a break of 10 minutes at 200 rpm; with a BPR of 20:1 of hardened chromium steel balls of 20 mm diameters.

## b) Mixing/ Rheological behaviour

A Brabender Plastograph W 50 mixer, with heating circulator T 300 B, led to optimise the mixture between powders and binder that means to evaluate the critical volume concentration of powders (CVCP) based on torque rheometry. A technique applied to optimise plastic compositions, but after 1995 has been widely applied to optimise feedstocks based on inorganic powder (metal and ceramic). The Plastograph has a mixing chamber of 55 cm<sup>3</sup> with possibility to attain 200 °C and blades made in tool steel. Counter-rotation towards each other at different speeds provides excellent compounding and mixing characteristics. A dynamometer coupled to the mixer measured the torque value continuously and recorded it along the time. The principle based on measuring resistance that material introduced in the chamber opposes to the rotating blades. The corresponding torque moves a dynamometer out of its zero position. In compliance with the existing standards and test specifications, a typical 'Plastogram®' recording torque and stock temperature vs. time for each material.

All tests begin by calibration of the dynamometer with the blades running in the empty chamber. After introduction of binder, with the corresponding decrease in temperature, adding different powder content step by step up to attain the limit able to be mixed. When the binder and the metallic powder are in the chamber, they offer a certain resistance to the free rotation of the blades and therefore the torque increases. As the mixture homogenizes, if the temperature is sufficient (at fixed speed) the torque decreases, and reaches a steady state regime. In each powder addition, the torque profile shows the fraction value at which it

is visible a transition from a stable mixing torque to unstable profile (non-homogeneous). The CPVC is defined by the maximum solids fraction which provided a mixing stability [10].

The conditions for all tests were, as follows: 30 rpm, under 30 – 40 minutes. Based on the thermal analysis of the selected binders, the optimization and feedstock production were performed at 180 °C (the work temperature should be lower than degradation temperature of binder 200 °C).

### c) Injection Moulding

Thermo Scientific HAAKE MiniJet Pro Piston Injection Moulding System was the injection equipment to manufacture parts/devices. The material consumption dramatically decreases in comparison with conventional injection moulding units, resulting in a smaller quantity of required material (3.5 g); and almost complete transportation of material into the mould, promoting minimal loss and waste.

All the feedstocks tested were injected into a tensile parts mould following the requirements of the – standard ISO 527-2-A5 (figure 2.1) [92].



Figure 2.1 – Design of moulds for tensile and flexure specimens

The injection test is slightly different from what happens in an industrial injection machine (microinjector). In this case, the procedure consists:

- to turn on the machine and wait until the mould and cylinder reaches the selected temperature (figure 2.2 a));
- to put the feedstock inside the cylinder and wait until it has a viscous behaviour (figure 2.2 b));
- to put the cylinder inside the machine and if all the temperatures and pressures fulfil the requirements, start the injection test (figure 2.2 c));
- and, extracted specimen from mould.

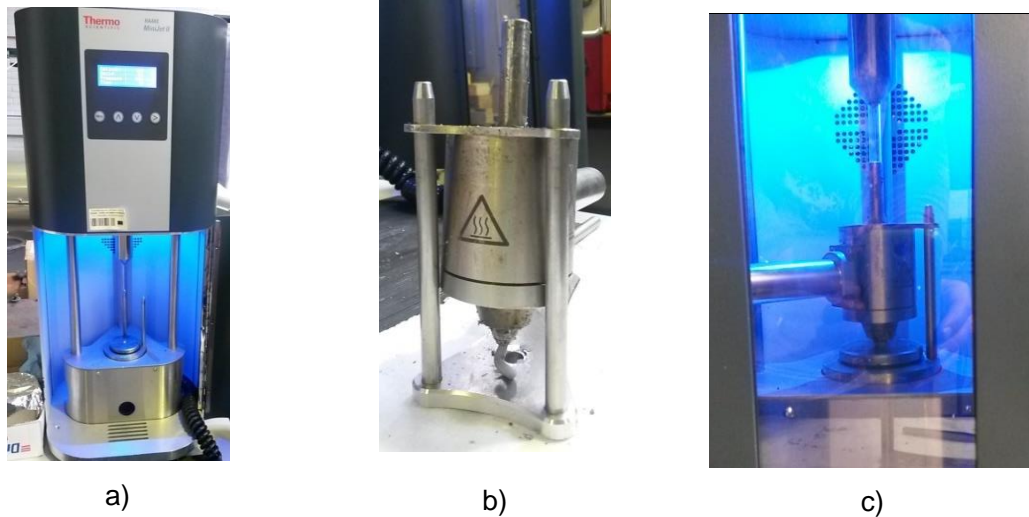


Figure 2.2 – MiniJet Pro Piston Injection Moulding System a) machine, b) cylinder and c) cylinder inside machine

#### d) Debinding

The debinding of the “green parts” and the heat treatment of sintering, utilized a furnace from Termolab – Superkental. This equipment has four lateral resistances; the minimum heating rate is 1 °C/min and allows achieving a maximum temperature of 1600 °C. This furnace was adapted to be able to perform thermal tests (debinding and sintering), by means of a cordierite tube, coupled to a vacuum system/gas introduction, for controlling atmosphere. The thermal cycle of debinding was based on the thermal analysis of binder (DSC and TGA) (figure 2.3). In this step, it was used the lowest heating rate admitted by this equipment (1 °C/min) to ensure a controlled heating that will not cause defects in parts. The atmosphere during thermal cycles was Ar+H<sub>2</sub> (5 %).

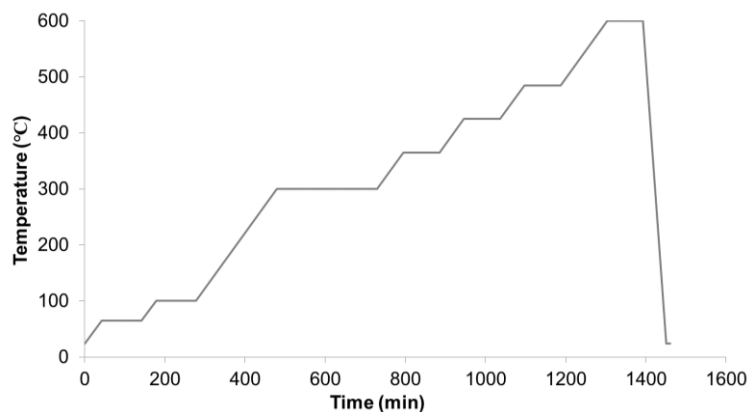


Figure 2.3 – Debinding cycle

The same procedure for all testes assured the reproducibility of the results. The procedure consists:

- to put the browns in cordierite tube under a support with holes (to facilitate the extraction of the binder);
- to do vacuum (3.0 Pa);
- Ar+H<sub>2</sub> (5.5 Pa) atmosphere
- and, start the thermal cycle.

After debinding, the cooling rate was 40 °C/min, under controlled atmosphere (Ar+H<sub>2</sub>), until room temperature. Before and after debinding the weighting of all specimens allowed evaluating the efficiency of binder removal.

## e) Sintering

In sintering of “brown parts”, the heating rate was 10 °C/min instead 1 °C/min of debinding treatment. Different sintering temperatures to validate the sintering cycle were tested (figure 2.4).

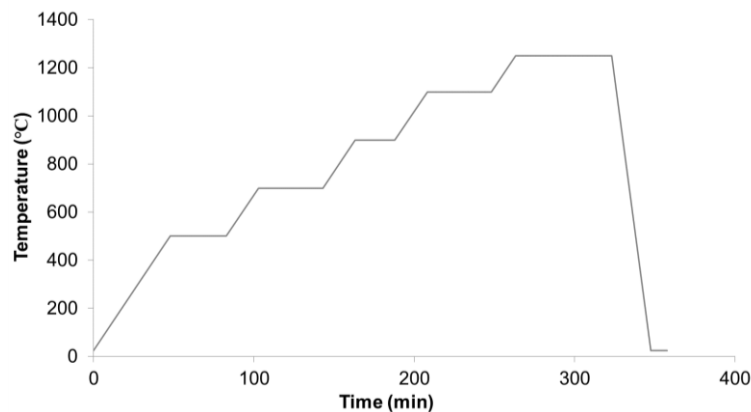


Figure 2.4 – Sintering cycle

The sintering procedure is similar to debinding but in this step, is necessary very caution since “brown parts” do not have physical resistance, due to lack of binder. Between the debinding and sintering steps, in order to remove the binder deposited on walls the cordierite tube oblige to their cleaning. After finishing the cycle, the components cool in the furnace, under controlled atmosphere, until room temperature. Once again, all the parts before and after the sintering test are weighted.

An analytical balance Mettler Toledo with a resolution of 0.01 mg and a digital calliper Mitutoyo with a resolution of 0.005 mm allow the measurements of weight and dimension variations after heat treatments.

## f) Coating

In order to protect the brown A thin coating of nickel was deposited onto the “brown parts” with the aim to “waterproof” the parts but also to prevent the removal of MWCNT and its reaction with oxygen. This deposition was performed by “sputtering”, a PVD technique, in a “home-made” magnetron equipment (figure 2.5). The process involves the evacuation of a chamber until a very low pressure is achieved. After, the ionisation of Argon, the inert gas usually responsible by the sputtering of target atoms. During sputtering, the atoms follow a typical distribution condensing on nearby surfaces. The deposition parameters were as follows: ultimate pressure:  $4 \times 10^{-4}$  Pa during 48 hours; target specific power:  $1.4 \times 10^{-2}$  Wmm<sup>-2</sup>; deposition pressure: 0.5 Pa; deposition time: 3 hours; and target to substrate distance: 150 mm.

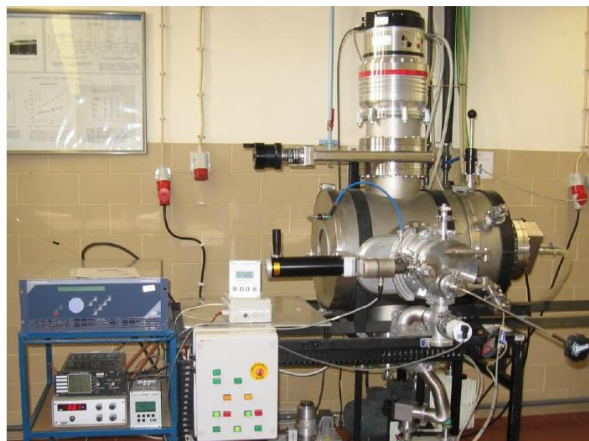


Figure 2.5 – Magnetron sputtering equipment

## 2.3 Characterization techniques

Several techniques were applied for characterization of raw materials and the parts/devices along several steps of  $\mu$ MIM technology

### a) Pycnometer density

The density is the ratio of weight to volume (excluding voids). The powders real density ( $\rho_{real}$ ) was measured by a Micrometrics Accupyc 1330 helium pycnometry. This

equipment evaluates the density through the volume by measuring the pressure change of helium in a calibrated volume (it also reports the chamber temperature) [93]. Helium is the most commonly used as the measurement gas, not only because of its small size but also for being inert and its behaviour similar to an ideal gas. This technique allowed the evaluation of the density of all the raw materials.

## b) Particle size distribution

The powder particle size distribution (PSD) was determined by laser diffraction spectrometry (LDS) on a Malvern Instruments Mastersizer 3000 equipment with the evaluation fulfilling the requirements of ISO 13320-2009 standard [94]. The particle size distribution is determined based on the Fraunhofer diffraction theory, stating that the angle of diffraction of light scattered by a particle is inversely proportional to the particle size. The measurements had water as dispersion media.

The distributions are quantified in  $d_{10}$ ,  $d_{50}$  and  $d_{90}$ , representing the particle diameter at which 10, 50 and 90 % of the distribution is below this diameter value (in micrometres).

The determination of the width of distribution,  $S_w$ , was made by the following equation [64], [73], [86]:

$$S_w = \frac{2.56}{\log_{10}(d_{90}) - \log_{10}(d_{10})} \quad (\text{Eq. 2})$$

Large values of  $S_w$ , correspond to narrower PSD and small values correspond to broader/wide distributions. The easiest powders to mould exhibit  $S_w$  values of 2 (very broad distributions), while some, more difficult, exhibit  $S_w$  values between 4 and 5. An even more difficult option is to use a narrow particle size distribution with  $S_w$  over 7 [64], [86].

## c) Specific surface area

The powder specific surface area per unit weight, known as  $S_m$ , is a very important parameter to understand its reactivity. The value of  $S_m$  depends on the characteristics of the powder particles, in particular the size, shape and porosity. For the same volume of solids, small particles have a much higher  $S_m$  than large ones and that gives an indirect information about the phenomena related to the powder sintering [59]. The specific surface area of the powders was measured with a nitrogen gas absorption on Micromeritics Instrument Corporation on ASAP 2000. The gas adsorption determines the surface area through the relationship between applied pressure and volume of gas forced into the specimen, known as BET (Brunauer, Emmett and Teller) method.

## d) Density (Archimedes method)

Apparent density of the final specimens was measured by the Archimedes method according to the ASTM B962 – 17 standard [95]. To the measurement of MIM specimens was necessary to coat them with varnish ( $\rho = 906.2 \text{ kg/m}^3$ ) to avoid the penetration of water in open porosity. The sintered density ( $D_s$ ) results from the following equation:

$$D_s = \frac{A \cdot \rho_w}{B - (C - E)} \quad (\text{Eq. 3})$$

where A is the weight of the sintered specimen in air, B is the weight of the specimens coated in air, C is the weight of the specimen coated and support, in water, E is the weight of the support in water, and takes into account the dependency of water's density ( $\rho_w$ ) with temperature (22 °C,  $\rho_w = 997.8 \text{ kg/m}^3$ )

## e) Phase composition

X-ray diffraction (XRD) is the technique suitable to obtain phases information present in crystalline materials. The X-rays are electromagnetic waves whose wavelengths are in the range of 1 – 10 nm, and can be scattered by interaction with matter, primarily through the matter's electrons. Phases and other structural information (orientation, lattice parameters, grain size) of a material are available from the diffractogram.

The diffractogram follows the Bragg equation:

$$n\lambda = 2d_{hkl} \sin \theta \quad (\text{Eq. 4})$$

where n is an integer number representing the diffraction order;  $\lambda$  is the wavelength of the anticathode;  $d_{hkl}$  is the interplanar spacing of the analysed crystal;  $\theta$  is the angle of the diffraction (Bragg angle).

The diffractogram peaks compared with a database maintained by the International Centre for Diffraction Data (ICDD) makes possible to ascertain the different phases present on the material.

The structural characterization of powder and MWCNT reinforced nanocomposites by XRD used a Philips X'Pert diffractometer. The anticathode was of cobalt with  $k_{\alpha 1}$  and  $k_{\alpha 2}$  values of 0.1788 nm and 0.1792 nm, respectively. The potential to accelerate the electrons was 40 kV and with a current intensity of 35 mA, and according to the Bragg-Brentano geometry ( $\theta - 2\theta$ ). The conditions of scanning were for  $2\theta$  angle from 20° to 120° or 40° to 65° in steps of 0.04° and time of acquisition of 1 second.

## f) Microstructure

### Optical Microscopy

Before optical microscopy analyse in Nikon OPTIPHOT metallographic polarizing microscope, the specimens were polished and chemical etched. The sintered specimens were mechanically polished up to suspensions of diamond up to 3  $\mu\text{m}$  of particle size. In order to analyse the grain size (ASTM E 407 – 07) and the microstructures features the reagent of chemical attack was HCl, HNO<sub>3</sub> and glycerol, 3.5:1:3, during about 1 minute [96].

### Scanning Electron Microscopy

Scanning electron microscopy (SEM) allowed assessing the particle morphology and microstructural details of different stages of processing of the nanocomposites. The combination of high magnification, high depth of focus, high resolution and easy observation makes SEM one of the most heavily used instruments. FEI Quanta 400 FEG ESEM /EDAX Genesis (Schottky) a high-resolution microscopy was the selected apparatus to the study. The powders and pre-mixtures dispersed and stuck on a carbon adhesive tape on a sample holder are the suitable preparation to analyse. Electron backscattered diffraction (EBSD) and energy dispersive spectroscopy (EDS) images and elemental maps by EDS were some of the functionalities capable to obtain extra information about the chemical composition and phase distribution. Fracture surface were the places preferable for the analyses performed.

The program *Image J* was used to treatment the elemental maps by EDS of fracture surface allows calculating the percentage to different phases by colours of the main elements presents.

### Transmission Electron Microscopy

The transmission electron microscopy (TEM) is a very useful device for structural analysis of ultra-thin foils. As transmission is essential, the sample must be transparent to electrons, which usually achieved with sample thickness of a few hundred nanometer.

The focused ion beam scanning electron microscopy (FIB-SEM) were the technique selected to prepare the samples without destruction of MWCNTs. While a scanning electron microscope uses a focused beam of electrons to image the sample in the chamber, a FIB setup employs a focused beam of ions (Ga). FIB-SEM is the unique combination of an ion gun and an electron gun, where specimens can be positioned at the intersection point of the electron and ion beam with an accuracy of much less than 1  $\mu\text{m}$ . This allows simultaneous ion milling, nanosectioning and secondary electron imaging of the region of interest with a spatial resolution within the nanometer range. Modern dual beam FIB-SEM machines incorporate both an electron and an ion beam column, allowing imaging of the same feature using either signal [97]. This specific FIB-SEM system utilized in this study (FEI DualBeam TM Helios 600 Nanolab TM) is equipped with the following primary components: a high-



resolution Field Emission Gun for SEM; multiple electron detectors for image acquisition, such as through-the-lens detector, an Everhart-Thornley detector, and a backscattered electron detector for compositional information; finally, a high-resolution focused Ga<sup>+</sup> ion beam (figure 2.6).

FIB prepared lamellas of nanocomposites reinforced for HRTEM. A JEOL 2010F HRTEM with a field emission gun equipped with a Gatan imaging filter was the equipment used in the study. This microscope provides a point-to-point spatial resolution of 0.17 nm.



Figure 2.6 – FIB-SEM

## g) Thermal analyses

Thermal gravimetric analysis (TGA) and differential thermal analysis (DTA), were essential to understand the behaviour of powders, binders, MWCNT, feedstocks and some nanoreinforced composites. The TGA signal could detect weight changes associated to decomposition, vaporization and sublimation, desorption and absorption, oxidation and chemical reactions, which is reflected in losses or gains of weight (when it is subjected to a temperature program in a selected atmosphere). The DTA signal gives information of the range temperature at which physical transformations occurs. The equipment was a Setaram Setsys (TGA sensibility of 0.1 mg).

## h) Infrared spectra

The Infrared (IR) spectroscopy plays an important role in physical characterization of polymers. The identification of IR absorption bands is by their specificity to individual chemical functionalities. One of the most limitations of IR spectroscopy often cited by polymer physicists has been the lack of unambiguous band assignments of chemical moieties for IR spectra of different polymers. The assignment of IR absorption bands for specific modes of molecular vibrations in polymers is not always straightforward. While it is true there have been numerous published IR spectroscopic studies of polymeric materials, relatively little

information is provided in a useful and practical tabulation for specific synthetic polymers, commonly studied by polymer physicists. IR bands can be strongly affected by several physical factors such as phase, morphology, samples history, and IR sampling techniques [98]. A Perkin-Elmer Spectrum 100 Fourier transform infrared (FTIR) spectrometer with a DGTS detector is the equipment for the global analysis of polymeric components of the binder. The acquisition of each spectrum was in the spectral range of 4000 – 500 cm<sup>-1</sup> at a resolution of 4 cm<sup>-1</sup> and eight scans per sample systematically allowed improving the signal-to-noise ratio.

## i) Apparent grain size

The apparent grain size determination was performed under the guidance of standard ISO 643:2012, applying the linear intercept segment method [99].

The relationship between grain size and YS is established since 1952 by Hall and Petch, an increasing of YS with the refinement of the grain is expected. The relation between the YS of the composite and the mean diameter grain (d) can be expressed by Hall-Petch equation [6], [24], [100]:

$$\sigma_y = \sigma_0 + \frac{K}{\sqrt{d}} \quad (\text{Eq. 5})$$

where  $\sigma_0$  and k are specific of each material ( $\sigma_0=163$  MPa K = 770 MPa.μm<sup>1/2</sup> for SS 316L) [100].

## j) Mechanical Tests

### Ultramicrohardness

Hardness is a property that declares the ability of the material to resist deformation when an external pressure is applied. The test consists on the measurement of an indentation, on a perfectly prepared, polished surface, when a known force is applied. In some cases, the registration of the load and unload curves during the test allows the evaluation of hardness but also of the Young's modulus (E). An ultramicrohardness test follows the same principles of microhardness; however, the applied force is very low. On the study, the surfaces of specimens were polished, not only to prepare the surface, but also to reveal any porosity and to determine the possible places where the hardness test could be evaluated [91]. A Fisherscope H100 ultramicrohardness was the equipment with a Vickers diamond indenter (Poisson coefficient of 0.3) and with a maximum load of 500 mN. The hardness values and Young's modulus were evaluated applying the equations and corrections described by *Antunes et al.* [101] and each specimen was tested 40 times although, after treatment, some tests were excluded.

### Tensile test

The microparts were tested in a Shimadzu SLBL testing machine with a 5 kN loading cell. The dimensions of the cross-section test of the parts were previously measured ( $6.8 \text{ mm}^2$ ) with a calliper; the gage length ( $L_0$ ) was 22 mm (figure 2.7). The tensile tests at performed at room temperature and a speed rate of 2.5 mm/min.

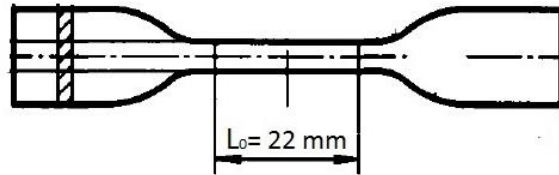


Figure 2.7 – Gage length ( $L_0$ ) of tensile specimen

# CHAPTER III

---

Results and discussion

The success of nanoreinforcement as MWCNT in metallic matrices depends on the powder selected characteristics and different steps of the powder technology selected to processing. Once the metallic powder injection moulding (MIM) is the elective manufacturing process for production of advanced composites, after characterization of main materials selected, the results presented had in mind the different steps of the process. Mixing metallic powders with polymeric binder, injection moulding, debinding and sintering, are the main different steps of PIM. Consequently, they are analysed one by one, because they have a significant role in the composite properties.

### 3.1 Materials

In the study, there are involved dissimilar materials with different roles in the final properties of the composite parts, as matrix: stainless steel 316L powders (AISI) and as nanoreinforcement: MWCNT; and as process aiding a binder constituted by a mixture of polymers and other organic compounds.

#### a) SS 316L powders

The figure 3.1 and table 3.1 show the Gaussian distribution for MIM or  $\mu$ MIM and the particle size and particle size distribution ( $S_w$ ) of SS316L powders.

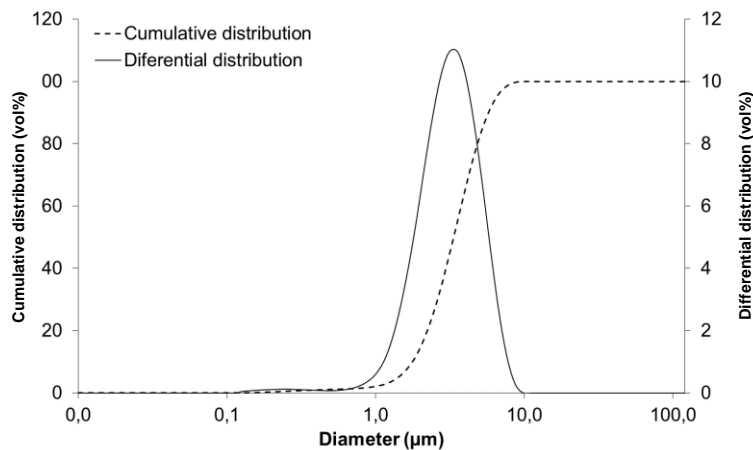


Figure 3.1 – Particle size distribution of SS 316L

The SS 316L powders (figure 3.2) shows particles with shape factor slight different of 1, typical of powders for injection moulding [55].

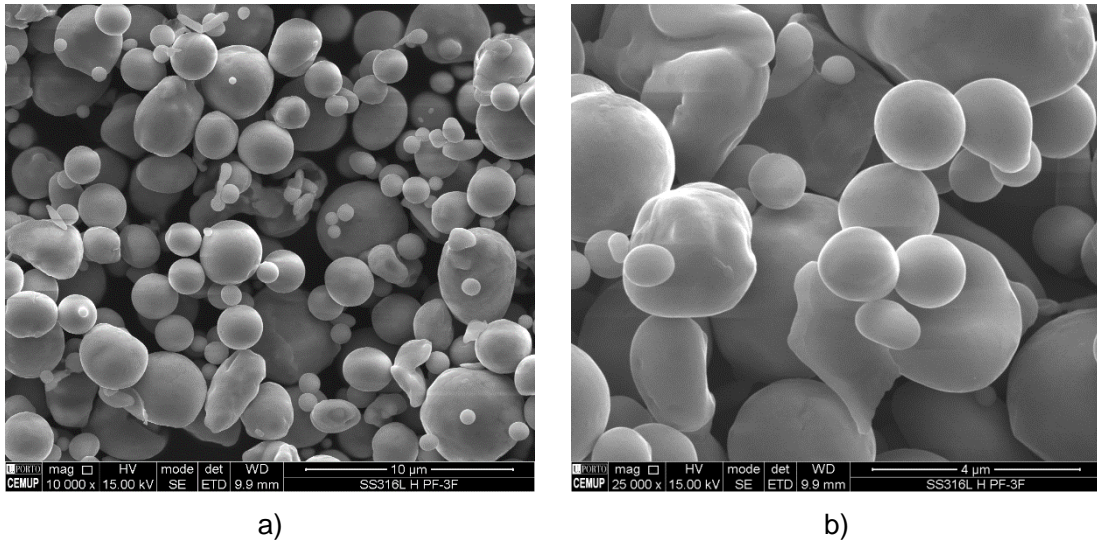


Figure 3.2 – Particle shape of SS 316L a) 10000x, b) 25000x

Figure 3.3 shows the structure of SS 316L powders (0.02 wt% C). The diffractogram are in accord to the austenite and martensite phases (ICDD number: 33-0397 and 87-0722, respectively – Annex I). However, the peaks at 52.4°, 77.2° and 99.4° are indexed as ferrite/martensite. Due to powder atomization conditions, fast cooling and small particles encourages high stress level suitable to induce in the particles conditions to promote the phase transformation of austenite into martensite. However, these peaks have a relative intensity different from other powder suppliers, due to under different conditions of atomization [58], [65], [81], [84].

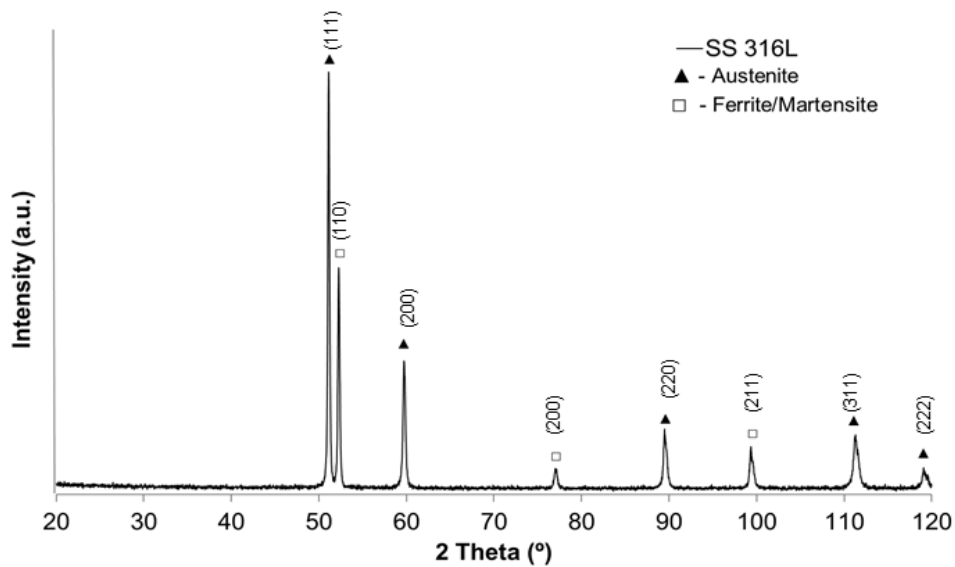


Figure 3.3 – X-ray diffractogram of pristine SS 316L powders (as received)

Table 3.1 summarizes the characteristics of SS 316L powders. The density measured (by helium pycnometry) is lower than expected for SS 316L ( $7990 \text{ kg/m}^3$ ) because, as shown previously, these powders are not completely austenitic and the presence of martensite contribute to decrease the density values. In what concerns the specific surface area ( $S_m$ ), it must be highlighted that low  $S_m$  means an improvement of sintering kinetics and surface finishing. By other way, the high value (5) of width particle size distribution ( $S_w$ ) - parameter that represents “the easiest powders to mould”-, is the maximal value consider suitable. Nevertheless, *E. Sequeiros et al.* [58] for a similar grain size particle distribution of SS 316L, with a  $S_w$  of 5.8 had yet attained good mould performance.

Table 3.1 – SS 316L powders characteristics

	Powder	cf. ATMIX
Density ( $\text{kg/m}^3$ )	$7715 \pm 25$	-
$d_{10}$ ( $\mu\text{m}$ )	1.76	1.67
$d_{50}$ ( $\mu\text{m}$ )	3.35	3.15
$d_{90}$ ( $\mu\text{m}$ )	5.76	5.32
$S_m$ ( $\text{m}^2/\text{kg}$ )	$408 \pm 5$	-
$S_w$	4.97	-

Figure 3.4 shows the effect of temperature on pristine SS 316L powders. After a loss of weight attributed to dehydration of powders, starts the oxidation of stainless steel in to different rates depending on oxide formation.

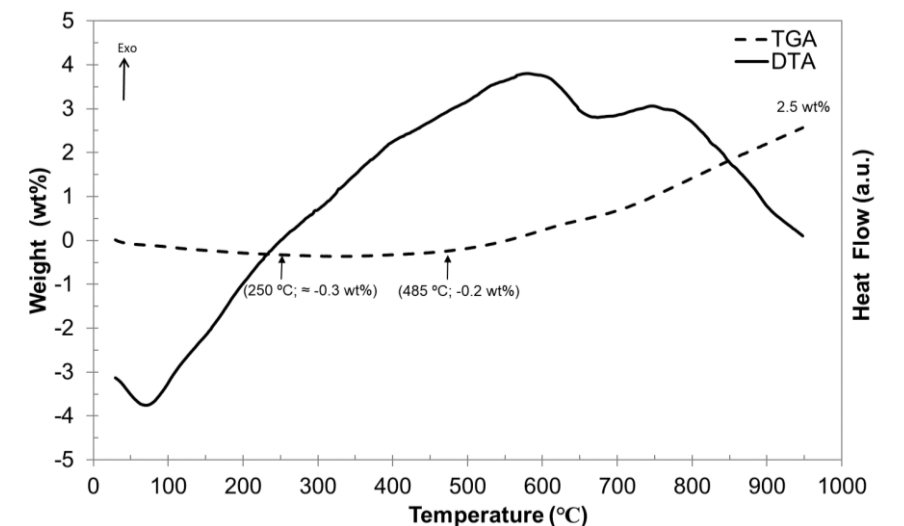


Figure 3.4 – TGA of pristine SS 316L powders (as-received)



## b) MWCNTs

The nanoreinforcement selected were multiwall carbon nanotubes (MWCNT). Their density measured was  $2134 \pm 14 \text{ kg/m}^3$ . The morphology of MWCNTs as received contained some impurities, indicated by arrows in the figure 3.5, where it is also possible to observe MWCNTs with and without some agglomeration. The diameter was much higher ( $\approx 19 - 31 \text{ nm}$ ) than the indicated in the technical sheet of the supplier (9.5 nm).

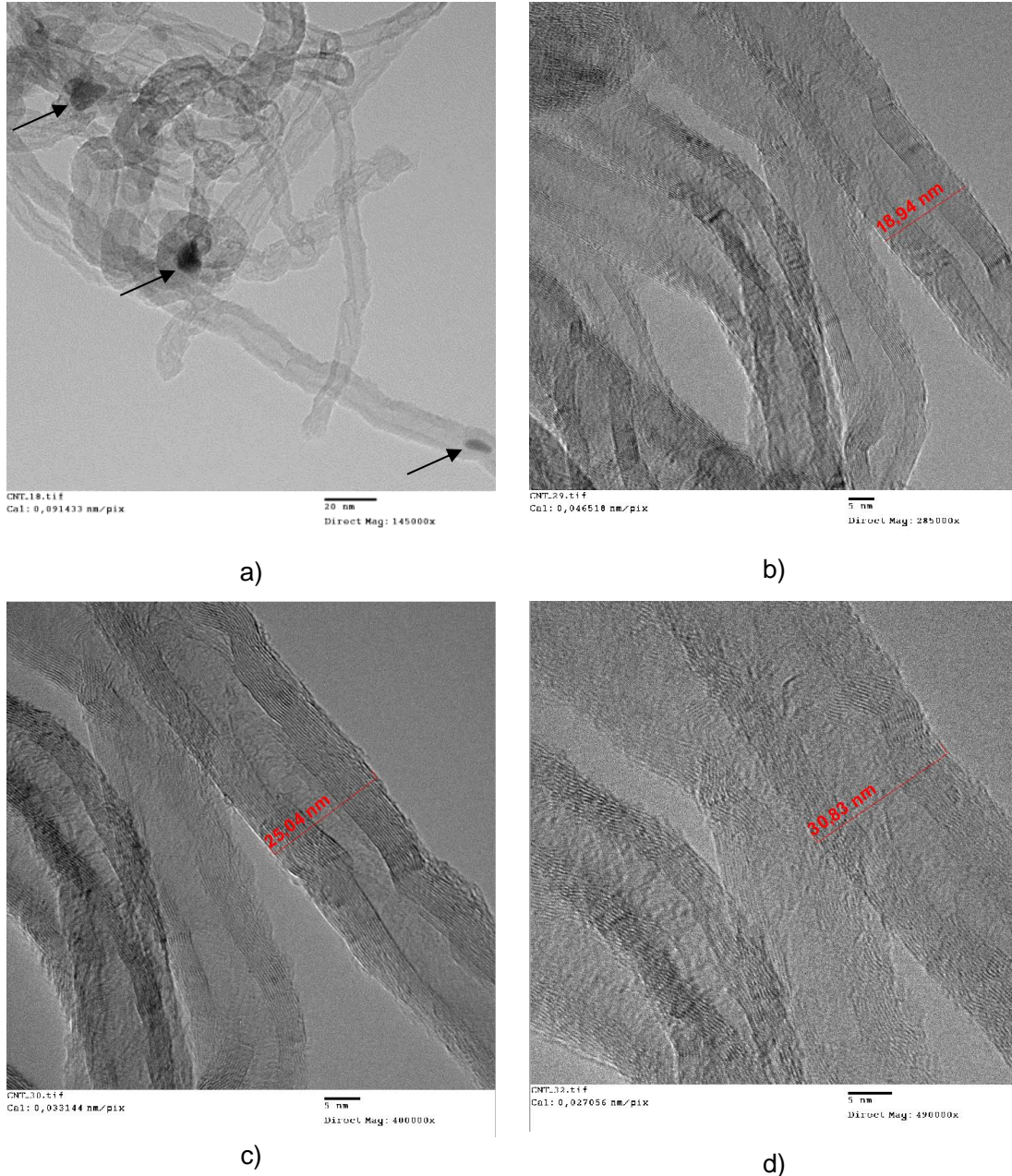


Figure 3.5 – Nanotubes shape of MWCNTs at different magnifications (TEM)

Figure 3.6 shows the thermal behaviour of MWCNTs as received up to 1300 °C into different atmospheres under a heating rate of 10 °C/min. In air atmosphere, any oxidation of the MWCNTs occurs up to 450 °C and for higher temperature the oxidation of carbon starts,



finishing at 950 °C and at 1300 °C a weight loss was about 90 %. These values are in accordance with the results of *A. Mahajan et al.* [50] also using thermogravimetric analyses. In air atmosphere, no weight evolution up to 420 °C occurs (figure 3.7 a)), above this temperature the weight loss starts due to the oxidation of MWCNTs. These authors also show that the heating rate has a strong influence on the thermal behaviour of MWCNTs (higher rates lead to lower losses of MWCNTs) [50].

In what concerns Ar+H<sub>2</sub> (5 %) atmosphere, the MWCNTs remain intact up to 680 °C (figure 3.6), higher temperature than in argon (430 °C – figure 3.7 b)). The degradation of MWCNTs starts at 680 °C with about 32 % of weight loss at 1300 °C. The studies concerning argon atmosphere show insignificant differences in oxidation temperatures of MWCNT. Figure 3.7 b) shows that even 40 °C/min, the MWCNTs degradation starts at 430 °C with about 30 % of weight loss at 1400 °C [50]. This is an important aspect because shows that the MWCNT (% of carbon) could be present after sintering conditions of SS 316L if the atmosphere is protective. Nevertheless, the hydrogen presents in atmosphere could be unsuitable for stainless steel, due its contribution to brittleness of matrix.

Carbon could be in solid solution into steel matrix, in carbides, or as nanotubes with or without defects. The comparison of thermogravimetric curves reveals that different atmospheres and heating rates are the major factor for the partial or total degradation of MWCNTs.

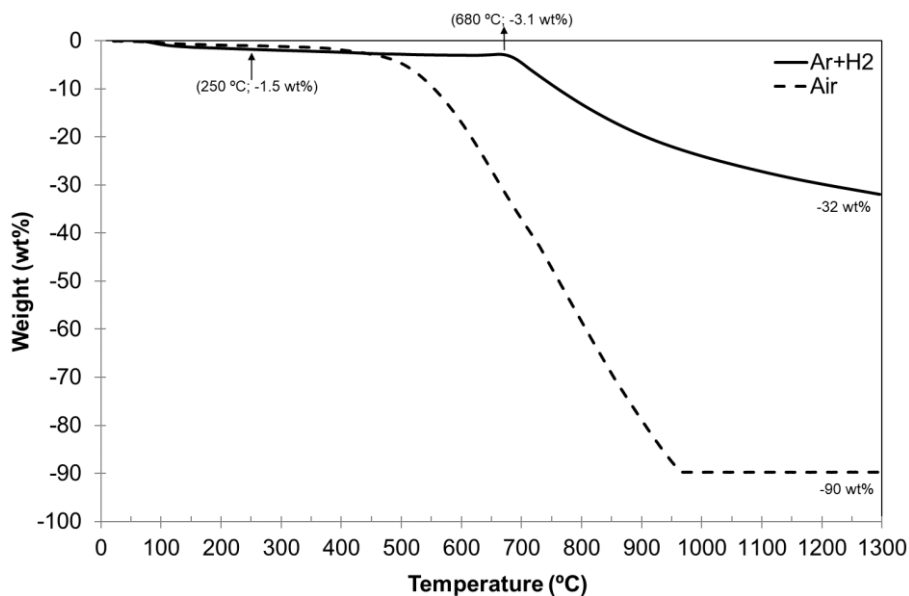


Figure 3.6 – TGA of MWCNTs in air and Ar+H<sub>2</sub> (5 %) atmospheres

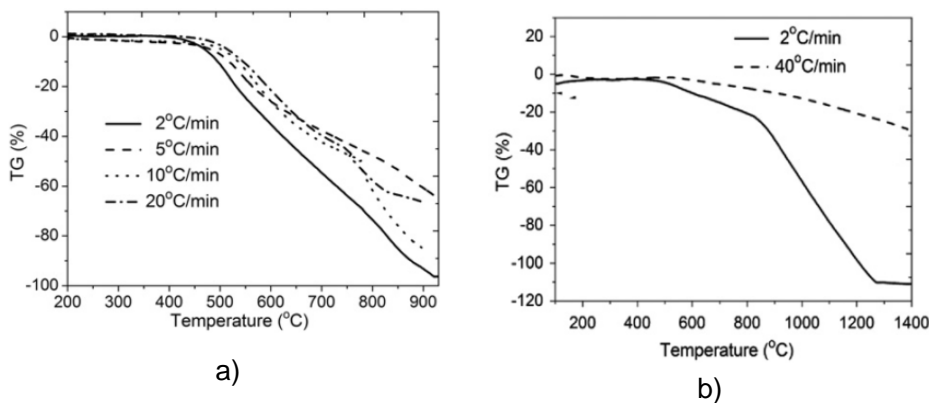


Figure 3.7 – TGA of MWCNTs in atmosphere a) air, b) argon, for different heating rates [50]

In order to highlight the behaviour of nanotubes in austenitic stainless steels during processing in same conditions, other nanoreinforcement were selected as standard. The selection of nanoparticles had in mind as characteristics, to be a ceramic material (oxide), stable during sintering thermal cycle in what concerns: carbon, oxygen and reactivity with matrix elements in solid solution. Thus, nanoparticles of  $\text{Al}_2\text{O}_3$  with 20 – 30 nm of diameter and density of  $3310 \text{ kg/m}^3$ .

### c) Binder

The binder selected ( $M_1$ ) where the density measured was  $970 \pm 1 \text{ kg/m}^3$  (by helium pycnometry) similar to the commercial datasheet (cf. Chap. II – Materials). The thermal analysis is extremely important to understand the thermal behaviour of this binder, giving information about critical temperatures and possible presence of carbon residues after debinding. Moreover, it is essential to define the debinding thermal cycle.

Figure 3.8 shows the thermal analyses of  $M_1$  binder up to 700 °C, at heating rate of 10 °C/min and under  $\text{Ar}+\text{H}_2$  dynamic atmosphere. Endothermic peaks in the range of 55 °C and 200 °C (DTA curve) correspond to melting temperatures of the binder constituents. In this range, the weight loss is not significant and is due to its dehydration. Up to 250 °C any significant weight change is observed (TGA), but increasing heating temperature it starts the process of binder degradation. In conclusion, the weight loss of the binder starts at 200 °C and finish at 485 °C, where the binder is completely removed.

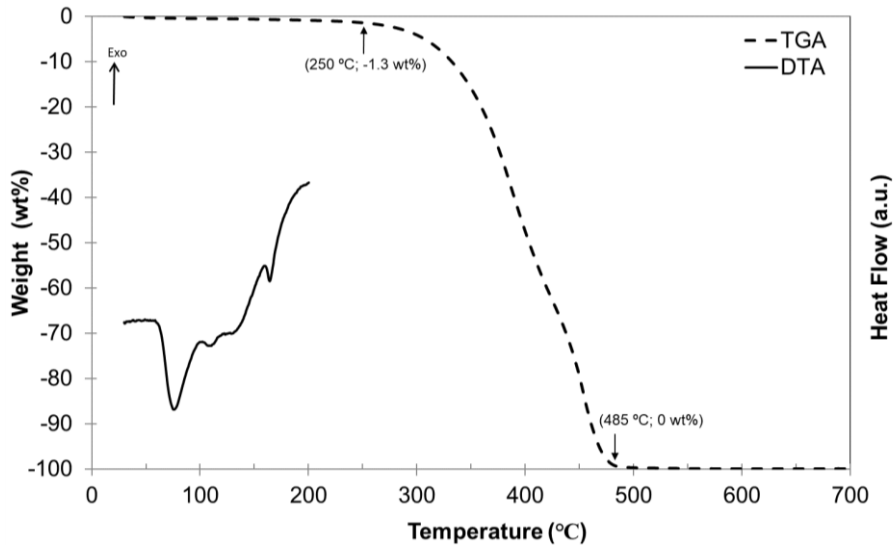


Figure 3.8 – TGA of binder M<sub>1</sub>

Moreover, it will be evident during the preliminary tests (route 1 a)) that the conventional binder was not enough to attain suitable rheological properties of metallic powders and MWCNTs mixtures. The solution was a supplementary stearic acid (SA) addition to the binder in different contents. In fact, SA seems to be the solution having in mind its role in different studies, where carbon nanotubes were mixed with metallic powders [6], [26]. This “lubricant” has a density value of  $983 \pm 1 \text{ kg/m}^3$  close to M<sub>1</sub> binder ( $970 \pm 1 \text{ kg/m}^3$ ), measured by helium pycnometry. The thermal analysis of SA conditions were as follows: heating up to 700 °C, at heating rate of 10 °C/min, under Ar+H<sub>2</sub> dynamic atmosphere (figure 3.9). The DTA curve presents a well-defined endothermic peak at 79 °C (melting temperature), from of 250 °C to 375 °C there is a large loss weight about 97 %, (TGA curve). After 375 °C the rate of weight loss changes and it becomes slow up to 550 °C, where all the SA is eliminated.

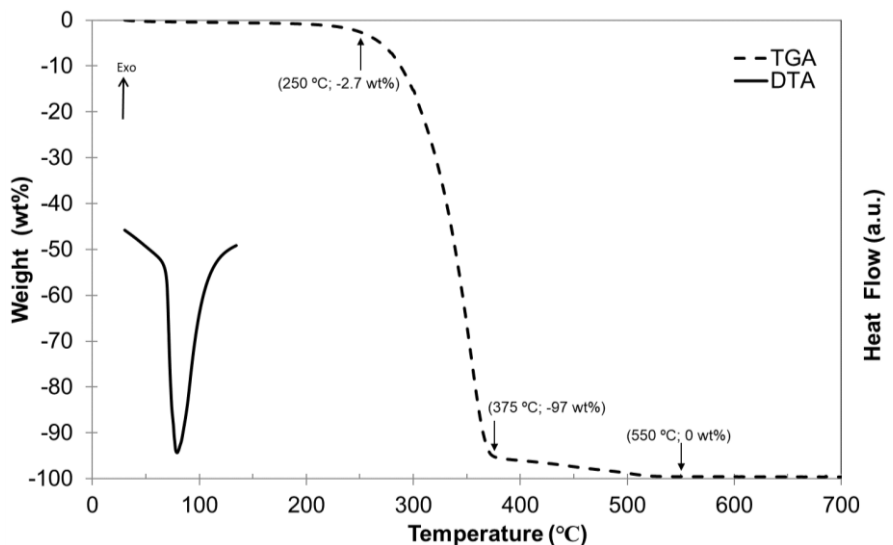


Figure 3.9 – TGA of SA

From the TGA analyse and the type of chemical bonds present in both: M<sub>1</sub> commercial binder and lubricant (Appendix I), it seems to be evident that their thermal behaviour as mix will be similar of each one. However, the TGA curve of the mixture used in this study (3:1 vol% or 2.9:1 wt% of M<sub>1</sub>: SA) shows different behaviours. The degradation of the mixture of M<sub>1</sub> binder with SA function of temperature changed (figure 3.10). As refereed, the pristine M<sub>1</sub> (figure 3.8) was total eliminated at 485 °C, but in the mixture, it degradation continues to 950 °C. The stearic acid, that showed to have more resistance with temperature (figure 3.9), seems to disappear not at 550 °C but only at 950 °C. In fact, at 550 °C in the mixture there are yet 3 %wt of binder with SA, that is constant up to 850 °C, having a total elimination only at 950 °C.

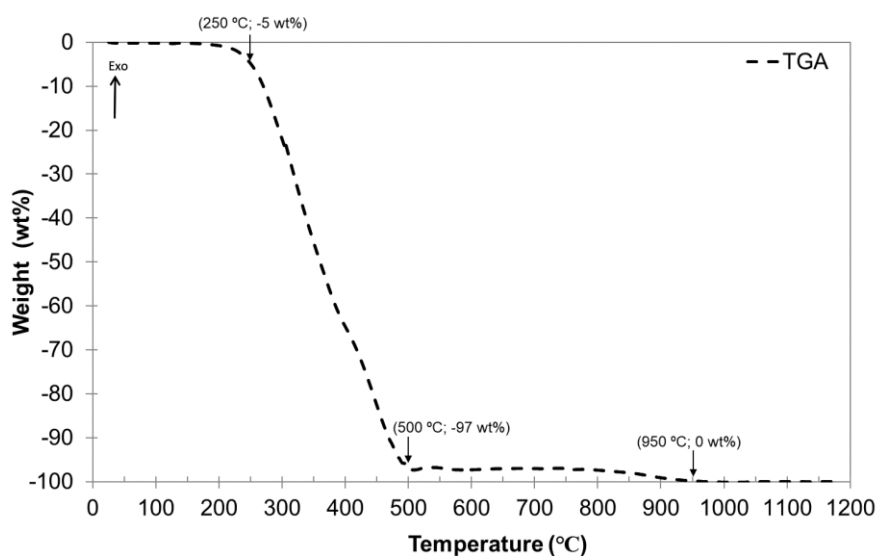


Figure 3.10 – TGA of binder M<sub>1</sub> with SA (3:1 vol%)

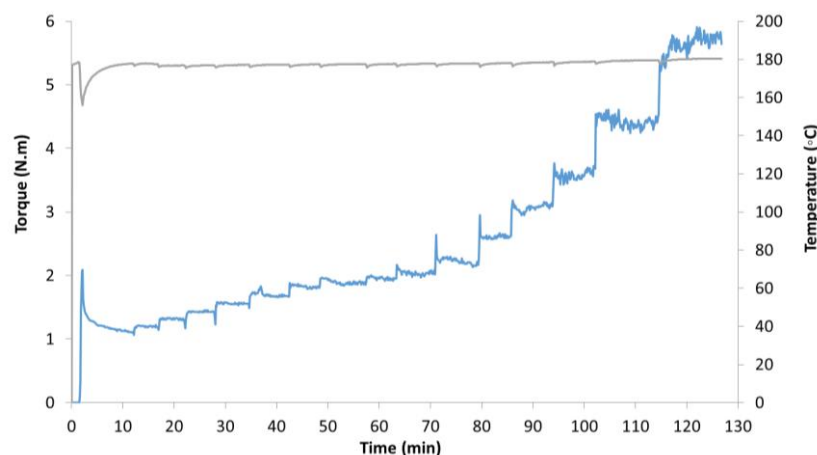
In conclusion, at the typical temperatures of feedstocks based on SS 316L powder are heat treated (600 °C) there are yet as residues about 3 % of binder. The temperature of 600 °C do not be overcome during thermal debinding, because the long stage of debinding cycle to contribute to the powders degradation, like reactions with environmental atmosphere and to prevent the integrity of MWCNTs. Thus, the debinding of M<sub>1</sub> with SA led to a total degradation at 950 °C, this unexpected behaviour could be explained by possible reaction between different constituents of M<sub>1</sub> and SA (since, while individually analysed, they are easily removed to lower temperatures).

## 3.2 Feedstocks nanocomposite powders for $\mu$ MIM

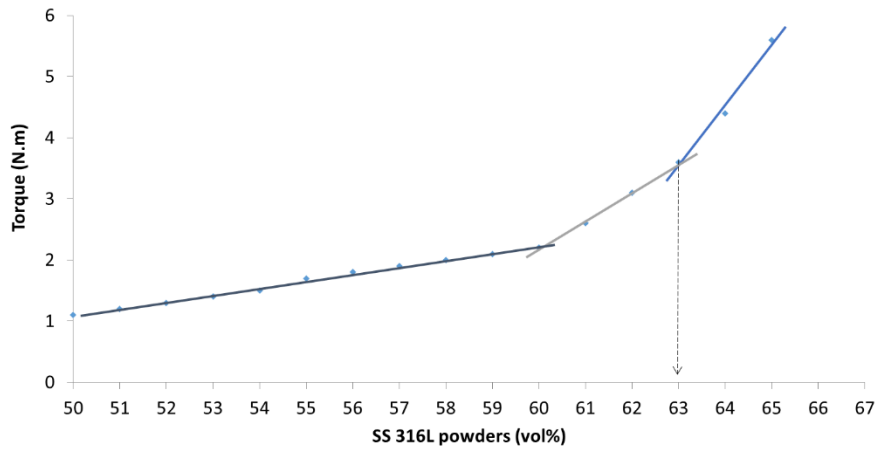
After materials characterization, it was necessary to adjust  $\mu$ MIM process (mixing, injection, debinding and sintering) to a new feedstock constituted by two dissimilar materials, where one is nanometric material (at least one dimension less than 100 nm) and the other austenite stainless steel powders (0.02 wt% C).

### a) Optimization of SS 316L powders

For production the feedstocks, the optimization of mixture is necessary and must be carried out at 180 °C and 30 rpm. Firstly, it was optimized the mixtures only with austenitic stainless steel powders, and after the nanocomposite based material (with nanoreinforcement addition). Figure 3.11 shows the adopted methodology for optimization of SS 316L powders with the M<sub>1</sub> binder. Three different regimes are evident, when the torque value increases by the consecutive addition of 1 vol% of powder. The first regime is between 50 and 60 vol%, where the torque values increase slightly after each addition. The second one is between 60 and 63 vol% where the variation of torque with powder addition assumes a visible slope. The maximum torque value attained was 5.6 N.m for 65 vol% of powders added, third regime. The ideal content of powders in feedstock is for a torque value lower than 4.0 N.m (CPVC) [63], [73]. Based on optimization, the optimal value to produce the mixtures should be 63 vol% of powder contents into mixture. However, having in mind the future addition of nanoreinforcement and their “perverse” role in the feedstock rheology, it was decided to use the minimum value of the second step (60 to 63 vol%) of torque function powder contents.



a)



b)

Figure 3.11 – SS 316L feedstock optimization versus a) time and b) SS 316L powders (vol%)

The feedstock with 60 vol% of SS 316L and 40 vol% of  $M_1$  has a stable torque value that reflects a homogeneity of the mixture, named as master feedstock (MF) (figure 3.12). The relation powders: binder is 60:40 vol% or 92.5:7.5 wt%.

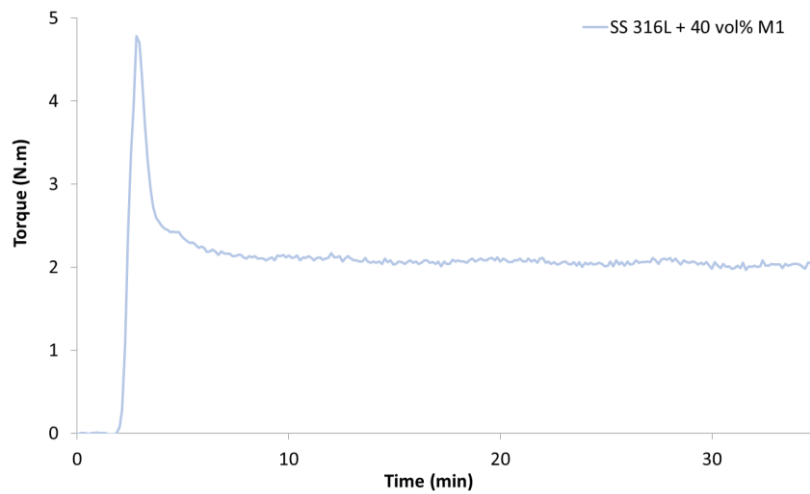


Figure 3.12 – SS 316L feedstocks with 40 vol% of  $M_1$  binder

The SS 316L feedstock was analysed by SEM (figure 3.13), another way of assessing the mixture homogeneity. This technique reveals that SS 316L powders are homogeneously dispersed in  $M_1$  binder, and for the highest magnification, powders exhibit to have an uniform coating of binder.

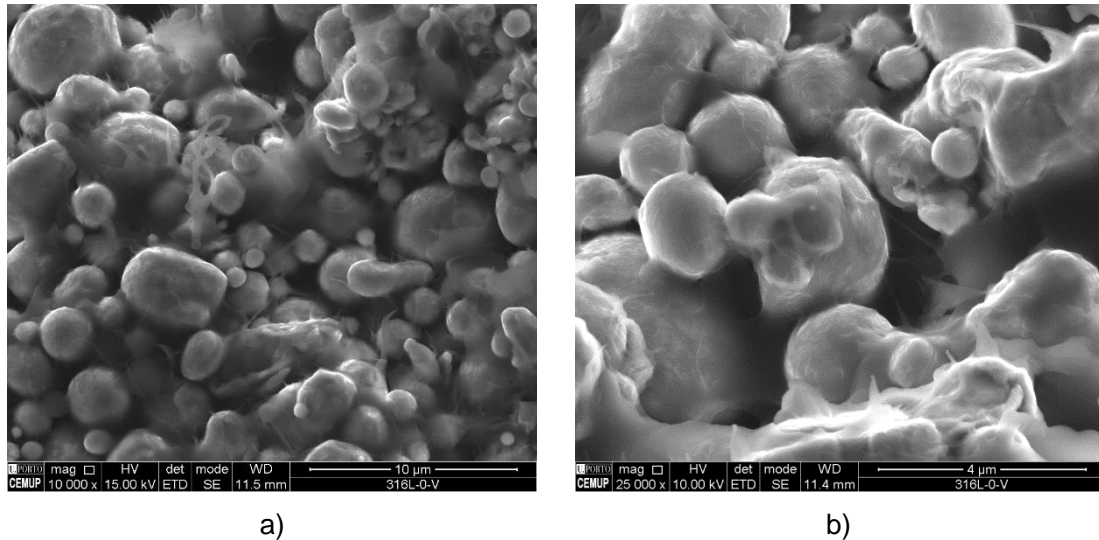


Figure 3.13 – Morphological analysis of SS 316L feedstock, at different magnifications a) 10000x and b) 25000x

The thermal behaviour of master feedstock ( $M_1$  without SA) up to 650 °C, at heating rate of 10 °C/min, under Ar+H<sub>2</sub> dynamic atmosphere, shows that binder degradation starts at same temperature of the feedstock per se, with a total weight loss content  $\approx$  7.7 wt%. However, this value corresponds also to the weight loss of SS 316L powder up to 250 °C ( $\approx$  0.2 wt%) (figure 3.14).

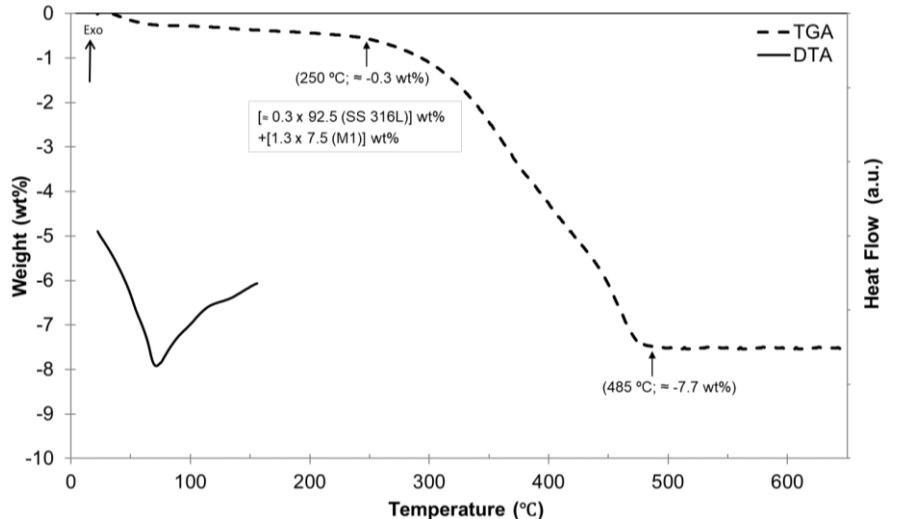


Figure 3.14 – TGA of SS 316L: $M_1$  feedstock 60:40 vol%

A study using copper powders with 3S's particle characteristics (cf. Appendix II: figures A.2 and A.3 and table A.1) similar to SS 316L, used in the present study, but with sintering temperature lower than the typical of austenitic stainless steel. The bibliographic references point to be copper sintering temperature (900 – 1050 °C), where there are not MWCNTs degradation. However, the most research works use other manufacturing

processes. A detailed study about the optimization of these nanocomposites based on copper (Appendix II).

## b) Feedstocks of composites

The master feedstock (with  $M_1$ ) was nanoreinforced with different percentages of MWCNT or nanoalumina powder: 0.8, 1.7, 2.5 and 3.3 vol%. The nanoreinforcement was directly added during the mixture time (route 1 a)) (figure 3.15).

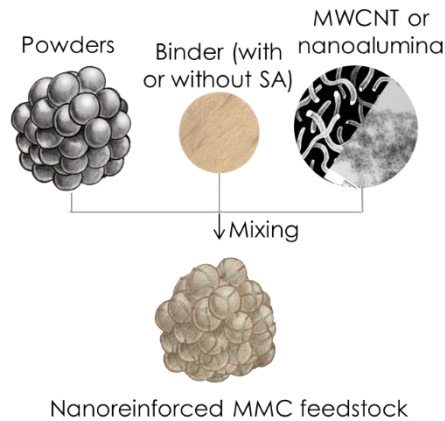
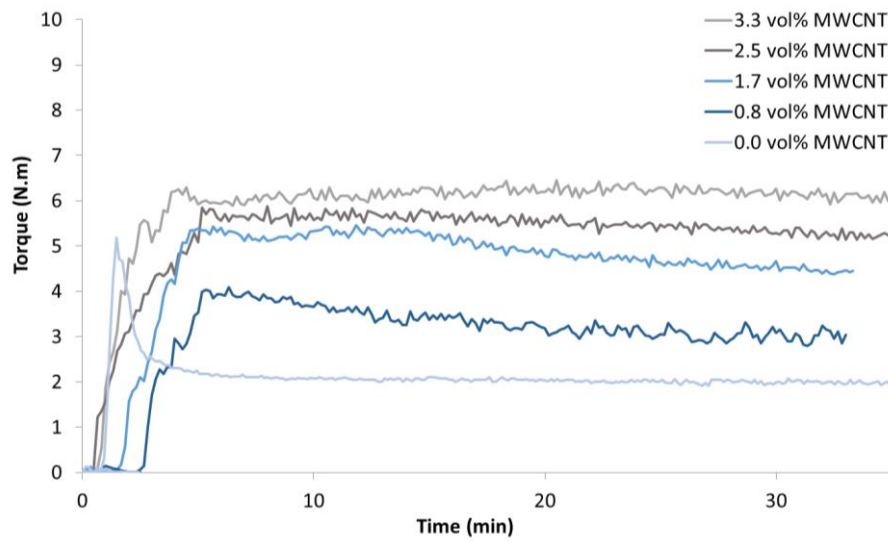


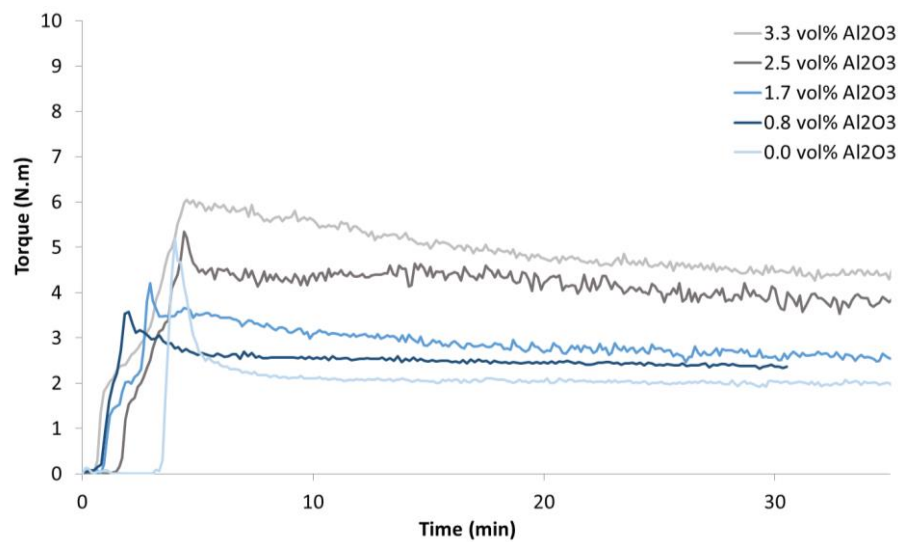
Figure 3.15 – Mixing procedure (route 1)

Figure 3.16 shows the behaviour of composites feedstocks with different nanomaterials (MWCNT and nanoalumina). The nanoreinforcement added directly to the optimized mixture (MF – route 1 a)), independently of their types, the torque value always increases with addition of nanoreinforcement content. The addition of MWCNTs produce nanoreinforced feedstocks with the following torque values 3.0, 4.5, 5.3 and 6.1 N.m, respectively (figure 3.16 a) and table 3.2). In what concerns to nanoalumina additions (figure 3.13 b)), the correspondent torque values were 2.4, 2.5, 3.7 and 4.2 N.m, respectively (table 3.2). Some of nanoreinforcements contents in feedstocks overcome the torque limit suitable to be injected (4.0 N.m). In order to overcome this problem, there are three solutions: addition only 0.8 vol% MWCNT or 2.5 vol% nanoalumina in SS 316L, or introduction a supplement in the binder (i.e. addition of SA) or decrease the powder content, but this last option not suitable to attain a high density of sintered parts.





a) MWCNT



b) Nanoalumina

Figure 3.16 – SS 316L and  $M_1$  composites feedstock nanoreinforced with a) MWCNT and b) nanoalumina (route 1a))

Table 3.2 –Torque values of SS 316L composites feedstocks nanoreinforced with MWCNT or nanoalumina

vol%	MWCNT	Nanoalumina
0.0	2.0	2.0
0.8	3.0	2.4
1.7	<u>4.5</u>	2.5
2.5	<u>5.3</u>	3.7
3.3	<u>6.1</u>	<u>4.2</u>

The same procedure was performed to a copper matrix (cf. Appendix II). After adding the nanoreinforcement to SS 316L:M<sub>1</sub>, the nanocomposites feedstocks present always lower torque values when compared with copper matrix, whatever the nanoreinforcement type (route 1 a)). One important conclusion is, for copper matrix is not possible to attain feedstocks with 3.3 vol% of nanoreinforcement.

In order to enlarge the nanoreinforcement contents in the matrices, the selected option was to mixture the feedstock with an aided flow – stearic acid, in different percentages (figure 3.17) [85]. The addition of 10 vol% of SA and 30 vol% M<sub>1</sub> to SS 316L matrix, decreases the torque value from 2.0 N.m to 1.0 N.m. The results show that higher percentage of SA added lower is the torque.

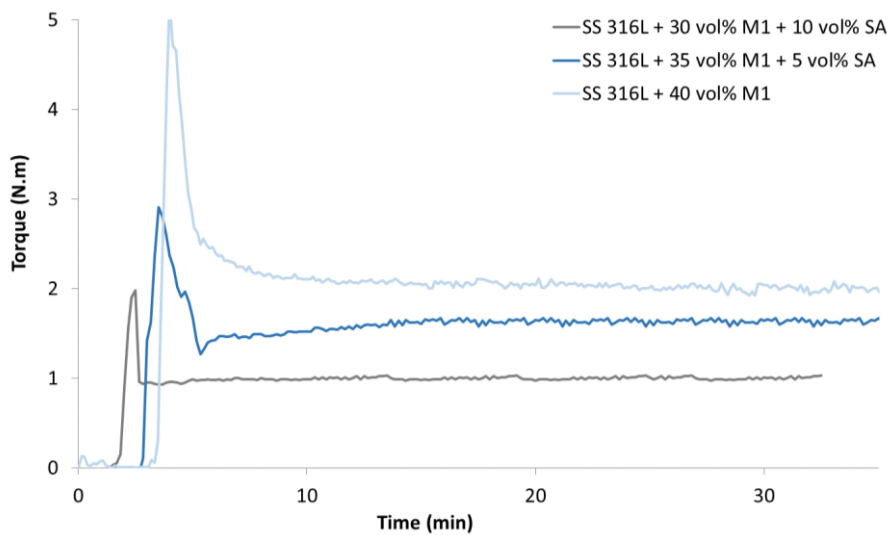


Figure 3.17 – SS 316L feedstocks with 0, 5 and 10 vol% of SA

The SS 316L feedstock with 10 vol% (1.9 wt%) of SA was analysed by SEM (figure 3.18 – route 1 b)). It is possible to observe that SS 316L powders are homogeneously dispersed in the modified binder and for high magnifications is perceptible that powders are also coated by the composite binder.

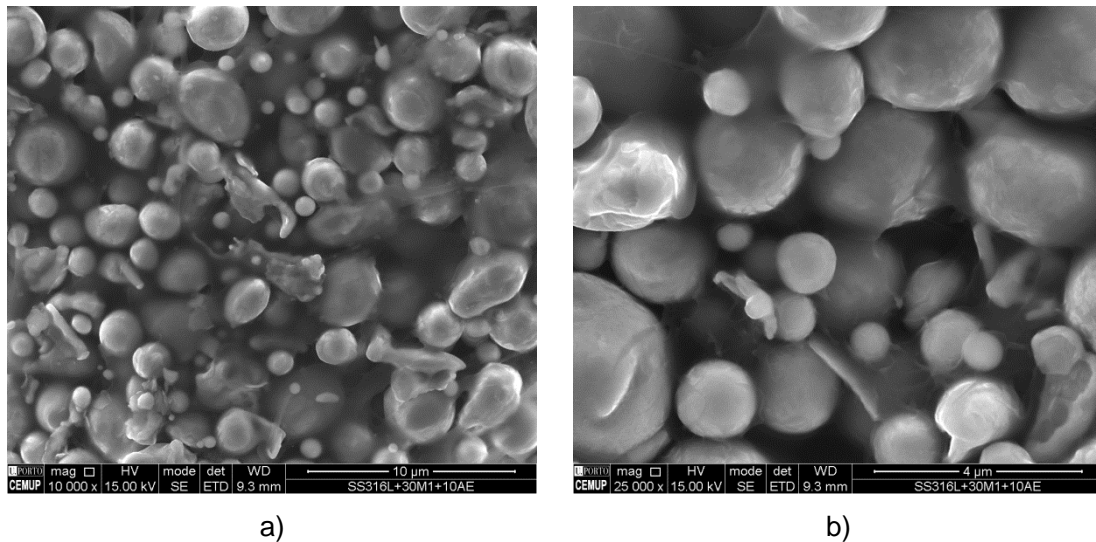


Figure 3.18 – Morphological analysis of SS 316L:binder (60:(30+10) vol%) a) 10000x and b) 25000x

Figure 3.19 shows the thermal behaviour of MF (with  $M_1$  and SA) up to 650 °C, also carried out under Ar+H<sub>2</sub> dynamic atmosphere, with same conditions used for conventional binder. Associated to decomposition of binder components with low number average molecular mass are the range from 45 to 250 °C, corresponding to endothermic reactions (DTA curve). A second range from 250 to 485 °C (TGA curve), which shows a significant weight loss, that is related to binder degradation (7.7 – 0.2 wt% (from SS 316L steel) = 7.5 wt%), percentage of binder in global feedstock. This unpredicted loss for the compounding binder (figure 3.19) could be related to the role of metallic powders during the mixing, inhibiting the reaction between the  $M_1$  and SA (methodology adopted it was first mix binder  $M_1$  with SA at 180 °C, secondly introduction of powder quantities). In conclusion, this compound mix can be total eliminated by thermal debinding.

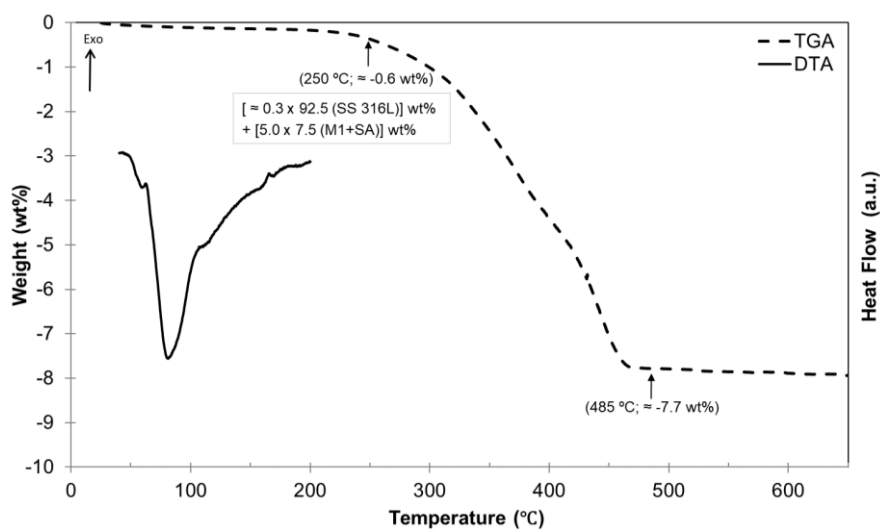
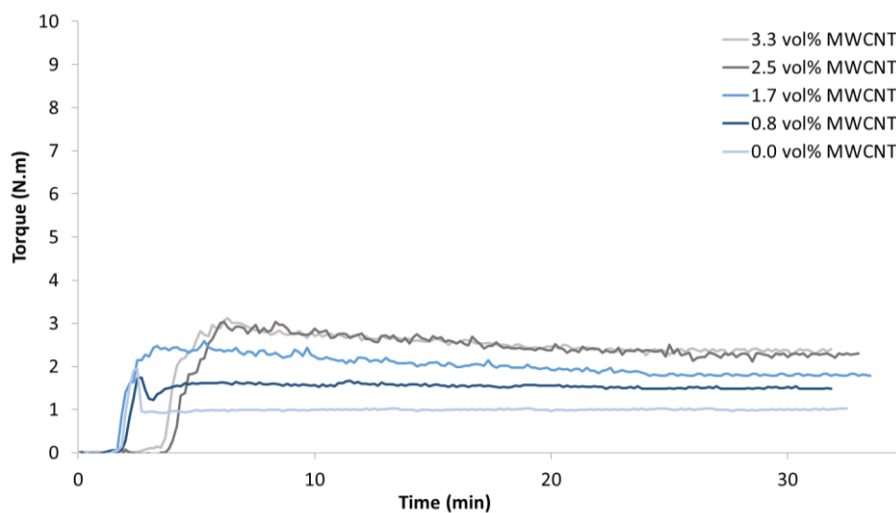


Figure 3.19 – TGA of SS 316L+( $M_1$ +SA) feedstock

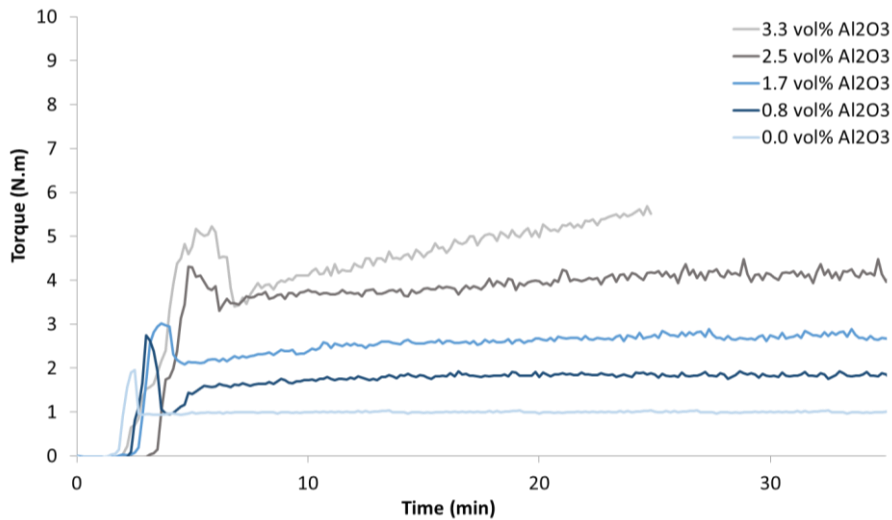
Comparing the same procedure applied to SS 316L and copper powders (without nanoreinforcements) the addition of 10 vol% of SA decrease the torque values of both feedstocks (being more evident in steel). The mixture homogeneity continuous to be attained whatever the metallic powders.

Henceforth, the master feedstock composition will be 60 % of SS 316L, 30 % of M<sub>1</sub> and 10 % of SA (vol%) and the study must be enlarged to the effect of nanotubes content in the behaviour of the feedstock (route 1 b)). Thus, the selected nanoreinforcement contents were 0.8, 1.7, 2.5 and 3.3 vol% of MWCNT or nanoceramic in metallic powders [85]. The new relation SS 316L/MWCNT: binder will be 92.3:7.7 (for the maximum quantity of MWCNT added).

Figure 3.20 shows the behaviour of nanocomposites feedstocks with MWCNTs and nanoalumina reinforcements. For similar compositions of the mixture, after addition of nanotubes, the torque measured was 1.6, 2.0, 2.3 and 2.4 N.m as the nanotubes increasing its content, respectively (figure 3.20 a)). In other hand, the standard composite using nanoalumina addition were tested and the torque values were attained for the same contents of reinforcement particles 1.8, 2.7, 4.1 N.m, respectively, but the high content of nanoreinforcement (3.3 vol%) was not taken into account, due to the torque value do not attained a steady regime (table 3.3). The nanoceramic additions produce feedstocks whose torque values present more instability than MWCNTs.



a) MWCNT



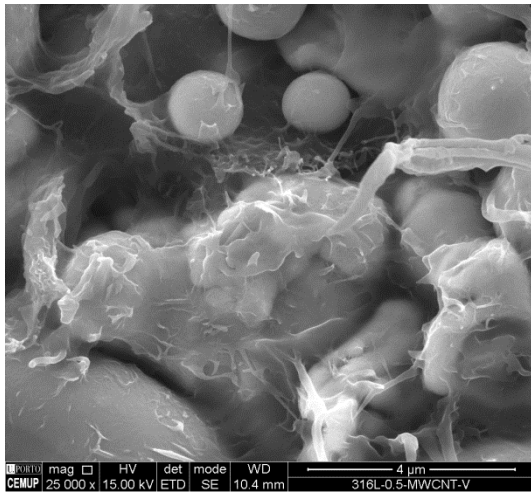
b) Nanoalumina

Figure 3.20 – SS 316L composites feedstock ( $M_1+SA$ ) nanoreinforced with a) MWCNT and b) nanoalumina

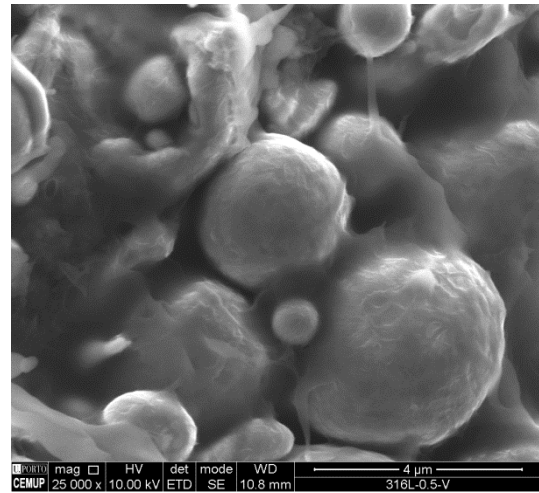
Table 3.3 –Torque values of SS 316L composites feedstocks nanoreinforced with MWCNT and nanoalumina

vol%	MWCNT	Nanoalumina
0.0	1.0	1.0
0.8	1.6	1.8
1.7	2.0	2.7
2.5	2.3	<u>4.1</u>
3.3	2.4	-

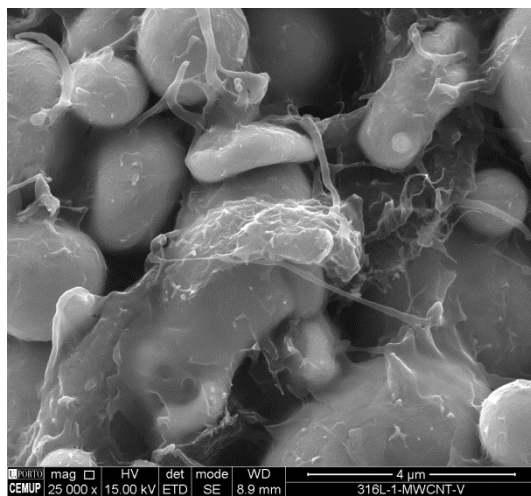
The feedstocks were analysed to assess the distribution of the various constituents in mixture. Figure 3.21 shows the differences between the addition of MWCNT and nanoalumina for the same matrix (SS 316L). A good distribution of powders in binder, but with a different morphology depending on the type of nanoreinforcement, is clear in figure 3.21. For MWCNT nanoreinforcement, it is perceptible that binder matched to the shape of the nanotubes. Nevertheless, a number of “fine wires” without binder are also detectable, a “large wires” corresponding to the nanotubes coated by binder (figure 3.21 a), c) and e)), and “compact zones” clusters of MWCNT and binder (figure 3.21 e) and g)) are visible. In what concern to ceramic nanoparticles, the binder seems more “soft” compared with the previous case study. With the increasing of nanoparticle content, the binder looks be more adherent to powder particles (figure 3.21 f) and h)), as is demonstrated by the torque value. This behaviour could contribute to a decrease of flowability.



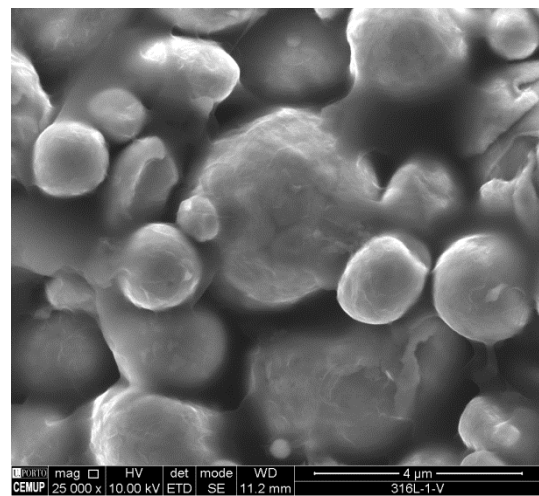
a) 0.8 vol% MWCNT



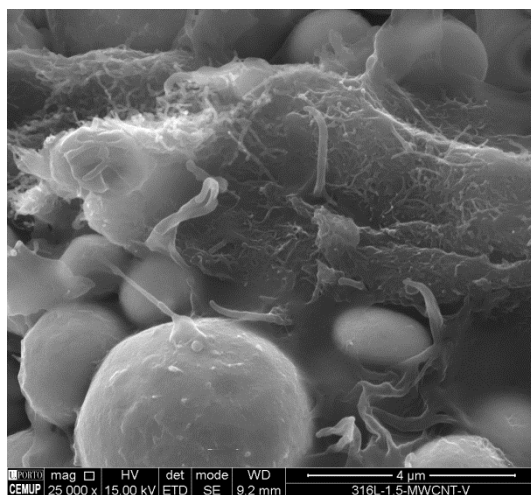
b) 0.8 vol% nanoalumina



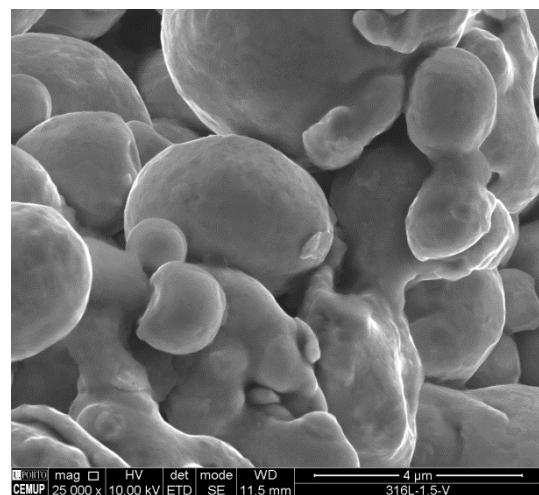
c) 1.7 vol% MWCNT



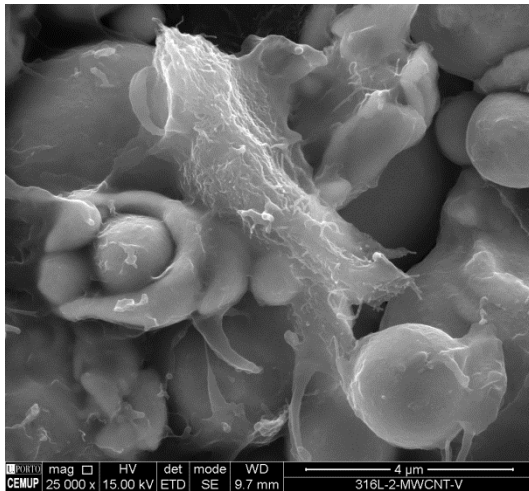
d) 1.7 vol% nanoalumina



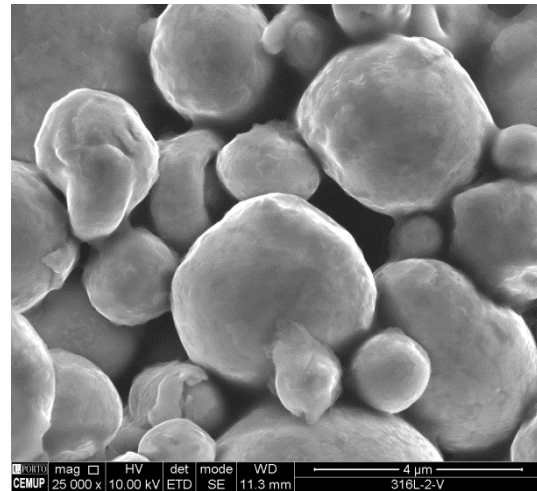
e) 2.5 vol% MWCNT



f) 2.5 vol% nanoalumina



g) 3.3 vol% MWCNT



h) 3.3 vol% nanoalumina

Figure 3.21 – Morphological analysis of SS 316L nanocomposites feedstocks with MWCNT (left) and nanoalumina (right)

The same procedure was applied to copper matrix (Appendix II – route 1 b)) and after adding MWCNTs, the feedstocks often-present higher torque values than for SS 316L matrix.

Until now, the production of nanocomposites feedstocks results from the introduction of nanoreinforcement during mixing time (route 1). However, this procedure caused two main problems:

- Nanocomposites feedstocks with higher torque value than the master feedstock.  
Whatever the matrix and the nanoreinforcement type, for the various percentage of nanoreinforcements tested (0.0 to 3.3 vol%), the increment of MWCNT/nanoalumina gives rise to an increasing of torque values, making these feedstocks difficult to be processed by  $\mu$ MIM;
- Presence of nanoreinforcements in binder.  
Increasing the possibility of the nanoreinforcement removal at the same time as binder.

Figure 3.20 a), shows that the mixture between MWCNT and SS 316L powders are the most stable and has the lowest torque values (comparatively to the nanoalumina). In order to overcome the problems identified was tried to produce the nanoreinforced composites feedstocks promoting a physical bond between metallic powders and MWCNT by a pre-mixing, using a ball milling (figure 3.22).



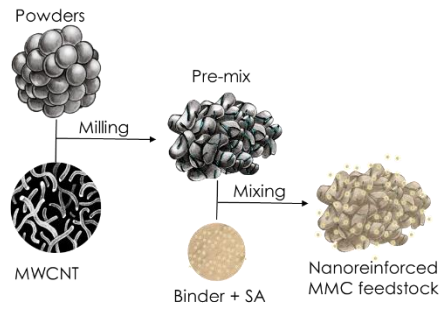
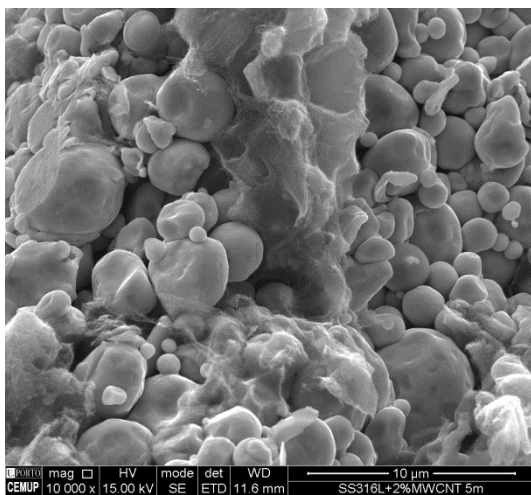
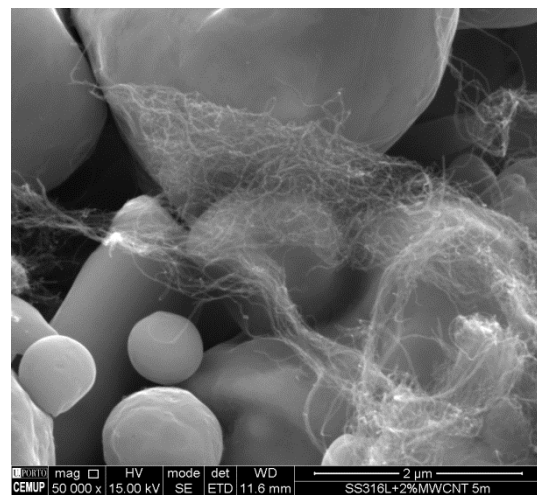


Figure 3.22 – Schema of feedstock preparation (route 2)

Through the pre-bonding of powders and MWCNTs it was possible to prevent their loss during debinding process. The morphology of pre-mixtures (SS 316L with 3.3 vol% of MWCNT) after being milled in a planetary ball milling during 5 + 10 and 15 minutes, total 30 minutes, are in figures 3.23. The pre-mixture after 5 and more 10 minutes presents agglomerations of MWCNTs. However, after more 15 minutes of milling (figures 3.23 e) and f)), some powder particles still have spherical shape and MWCNTs recover their individuality. The presence of MWCNTs on powder surface, revealing an efficient deagglomeration by milling, with MWCNTs embedded in flatted powders. This is due to the ductile character of metallic powders after being submitted to several impact collisions of balls in the jar. In spite of agglomerates be still visible, but to prevent the damage of MWCNTs the process was finished. In conclusion, the mixing parameters selected were as follows: total time 30 minutes (15 minutes, with a break of 10 minutes, and more 15 minutes) and rotation speed of 200 rpm, under Ar+H<sub>2</sub>.

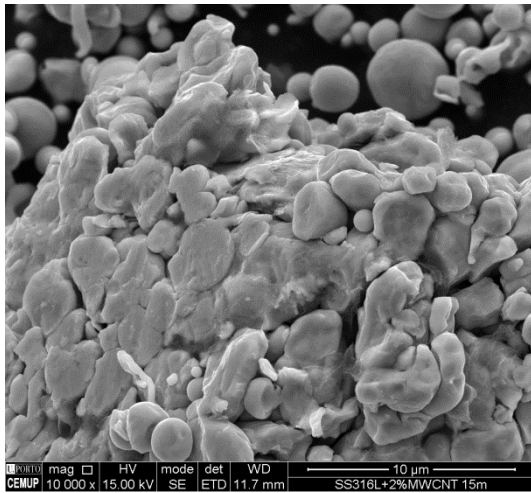


a) 5 minutes

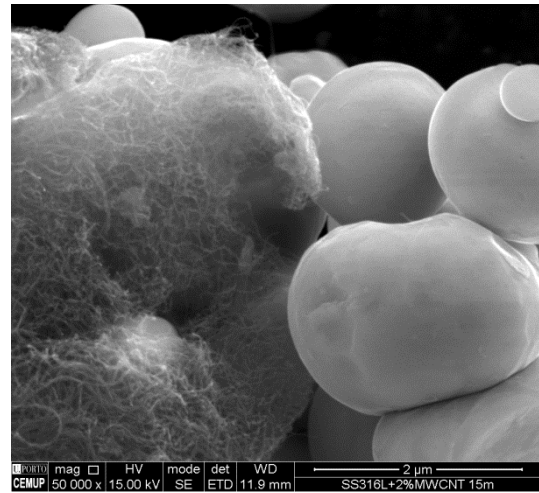


b) 5 minutes

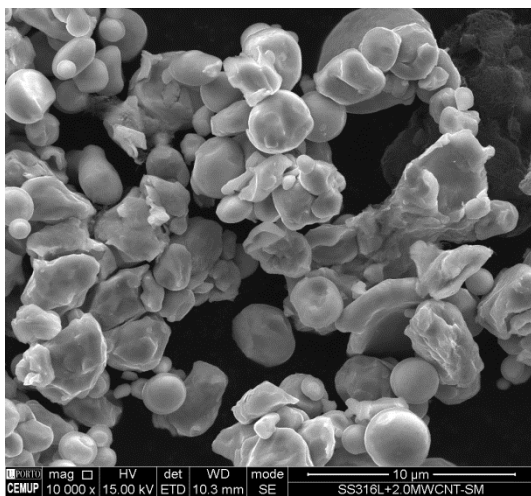




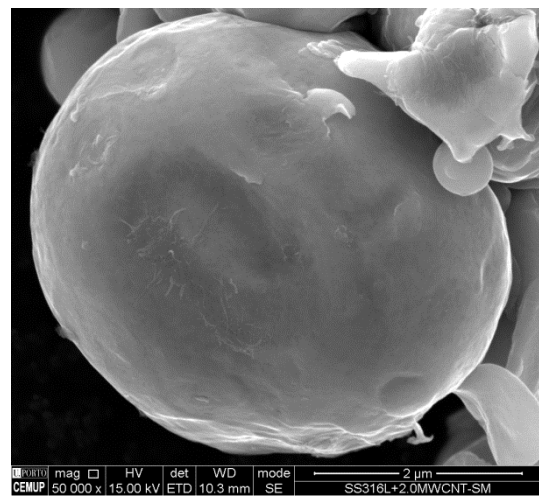
c) 15 minutes



d) 15 minutes



e) 30 minutes



f) 30 minutes

Figure 3.23 – Morphological analysis of pre-mixture a), b) 5 minutes, c), d) 15 minutes, e), f) 30 minutes 10000x (left) and 50000x (right)

After milling optimisation, the pre-mixture (SS 316L and MWCNT) was mixed with master binder for each composition using Brabender Plastograph, under the same conditions that induces stable torque values (figure 3.24). For the compositions tested, the torque values were 0.9, 0.9, 0.9, 1.3 and 2.2 N.m, respectively (table 3.4). These new nanocomposites feedstocks are lower than any procedure used previously. In feedstocks with high nanoreinforcement content, is perceptible a slight loss of flowability (that can be harmful during injection moulding step). Nevertheless, all these nanocomposites feedstocks are suitable to  $\mu$ MIM process, due to a guaranteed homogeneity and low torque values.

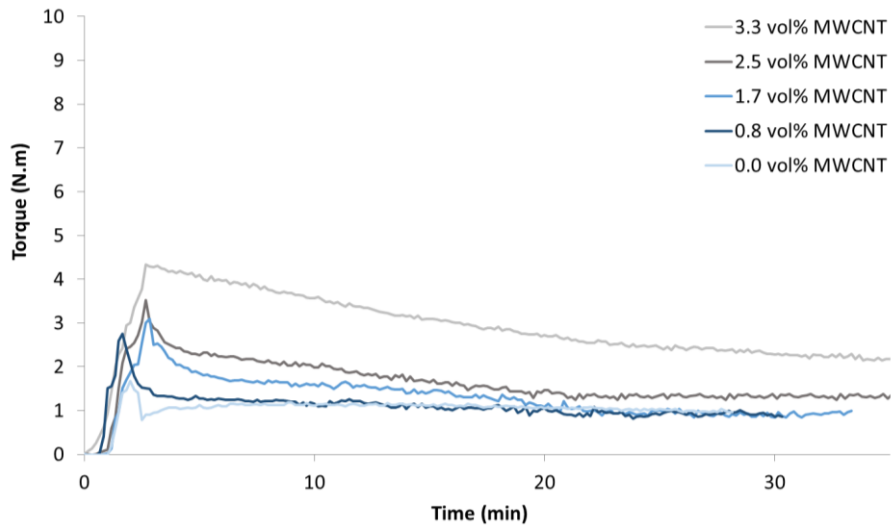
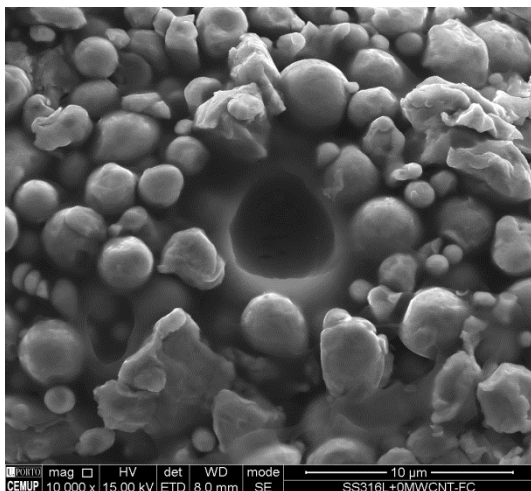


Figure 3.24 – SS 316L nanoreinforced composite feedstock with MWCNT (pre-mixture) (route 2)

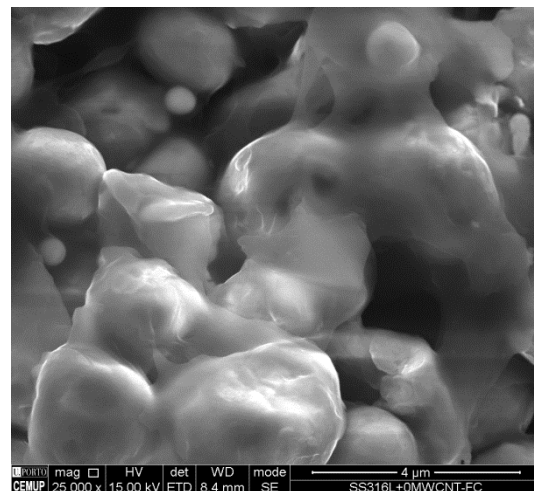
Table 3.4 – Torque values of SS 316L composites feedstocks nanoreinforced with MWCNT (route 2)

vol%	Torque (N.m)
0.0	0.9
0.8	0.9
1.7	0.9
2.5	1.3
3.3	2.2

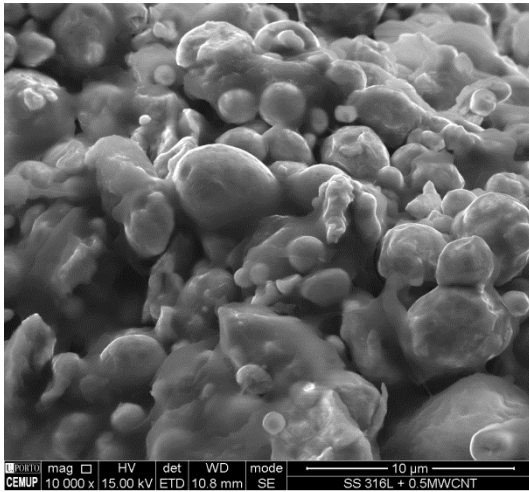
The nanocomposites feedstocks were analysed by SEM but with some limitation due to poor conductivity of set. With the addition of nanoreinforcement, it is visible same differences mainly in binder morphology. That seems to be out of powder particles, with the increasing of MWCNTs content (figure 3.25).



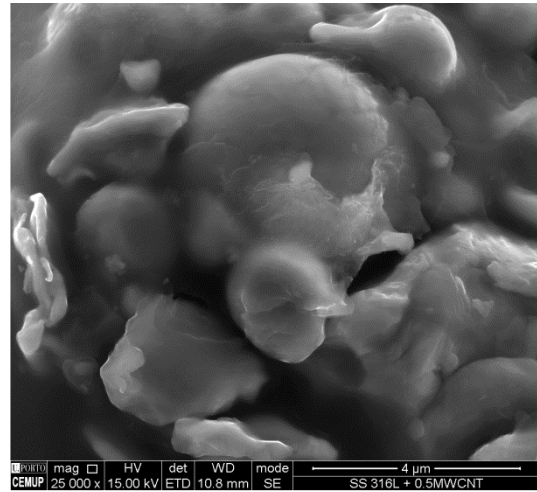
a) 0.0 vol%



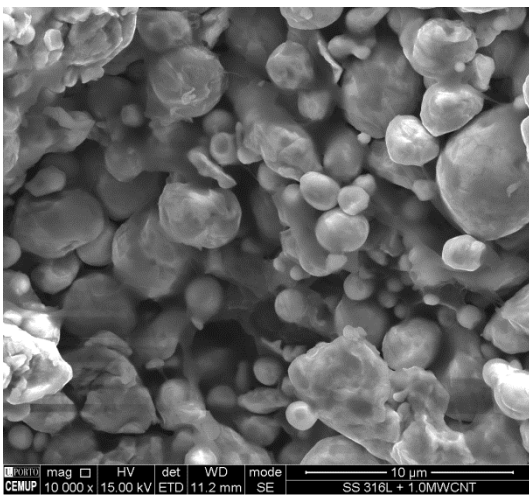
b) 0.0 vol%



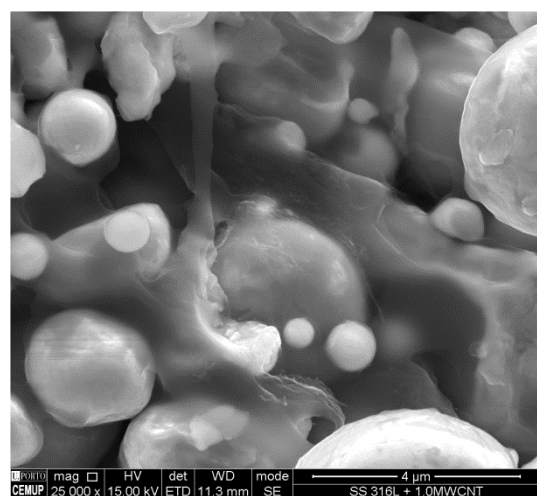
c) 0.8 vol%



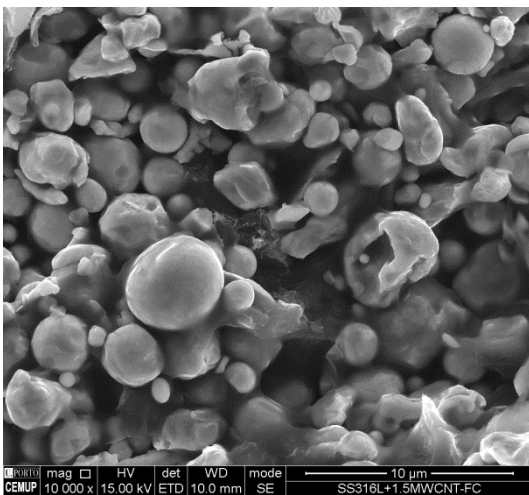
d) 0.8 vol%



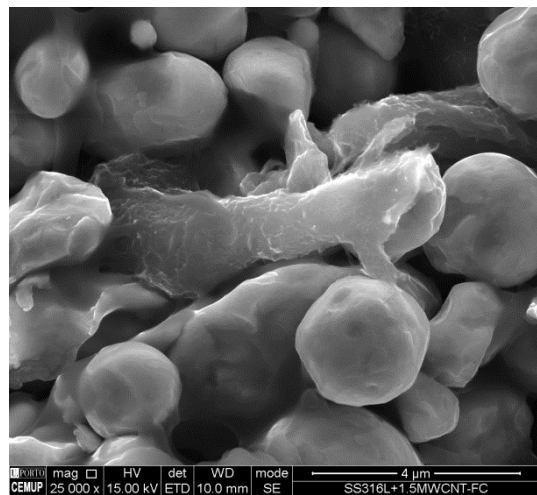
e) 1.7 vol%



f) 1.7 vol%



g) 2.5 vol%



h) 2.5 vol%

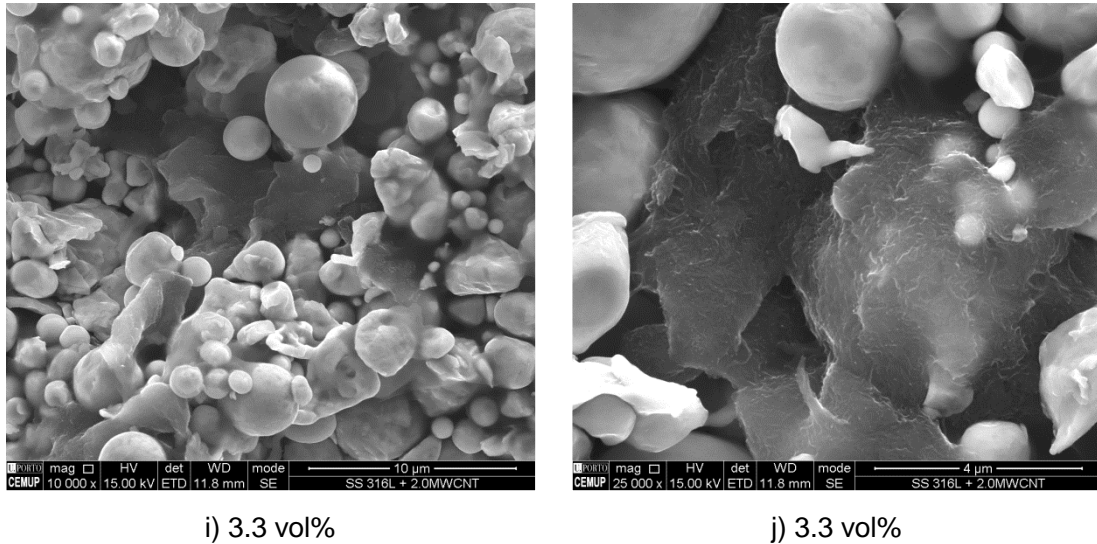


Figure 3.25 – Morphological analysis of nanocomposites feedstocks with different contents a), b) 0.0, c), d) 0.8, e), f) 1.7, g), h) 2.5, i), j) 3.3 of MWCNTs (vol%) 10000x (left) and 25000x (right)

Figure 3.26 shows the thermal analysis of MF reinforced with 3.3 vol% (0.8 wt%) of MWCNT, carried out under the same condition of previous thermal analysis. Once again, it is possible to observe a first range between 40 °C and 210 °C corresponding to endothermic reactions. The range from 200 °C to 485 °C shows a significant weight loss (TGA curve), related to the percentage of master binder degradation (8.0 – 0.3 wt% (from SS 316L steel and MWCNT) = 7.7 wt%) in global reinforced feedstock. Once again, this analysis confirms that the binder is completely removed when are guaranteed the atmospheric ideal conditions in the thermal debinding.

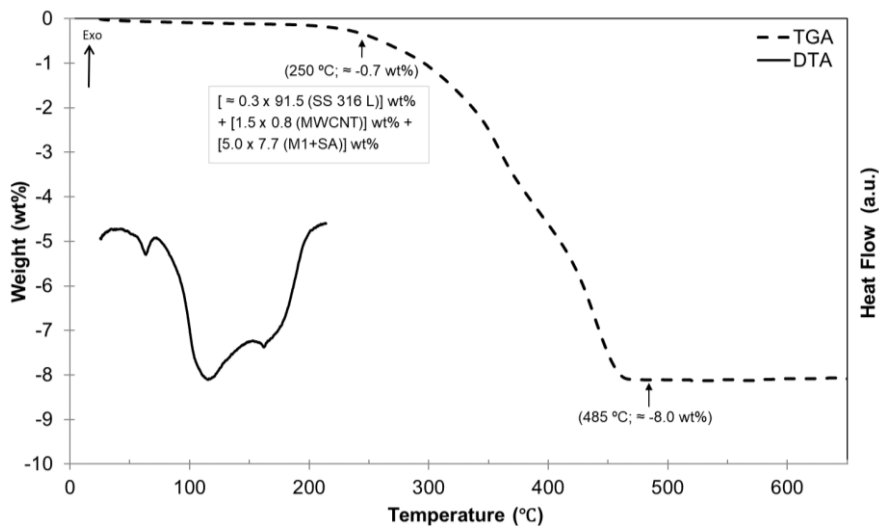


Figure 3.26 – TGA of SS 316L MF with 3.3 vol% (0.8 wt%) MWCNT

The master feedstock produced from SS 316L powders, and the composites feedstocks nanoreinforced, were granulated in pellets to injection moulding step. For the similar contents of MWCNTs added in copper matrix, the procedure was the same (Appendix II). Once again, the copper matrix has higher torque values than SS 316L matrix. For the highest contents of nanotubes (3.3 vol%), the torque of the copper composite feedstock is high unsuitable for  $\mu$ MIM technology.

### 3.3 Injection Moulding

After selected the best conditions for injection the SS 316L MF reinforced and no reinforced granulated feedstocks (with SA addition), the injection was performed in a moulding with a tensile specimen design (figure 3.27).

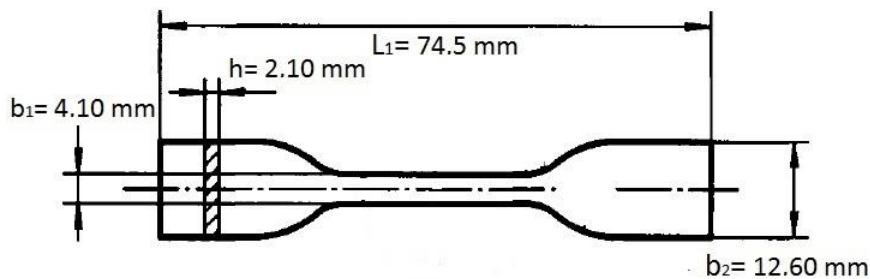


Figure 3.27 – Design of specimen

The optimized conditions for injection moulding were performed using firstly master feedstock (with SA addition) and after readjusted for reinforced composite feedstocks (with SA addition). The first conditions optimized were the temperature (cylinder and mould) to guarantee a correct feedstock fluid behaviour when injected on mould. When temperatures were  $80$  °C and  $160$  °C for mould and cylinder respectively, and pressure about  $25$  MPa, the feedstock was not injectable (revealing insufficient pressure). However, maintaining the temperature and increasing the pressure to  $50$  MPa, the mould cavity is almost fulfilled (figure 3.28 a)). “Green parts” with good quality are injected with a mould temperature of  $82$  °C, for the remaining conditions constants (figure 3.28 b)).

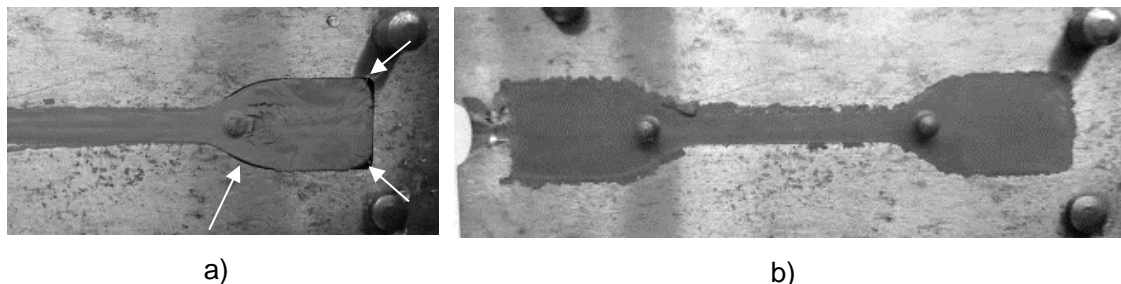


Figure 3.28 – a) Unfilled mould cavity –  $T_{\text{mould}} = 80$  °C and b) fulfilled mould cavity –  $T_{\text{mould}} = 82$  °C



The optimized parameters were also suitable for MF nanoreinforced with 0.0, 0.8 and 1.7 vol% of MWCNTs, demonstrated by similar torque value. However, these parameters are not suitable for feedstocks reinforced with 2.5 vol% of nanotubes (figure 3.29 a)) and 3.3 vol% (figure 3.29 b)). As showed in the mixing step, the addition of MWCNTs to matrix increases the torque value and loss the flowability the nanocomposite feedstock.

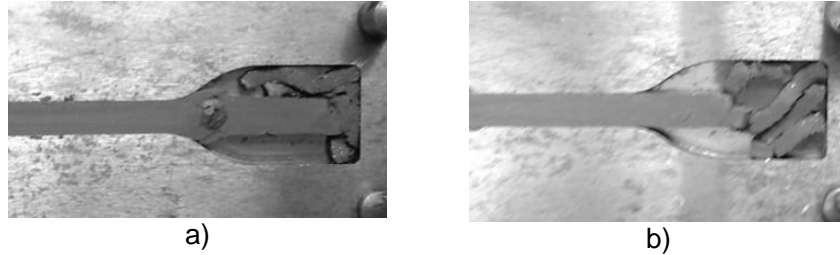


Figure 3.29 – Unfilled mould cavity with  $T_{mould} = 82\text{ }^{\circ}\text{C}$  a) 2.5 vol%, b) 3.3 vol% MWCNT

Due to high torque value of MF nanoreinforced with 2.5 vol% and 3.3 vol% it was necessary to increase the mould temperature ( $85\text{ }^{\circ}\text{C}$ ) to fill the mould (figure 3.30).



Figure 3.30 –SS 316L “green microspecimen”

Table 3.5 summarizes the injection parameters for various feedstocks, namely the MF (without milling pre-treatment) and the composites feedstocks produced by route 2, as well as the torque values, where it is perceptible that the increasing of the torque values requires higher mould temperatures.

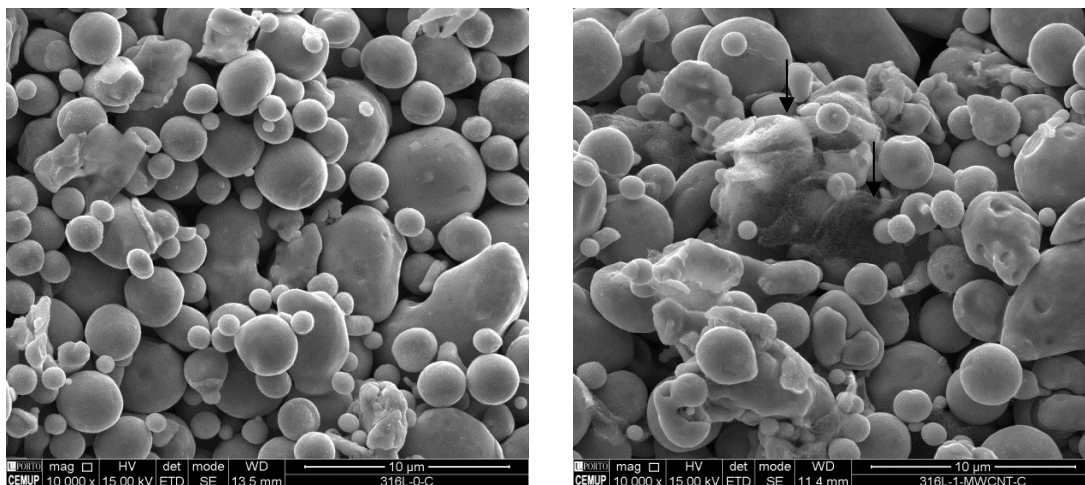
Table 3.5 – Injection parameters

vol%	Torque (N.m)	Parameters
MF	1.0	$T_{mould} = 82\text{ }^{\circ}\text{C}$
0.0	0.9	$T_{cylinder} = 160\text{ }^{\circ}\text{C}$
0.8	0.9	1 <sup>st</sup> and 2 <sup>nd</sup> pressures = 50 MPa
1.7	0.9	
2.5	1.3	$T_{mould} = 85\text{ }^{\circ}\text{C}$
3.3	2.2	$T_{cylinder} = 160\text{ }^{\circ}\text{C}$ 1 <sup>st</sup> and 2 <sup>nd</sup> pressures = 50 MPa

### 3.4 Debinding

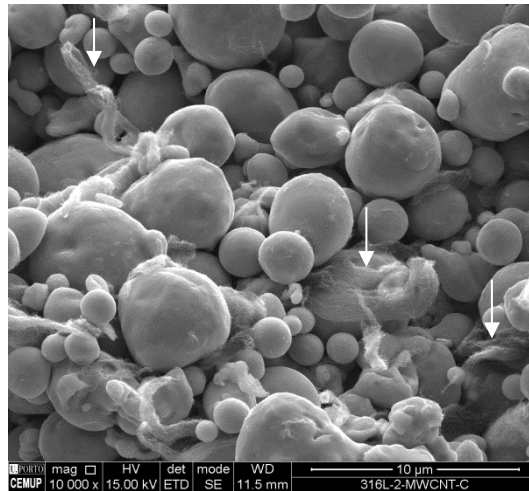
The debinding step of injected “green microcomponents” was carried out under the optimized thermal cycle. This was designed based on thermal analysis of the  $M_1+SA$  binders and respective peaks corresponding to weight loss, as well as the thermal analysis of the MWCNTs. During the debinding and sintering tests, a porous support promoted a great flow of gas (mainly during debinding). All tests were performed under  $Ar+H_2$  atmosphere, heating rate of  $1\text{ }^\circ\text{C}/\text{min}$  and maximum temperature of  $600\text{ }^\circ\text{C}$ , since higher temperatures can contribute to the degradation of nanotubes (figure 3.6). It is important to highlight that low heating rate in debinding step is crucial to an efficient and slowly binder removal, guarantying “brown parts” without defects. All the components tested were weighed before and after the debinding tests to evaluate the efficiency of removal binder. The fraction of removed binder was between 97 and 99 %, and not 100 %, due to a saturation of the environmental atmosphere during the removal tests. The worst removal rates were evaluated for the nanocomposite “brown parts” subjected to the pre-milling treatment. The carbon residues are an inherent problem in the  $\mu\text{MIM}$  process [55]. The microstructure after debinding and sintering could be affected due to possible affinity of carbon to elements in metallic matrix. In the present study, residual carbon from binder can react, particularly with chromium in solid solution in austenitic matrix, leading to the formation of chromium carbides. This could hide the role of nanotubes during sintering. A detail study about the chromium carbides formation during sintering with and without nanotubes let to distinguish the role of nanotubes.

The “brown parts” with (0.5 and 0.9 wt%) and without MWCNTs, were analysed. Figure 3.31 shows that powders seem to be free from binder and MWCNT (individual and clusters) are visible on metallic powders (indicated by arrow). This presence shows that milling process is efficient to maintain the nanotubes in mixture/matrix, after debinding (figure 3.32). However, the presence of MWCNT clusters reveals that milling step is not completely effective to the dispersion and disaggregation of MWCNT.



a) 0.0 wt%

b) 0.5 wt%



c) 0.9 wt%

Figure 3.31 – Morphological analysis of SS 316L nanocomposites with a) 0.0, b) 0.5 and c) 0.9 of MWCNT (wt%)

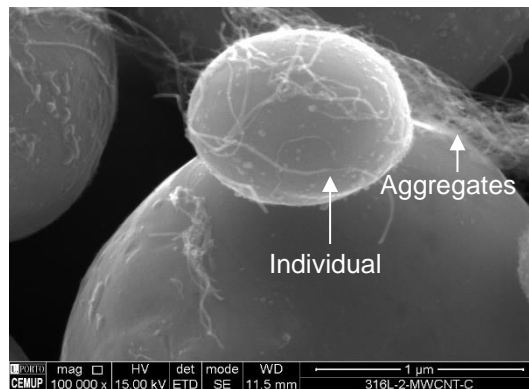


Figure 3.32 – Morphological analysis of SS 316L brown nanocomposites reinforced with 0.9 of MWCNT (wt%)

In conclusion, it is important to mention that although there was a gas extraction circuit, the debinding occurred in a saturated atmosphere that prohibited the efficiently extraction of binder and consequently the presence of carbonaceous residues in “brown parts”.

Figure 3.33 shows the structure of SS 316L “brown parts” (without MWCNT addition and milling pre-treatment), where is evident that after thermal debinding (600 °C) the powders structure change from austenite + martensite to austenite phase (comparatively to pristine powders – figure 3.3). Thus, is expected that powders (of brown part) after debinding has a higher density than the initial ones.



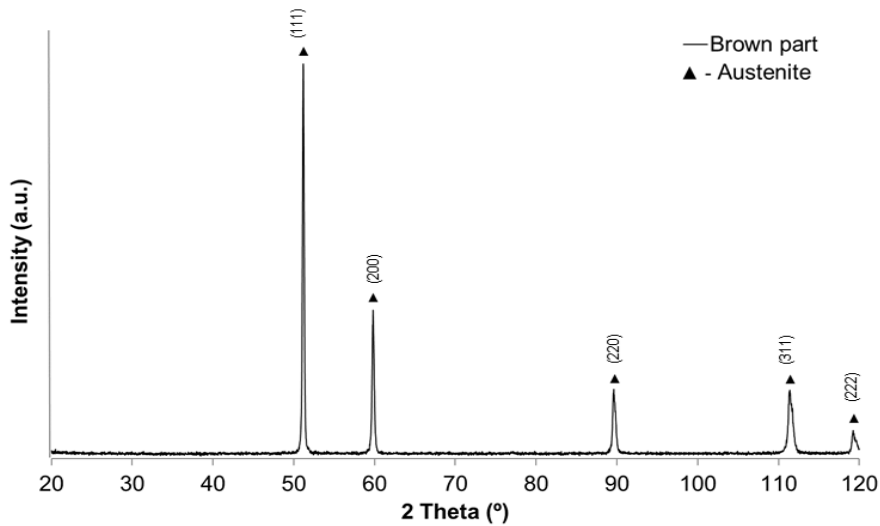


Figure 3.33 – X-ray diffractogram of SS 316L “brown part” (without MWCNT addition and milling pre-treatment)

At this moment, it is crucial to understand the effect of the thermal debinding (600 °C) over the “brown parts”, with or without milling pre-treatment and MWCNTs additions. The thermal behaviour of the “brown parts” were evaluated (figure 3.34) using a heating rate similar to the thermal debinding. Until 950 °C, the three specimens analysed reveal a steady regime, without weight variation. However, there are differences between the parts with or without milling pre-treatment (both without MWCNT added), showing that the change of powder shape gives rise to retaining binder residues in “brown parts”, revealed by the late weight loss. Hence, it must be highlighted that because the milling pre-treatment and debinding atmosphere saturation the “brown parts” subjected to milling have higher carbonaceous residue than the pristine SS 316L “brown parts”. These residues are finally removed for higher temperatures (above 950 °C), as shown the TGA. Probably, the difference in weight loss (0.1 wt%) between the “brown parts” with or without MWCNTs (both with milling pre-treatment) could be related with the amount of MWCNTs degraded ( $\approx 10\%$  of total added).

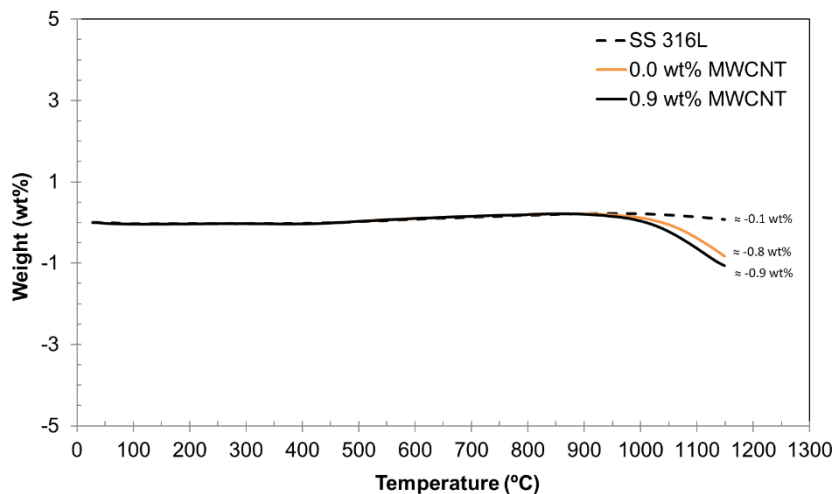


Figure 3.34 – TGA of SS 316L “brown parts” with or without milling pre-treatment and MWCNTs additions

## 3.5 Sintering

The sintering of SS 316L “brown parts” were performed under Ar+H<sub>2</sub> atmosphere, using a heating rate of 10 °C/min [66], 60 minutes of holding time and cooling rate of 40 °C/min at environmental temperature in the furnace. First, it was analysed the effect of sintering temperature (1150, 1200, 1250 and 1300 °C) on the pristine SS 316L, with two different pre-treatments (with and without milling). Henceforth, the sintering selected temperature was the same for all the different nanocomposites, allowing the evaluation of the viability of MWCNTs throughout the process.

### a) Selection of sintering temperatures

First of all, the shrinkage, density/porosity, microstructure, hardness, Young’s modulus, tensile strength and fracture surface morphology of the final parts function of sintering temperatures were evaluated.

#### *Physical properties*

The SS 316L parts processed by  $\mu$ MIM, due to their high sintered densities, exhibit mechanical properties that are similar to bulk parts. The figure 3.35 shows the dimensional variations of “green part” for different thermal cycles. After the debinding and sintering steps, any defects are visible in the parts, whatever the thermal cycle selected.

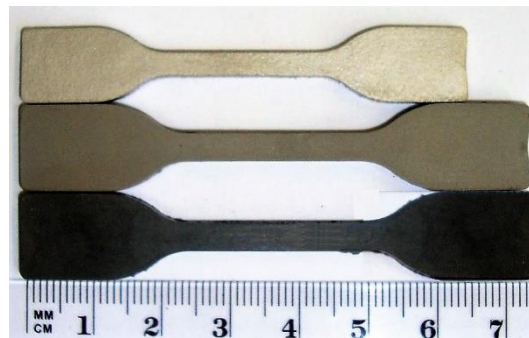


Figure 3.35 – Dimensions of green, brown and final specimens ( $T_{\text{sint.}} = 1250$  °C)

Figure 3.36 shows the shrinkages of sintered specimens, based on dimensions comparison after injection and sintering. A homogeneous shrinkage, in range from 10.0 to 16.8 %, whatever sintering temperatures is evident. However, a slight increasing of minimum and decreasing of maximum values occurs for the highest sintering temperatures (> 1200 °C). Nevertheless, the milling pre-treatment induces a slight decrease in dimensional variations when compared with the conventional mixing process. The porosity of sintered specimens diverges between 1.1 and 3.2 % (figure 3.36). The presence of some porosity is typical in components produced by MIM.

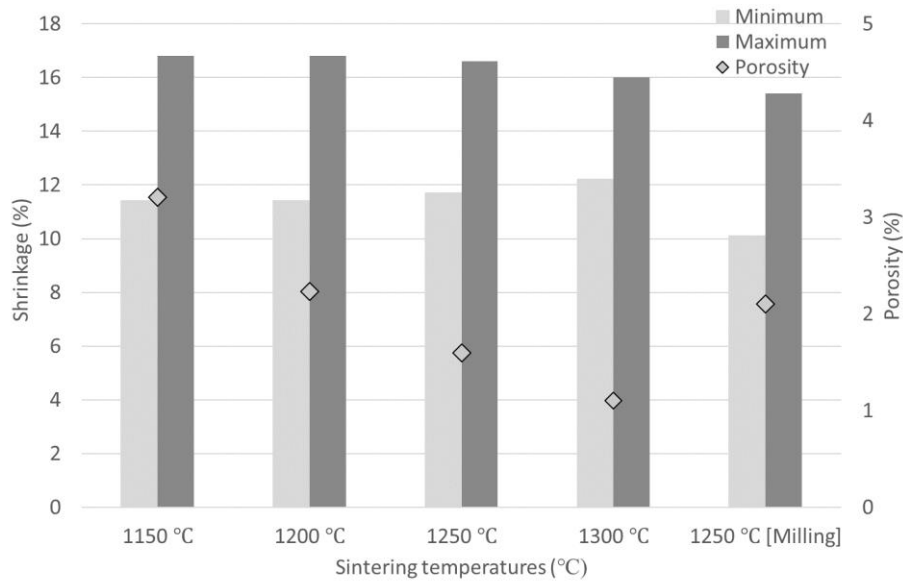


Figure 3.36 – Shrinkage and porosity versus sintering temperature

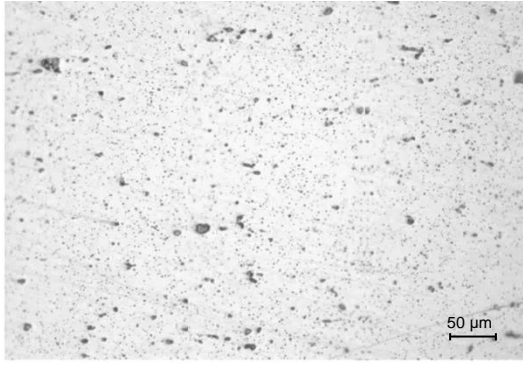
The apparent density values of sintered specimens with sintering temperatures are sight low than expected for this material (table 3.6). The increasing density with the sintering temperature, as result of a better densification. In what concern to sintered parts with or without milling step, sintered at same temperature (1250 °C), the specimens exposed to milling seems to have lower density than the parts without milling. *L. Castro et al.* [102] studied the effect of sintering temperature on density of final parts and showed an increasing of density with sintering temperatures (1150 – 1350 °C).

Table 3.6 – Apparent density of sintered at different temperatures

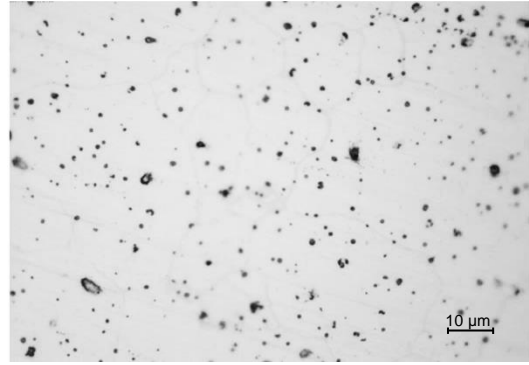
Sintering temperature	1150 °C	1200 °C	1250 °C	1300 °C	1250 °C (with milling)
Apparent density (kg/m <sup>3</sup> )	7729	7745	7832	7859	7802

### Microstructure

The micrographies of diamond suspension (3 µm) polished sintered parts, without etching (figure 3.37) show the presence of some porosity (black points) decreasing with sintering temperature. For the highest temperatures (1250 °C and 1300 °C), there are small rounded pores, uniformly distributed along surface. For sintered parts at 1250 °C, the milling step seems to contribute for increasing porosity (figure 3.37 g) and h)), when compared with homologue without pre-treatment of milling (similar sintering conditions).



a) 1150 °C



b) 1150 °C



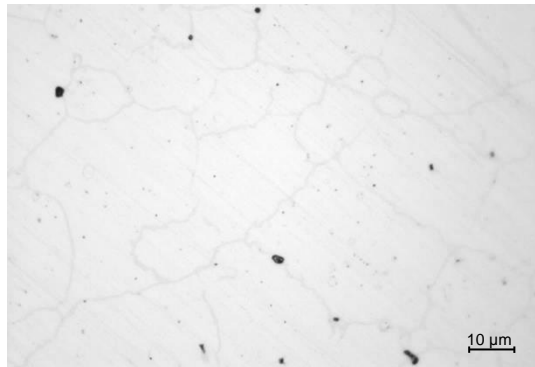
c) 1200 °C



d) 1200 °C



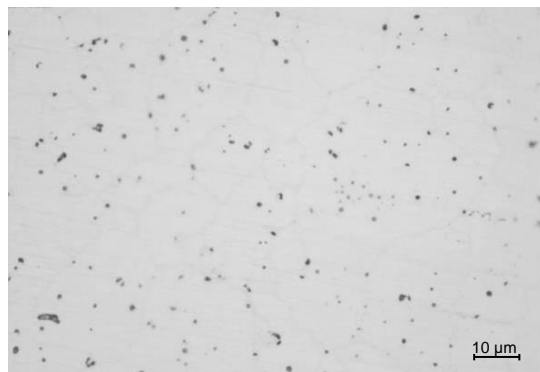
e) 1250 °C



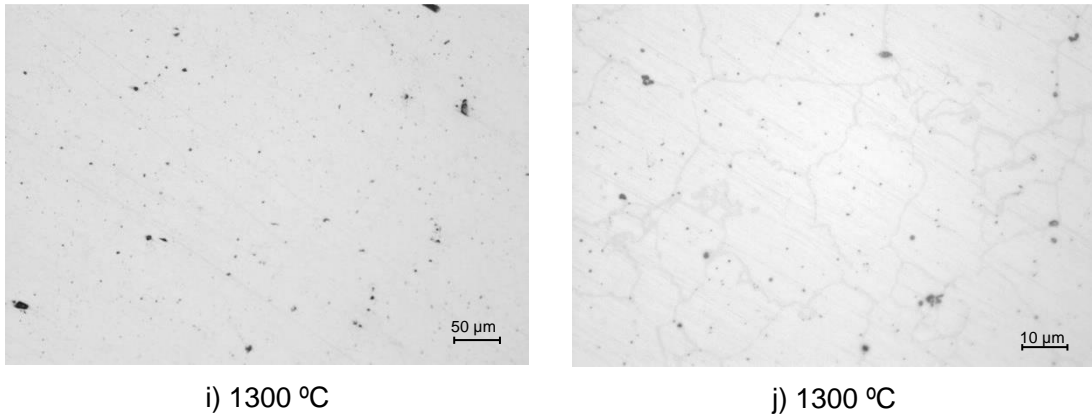
f) 1250 °C



g) 1250 °C (Milling)



h) 1250 °C (milling)



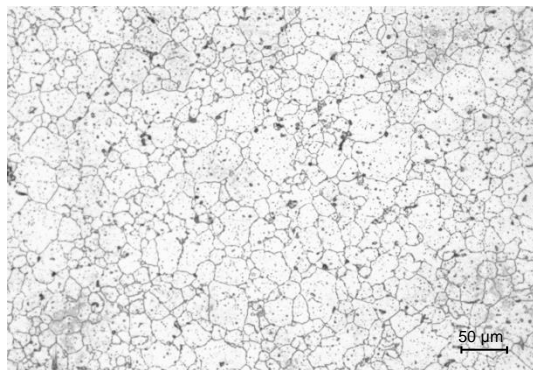
i) 1300 °C

j) 1300 °C

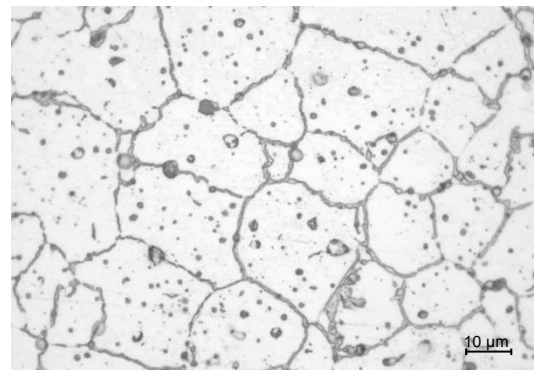
Figure 3.37 – Optical micrographs of polished sintered surface parts at a), b) 1150 °C, c), d) 1200 °C, e), f) 1250 °C, g), h) 1250 °C (milling) and i), j) 1300 °C

After etching (HCl:HNO<sub>3</sub>:glycerol), the sintered parts exhibit microstructures typical of SS 316L processed by μMIM (figure 3.38) [55], [58], [59], [65], [72], [73]. For all sintering temperatures, they show a good interparticle bonding with dispersed circular pores, as well as some precipitation in the grain boundaries of austenite matrix.

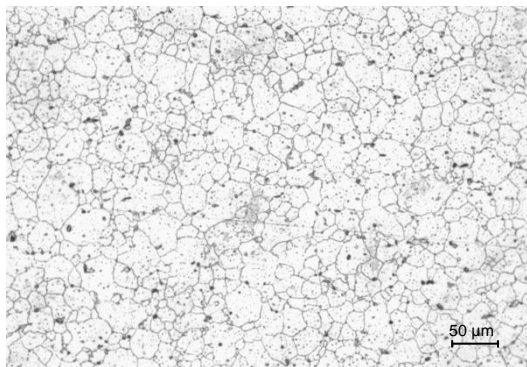
The mean diameter grain size determined by ISO 642:2012 and for all tested conditions; it has a mean diameter of grain about 22.1 μm. The mean grain size does not seem to be influenced by the different sintering temperatures (figure 3.38). However, the sintered parts (1250 °C), with pre-treatment of milling, have a slight difference in what concern the grain boundaries (figures 3.38 g) and h)).



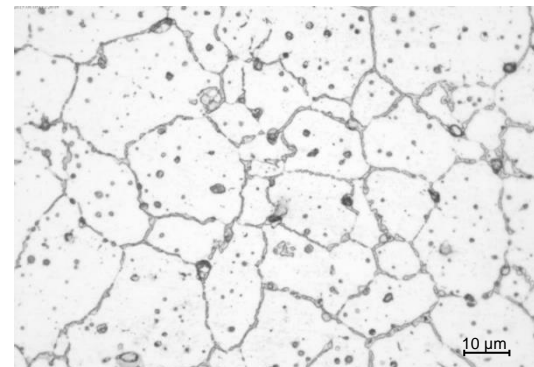
a) 1150 °C



b) 1150 °C



c) 1200 °C



d) 1200 °C

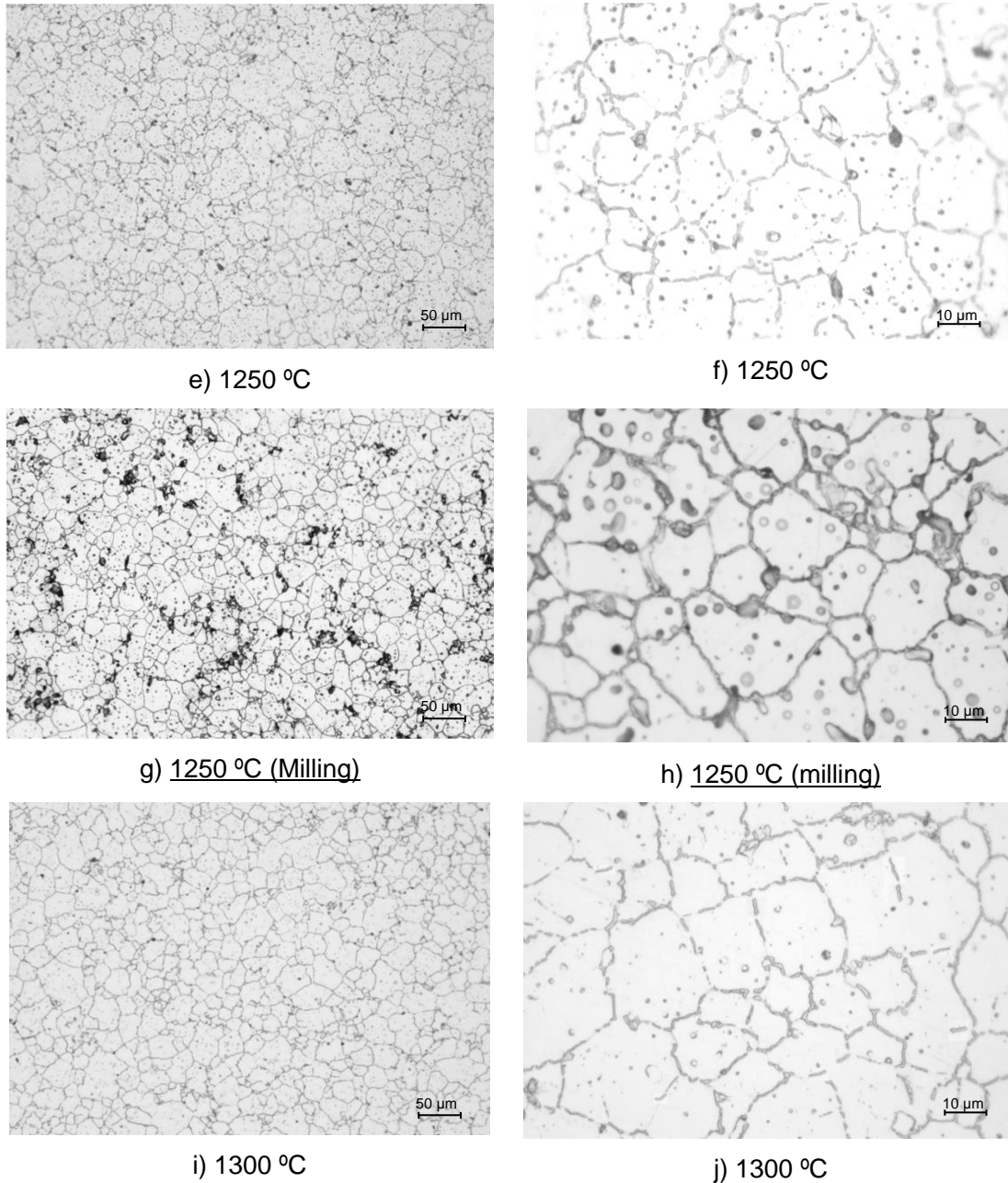


Figure 3.38 – Optical micrographs after etching of sintered surface parts at a), b) 1150 °C, c), d) 1200 °C, e), f) 1250 °C, g), h) 1250 °C (milling) and i), j) 1300 °C

All the sintered parts have a matrix structure constituted by austenitic phase (figure 3.39); the martensitic phase of pristine powders has disappeared after thermal debinding step. Moreover, whatever of sintering temperature selected ( $< 1300\text{ °C}$ ) it is clear the presence of chromium carbide ( $\text{Cr}_{23}\text{C}_6$ ), that was not detected in powders. In fact, after debinding there are carbonaceous residues in “brown parts”, resulting from the binder to be a mixture of  $\text{M}_1+\text{SA}$  (figure 3.10) and saturated atmosphere, thus during cooling after sintering, giving rise to chromium carbide. A detailed analyse of the diffractogram (figure 3.39) between  $40$  and  $65^\circ$  ( $2\theta$ ), shows the presence of this chromium carbides –  $\text{Cr}_{23}\text{C}_6$  after sintering at  $1150$ ,  $1200$  and  $1250\text{ °C}$ . Because the higher affinity of chromium to carbon than

iron (master element). Figure 3.40 shows the limit of solubility of carbon in an austenitic phase as a function of sintering temperature. Based on these data, the maximum amount of carbon soluble in an austenitic phase should be approximately 0.03 %, and this way prevent the sensitization (by restrict the carbon content). The  $Cr_{23}C_6$  can form when the carbon content is higher than 0.03 %. After the debinding cycle, there are about 0.23 C (wt%) in “brown parts”, due to carbonaceous residual content in the binder to be 3.9 (wt%). After sintering, and during cooling, this carbon induces  $\approx 4$  wt% of  $Cr_{23}C_6$ . At 1300 °C of sintering temperature, it does not exist in matrix chromium and carbon enough to form chromium carbides during the cooling, due to it low vapour pressure.

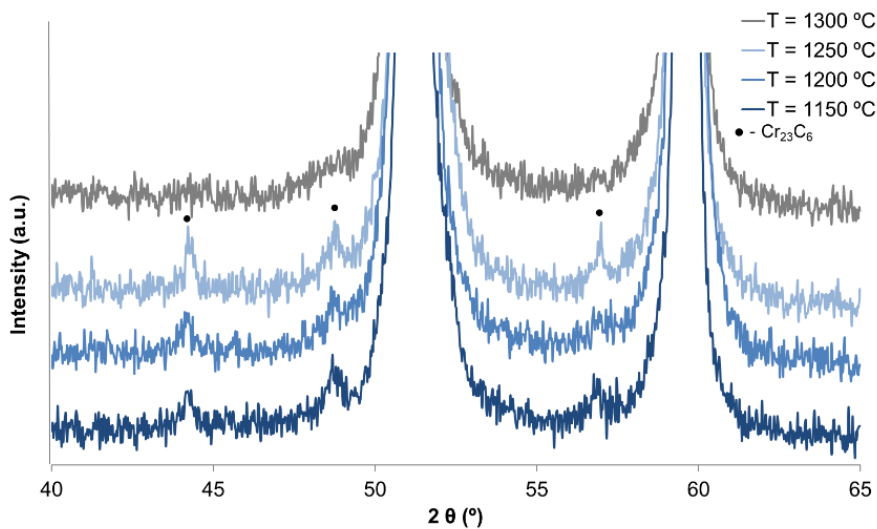


Figure 3.39 – X-ray diffractogram of sintered parts at different temperatures (zoom)

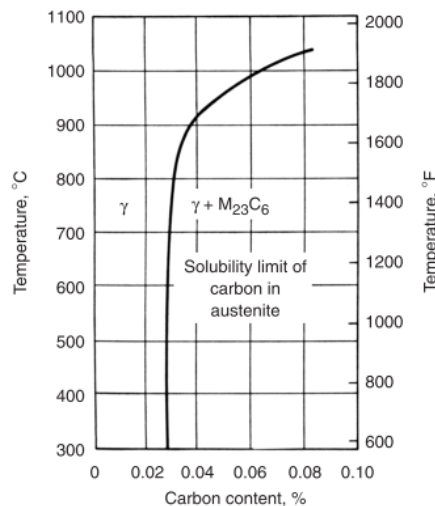


Figure 3.40 – Solid solubility of carbon in austenitic SS [59]

The carbide formation is usually undesired because it can decrease the corrosion resistance and some mechanical properties (e.g. the fatigue life). Some authors showed the carbide particles in non-equilibrium (*paraequilibrium*) and found three different carbide modifications:  $M_3C_2$ ,  $M_7C_3$  and  $M_{23}C_6$ , where M metal atoms in the solid solution (M = Cr, Fe, Ni) [103], [104]. In austenitic stainless steels, if there is carbon in matrix, the formation of a carbide enriched in chromium occurs during cooling in the temperature range of 816 °C to 538 °C [59]. Hence, during cooling from an elevated temperature, after sintering, any carbon present in excess of the limit of solubility can easily migrate out of the matrix to the grain boundaries, where it would combine with chromium to form chromium carbide. *Meng et al.* [72] verified that SS 316L sintering in vacuum had two phases, austenite matrix and  $M_{23}C_6$  carbide. This contribute for decrease the content of chromium in matrix and consequently loss of corrosion resistance. If heat-treated the sinter the chromium carbides dissolves in austenite from 950 to 1050 °C.

It is clear that powders structure changed with temperature, the pristine powders were austenite + martensite, after debinding the “brown parts” are essentially austenitic (but with some carbonaceous residue from binder) and after sintering, during cooling there is the formation of chromium carbides. In this case,  $Cr_{23}C_6$  have a density of 6970 kg/m<sup>3</sup>, contribute for decreasing the density of sintered specimens.

### *Mechanical properties*

After microstructure analyses some mechanical properties like hardness and Young's modulus were measured in sintered parts at 1150, 1200, 1250 (with and without milling pre-treatment), and 1300 °C, having as standard the bulk material<sup>1</sup> (Annex II). The hardness slight increases with sintering temperature (figure 3.41) and is always higher than the bulk. For the same sintering temperature (1250 °C) to be or not be pre-treated (milling) has influence on hardness value; for the pre-treated the hardness is lower than the untreated.

The minimum value measured was  $1.54 \pm 0.12$  GPa for 1150 °C and the maximum  $1.64 \pm 0.10$  GPa for 1300 °C. The hardness of the sinter increases with the sintering temperature. In fact, the grain size is almost unchanged with sintering temperature, thus the improvement of hardness results of a better sintering effect. Comparing the hardness value after sintering at 1250 °C with standard values indicated for same steel bulk, they are similar. The hardness values measured in this study was 1.65 GPa, higher than 1.05 GPa [105], 1.32 GPa [106], and 1.53 GPa [74] (all sintered in hydrogen atmosphere). The last one also measured higher hardness when sintered in vacuum, 1.73 GPa [72].

---

<sup>1</sup> MatWeb: AISI 316L Stainless Steel, annealed plate (Annex II).



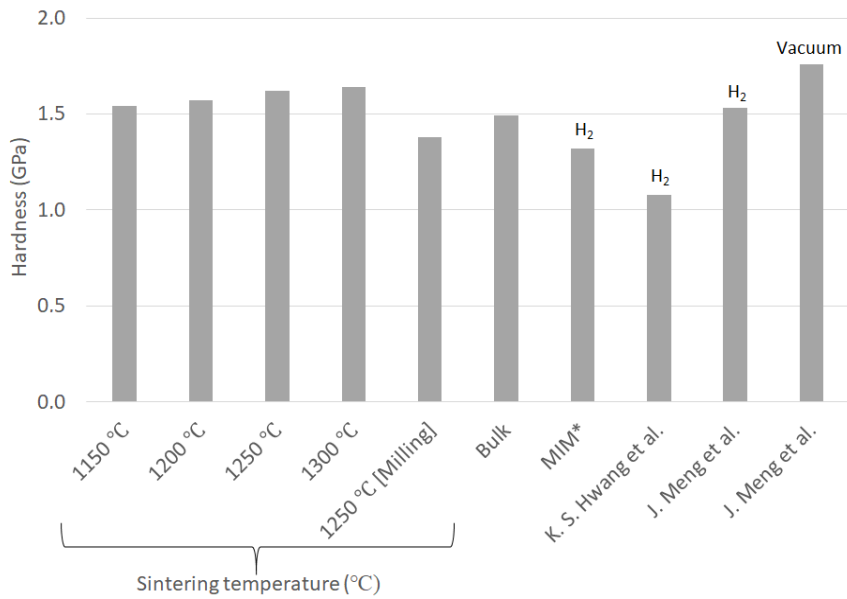


Figure 3.41 – Hardness values of sintered parts (MIM\* is from Powder Injection Moulding Journal – tensile properties of representative MIM alloys [106])

The Young's modulus (despite being an intrinsic property of the material) is constant with sintering temperature, but lower when compared with bulk material (193 GPa) (figure 3.42). However, sintered parts with milling pre-treatment have the lowest Young's modulus value.

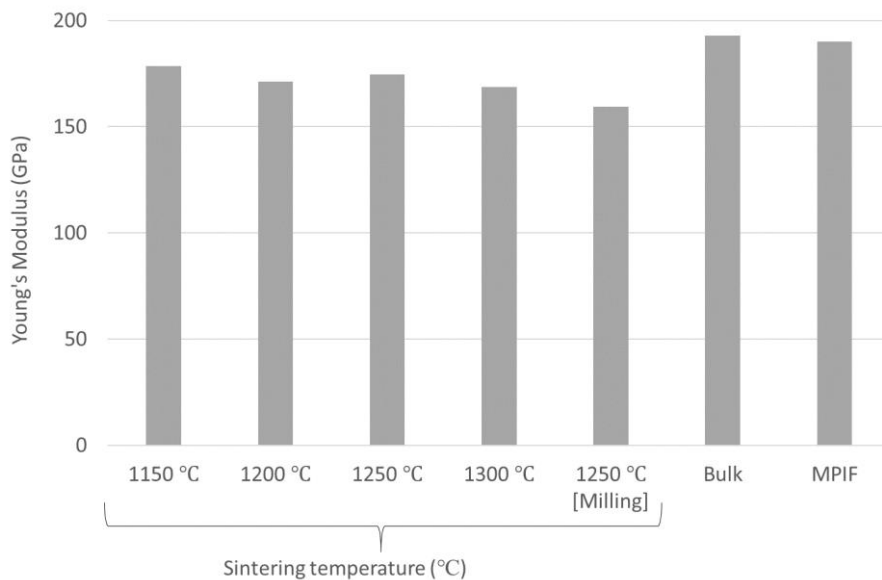


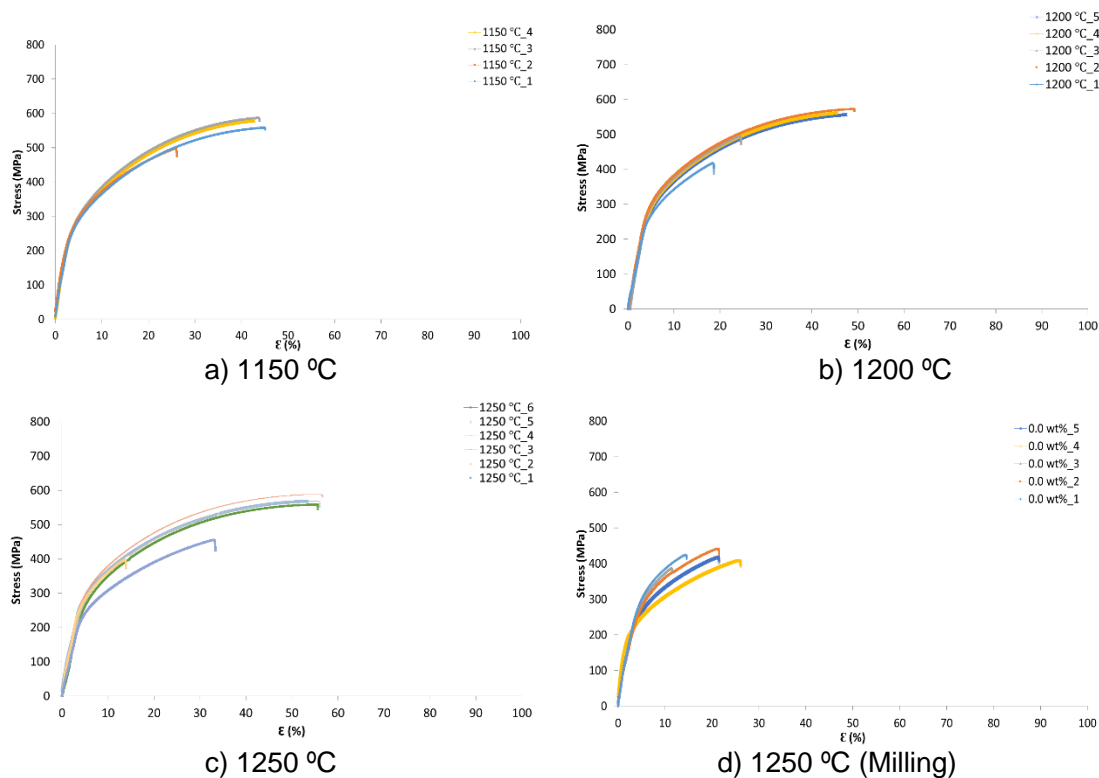
Figure 3.42 – Young's modulus values of sintered parts

The  $\epsilon$ , YS and UTS were evaluated by tensile tests on the sintered specimens (figure 3.43). The mechanical properties of sintered parts can differ slightly, even when the same sintering temperature is used. This suggests that even though the setup of the moulding,

debinding and sintering process parameters were always constant, some aleatory heterogeneity in specimens can be present. This behaviour is typical in tests of parts resulting from powder technology, where statistics of Weibull is welcome. However, the number of specimens tested are not suitable to evaluate the Weibull modulus and the dispersion of properties results.

Most of the specimens have a clean fracture surface (figure 3.44 a)), however for the different sintering temperatures were observed diverse types of defects (figure 3.44 b) to d)). Even starting from homogeneous feedstocks, the defects coming from injection step and subsequently thermal cycles, have a strong influence on the mechanical properties. A defect on work zone, denominated by “gage length” is crucial to the failure of tensile parts. The differences between specimens under same conditions may be due to defects introduced during injection moulding step.

However, the YS values for the different temperatures of sintering are quite similar, in agreement with the previewed by Hall-Petch equation, since the mean grain size was constant for the different tested sintering temperatures. YS calculated by the equation 5 (327 MPa) is higher than measured by the tensile tests (270 MPa). In what concerns sintered at 1250 °C with and without milling pre-treatment, once again was visible significant differences of YS, with the worst properties for the pre-treated specimens.



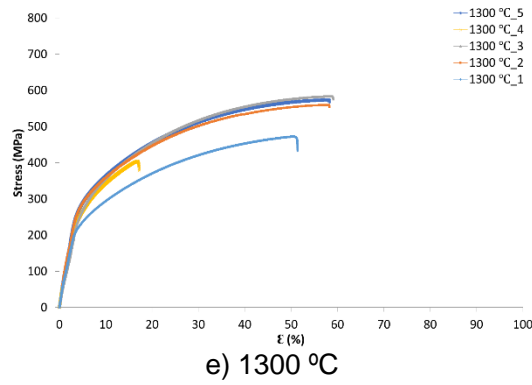


Figure 3.43 – Stress-strain curves for sintered parts at a) 1150 °C, b) 1200 °C, c) 1250 °C, d) 1250 °C (milling) and e) 1300 °C

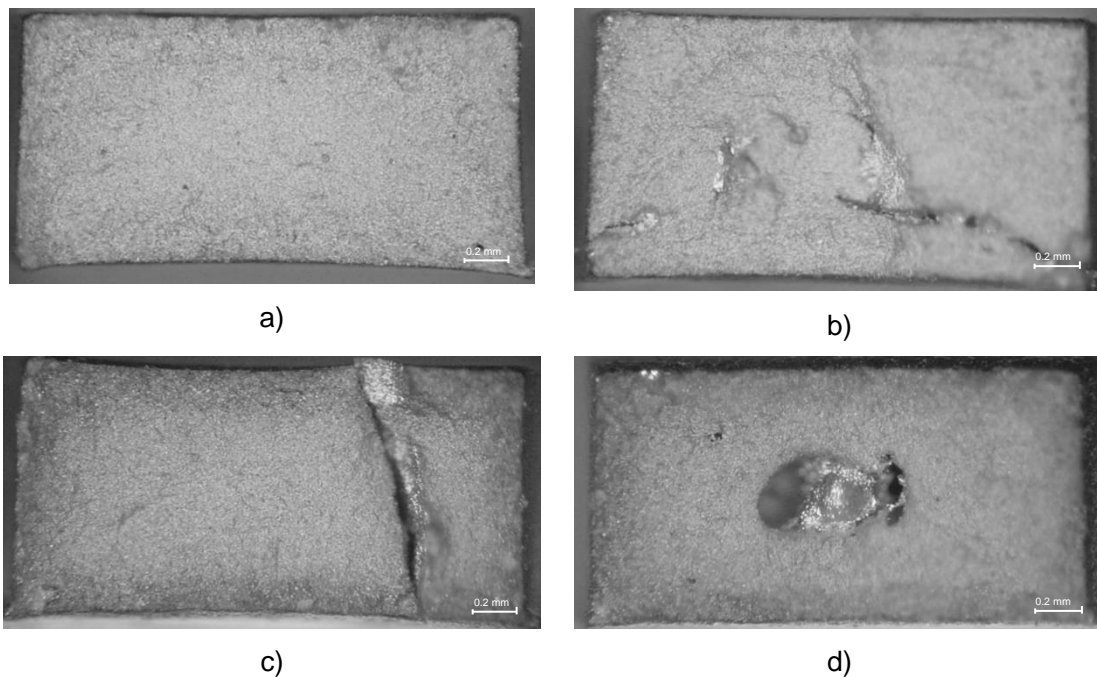


Figure 3.44 – Fracture surface of sintered a) without defect, b), c) and d) with defect

Major results let to compare the YS, UTS and  $\epsilon$  for different sintering temperatures, with bulk steel and others works (figure 3.45). In conclusion, for different sintering temperatures the YS and UTS values are similar between then and with bulk steel. Moreover, they are higher than the most of the values of others research works ([59], [91], [105]–[107]) (figure 3.45). The maximal temperature selected for sintering was 1250 °C. due to corresponds to the best compromise between density, structure and mechanical properties/performance.

Nevertheless, it is also evident that with milling pre-treatment there are a dramatically drop in YS, UTS and elongation average values, but this treatment is essentially to attain a good mixture, without destroy the nanotubes structure. Whatever the nanoreinforcement

content, it obliges to a milling pre-treatment of mixing (cf. 3.2 b)), but having in mind the optimised thermal cycle, the results are not the predictable (figure 3.45). However, high temperatures are not welcome, due to the possible degradation of the nanotubes in the “brown parts” during sintering. Consequently, the optimised cycle of the matrix powders with and without nanoreinforcement was the same.

Despite mechanical properties of the SS 316L milling sintered to have lower density and poor mechanical properties than the sintered without pre-treatment (table 3.7), this could highlight the role of nanotubes as reinforcement of the matrix. The target of the present study is to study the role of nanotubes as reinforcement of a SS 316L matrix produced by powder metallurgy.

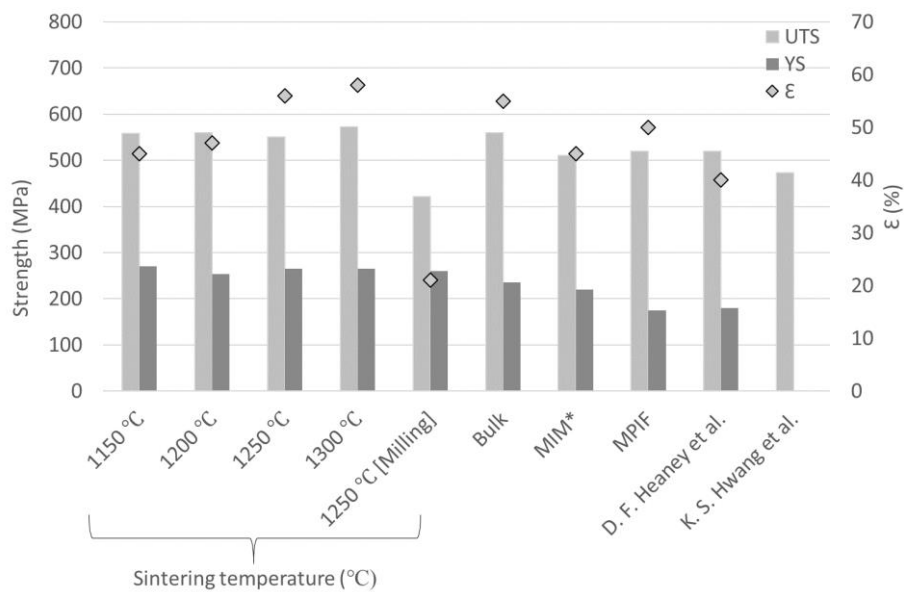


Figure 3.45 – ε, YS and UTS (MIM\* is from Powder Injection Moulding Journal – tensile properties of representative MIM alloys [106])

Table 3.7 – Properties of “brown parts” sintered at different temperatures and bulk material

	1150 °C	1200 °C	1250 °C	1300 °C	1250 °C (with milling)	Bulk
Apparent density (kg/m <sup>3</sup> )	7729	7745	7832	7859	7802	-
H (GPa)	1.54 ± 0.12	1.57 ± 0.10	1.62 ± 0.08	1.64 ± 0.10	1.38 ± 0.09	1.49
E (GPa)	178 ± 6	171 ± 5	175 ± 6	168 ± 12	159 ± 5	177 - 193
ε (%)	45 ± 1	47 ± 2	56 ± 1	58 ± 1	21 ± 5	55
0.2% YS (MPa)	270 ± 5	254 ± 4	265 ± 11	265 ± 8	260 ± 19	235
UTS (MPa)	558 ± 20	560 ± 9	550 ± 33	573 ± 26	421 ± 13	560

## b) Role of nanoreinforcement content

The shrinkage, porosity, microstructure, hardness, Young's modulus, tensile strength and fracture surface morphology of the sinter nanoreinforced composites were evaluated.

### *Physical properties*

The shrinkages of nanoreinforced composite parts sintered are from 10.0 to 16.0 %, showing a slight increasing of maximum and minimum with MWCNTs addition. On the other hand, the porosity of the composites decreases with content of MWCNTs (figure 3.46), revealing an efficient interconnection between matrix and nanoreinforcement.

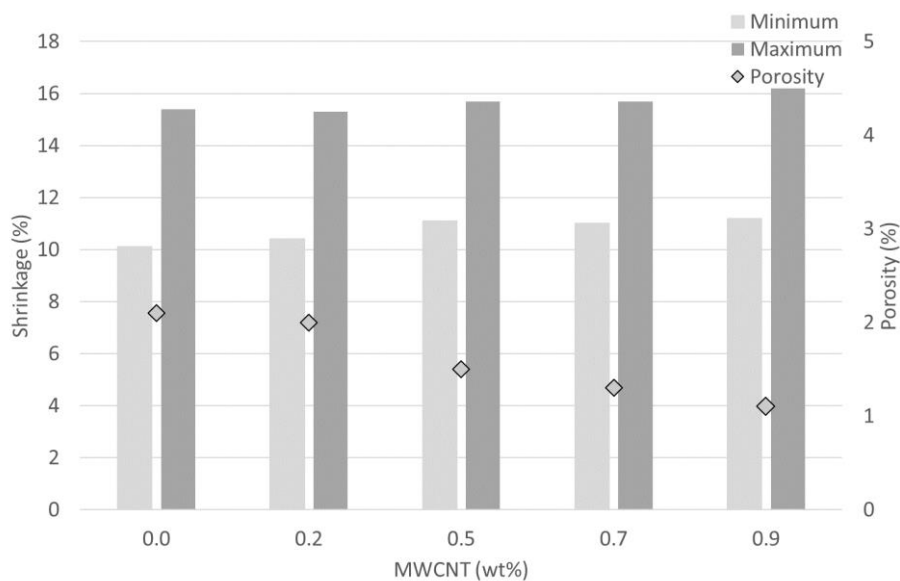


Figure 3.46 – Shrinkage and porosity of nanoreinforced composite specimens

The apparent densities of nanoreinforced composite sintered with and without MWCNTs show that additions of MWCNTs contribute to increase the apparent density (table 3.8). However, the density is always lower than expected for this material, due to the presence of carbides after debinding, resulting from the carbonaceous residue of binder (stearic acid).

Table 3.8 – Apparent density of nanoreinforced composite specimens

wt%	0.0	0.2	0.5	0.7	0.9
Apparent density (kg/m <sup>3</sup> )	7802	7837	7829	7836	7828

## Microstructure

In the diamond polished surfaces, when MWCNTs content increases in the matrix it is perceptible a decreasing of porosity (figure 3.47).



a) 0.0 wt%



b) 0.0 wt%



c) 0.2 wt%



d) 0.2 wt%



e) 0.5 wt%



f) 0.5 wt%

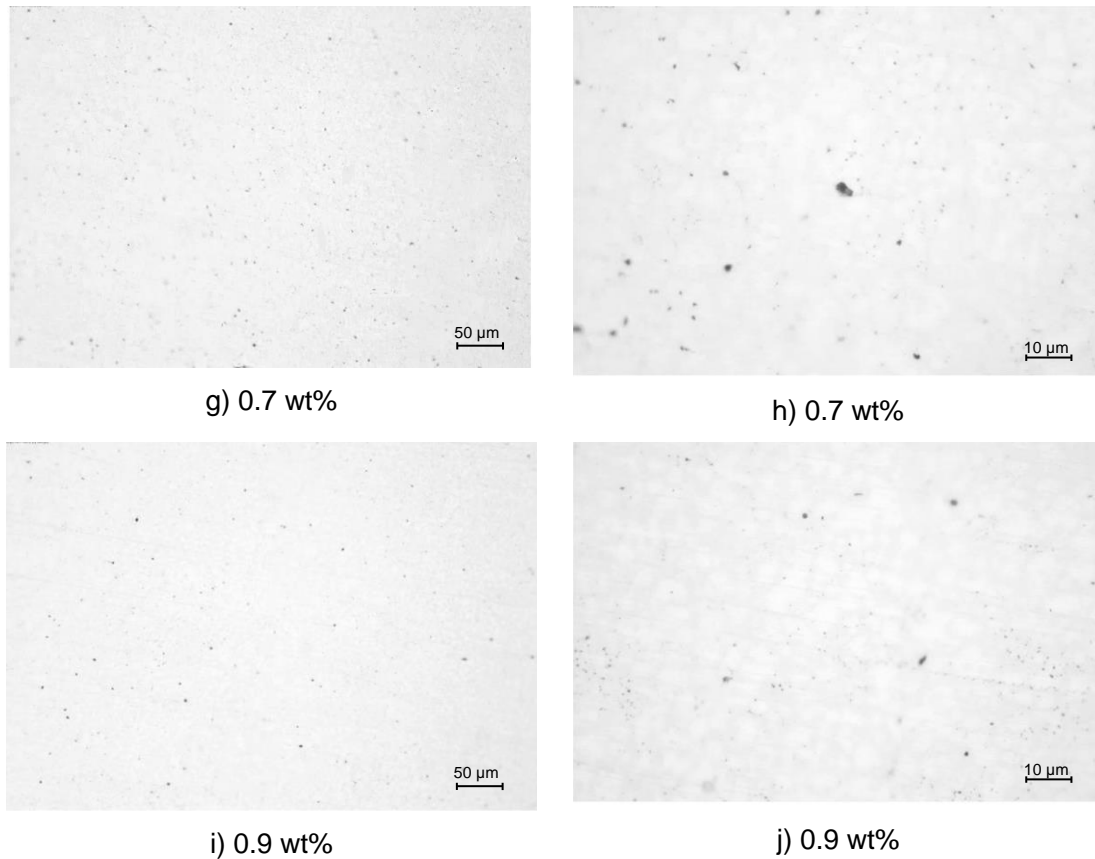


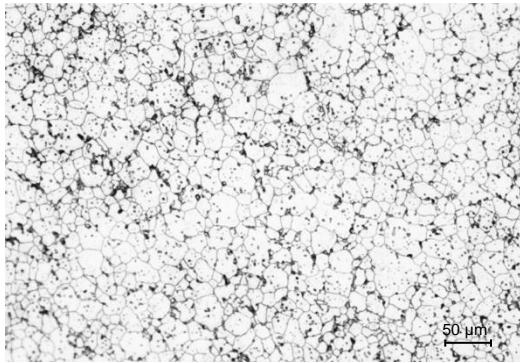
Figure 3.47 – Optical micrographs of polished sintered surface parts with a), b) 0.0, c), d) 0.2, e), f) 0.5, g), h) 0.7 and i), j) 0.9 of MWCNTs (wt%)

The milling step and/or the addition of MWCNTs seems to have a strong influence on the microstructure, mainly with respect to grain size (figure 3.48). When the content of MWCNTs was 0.2 wt%, is visible thicker grain boundaries than without addition of nanotubes. The precipitation occurs essential in grain boundaries, have a mean size of 2 – 3  $\mu\text{m}$ . When the content of MWCNTs was higher than 0.5 wt%, the grain boundaries becomes thinner and the grain size decreases (figure 3.48 (e to j)). In this nanocomposite, the carbides appear more evident in the triple points and inside grains. The mean grain size of different sintered composites was measured function of MWCNTs content (table 3.9) and decreased from 22.1 to 5.5  $\mu\text{m}$ . However, the highest decreasing is for additions above 0.5 of MWCNTs (wt%). The reduction of mean grain size with addition of MWCNTs to different metallic matrices, was also referred by other authors [6], [25], [28], [30].

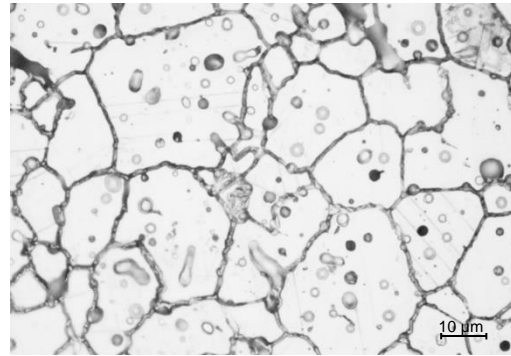
A substantial increase in YS due to the decreasing grain size. Based on grain refinement function MWCNTs addition, the Hall-Petch equation envisage an improvement about 21 % for 0.5 wt% of MWCNTs (over the SS 316L) and a maximum improvement of 50 % for the highest MWCNTs addition (> 0.5 wt%). *H. Deng et al.* [24] by the equation 5 show a changing in YS of MWCNT/Cu composite, about 51 % above of the pure copper.

Table 3.9 – Mean grain size versus  $\sigma_y$  for different additions of MWCNTs (wt%)

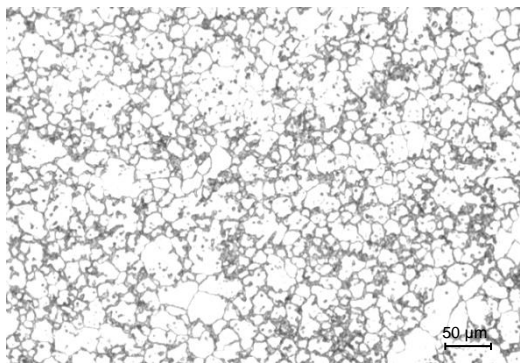
wt%	0.0	0.2	0.5	0.7	0.9
Mean grain size ( $\mu\text{m}$ )	22.1	22.1	11.0	5.5	5.5
$\sigma_y$ (Eq. 5) (MPa)	327		395	491	



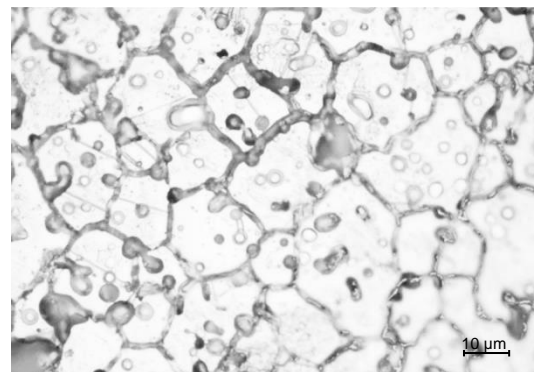
a) 0.0 wt%



b) 0.0 wt%



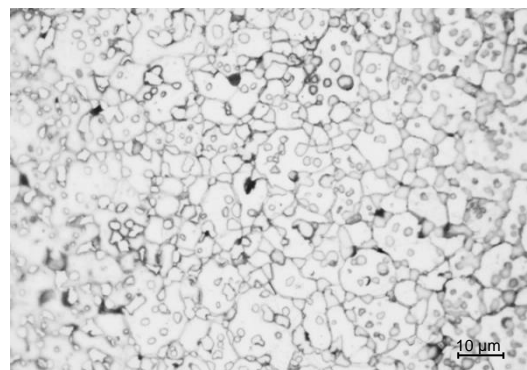
c) 0.2 wt%



d) 0.2 wt%



e) 0.5 wt%



f) 0.5 wt%



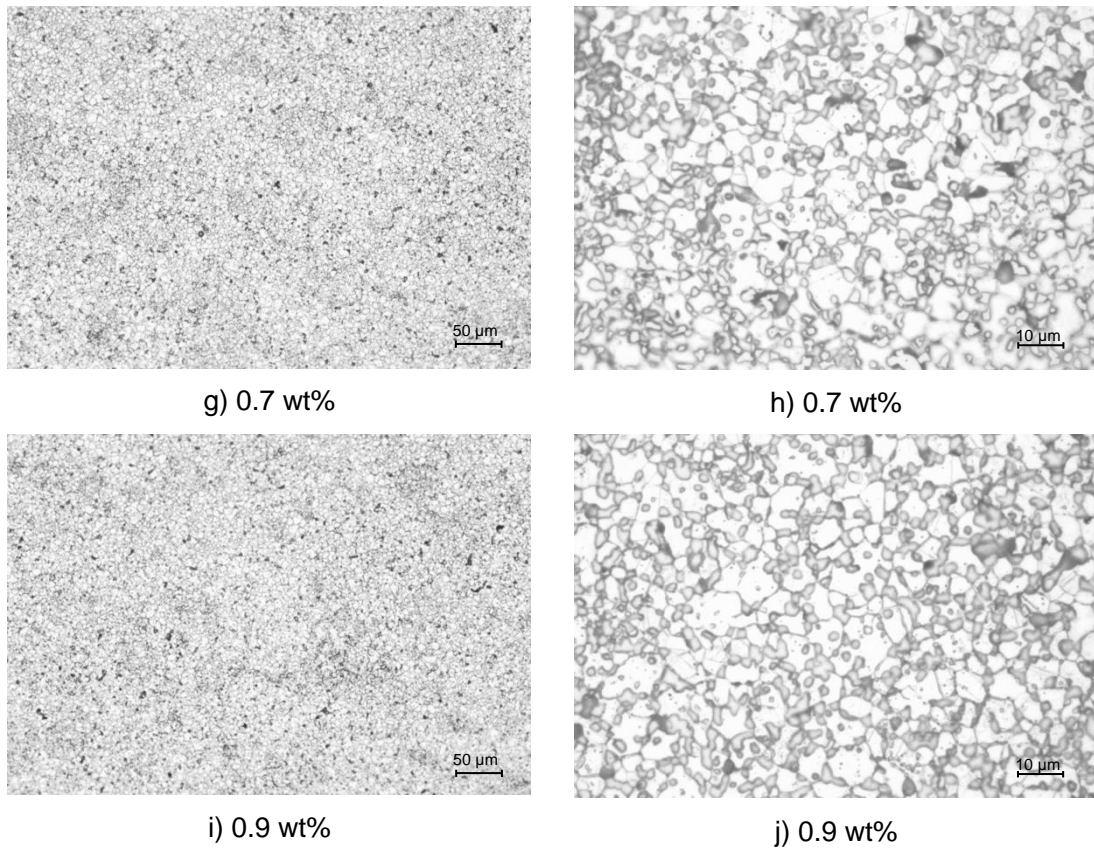


Figure 3.48 – Optical micrographs of etched sintered surface parts with a), b) 0.0, c), d) 0.2, e), f) 0.5, g), h) 0.7 and i), j) 0.9 of MWCNTs (wt%)

Figure 3.49 shows the phase analysis versus sintered parts with or without different MWCNTs content. In nanocomposites reinforced up to 0.2 wt% MWCNTs, it is visible that chromium carbide  $\text{Cr}_{23}\text{C}_6$  continuous to increase. Due to carbon from powders, binder residues and some MWCNTs degraded. For contents above, 0.2 wt% of MWCNTs was identified the presence of new carbide,  $\text{Cr}_7\text{C}_3$ . In fact, this is the demonstration that the content of carbon dissolved in matrix increase with the presence of allotropes of carbon, but is not total converted in carbides. Up to 0.9 wt% of MWCNTs there is an increase of  $\text{Cr}_7\text{C}_3$  quantity in matrix, while the  $\text{Cr}_{23}\text{C}_6$  disappear. This behaviour means that there is a partial degradation of nanotubes, during sintering, which stay essentially in the matrix in solid solution, available for the formation of chromium carbides. Some authors also referred the formation of carbides in different matrix type, e. g.  $\text{NiC}_3$  on MWCNT/nickel composite [30].

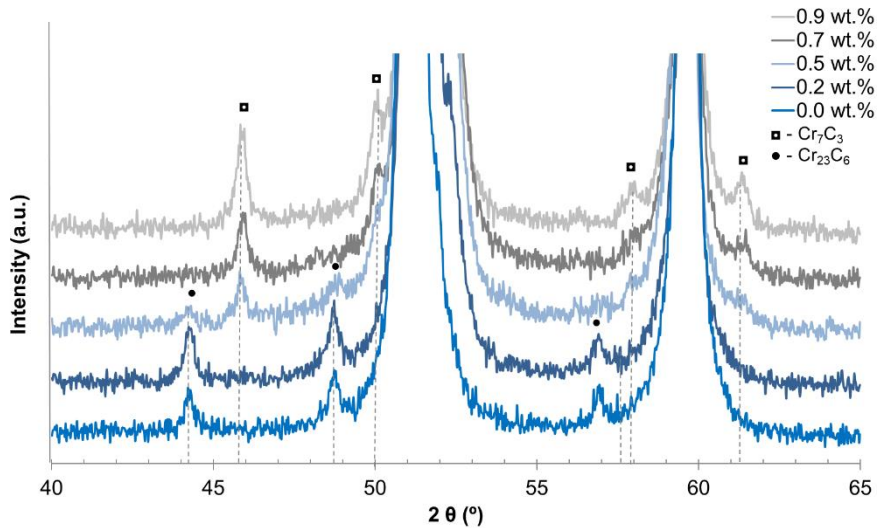


Figure 3.49 – X-ray diffractogram of nanoreinforced composites sintered with different contents of MWCNTs (0.0, 0.2, 0.5, 0.7 and 0.9 wt%)

Once again, after verifying the presence of different types of chromium carbides in the matrix, function of MWCNTs (wt%), it is acceptable that the density of the nanocomposites specimens is lower than expected.

### *Mechanical properties*

After microstructure analyses, the mechanical properties of nanocomposites were measured. The addition of MWCNTs reveals an improvement in hardness of sintered nanocomposites (figure 3.50 and table 3.10). From 0.5 and 0.9 wt% of MWCNTs, the hardness values are higher than the bulk SS 316L. However, a remarkable increase of 40 % ( $1.92 \pm 0.11$  GPa) was measured in sintered nanocomposites with 0.9 wt% of MWCNTs additions (over the 0.0 wt%). These results demonstrate that only the additions above 0.2 wt% of MWCNTs were effective in increasing the hardness of the composite based on SS 316L (superior to bulk material).

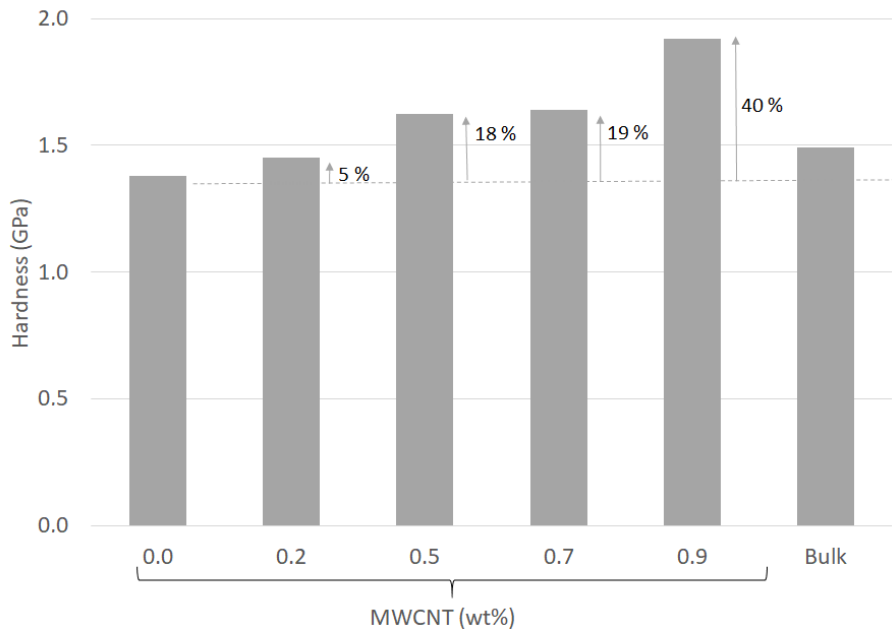


Figure 3.50 – Hardness versus MWCNTs (wt%)

Young's modulus values have a slight increase function of MWCNTs additions (figure 3.51 and table 3.10), however, lower than expected due to some porosity. All the sintered composites have lower Young's modulus value comparatively to bulk SS 316L (193 GPa).

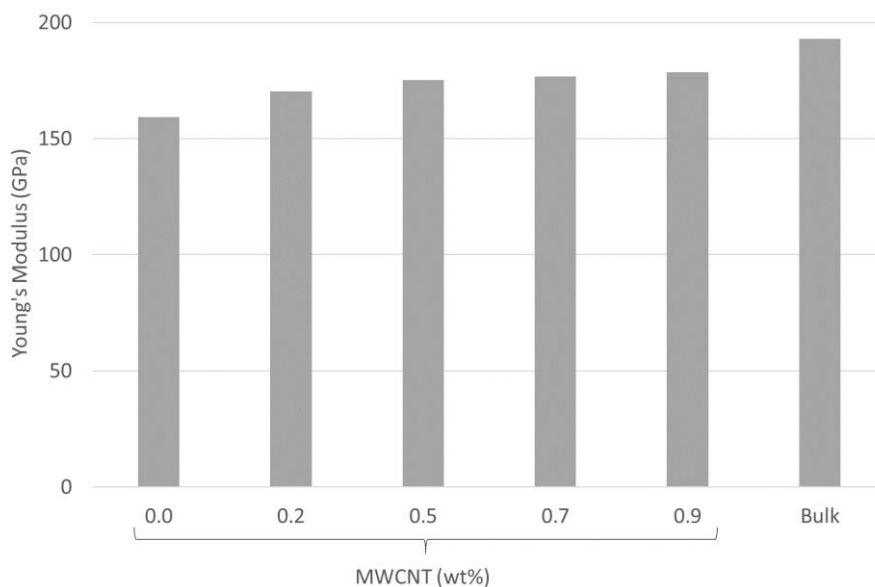


Figure 3.51 – Young's modulus versus MWCNT (wt%)

Figure 3.52 shows the stress-strain curves of sintered composites nanoreinforced with different contents of MWCNTs. Some divergence in the mechanical behaviour for the same tested condition has also detected. The nanocomposites with increasing MWCNTs contents tend to a brittle material. The most of specimens have a fracture surface without

defects (figure 3.53 a)) and the low values can be explained due to internal defect in gage length (figure 3.53 b) to d)). In nanocomposites with 0.0 wt% MWCNTs, the mean values of UTS and elongation were 421 MPa and 21 %, respectively. The nanocomposites with 0.5 wt% of MWCNTs have high UTS (561 MPa) than previous. In order to the composites with 0.7 wt% MWCNTs, in general they have also a fracture surface without defects, nevertheless they present a brittle behaviour. For the nanocomposites with 0.9 wt% MWCNTs was measured the highest YS and UTS values. Resuming, the YS and UTS improve with the increasing of MWCNTs content in SS 316L matrix (table 3.10).

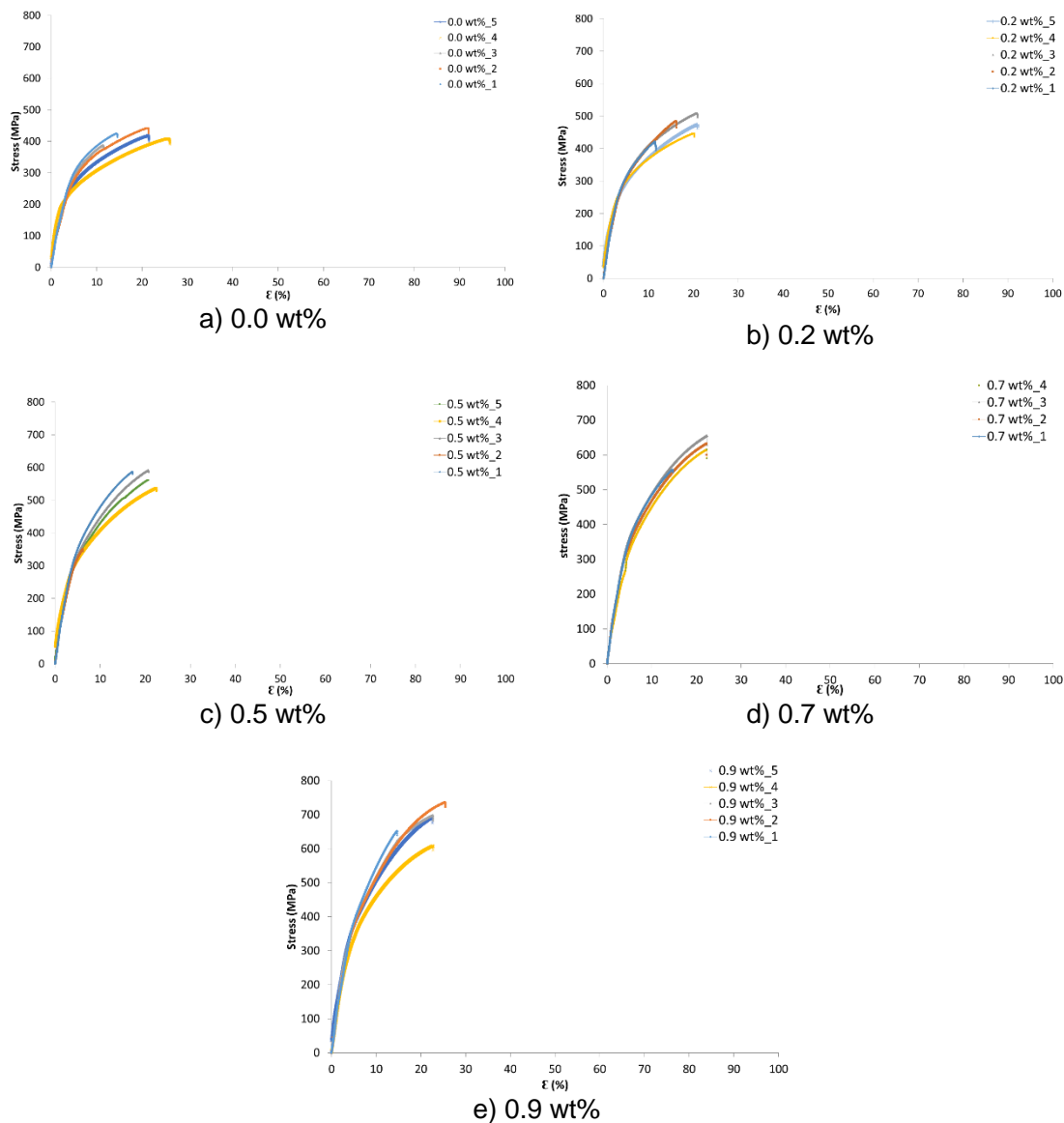


Figure 3.52 – Stress-strain curves of a) 0.0, b) 0.2, c) 0.5, d) 0.7 and e) 0.9 of MWCNTs (wt%)

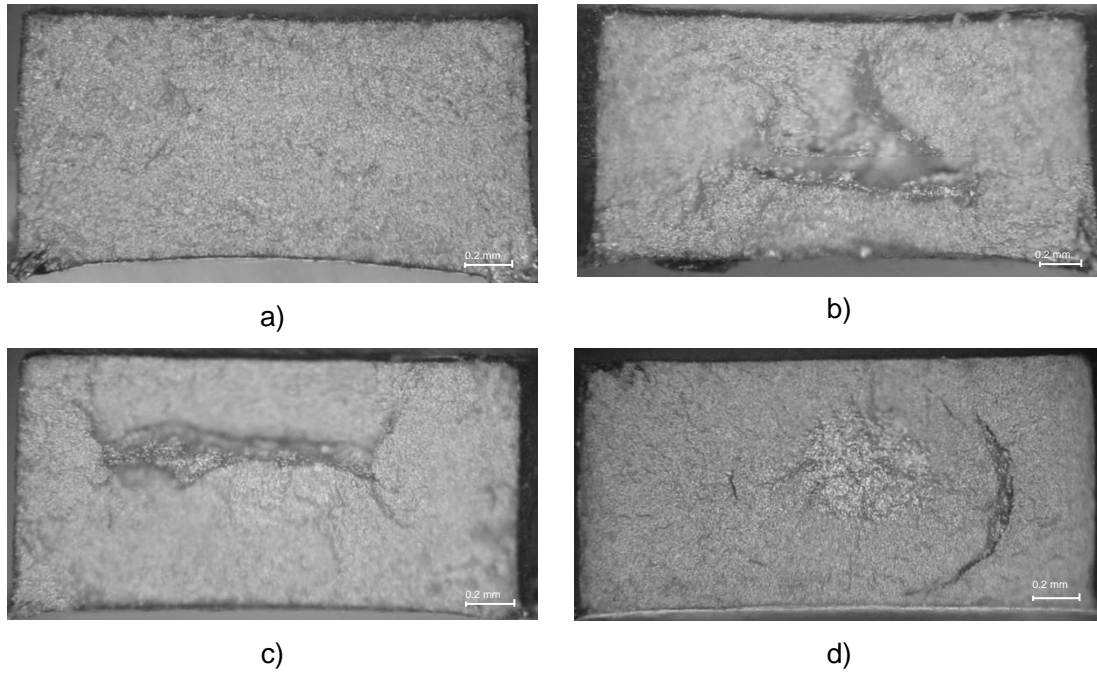
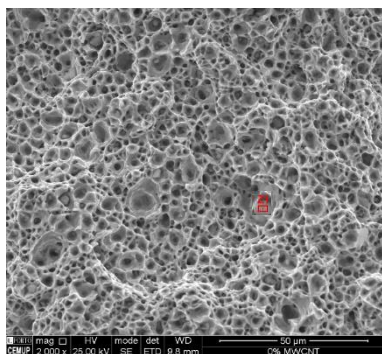
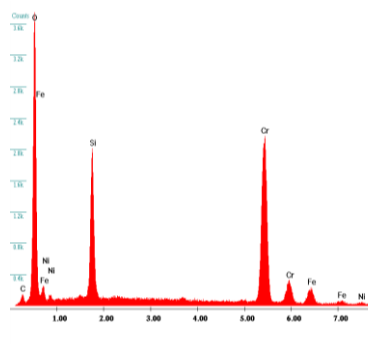


Figure 3.53 – Fracture surface of sintered nanocomposites a) without defect, b), c) and d) with defects

The morphology of composites fracture surfaces was analysed in detail (figure 3.54) and shown some difference with MWCNTs addition. The fracture of sintered specimens with 0.0 wt% MWCNT have an opened structure and with some oxides (figures 3.54 a) and b). Oxidation occurred after the fracture of the specimens. Sintered composite with 0.5 wt% MWCNTs (figures 3.54 c) to e)), have a more compact structure. By EDS was possible to identify zones corresponding to chromium carbides (Z2) and some chromium carbides appear with fractures. The nanocomposite with higher percentage of MWCNTs added (0.9 wt%), has a more compact structure, without evidence of porosity and with more exposed carbides (figure 3.54 f) to h)).



a) 0.0 wt%



b) EDS – Z1



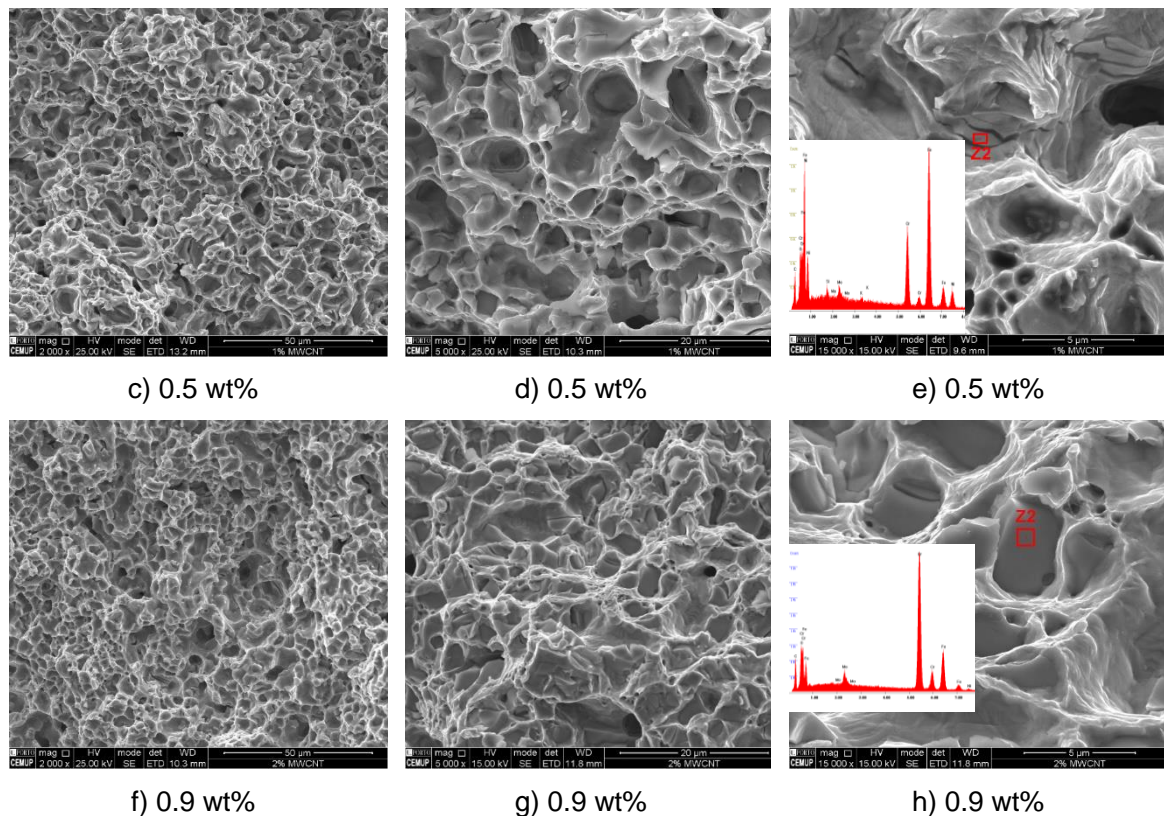


Figure 3.54 – Morphological analyses of fracture surface of sintered nanoreinforced steel: a) 0.0 wt%, b) EDS - Z1, c), d), e) 0.5 wt%, f), g) and h) 0.9 wt%

In order to identify the distribution of elements/phases were performed elemental maps by SEM/EDS on fracture surface of previous sintered composites. Without addition of nanotubes, the X-ray map (figure 3.55 b)) shows the chromium (red) uniformly distributed in the matrix and some red dots, which are related chromium carbides, that corresponds to 17 vol% or 14.5 wt% of  $\text{Cr}_{23}\text{C}_6$ . The addition of 0.5 of MWCNTs (figure 3.55 d)), improves the concentration of red areas, the carbide continues to be formed but in a new combination ( $\text{Cr}_{23}\text{C}_6 + \text{Cr}_7\text{C}_3$ ), they represent 20 vol%. This improvement is due not only to the presence of binder residues in steel, but also to some carbon resulting from the degradation of carbon of nanotubes, to form chromium carbides. On the other hand, the maximum addition of MWCNTs (0.9 wt%) induces a change in the type and morphology of chromium carbides compared to the observed for 0.5 wt% MWCNT, but in similar percentage (18 vol% or 15.6 wt% of  $\text{Cr}_7\text{C}_3$ ). For MWCNTs (0.9 wt%), the type of chromium carbide is only  $\text{Cr}_7\text{C}_3$ . However, it is important to highlight that the content of carbides do not increase (in proportion) with the addition of MWCNTs. This means that between 0.9 and 0.0 wt%, there is a difference in carbon supplied to the matrix about 0.6 wt% C, that corresponds to the amount of degraded MWCNTs that contributed to the formation of carbides (about 60 % of pristine MWCNTs added).

In conclusion, maintaining the processing parameters and changing only the quantity of MWCNTs added is evident different types, contents, size and distribution of carbides. However, it is important to note that about 40 % of MWCNTs initially added remains intact in the sintered nanocomposite, after thermal treatments (debinding and sintering); and it is only this quantity that contributes effectively to the improvement of the mechanical properties of the composite.

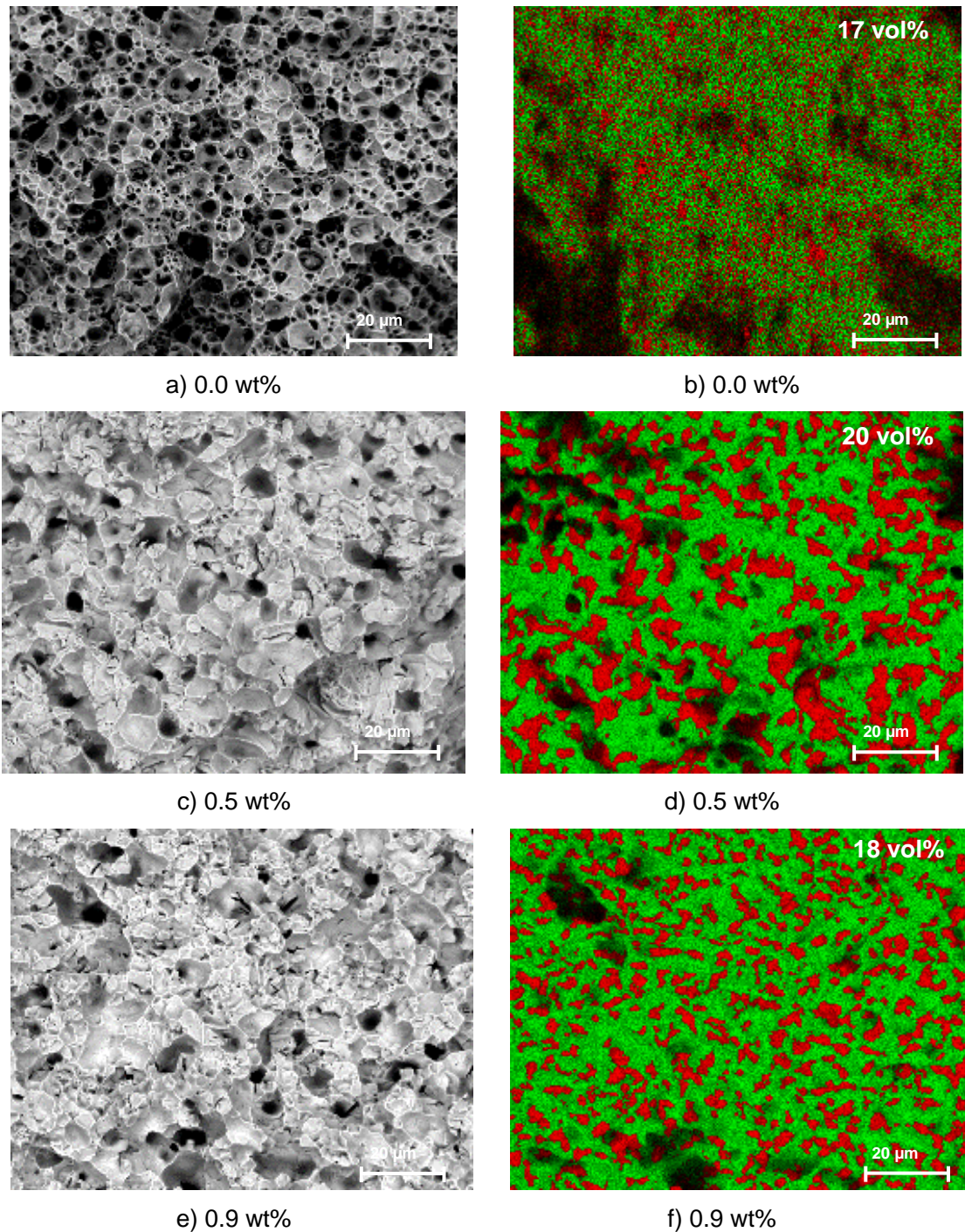


Figure 3.55 – Sintered composite with: a), b) 0.0 wt%, c), d) 0.5 wt%, e), f) 0.9 wt% (left: fracture surface and right: X-ray map of iron (green) and chromium (red))

Sintered composites (0.0, 0.5 and 0.9 wt%), all with chromium carbides were thermal analysed. Whatever the MWCNT contents, they have a similar thermal behaviour, with a maximum weight loss of about 0.1 wt% at 1300 °C (figure 3.56). This suggests that the chromium carbide content resulting from binder and due to the presence of MWCNTs into the sintered nanocomposites have an irrelevant role on the last loss of weight.

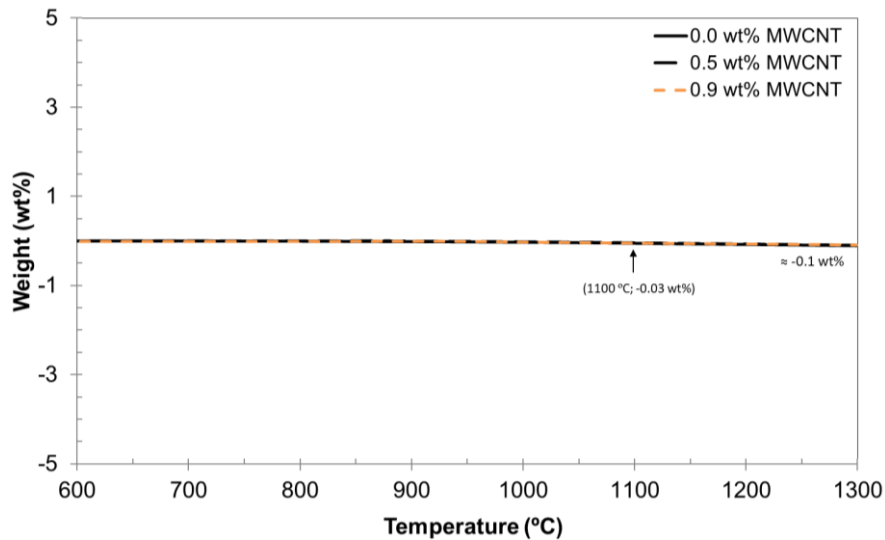
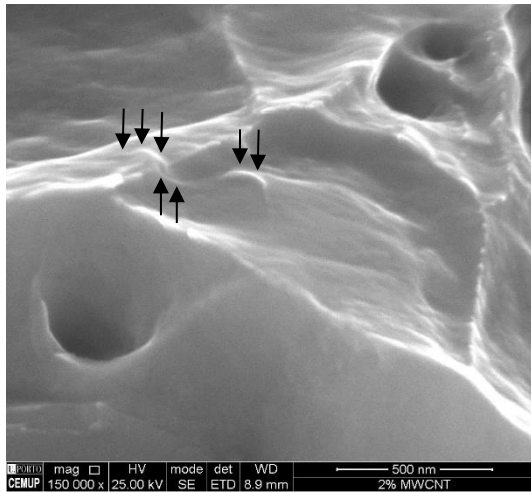


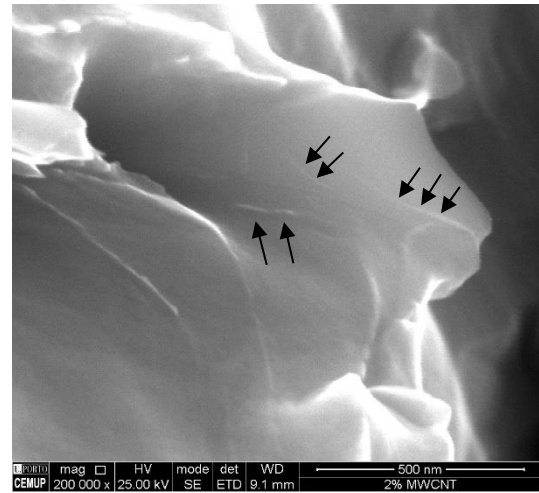
Figure 3.56 – TGA of sintered SS 316L specimens with 0.0, 0.5 and 0.9 of MWCNTs (wt%)

Up to now, it was possible to establish a relationship between the increasing of chromium carbides with the partial degradation of MWCNTs (about 60 %). The presence of nanotubes in austenitic matrix after sintering must be possible to detect. The fracture surface of sintered composite with 0.9 MWCNTs (wt%) was observed in detail by SEM (figure 3.57). Some MWCNTs elongated and embedded in matrix. Different tops of nanotubes, due to the last contact point during the tensile test, are distinguished.





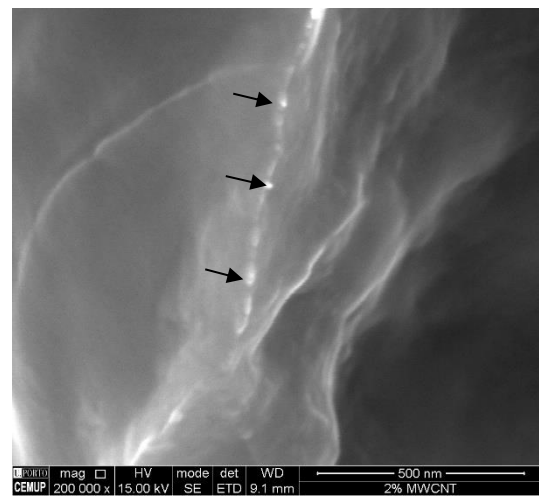
a)



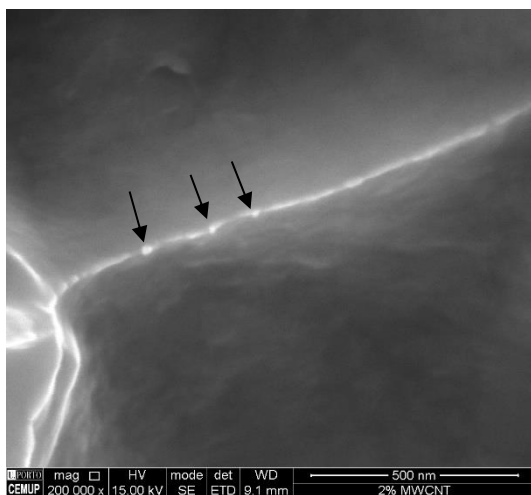
b)



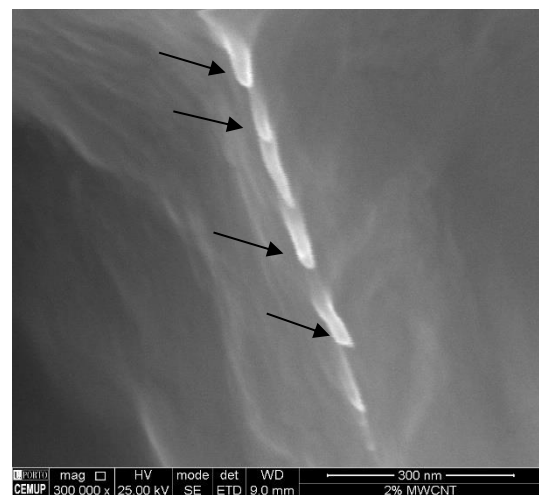
c)



d)



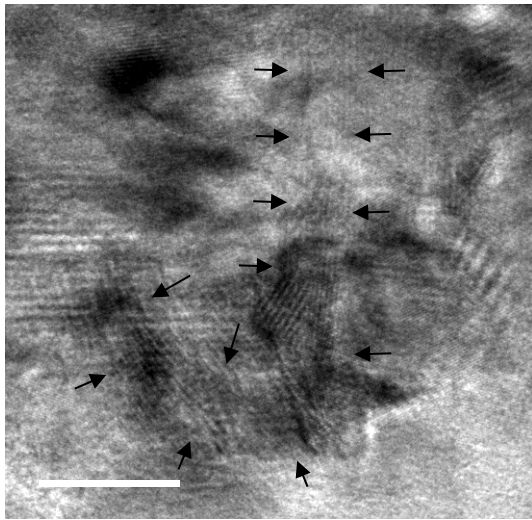
e)



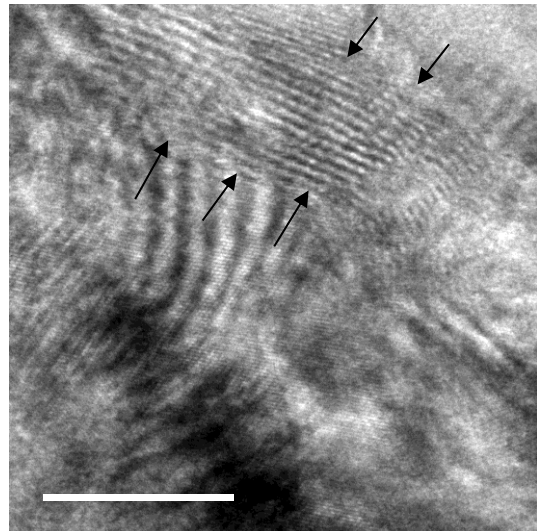
f)

Figure 3.57 – SEM of sintered nanocomposite reinforced with 0.9 of MWCNTs (wt%)

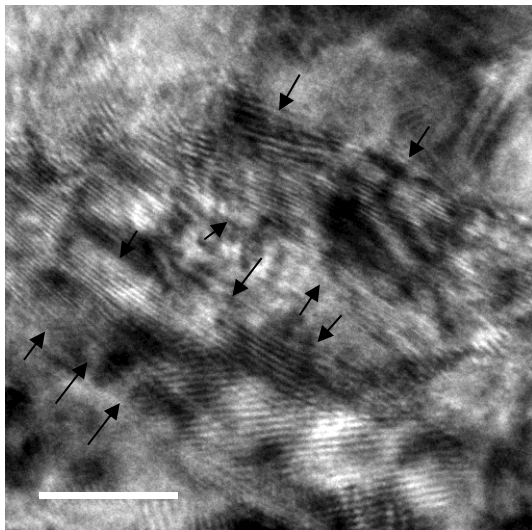
HRTEM was also the technique to allow a better understanding of the presence of MWCNTs in sintered composites (0.9 wt% MWCNTs). Thin foils were prepared by FIB. Once again, it was possible to identify the presence of MWCNTs in the sintered part (figure 3.58).



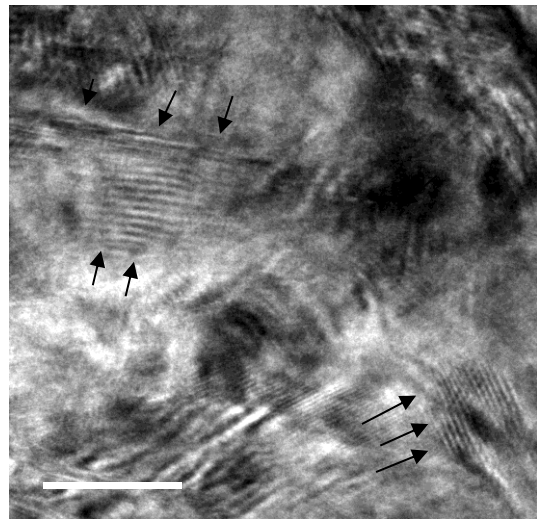
a)



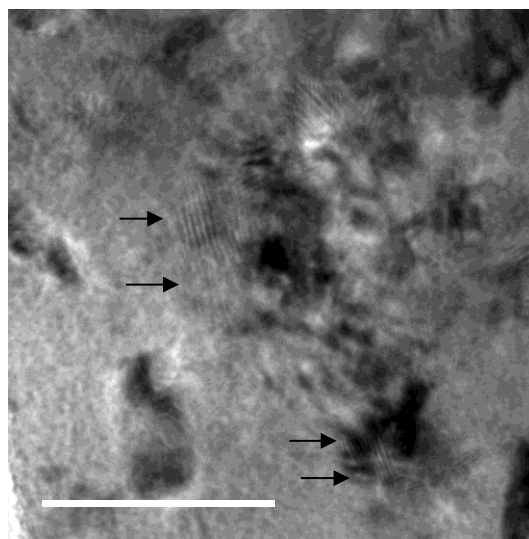
b)



c)



d)



e)

Figure 3.58 – FIB/HRTEM images of sintered composites with 0.9 of MWCNTs (wt%)

In conclusion, the main mechanical properties/characteristics of the sintered nanocomposites reinforced with MWCNTs in a lower percentage than the present in feedstock (only 40 % of total added (0.9 wt%) subsisted to the manufacturing process) (figure 3.59 and table 3.10). In fact, there is an improvement in ultramicrohardness, YS and UTS values, with only 0.3 (about 40 % of 0.9 wt%) of MWCNTs (wt%) and not with the total of nanotubes added. These composites nanoreinforced have lower ductility than the sintered SS 316L (without milling) and bulk 316L materials. The significant elongation reduction of composites is due to crack initiation in the matrix/MWCNT interface under high stress loading, probably due to the nanotubes not be functionalized [33]. Moreover, YS also showed an improvement with addition of MWCNTs, the maximum of 55 % for 0.9 wt% of MWCNTs (similar to predicted by the Hall-Petch equation), attributed to the grain size refinement due to the presence of nanotubes. By other hand, the UTS grows with the increasing of MWCNTs (wt%), for 0.9 wt%. attaining 70 % in relation to sintered steel. The improvement of UTS is benefited from the load transfer from SS 316L matrix to the MWCNT based on the strengthening mechanism.

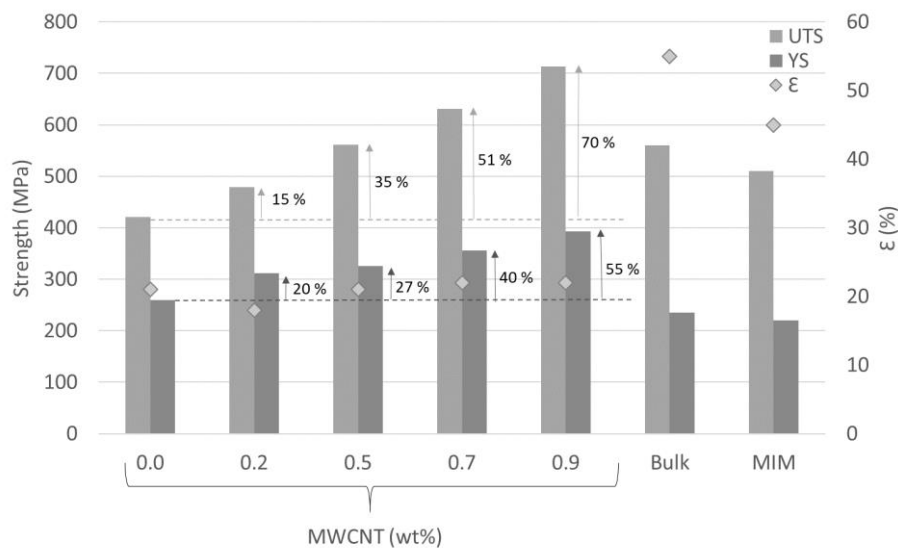


Figure 3.59 – ε, YS and UTS

The improvement of UTS is benefited from the load transfer from SS 316L matrix to the MWCNT based on the strengthening mechanism. Although the actual YS values and the  $\sigma_y$  (Hall-Petch equation) are not equal, but the expected increase attained by the last one on the same magnitude.

Table 3.10 – Resume of all the properties of nanoreinforced composites sintered at 1250 °C

wt%	0.0	0.2	0.5	0.7	0.9
Apparent density (kg/m <sup>3</sup> )	7802	7837	7829	7836	7828
H (GPa)	1.38 ± 0.09	1.45 ± 0.10	1.63 ± 0.07	1.64 ± 0.10	1.92 ± 0.11
E (GPa)	159 ± 5	170 ± 6	175 ± 4	177 ± 9	178 ± 6
ε (%)	21 ± 5	18 ± 2	21 ± 3	22 ± 5	22 ± 2
0.2 % YS (MPa)	260 ± 19	312 ± 12	325 ± 12	356 ± 6	393 ± 16
UTS (MPa)	421 ± 13	479 ± 20	561 ± 26	631 ± 23	713 ± 22

In conclusion, there is an increase of ultramicrohardness, YS and UTS of 40%, 55 % and 70 %, respectively, when was added in maximum 0.9 wt% of MWCNT, highlight the role of MWCNTs as nanoreinforcement. These values are higher than bulk materials (c.f. Annex II) and by other authors [91], [105]–[107]. Thus, these improvements suggest a relationship with MWCNTs additions. Only 40 % of the MWCNTs added can contribute to the effective increasing of mechanical properties, as shown.

### c) New approach

Besides the good properties obtained, it became imperative to carry out a new procedure, as the main objective will be the protection of MWCNTs from the inside and outside atmosphere, after debinding susceptible of damaging MWCNTs during sintering thermal cycle. Where the main challenge is to increase the viability of MWCNT during all the process, through a coating. Thus, after removing the binder from “green parts”, the “brown parts” were submitted during 48 hours to high vacuum ( $4 \times 10^{-4}$  Pa), in a sputtering vacuum chamber. A thin coating of nickel element (about 5 μm) deposited onto the “brown parts” with the aim to protect them from the new invasive atmosphere. Magnetron sputtering was the deposition technique. Only the “brown parts” with 0.5 and 0.9 wt% were coated and sintered under the same conditions previously defined (1250 °C, 10 °C/min, 60 minutes, Ar+H<sub>2</sub>).

Figure 3.60 shows the coated sintered parts nanoreinforced with 0.5 and 0.9 wt% of MWCNT. Comparing the morphology of sintered nanocomposite fracture surface with 0.5 wt% of MWCNTs (figure 3.54 c) to e)) coated and uncoated (figure 3.60 a) and b)), there are no significant differences. However, in what concern the elemental maps for the coated sintered parts it is possible to identify some differences. The coated sintered nanocomposite

with 0.5 wt% of MWCNTs (figure 3.61 b)) shows a significant change in the chromium carbide content and distribution when compared with uncoated. A reduction in area of about 50% and a small chromium carbide are visible. Nevertheless, the elemental maps of coated sintered nanocomposite with 0.9 wt% of MWCNT, show a distribution of the carbides more refined (figures 3.61 d)) than uncoated one. The reduction of chromium carbides area is not so notorious as for the 0.5 wt% of MWCNT (16.8 vol% or 14.5 wt% of  $\text{Cr}_7\text{C}_3$ ). This means, once again that the quantity of chromium carbides is not directly related with MWCNT content added to steel matrix, it seems to have a “saturation”. However, it is important to highlight the protective role of the coating, which decreases the degradation of the nanotubes of about 25 % in reference to uncoated and consequently the formation of less carbides. This means that between 0.9 (coated) and 0.0 wt%, there is a difference in carbon in matrix of about 0.5 wt% of C, that corresponds to the amount of carbon from nanotubes that contributed for the formation of  $\text{Cr}_7\text{C}_3$ , about 50 % of MWCNTs maintains intact in the matrix.

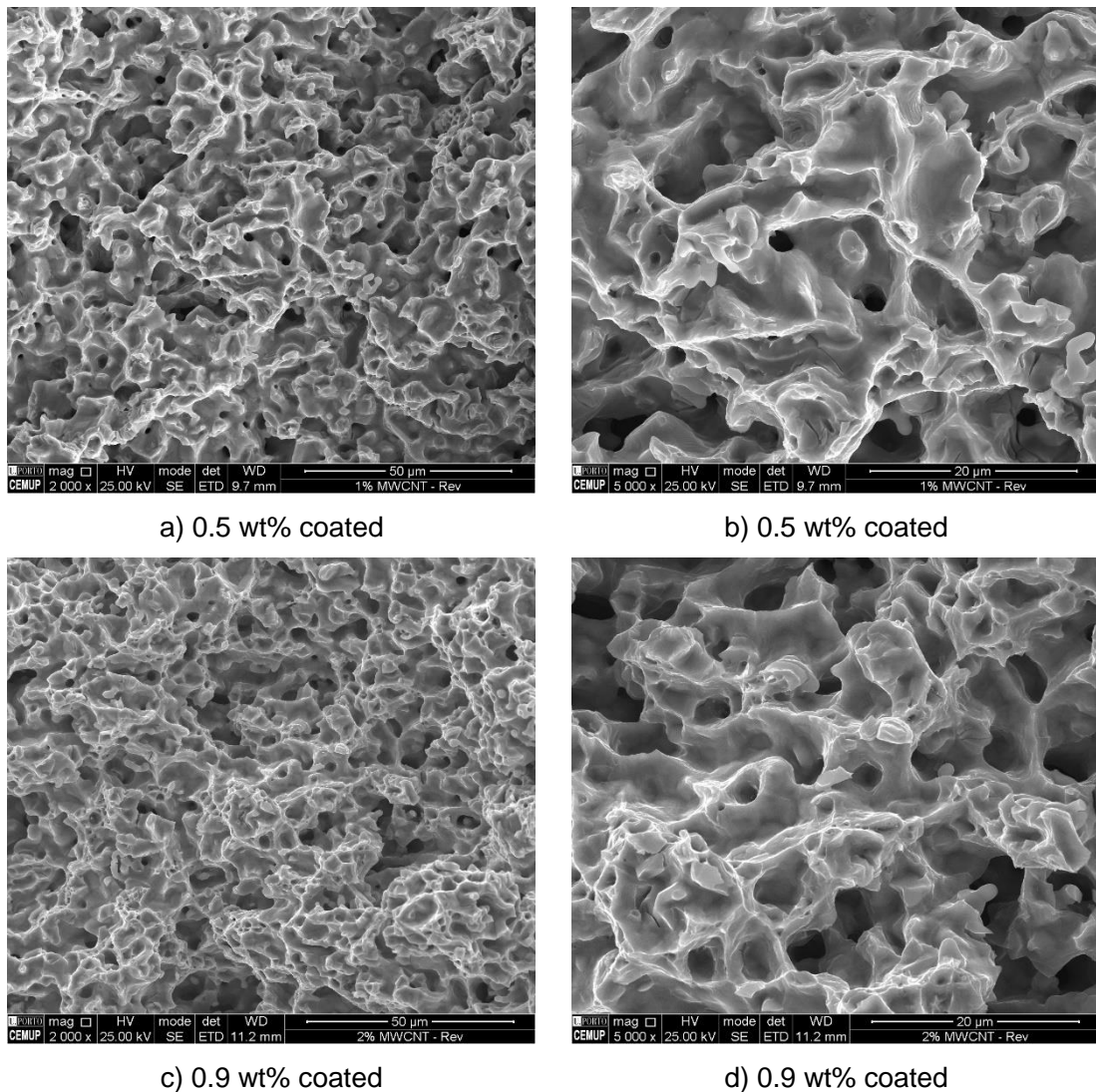


**Figure 3.60 – Morphological analysis of fracture surface of coated sintered nanocomposites with a), b) 0.5 wt%, c), d) 0.9 wt% of MWCNTs**



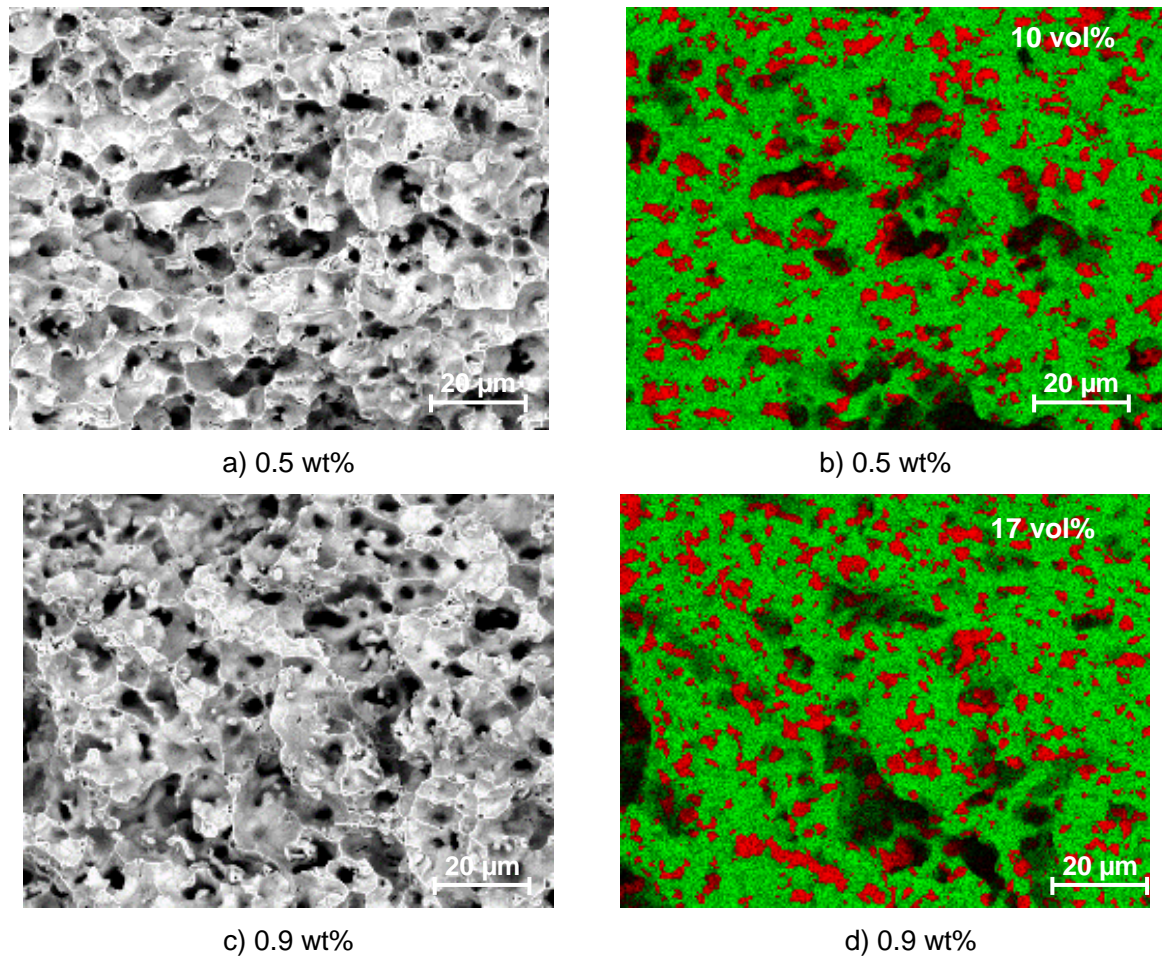


Figure 3.61 – Coated sintered composite a), b) 0.5 wt% and c), d) 0.9 wt% of MWCNTs (left: fracture surface and right X-ray map of iron (green) and chromium (red) elements)

Thermal analyses corroborate the efficacy of coating over the protection of MWCNTs (figure 3.62). After sintering, the thermal analysis of coated parts suggests that up to 1100 °C there is no difference between the coated and uncoated specimens, with or without MWCNTs additions. After this temperature, there are a weight loss of 0.4 and 0.7 wt% for sintered coated with 0.5 and 0.9 wt% of MWCNT, respectively. Taking into account that standard specimen has a loss of weight 0.1 wt%, the total loss of each nanocomposite will be around 0.3 and 0.6 wt%, respectively. This loss can correspond (approximately) to the quantity of MWCNT presents in specimens that does not contributed to the formation of chromium carbides due to the protection of the coating. However, it is important to highlight that the sintering tests had as thermal cycle a heating rate of 10 °C/min and in this specific thermal analysis 2.5 °C/min. This suggests that during sintering, due to high heating rate, the MWCNT could be preserved like during thermal tests to MWCNT alone (figure 3.6) and when were submitted to low heating rate, they loss carbon. *A. Mahajan et al.* [50] show that higher heating rate (40 °C/min) induce lower MWCNTs weight loss, when compared to lower heating rate (2 °C/min).

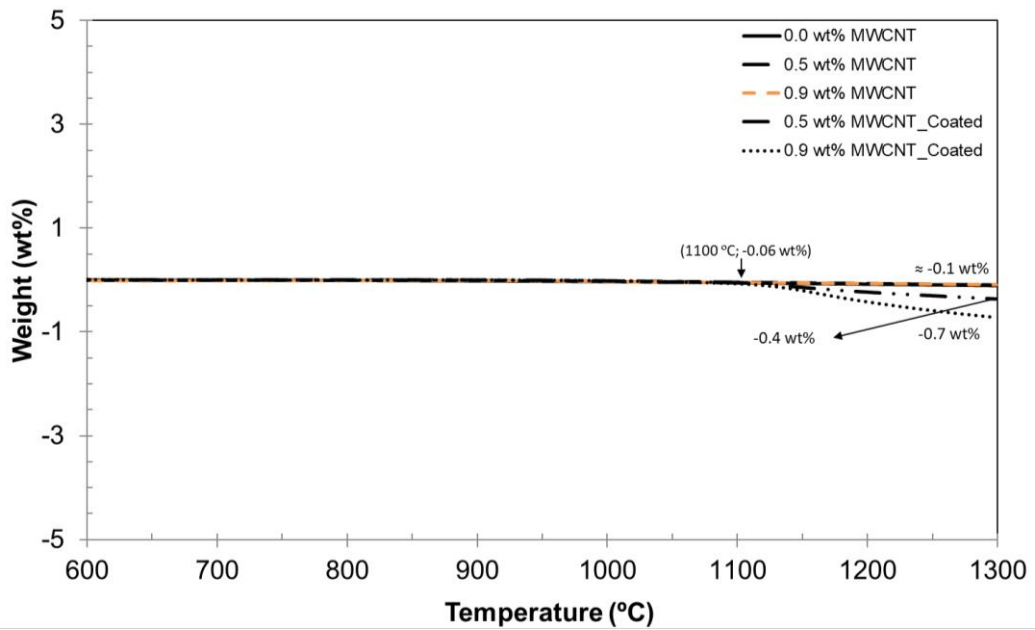
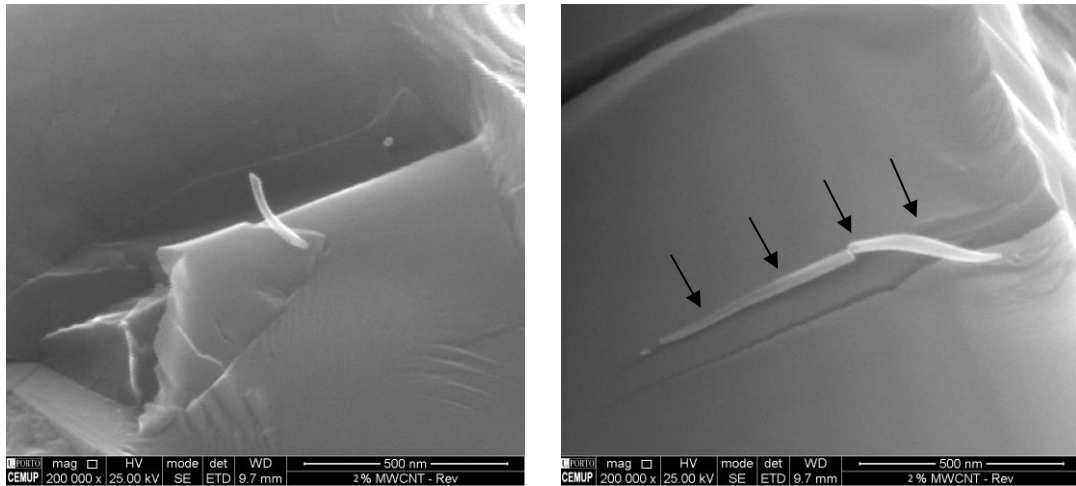


Figure 3.62 – TGA of sintered SS 316L parts with 0.0, 0.5 and 0.9 of MWCNT (wt%) coated

The coated composite with 0.9 wt% of MWCNTs, real 50% of 0.9 wt%, were analysed with detail to demonstrate the presence of MWCNTs. Figure 3.63 shows MWCNTs inserted in the steel matrix in several ways.



a)

b)

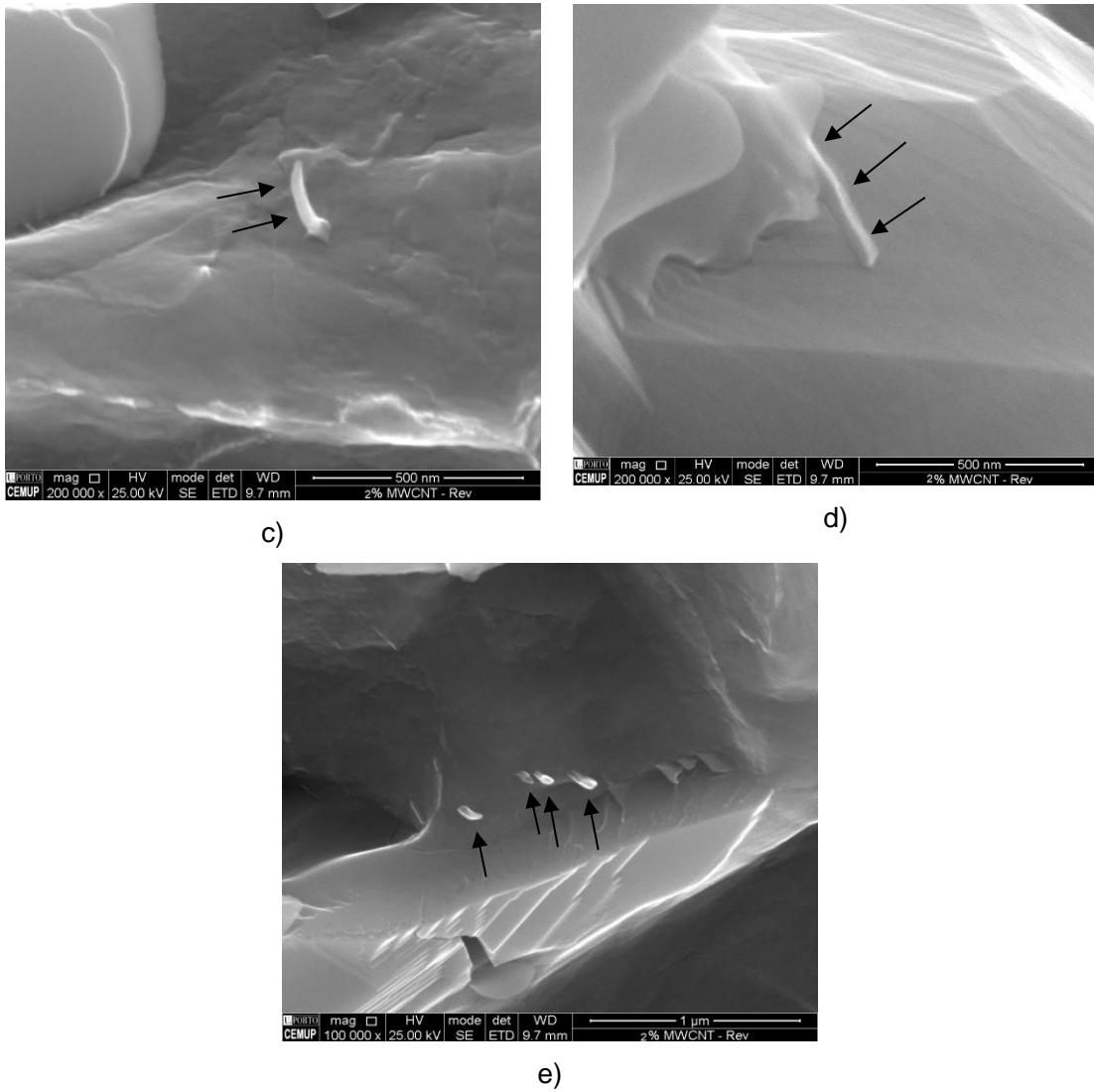
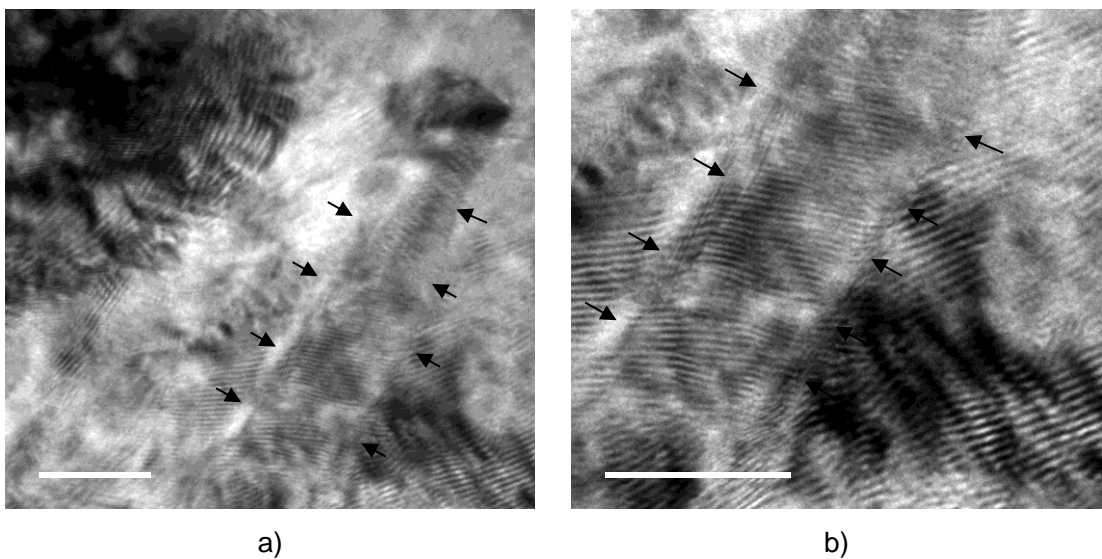


Figure 3.63 – Fracture surface of coated composites with 0.9 of MWCNTs (wt%)

The coated composite with 0.9 wt% MWCNTs was prepared by FIB technique and observed in HRTEM (similar to non-coated composite with 0.9 wt% MWCNTs). In figure 3.64, it is possible to identify the multiwall carbon nanotubes present in sintered part.





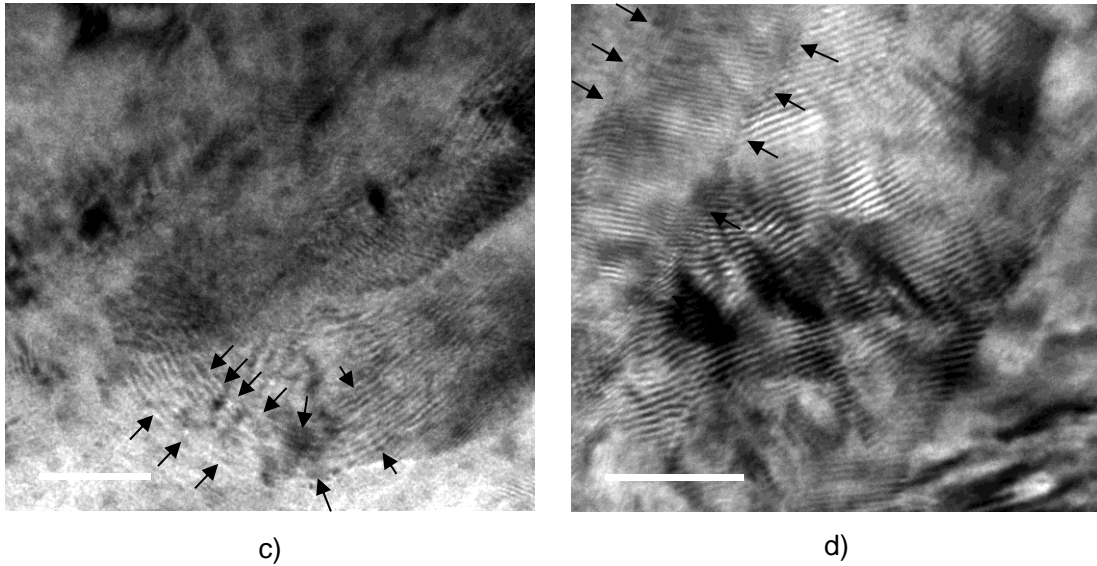


Figure 3.64 – FIB/HRTEM images of coated composite with 0.9 of MWCNTs (wt%)

In conclusion, based on previous thermal analysis, elemental maps and SEM/TEM, it is obvious that the coating of the “brown parts” followed by sintering, influences the internal structure of the sintered composites: content, distribution and size of the carbides. Besides that, the coating act as a protector of MWCNT, since inhibit their contact with oxygen species, and prevents the MWCNTs degradation, more or less 50 % of the MWCNTs added has been preserved and contributes to the strengthening of the SS 316L matrix. Thus, the coating contributes to increase the sustainability of MWCNTs in austenitic stainless steel processed by  $\mu$ MIM and sintered at 1250 °C.

# CONCLUSIONS

---

Summarized the main conclusions of this study

The work presented focused in improve the viability of MWCNTs during the production of SS 316L nanocomposites reinforced, using  $\mu$ MIM. Along the different steps of processing, measuring the content of MWCNTs present in matrix, with aim to understand their influence on possible degradation of the nanoreinforcement. The target was to stablish the best methodology for manufacturing nanocomposites efficiently.

Up to the injection step, two matrices SS 316L and copper (standard), and two nanoreinforcement with different shapes (nanotubes and nanoparticles) highlight the role in procedures that are distinguished of other processes of shaping powders. The binders are similar, and the preparation of the mixtures carried out by torque rheometry technique.

From the several aspects of production of nanocomposites feedstocks, it was possible to conclude for future:

#### A. Feedstocks

- The addition of nanoreinforcements induces always an increase of the torque values of the feedstocks, in some cases overcoming the permissible limit (4 N.m), making the mixture non-processable.
- The addition of stearic acid to the both matrices (SS 316L and copper) evidenced to be an essential procedure, for the feedstock be suitable for injection moulding.
- In case of SS 316L composites feedstock, the addition of SA revealed a significant decrease of the torque values. This decreasing was more notorious for MWCNTs rather than nanoalumina.
- When the matrix is copper, MWCNTs induces always feedstocks composites with higher torque value rather than nanoalumina additions (with or without SA addition).
- In both matrices, the addition of MWCNTs give rises to nanocomposite feedstocks with a steady regime over the composites feedstocks with nanoalumina additions.
- The pre-treatment (milling) between powders and the MWCNTs revealed to be essential not only to create a physical bond between matrix and nanoreinforcement, but also to produce feedstocks with low torque value.
- The production of composite feedstocks, based on the pre-mixture, showed that for the same type of nanoreinforcement (MWCNTs), the feedstocks composite of SS 316L matrix have lower torque values than the same additions to the copper matrix. Only after pre-mixing, the feedstock with 3.3 vol% MWCNTs already becomes possible to process (copper). Nonetheless, these copper feedstocks showed a higher torque value than the produced by the first route.
- All the composite feedstocks produced have stable torque values along the mixing time, as well as a homogeneous distribution of reinforcement.
- Binders selected to produce the feedstocks based on 316L stainless steel with nanotubes oblige to add acid stearic (10 vol%).

- At last, the thermal analysis performed to the several feedstocks showed that only the carbonaceous residues of stearic acid are not total disappearing after debinding temperature (600 °C).

The limits of nanoreinforcement content addition (maximum 3.3 vol%) is a consequence of the significant decreasing of the feedstock flowability. In spite of mould temperature be adjusted function of nanoreinforcement content it was impossible to overcome 3.3 vol% of MWCNTs. The tensile specimens of “green parts” exhibit good surface quality and resistance enough to be handling.

#### B. Debinding

The debinding thermal cycle based on the loss of weight and modification during the procedure in thermal analysis (DSC and TGA) of the polymeric mixture with stearic acid selected, that allowed to establish the best thermal cycle. After removal, the “brown parts” were fragile, but no cracks or blistering caused by the removal of the binder, were visible in specimens. The removal of binder seems to be affected by the saturated atmosphere during debinding and the milling pre-treatment performed on powders. The thermal analysis of “brown part” of powders pre-treated (without MWCNTs) showed a retention about 0.8 wt% of carbonaceous residues in specimens. Comparing with the homologue without pre-treatment and MWCNTs, this kind of residues are almost disappeared at temperatures above 950 °C. The slight difference (0.1 wt%) relative to “brown parts” of powders pre-treated with MWCNTs reveals, that only above 950 °C the MWCNTs seems to be affected by this thermal treatment and some of them was degraded (about 10 %).

#### C. Sintering

Regarding to sintering of SS 316L without reinforcement “brown parts”, the study was focused on two main aspects: the effect of sintering temperature on SS 316L; and the role of the MWCNTs added (for the optimized thermal cycle), during the processing. In first case, the shrinkage varied between 10.0 and 16.8 %, whereas the relative density increases with the increasing of the sintering temperature. The reaction between carbon coming from binder residues and chromium in solid solution in austenite are essential to the presence of chromium carbides. The presence in austenitic matrix of chromium carbides decreases the density of sintered specimens comparatively to austenitic SS 316L. After 1150 °C of sintering temperature the grain size remained constant (22.1 µm) and it were not observed significant changes in the mechanical properties. The sintered specimens produced by µMIM showed better properties than the bulk material. The best compromise between density, structure and mechanical properties/performance was for 1250 °C. However, to attain a good mixture between powders and MWCNT, obliged to a previous milling but the performance after sintering were never attained. The milled steel was the selected as the standard for the study.

The sintered nanocomposites presented shrinkage ranging from 10 to 16 %. The additions of MWCNTs higher than 0.2 wt% refined grain size (from 22.1 to 5.5  $\mu\text{m}$ ) and contribute to decrease of  $\text{Cr}_{23}\text{C}_6$  in benefit of  $\text{Cr}_7\text{C}_3$  in austenitic matrix. The formation of  $\text{Cr}_7\text{C}_3$  shows that there is a carbon source in the matrix, other than binder residues, which is the carbon from degraded nanotubes. By several techniques was possible quantify the percentage of chromium carbides formed in sintered specimens with 0.0 wt% (14.5 wt% of  $\text{Cr}_{23}\text{C}_6$ ) and 0.9 wt% (15.6 wt% of  $\text{Cr}_7\text{C}_3$ ). This difference allowed estimating that approximately 40 % of MWCNT initially added survived to manufacturing process. Nonetheless, there was an improvement of the mechanical properties of the sintered nanocomposite with increasing the MWCNTs content.

The coating of browns with different MWCNTs contents induces a reduction of chromium carbides, showing that the carbon available is lower than in uncoated ones. This procedure contributes to an increasing of intact MWCNTs of more 25 %. The amount to 50 % of the WMWCNTs is functional in the 316.L stainless steel matrix.

Only additions higher than 0.2 wt% of MWCNTs induces properties improvement in sintered nanocomposite. For the highest addition (0.9/0.4<sub>effective</sub> wt%) corresponds to a maximum improvement of 40 % of ultramicrohardness, 55 % of YS and 70 % of UTS (compared with non-reinforced and submitted to the same methodology of processing).

The study presented opens new possibilities with respect to the viability of MWCNTs in adverse processing condition. The production of nanocomposites with MWCNTs by  $\mu\text{MIM}$  is possible, but it need yet some re-adjustments in the binders and/or processing. The nanoreinforcement with MWCNTs is the solution for small size /lightweight parts/devices, to answer to mechanical requirements that is the challenge of today's times.

As future works, it is imperative to improve the efficacy of MWCNTs by:

- search new solutions to increase flowability of the nanocomposite feedstock;
- studying the role of carbon and elements with affinity to carbon in the matrix on preservation of nanotubes content added to the pristine powders of matrix.

# BIBLIOGRAPHY

---

- [1] A. Agarwal, S. R. Bakshi, and D. Lahiri, *Carbon Nanotubes: Reinforced Metal Matrix Composites*, Ed. M. Mey. Taylor and Francis Group, 2011.
- [2] S. C. Tjong, *Carbon Nanotubes Reinforced Composites: Metal and Ceramic Matrices*, Ed. Wiley-VCH, 2009.
- [3] S. Suárez, L. Reinert, and F. Mücklich, *Carbon Nanotube (CNT) -Reinforced Metal Matrix Bulk Composites : Manufacturing and Evaluation*. INTECH, 2016.
- [4] A. Singh, T. R. Prabhu, A. R. Sanjay, and V. Koti, "An overview of processing and properties of Cu/CNT nano composites," *Mater. Today Proceedings*, vol. 4, pp. 3872–3881, 2017.
- [5] D. B. Miracle, "Metal matrix composites – From science to technological significance," *Compos. Sci. Technol.*, vol. 65, pp. 2526–2540, 2005.
- [6] B. Chen, J. Shen, X. Ye, L. Jia, S. Li, and J. Umeda, "Length effect of carbon nanotubes on the strengthening mechanisms in metal matrix composites," *Acta Mater.*, vol. 140, pp. 317–325, 2017.
- [7] I. M. Melendez, E. Neubauer, P. Angerer, H. Danninger, and J. M. Torralba, "Influence of nano-reinforcements on the mechanical properties and microstructure of titanium matrix composites," *Compos. Sci. Technol.*, vol. 71, pp. 1154–1162, 2011.
- [8] H. Ye, X. Y. Liu, and H. Hong, "Fabrication of metal matrix composites by metal injection molding — A review," *J. Mater. Process. Technol.*, vol. 200, pp. 12–24, 2008.
- [9] M. T. Vieira, A. G. Martins, F. M. Barreiros, M. Matos, and J. M. Castanho, "Surface modification of stainless steel powders for microfabrication," *J. Mater. Process. Technol.*, vol. 201, no. 1–3, pp. 651–656, 2008.
- [10] F. M. Barreiros, "Optimização da moldação por injeção de pós de resíduos industriais inorgânicos," Universidade de Coimbra, 2002.
- [11] P. J. F. Harris, *Carbon Nanotube Science: Synthesis, Properties and Applications*. Cambridge: Ed. University of Reading, 2011.
- [12] A. S. Muhsan and F. Ahmad, "Development of nanocomposites heat sink (MWCNTs/Cu) using powder injection moulding for electronic applications," *Natl. Postgrad. Conf. - Energy Sustain. Explor. Innov. Minds, NPC*, pp. 1–6, 2011.
- [13] G. Goudah, F. Ahmad, and O. Mamat, "Microstructural studies of sintered carbon nanotubes reinforced copper matrix composite," *J. Eng. Sci. Technol.*, vol. 5, no. 3, pp. 272–283, 2010.
- [14] A. K. Shukla, N. Nayan, S. V. S. N. Murty, S. C. Sharma, P. Chandran, and S. R. Bakshi, "Processing of copper – carbon nanotube composites by vacuum hot pressing technique,"

*Mater. Sci. Eng. A*, vol. 560, pp. 365–371, 2013.

- [15] A. A. S. Parab, B. S. K. Gade, C. G. V. Lavate, and D. K. N. Patil, "Fabrication of Copper (Cu) -Carbon Nanotubes (CNTs) Composite by powder injection route," *Inst. Technol.*, pp. 8–10, 2011.
- [16] K. Dash, B. C. Ray, and D. Chaira, "Synthesis and characterization of copper-alumina metal matrix composite by conventional and spark plasma sintering," *J. Alloys Compd.*, vol. 516, pp. 78–84, 2012.
- [17] S. C. Tjong, "Recent progress in the development and properties of novel metal matrix nanocomposites reinforced with carbon nanotubes and graphene nanosheets," *Mater. Sci. Eng. R*, vol. 74, no. 10, pp. 281–350, 2013.
- [18] S. M. Uddin, T. Mahmud, C. Wolf, C. Glanz, I. Kolaric, and C. Volkmer, "Effect of size and shape of metal particles to improve hardness and electrical properties of carbon nanotube reinforced copper and copper alloy composites," *Compos. Sci. Technol.*, vol. 70, no. 16, pp. 2253–2257, 2010.
- [19] V. T. Pham, H. T. Bui, B. T. Tran, V. T. Nguyen, D. Q. Le, and X. T. Than, "The effect of sintering temperature on the mechanical properties of a Cu/CNT nanocomposite prepared via a powder metallurgy method," *Adv. Nat. Sci. Nanosci. Nanotechnol.*, vol. 2, no. 1, pp. 1–4, 2011.
- [20] G. N. Kim, H. J. Kim, J. S. Park, B. Y. Choi, and S. C. Huh, "A Study on characteristic evaluation and fabrication of sintered Cu-CNT composite," *9th Int. Conf. Fract. Strength Solids*, pp. 1–8, 2013.
- [21] A. A. Sahraei, A. Fathi, M. K. B. Givi, S. Boroun, and M. H. Pashaei, "Enhanced hardness and electrical properties of copper nanocomposites reinforced by functionalized MWCNTs," *J. Compos. Mater.*, vol. 48, no. 28, pp. 3485–3497, 2014.
- [22] A. S. Muhsan, F. Ahmad, N. M. Mohamed, P. S. M. M. Yusoff, and M. R. Raza, "Homogeneous Distribution of Carbon Nanotubes in Copper Matrix Nanocomposites Fabricated via Combined Technique," *Nanosci. Nanotechnol. Lett.*, vol. 6, no. 10, pp. 865–874, 2014.
- [23] M. R. Akbarpour, M. Farvizi, D. J. Lee, H. Rezaei, and H. S. Kim, "Effect of high-pressure torsion on the micro-structure and strengthening mechanisms of hot-consolidated Cu-CNT nanocomposite," *Mater. Sci. Eng. A*, vol. 638, pp. 289–295, 2015.
- [24] H. Deng, J. Yi, C. Xia, and Y. Yi, "Mechanical properties and microstructure characterization of well-dispersed carbon nanotubes reinforced copper matrix composites," *J. Alloys Compd.*, pp. 1–13, 2017.
- [25] H. Wang, Z.-H. Zhang, H.-M. Zhang, Z.-Y. Hu, and S.-L. Li, "Novel synthesizing and



- characterization of copper matrix composites reinforced with carbon nanotubes,” *Mater. Sci. Eng. A*, vol. 696, pp. 80–89, 2017.
- [26] J. Liao and M. J. Tan, “Mixing of carbon nanotubes (CNTs) and aluminum powder for powder metallurgy use,” *Powder Technol.*, vol. 208, no. 1, pp. 42–48, 2011.
- [27] Y. Wu and G. Y. Kim, “Carbon nanotube reinforced aluminum composite fabricated by semi-solid powder processing,” *J. Mater. Process. Technol.*, vol. 211, no. 8, pp. 1341–1347, 2011.
- [28] B. Chen, S. Li, H. Imai, L. Jia, J. Umeda, and M. Takahashi, “An approach for homogeneous carbon nanotube dispersion in Al matrix composites,” *Mater. Des.*, vol. 72, pp. 1–8, 2015.
- [29] S. Simões, F. Viana, M. A. L. Reis, and M. F. Vieira, “Aluminum and Nickel Matrix Composites Reinforced by CNTs: Dispersion/Mixture by Ultrasonication,” *MDPI Met.*, vol. 7, no. 279, pp. 1–11, 2017.
- [30] S. Suárez, E. Ramos-Moore, B. Lechthaler, and F. Mucklich, “Grain growth analysis of multiwalled carbon nanotube-reinforced bulk Ni composites,” *Carbon N. Y.*, vol. 70, no. 681, pp. 173–178, 2014.
- [31] I. S. M. Carneiro, “Produção e caracterização de compósitos de matriz de níquel reforçados com nanotubos de carbono,” Universidade do Porto, 2017.
- [32] P. Wang, T. Li, Y.-F. Lim, C. K. I. Tan, and D. Chi, “Sintering and mechanical properties of mechanically milled Inconel 625 superalloy and its composite reinforced by carbon nanotube,” *Met. Powder Rep.*, vol. 72, no. 4, pp. 271–275, 2017.
- [33] P. Wang, B. Zhang, C. C. Tan, S. Raghavan, Y.-F. Lim, and C.-N. Sun, “Microstructural characteristics and mechanical properties of carbon nanotube reinforced Inconel 625 parts fabricated by selective laser melting,” *Mater. Des.*, vol. 112, pp. 290–299, 2016.
- [34] Y. Gogotsi, *Carbon nanomaterials*. USA: Ed. Taylor and Francis Group, 2006.
- [35] A. Eatemadi, H. Daraee, H. Karimkhanloo, M. Kouhi, N. Zarghami, and A. Akbarzadeh, “Carbon nanotubes: properties, synthesis, purification, and medical applications,” *Nanoscale Res. Lett.*, vol. 9, no. 1, pp. 393–406, 2014.
- [36] S. R. Bakshi, D. Lahiri, and A. Agarwal, “Carbon nanotube reinforced metal matrix composites - a review,” *Int. Mater. Rev.*, vol. 55, no. 1, pp. 41–64, 2010.
- [37] N. M. Mubarak, E. C. Abdullah, N. S. Jayakumar, and J. N. Sahu, “An overview on methods for the production of carbon nanotubes,” *J. Ind. Eng. Chem.*, vol. 20, no. 4, pp. 1186–1197, 2014.
- [38] “Carbon Nanotubes Market by Type, Method, Application - Global Forecast to 2022,”

*Advanced Material Market Trends*, 2017. [Online]. Available: <http://www.reportlinker.com/p05045705/Carbon-Nanotubes-Market-by-Type-Method-Application-Global-Forecast-to.html>. [Accessed: 20-Jul-2007].

- [39] E. Neubauer, M. Kitzmantel, M. Hulman, and P. Angerer, "Potential and challenges of metal-matrix-composites reinforced with carbon nanofibers and carbon nanotubes," *Compos. Sci. Technol.*, vol. 70, no. 16, pp. 2228–2236, 2010.
- [40] R. B. Patel, J. Liu, J. V. Scicolone, S. Roy, S. Mitra, and R. N. Dave, "Formation of stainless steel – carbon nanotube composites using a scalable chemical vapor infiltration process," *J. Mater. Sci.*, vol. 48, pp. 1387–1395, 2013.
- [41] D. Kaewsai, A. Watcharapasorn, P. Singjai, S. Wirojanupatump, P. Niranatlumpong, and S. Jiansirisomboon, "Thermal sprayed stainless steel/carbon nanotube composite coatings," *Surf. Coatings Technol.*, vol. 205, no. 7, pp. 2104–2112, 2010.
- [42] S. Cho, K. Kikuchi, T. Miyazaki, K. Takagi, and A. Kawasaki, "Multiwalled carbon nanotubes as a contributing reinforcement phase for the improvement of thermal conductivity in copper matrix composites," *Scr. Mater.*, vol. 63, no. 4, pp. 375–378, 2010.
- [43] A. S. Muhsan, F. Ahmad, N. M. Mohamed, and M. R. Raza, "Fabrication and Microstructural Analysis of CNTs Reinforced Copper Matrix Nanocomposites via MIM Technique," *Appl. Mech. Mater.*, vol. 459, pp. 11–17, 2014.
- [44] K. Chu, Q. Wu, C. Jia, X. Liang, J. Nie, and W. Tian, "Fabrication and effective thermal conductivity of multi-walled carbon nanotubes reinforced Cu matrix composites for heat sink applications," *Compos. Sci. Technol.*, vol. 70, no. 2, pp. 298–304, 2010.
- [45] L. Shuquan, T. Yan, Z. Yong, and Z. Jie, "The Rheological Effect of Carbon Nanotubes on the Iron Based Metal Powder Injection Molding Feedstock," *Adv. Mater. Res.*, vol. 79–82, pp. 469–472, 2009.
- [46] A. S. Muhsan, F. Ahmad, N. M. Mohamed, and M. R. Raza, "Flow Behavior of Cu/CNTs Feedstocks for Powder Injection Molding," *Int. J. Appl. Phys. Math.*, vol. 1, no. 3, pp. 199–202, 2011.
- [47] M. J. Yu, X. L. Cai, Z. Lei, H. Cui, L. Zheng, and Y. Feng, "Effect of balls/powder weight ratio in milling on microstructure and properties of MWCNTs/Cu composites," *Key Eng. Mater.*, vol. 609–610, pp. 394–399, 2014.
- [48] A. S. Muhsan, F. Ahmad, N. M. Mohamed, P. Yusoff, and M. R. Raza, "Carbon Nanotubes Reinforced Copper Matrix Nanocomposites via Metal Injection Molding Technique," *J. Appl. Sci.*, vol. 12, no. 23, pp. 2397–2403, 2012.
- [49] V. J. Pillewan, D. N. Raut, and K. N. Patil, "Metal Matrix Composite by Powder Injection Molding Route," *Int. J. Emerg. Technol. Adv. Eng.*, vol. 5, no. 5, pp. 514–520, 2015.

- [50] A. Mahajan, A. Kingon, Á. Kukovecz, Z. Konya, and P. M. Vilarinho, "Studies on the thermal decomposition of multiwall carbon nanotubes under different atmospheres," *Mater. Lett.*, vol. 90, pp. 165–168, 2013.
- [51] J. G. Gutiérrez, G. B. Stringari, and I. Emri, *Powder Injection Molding of Metal and Ceramic Parts: Some Critical Issues for Injection Molding*. INTECH, 2012.
- [52] K. Nishiyabu, *Micro Metal Powder Injection Molding: Some Critical Issues for Injection Molding*. Ed. Jian Wang, 2012.
- [53] B. Y. Tay, L. Liu, N. H. Loh, S. B. Tor, Y. Murakoshi, and R. Maeda, "Characterization of metallic micro rod arrays fabricated by micro MIM," *Mater. Charact.*, vol. 57, no. 2, pp. 80–85, 2006.
- [54] U. M. Attia and J. R. Alcock, "A review of micro-powder injection moulding as a microfabrication technique," *J. Micromechanics Microengineering*, vol. 21, no. 4, pp. 1–22, 2011.
- [55] D. F. Heaney, *Handbook of metal injection molding*. Ed. Woodhead Publishing in Materials, 2012.
- [56] V. J. Pillewan, D. N. Raut, and K. N. Patil, "Microscopic Analysis of Carbon Nano Tubes based Metal Matrix Composite," *J. Eng. Technol.*, vol. 4, no. 1, pp. 6–10, 2015.
- [57] X. Kong, "Development and characterization of polymer- metallic powder feedstocks for micro-injection molding," L'Université de Franche-Comte, 2013.
- [58] E. W. Sequeiros, "Microfabricação de Componentes Metálicos por Microgravação," Universidade do Porto, 2014.
- [59] E. Klar and P. K. Samal, *Powder Metallurgy Stainless Steels: Processing, Microstructures and Properties*. Ed. ASM International, 2007.
- [60] ASM International Handbook Committee, *Powder Metal Technologies and Applications*, vol. 7. Oxford: Ed. ASM International, 1998.
- [61] B. Y. Tay, N. H. Loh, S. B. Tor, F. L. Ng, G. Fu, and X. H. Lu, "Characterisation of micro gears produced by micro powder injection moulding," *Powder Technol.*, vol. 188, no. 3, pp. 179–182, 2009.
- [62] L. Liu, N. H. Loh, B. Y. Tay, and S. B. Tor, "Microstructure evolution of 316L stainless steel micro components prepared by micro powder injection molding," *Powder Technol.*, vol. 206, no. 3, pp. 246–251, 2011.
- [63] F. M. Barreiros, *Manual de microfabricação B3 - Processos de replicação*. CEMICRO, 2008.
- [64] M. E. Sotomayor, A. Várez, and B. Levenfeld, "Influence of powder particle size distribution

- on rheological properties of 316L powder injection moulding feedstocks,” *Powder Technol.*, vol. 200, no. 1–2, pp. 30–36, 2010.
- [65] A. R. Farinha, A. J. Cavaleiro, T. J. Ferreira, F. M. Barreiros, M. T. Vieira, and T. Barrière, “Optimization of nanocrystalline size of powder coating for  $\mu$ MIM,” *World Powder Metall. Congr. Exhib. (PM 2010)*, pp. 455–463, 2010.
- [66] C. Quinard, T. Barriere, and J. C. Gelin, “Development and property identification of 316L stainless steel feedstock for PIM and micro PIM,” *Powder Technol.*, vol. 190, no. 1–2, pp. 123–128, 2009.
- [67] T. J. Ferreira, “Estudo comparativo de ligantes para optimização de misturas de aço inoxidável para  $\mu$ -MIM,” Universidade de Coimbra, 2011.
- [68] J. Meng, N. H. Loh, G. Fu, S. B. Tor, and B. Y. Tay, “Replication and characterization of 316L stainless steel micro-mixer by micro powder injection molding,” *J. Alloys Compd.*, vol. 496, no. 1–2, pp. 293–299, 2010.
- [69] M. R. Raza, F. Ahmad, M. A. Omar, and A. S. Muhsan, “Development of defects free stainless steel parts using powder injection molding,” *Asian J. Sci. Res.*, vol. 6, no. 2, pp. 307–314, 2013.
- [70] G. Fu, N. H. Loh, S. B. Tor, Y. Murakoshi, and R. Maeda, “Replication of metal microstructures by micro powder injection molding,” *Mater. Des.*, vol. 25, no. 8, pp. 729–733, 2004.
- [71] Y. L. Li, L. Li, and K. A. Khalil, “Effect of powder loading on metal injection molding stainless steels,” *J. Mater. Process. Technol.*, vol. 183, no. 2–3, pp. 432–439, 2007.
- [72] J. Meng, N. H. Loh, B. Y. Tay, G. Fu, and S. B. Tor, “Tribological behavior of 316L stainless steel fabricated by micro powder injection molding,” *Wear*, vol. 268, no. 7–8, pp. 1013–1019, 2010.
- [73] F. M. Barreiros, M. T. Vieira, and J. M. Castanho, “Fine tuning injection feedstock by nano coating SS powder,” *Met. Powder Rep.*, vol. 64, no. 9, pp. 18–21, 2009.
- [74] L. Liu, N. H. Loh, B. Y. Tay, S. B. Tor, Y. Murakoshi, and R. Maeda, “Mixing and characterisation of 316L stainless steel feedstock for micro powder injection molding,” *Mater. Charact.*, vol. 54, no. 3, pp. 230–238, 2005.
- [75] A. Bose, I. Otsuka, T. Yoshida, and H. Toyoshima, “Metal Injection Molding of Ultra-Fine 316L Stainless Steel Powders,” *Adv. Powder Metall. Part. Mater.*, pp. 1–12, 2007.
- [76] Z. Y. Liu, N. H. Loh, S. B. Tor, K. A. Khor, Y. Murakoshi, and R. Maeda, “Micro-powder injection molding,” *J. Mater. Process. Technol.*, vol. 127, pp. 165–168, 2002.
- [77] N. H. Loh, S. B. Tor, B. Y. Tay, Y. Murakoshi, and R. Maeda, “Fabrication of micro gear

- by micro powder injection molding," *Microsyst. Technol.*, vol. 14, no. 1, pp. 43–50, 2007.
- [78] Z. Y. Liu, N. H. Loh, S. B. Tor, K. A. Khor, Y. Murakoshi, and R. Maeda, "Binder system for micropowder injection molding," *Mater. Lett.*, vol. 48, no. 1, pp. 31–38, 2001.
- [79] C. Quinard, J. Song, T. Barriere, and J. C. Gelin, "Elaboration of PIM feedstocks with 316L fine stainless steel powders for the processing of micro-components," *Powder Technol.*, vol. 208, no. 2, pp. 383–389, 2011.
- [80] J. H. García, "Development of binder systems based on CAB for powder injection moulding (PIM) and micro powder injection moulding ( $\mu$ -PIM) of Zircon and Invar powders," Carlos III de Madrid University, 2013.
- [81] T. J. Ferreira and M. T. Vieira, "Behavior of feedstocks reinforced with nanotubes for micromanufacturing," *World Powder Metall. Congr. Exhib. (PM 2014)*, vol. 3, 2014.
- [82] T. J. Ferreira, M. T. Vieira, J. Costa, M. Silva, and P. T. Gago, "Manufacturing Dental Implants using Powder Injection Molding," *J. Orthod. Endod.*, vol. 2, no. 1:21, pp. 1–7, 2016.
- [83] T. J. Ferreira, C. P. Fernandes, A. P. Piedade, J. Tondela, and M. T. Vieira, "Mechanical behaviour of dental implants manufactured from metallic powders by microMIM," *Cienc. e Technol. dos Mater.*, vol. 26, no. 2, pp. 89–95, 2014.
- [84] T. J. Ferreira, M. T. Vieira, M. Silva, and P. T. Gago, "Production of micro invasive biomedical devices by micro MIM," *O Molde - Tool. na Aeronaut.*, vol. 1, no. 95, pp. 46–52, 2012.
- [85] T. J. Ferreira and M. T. Vieira, "Optimization of MWCNT – Metal Matrix Composites feedstocks," *Sci. Technol. Mater.*, vol. 29, no. Special Issue "Materiais 2015," pp. 87–91, 2017.
- [86] R. M. German and A. Bose, *Injection Molding of Metals and Ceramics*. Ed., 1997.
- [87] C. Quinard, "Experimentation, modelisation et simulation dans le domaine de l'elaboration de micro-composants injectes a partir de poudres," L'Université de Franche-Comte, 2008.
- [88] L. Moballegh, J. Morshedian, and M. Esfandeh, "Copper injection molding using a thermoplastic binder based on paraffin wax," *Mater. Lett.*, vol. 59, no. 22, pp. 2832–2837, 2005.
- [89] G. Goudah, F. Ahmad, O. Mamat, and M. A. Omar, "Preparation and characterization of copper feedstock for metal injection molding," *J. Appl. Sci.*, vol. 10, no. 24, pp. 3295–3300, 2010.
- [90] V. Piotter, W. Bauer, R. Knitter, M. Mueller, T. Mueller, and K. Plewa, "Powder injection moulding of metallic and ceramic micro parts," *Microsyst. Technol.*, vol. 17, no. 2, pp. 251–

263, 2011.

- [91] "MPIF Standard 35: Materials Standards for Metal Injection Molded Parts," 2007.
- [92] "ISO 527-2: Test conditions for moulding and extrusion plastics," 2012.
- [93] M. I. Corporation, "AccuPyc 1330 Pycnometer: Operator's Manual V3.03," 1996.
- [94] "ISO 13320:2009: Particle size analysis - Laser diffraction methods," 2009.
- [95] ASTM International, "ASTM B962-17: Standard Test Methods for Density of Compacted or Sintered Powder Metallurgy (PM) Products Using Archimedes' Principle," 2017.
- [96] ASTM International, "ASTM E407-07: Standard Practice for Microetching Metals and Alloys," 2007.
- [97] U. V Amadoz, A. Benedetti, J. Méndez, L. M. Sender, and J. B. Diez, "Focused ion beam nano-sectioning and imaging : a new method in characterisation of palaeopalynological remains," *Grana*, vol. 51, no. 1, pp. 1–9, 2012.
- [98] J. E. Mark, *Physical Properties of Polymers Handbook*. Ed., 2007.
- [99] "ISO 643:2012 Steels. Micrographic determination of the apparent grain size," 2012.
- [100] O. A. Hilders, N. Zambrano, and R. Caballero, "Microstructure, Strength, and Fracture Topography Relations in AISI 316L Stainless Steel, as Seen through a Fractal Approach and the Hall-Petch Law," *Int. J. Met.*, pp. 1–10, 2015.
- [101] J. M. Antunes, A. Cavaleiro, L. F. Menezes, M. I. Simoes, and J. V. Fernandes, "Ultra-microhardness testing procedure with Vickers indenter," *Surf. Coatings Technol.*, vol. 149, pp. 27–35, 2002.
- [102] L. Castro, S. Merino, B. Levenfeld, A. Várez, and J. M. Torralba, "Mechanical properties and pitting corrosion behaviour of 316L stainless steel parts obtained by a modified metal injection moulding process," *J. Mater. Process. Technol.*, vol. 143–144, no. 1, pp. 397–402, 2003.
- [103] F. Ernst, D. Li, H. Kahn, G. M. Michal, and A. H. Heuer, "The carbide M7C3 in low-temperature-carburized austenitic stainless steel," *Acta Mater.*, vol. 59, pp. 2268–2276, 2011.
- [104] G. M. Michal, F. Ernst, and A. H. Heuer, "Carbon Paraequilibrium in Austenitic Stainless Steel," *Metall. Mater. Trans. A*, vol. 37A, no. June, pp. 1819–1824, 2006.
- [105] K. S. Hwang and Y. W. Hsueh, "Post-sintering thermal treatment of nitrogen containing pressed and sintered and PIM stainless steels," *Powder Metall.*, vol. 50, no. 2, pp. 165–171, 2007.
- [106] "Tensile properties of representative MIM alloys," *Powder Injection Moulding*, 2017.

- [Online]. Available: <http://www.pim-international.com/metal-injection-molding/tensile-properties-of-representative-mim-alloys/>. [Accessed: 03-Jan-2017].
- [107] D. F. Heaney, T. J. Mueller, and P. A. Davies, "Mechanical properties of metal injection moulded 316l stainless steel using both prealloy and master alloy techniques," *Powder Metall.*, vol. 47, no. 4, pp. 1–7, 2004.
- [108] P. Sawunyama, L. Jiang, A. Fujishima, and K. Hashimoto, "Photodecomposition of a Langmuir-Blodgett Film of Stearic Acid on TiO<sub>2</sub> Film Observed by in Situ Atomic Force Microscopy and FT-IR," vol. 101, no. Physical Chemistry B, pp. 11000–11003, 1997.
- [109] M. Regert, J. Langlois, E. Laval, A. S. Le Hô, and C. Pagès, "Elucidation of molecular and elementary composition of organic and inorganic substances involved in 19th century wax sculptures using an integrated analytical approach," *Anal. Chim. Acta*, vol. 577, pp. 140–152, 2006.
- [110] A. S. Luyt, I. Krupa, H. J. Assumption, E. E. M. Ahmad, and J. P. Mofokeng, "Blends of polyamide 12 and maleic anhydride grafted paraffin wax as potential phase change materials," *Polym. Test.*, vol. 29, no. 1, pp. 100–106, 2010.
- [111] H. Krump, P. Alexy, and A. S. Luyt, "Preparation of a maleated Fischer-Tropsch paraffin wax and FTIR analysis of grafted maleic anhydride," *Anal. Method*, vol. 24, no. 2, pp. 129–135, 2005.

# APPENDIX I

---

Binders characterization



Figure A.1 shows the IR spectrums of binder M<sub>1</sub> and SA. It is possible to see that there are many overlapping peaks between the two binders and the identification was possible by comparison with published results. The C-H stretching region band at 2958 cm<sup>-1</sup> is the asymmetric in-plane C-H stretching mode of the CH<sub>3</sub> group [108], [109]. The bands at 2920 cm<sup>-1</sup> and 2850 cm<sup>-1</sup> are the asymmetric and symmetric C-H stretching modes of the CH<sub>2</sub> group, respectively [98], [108]–[111]. The band at 1736 cm<sup>-1</sup> corresponds to the C=O stretching of ester function [109], [110], while a strong absorption band at 1707 cm<sup>-1</sup>, is characteristic of carboxylic acids and esters (C=O) [110]. When PE is crystalline in two samples, at 1473 and 1464 cm<sup>-1</sup>, the CH<sub>2</sub> bending vibrations, were also observed, [98], [109], [110]. The peaks at 1368 cm<sup>-1</sup> is associated to C-H bending vibrations [98], [110]. The peaks in the range from 1256 to 1180 cm<sup>-1</sup> correspond to C–C chain stretch, CH<sub>3</sub> rock, CH bend and CH<sub>2</sub> twist [98]. However, the OH bending vibrations is also associated to peaks at 1243 cm<sup>-1</sup> [109]. In two binders, close to 1078 cm<sup>-1</sup>, the C-C stretching vibrations, were also observed [98]. The band 960 cm<sup>-1</sup> corresponds to aromatic groups [109]. At 888 cm<sup>-1</sup> it is possible to observe a rocking vibration of CH<sub>2</sub> amorphous [98]. The CH<sub>2</sub> deformation (rocking vibration) is visible for two samples at 720 cm<sup>-1</sup>, when PE is crystalline [98]. By comparison, of the two spectra it is possible to see in both binders the same types of bonds.

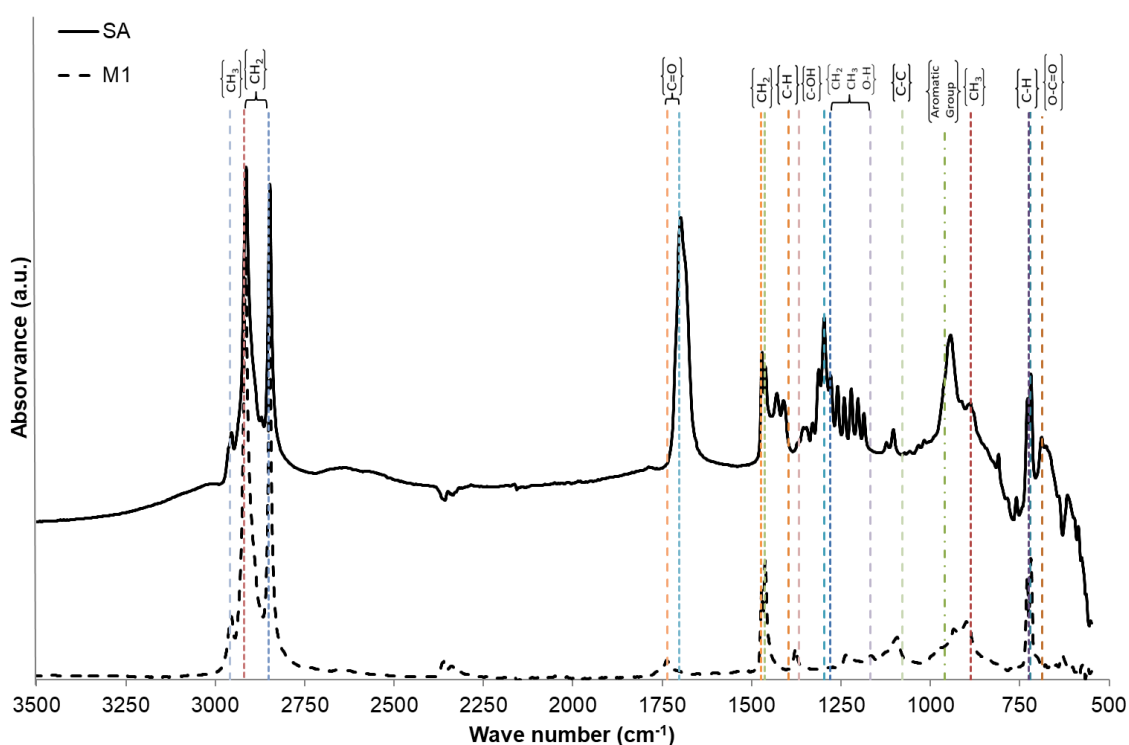


Figure A.1 – IR spectra of M<sub>1</sub> and SA binders

# APPENDIX II

---

Case study: copper powders and nanocomposites

## Characterization

The figure A.2 and table A.2 show the Gaussian distribution, the particle size, and the particle size distribution ( $S_w$ ) of copper powders.

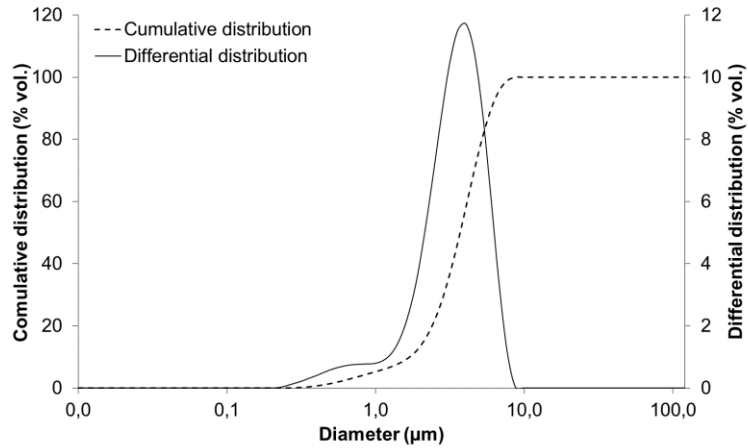


Figure A.2 – Particle size distribution of copper powders

The major part of powders (figure A.3) shows shape factor close to 1 (despite being produced by water atomization).

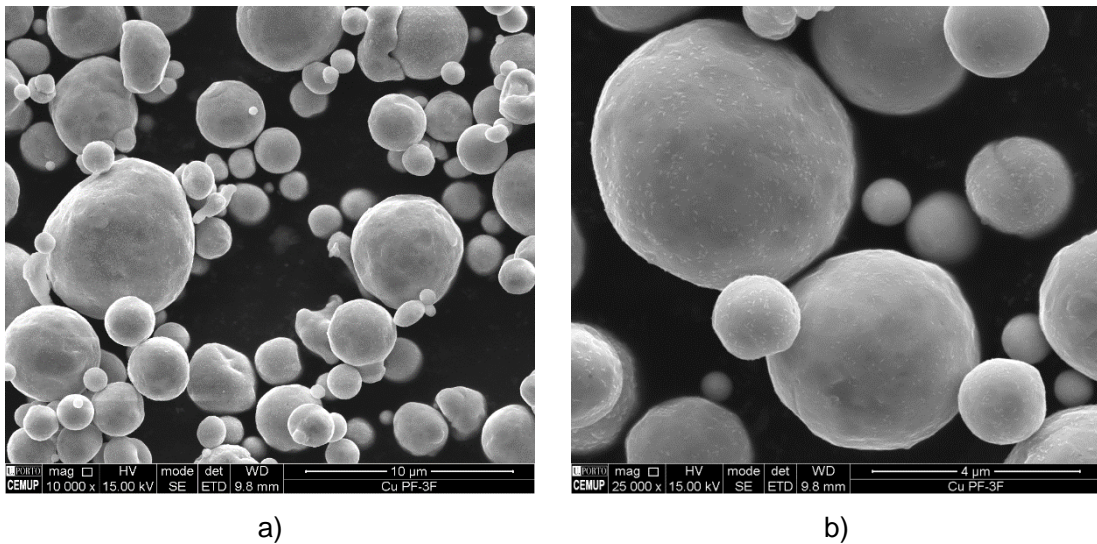


Figure A.3 – Particle shape of copper powders: a) 10000x b) 25000x

The structure of copper powders (figure A.4) is similar to the pure copper (ICDD number: 85 – 1326, Annex I).

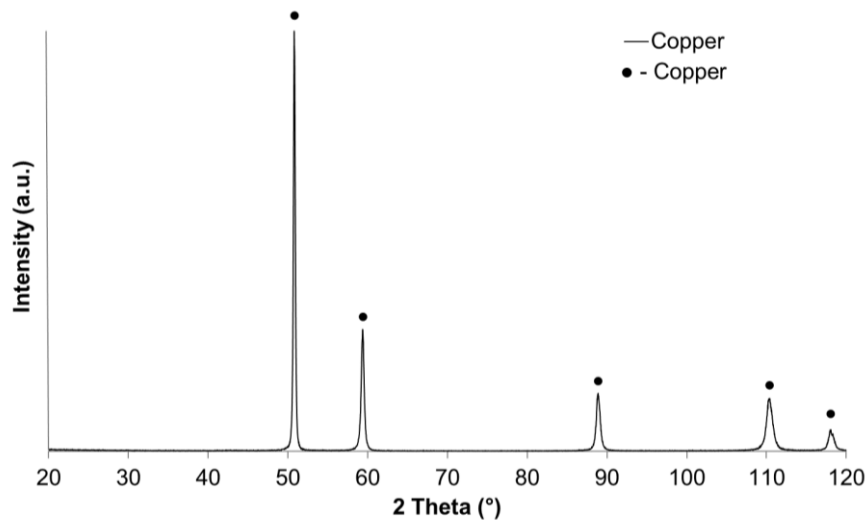


Figure A.4 – X-ray diffraction of copper powders (as received)

Table A.1 summarizes the characteristics of copper powders. In comparison with SS 316L powders, the copper powders have high specific surface area ( $S_m$ ) and low width particle size distribution ( $S_w$ ).

Table A.1 – Copper powders characteristics

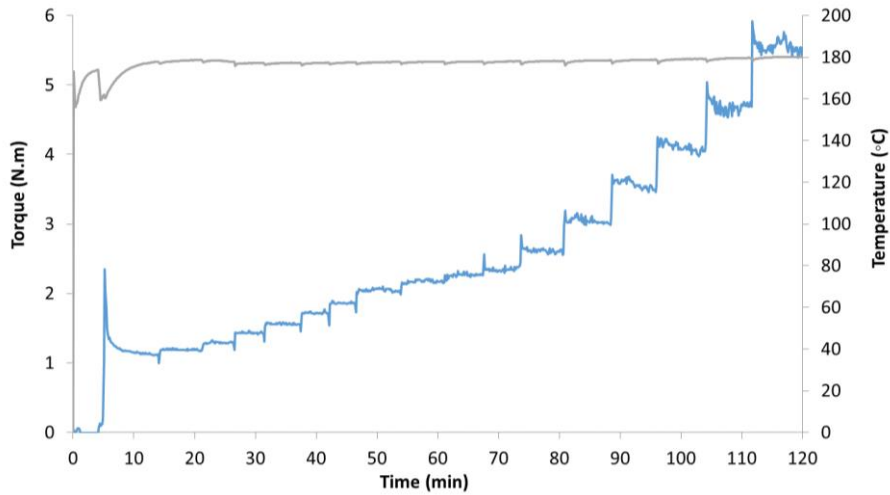
	<b>Powder</b>	<b>cf. ATMIX</b>
Density (kg/m <sup>3</sup> )	8655 ± 17	-
d <sub>10</sub> (µm)	1.69	1.57
d <sub>50</sub> (µm)	3.71	3.43
d <sub>90</sub> (µm)	6.03	6.01
$S_m$ (m <sup>2</sup> /kg)	345 ± 4	380
$S_w$	4.63	-

### *Optimization of copper powders feedstocks*

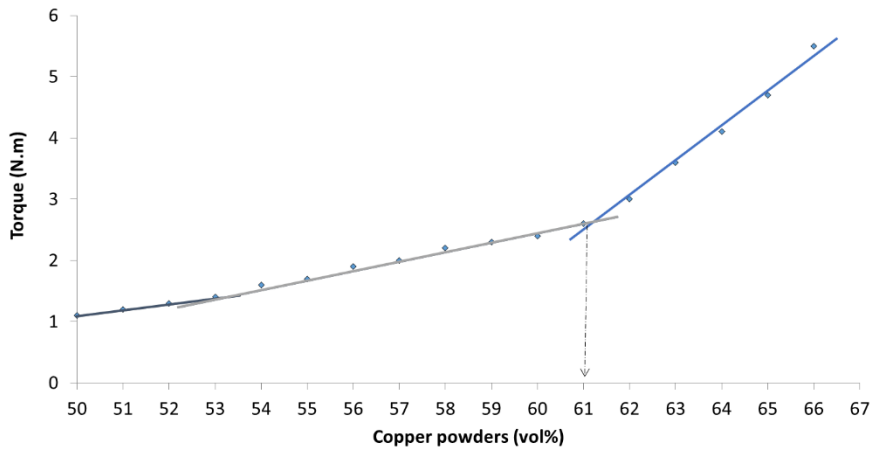
After the characterization of copper powders, the optimization of mixture was similar to the SS 316L. Firstly, it was optimized the mixtures only with copper powders, and after the nanocomposite based material (with nanoreinforcement addition). The parameters previously selected were 180 °C and 30 rpm.

Figure A.5 a) shows the selected methodology for optimization of copper powders with the M<sub>1</sub> binder. Three different regimes are evident (figure A.5 b)), when the torque value increases by the consecutive addition of 1 vol% of powder. The first regime is between 50 and 53 vol%, where torques value are very low. The second one is between 53 and 61 vol%, where the torque value is slightly high. The maximum torque value attained was 5.5 N.m for

67 vol% of metallic powder, third regime (61 and 67 vol%). From the practical knowledge, the optimal value to produce the mixtures should be 61 vol% of powder contents into mixture. However, have in mind the future addition of nanoreinforcements and their “perverse” role in the feedstock rheology and to facilitate the comparison with SS 316L case study, it was decided to use 60 vol% of copper powders.



a)



b)

Figure A.5 – Copper feedstock optimization versus a) time and b) copper powders (vol%)

The feedstock with 60 vol% of copper and 40 vol% of M<sub>1</sub> has a stable torque value (2.2 N.m) that reflects a homogeneity of the mixture, named as master feedstock – MF (figure A.6).

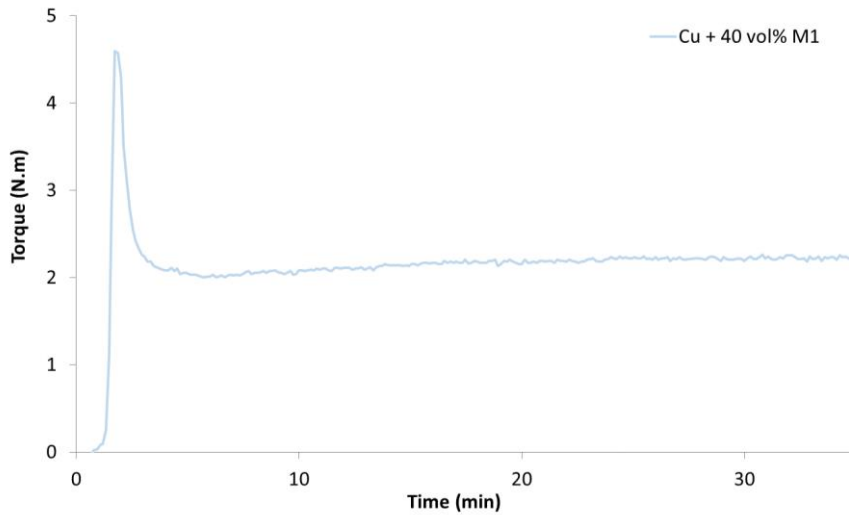


Figure A.6 – Copper feedstock with 40 vol% of M<sub>1</sub> binder

The copper feedstock was analysed by SEM (figure A.7), another way of assessing the mixture homogeneity. This technique reveals that copper powders are uniformly dispersed in M<sub>1</sub> binder, and for the highest magnification, powders exhibit an uniform coating of binder.

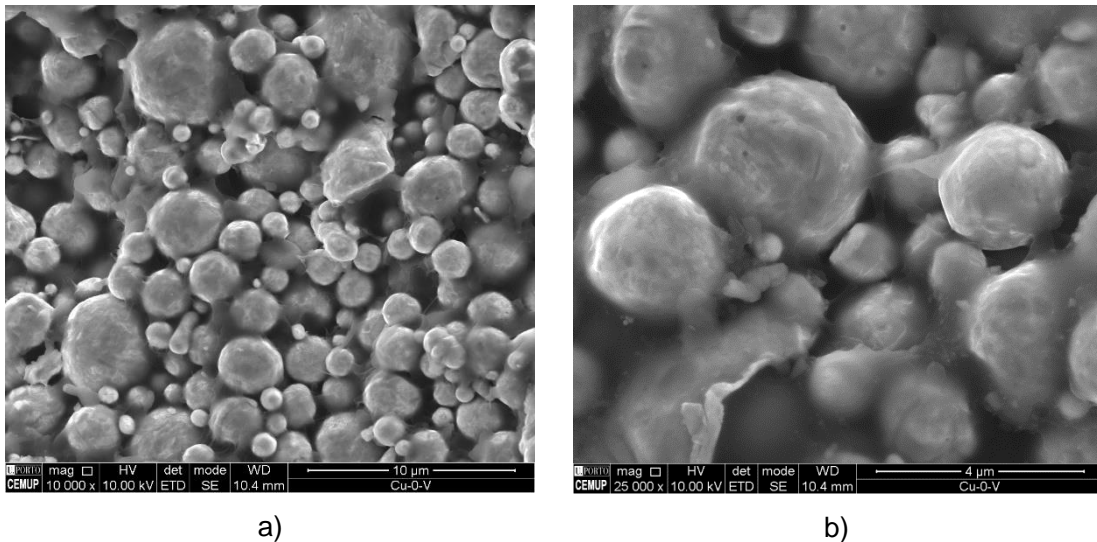
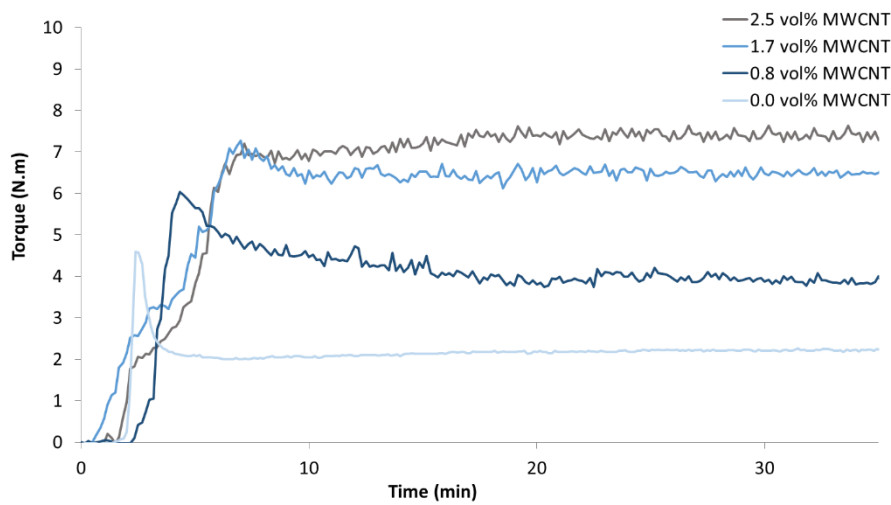


Figure A.7 – Morphological analysis of copper feedstock with 40 vol% of M<sub>1</sub>, at different magnifications a) 10000x and b) 25000x

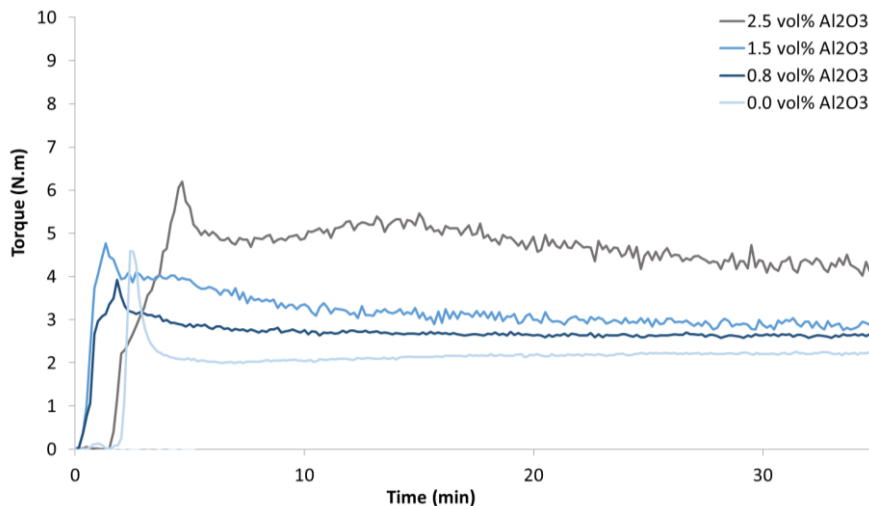
### *Feedstocks of composites*

The master feedstock (based on M<sub>1</sub>) was nanoreinforced with different percentages of MWCNT or nanoalumina powder: 0.8, 1.7, 2.5 and 3.3 vol%. During the mixture time (route 1 a)) the nanoreinforcement was added directly (figure 3.15).

Figure A.8 shows the behaviour of composites feedstocks with different nanomaterials (MWCNT and nanoalumina). Once again, independent of type the nanoreinforcement added directly to the optimized mixture (MF – route 1 a)), the torque value always increases with addition of nanoreinforcement content. The addition of MWCNTs produce nanoreinforced feedstocks with torque values, as follows: 3.9, 6.5 and 7.3 N.m, respectively (figure A.8 a) and table A.3). In this case, it was not possible to make the feedstock with 3.3 vol% of MWCNT, because there was not a link between the matrix (Cu and the nanoreinforcement ( $M_1$ )). In what concerns to nanoalumina additions, the correspondent torque values were 2.6, 2.9 and 4.2 N.m, respectively ((figure A.8 b) and table A.3). Once again, it was not possible to make the composite feedstock with 3.3 vol% of nanoalumina.



a) MWCNT



b) Nanoalumina

Figure A.8 – Copper and  $M_1$  composites feedstock nanoreinforced with a) MWCNT and b) nanoalumina

Comparing the different nanoreinforcements added the MWCNTs produce composites feedstocks with high torque value than by addition of nanoalumina (table A.2). Some of nanoreinforcements contents in feedstocks overcome the torque limit suitable to be injected (4.0 N.m). In order to overcome this problem, the selected solution was the addition of a supplement in the binder –stearic acid maintaining the powder content.

Table A.2 –Torque values of copper composites feedstocks nanoreinforced with MWCNT or nanoalumina

vol%	MWCNT	Nanoalumina
0.0	2.2	2.2
0.8	3.9	2.6
1.7	<u>6.5</u>	2.9
2.5	<u>7.3</u>	<u>4.2</u>
3.3	*	*

\* The mixing of copper feedstock nanoreinforced with 3.3 vol% was not possible.

In order to enlarge the nanoreinforcement contents in the matrices, the selected option was to mix the feedstock with SA, in different percentages (figure A.9) [85]. The addition of 10 vol% of SA and 30 vol% M<sub>1</sub> to copper matrix, decreases the torque value from 2.2 N.m to 1.7 N.m.

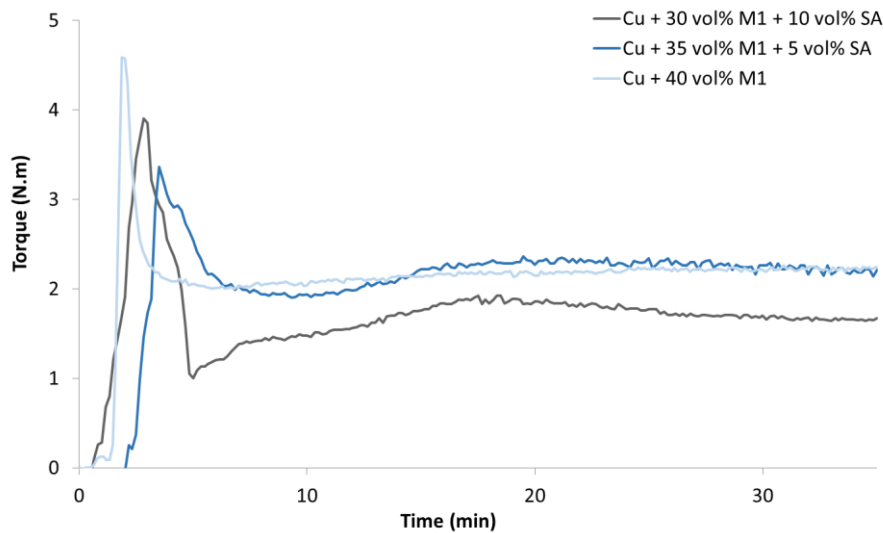


Figure A.9 – Copper feedstocks with 0, 5 and 10 vol% SA



The copper powders are coated by binder (figure A.10), similar to SS 316L matrix.

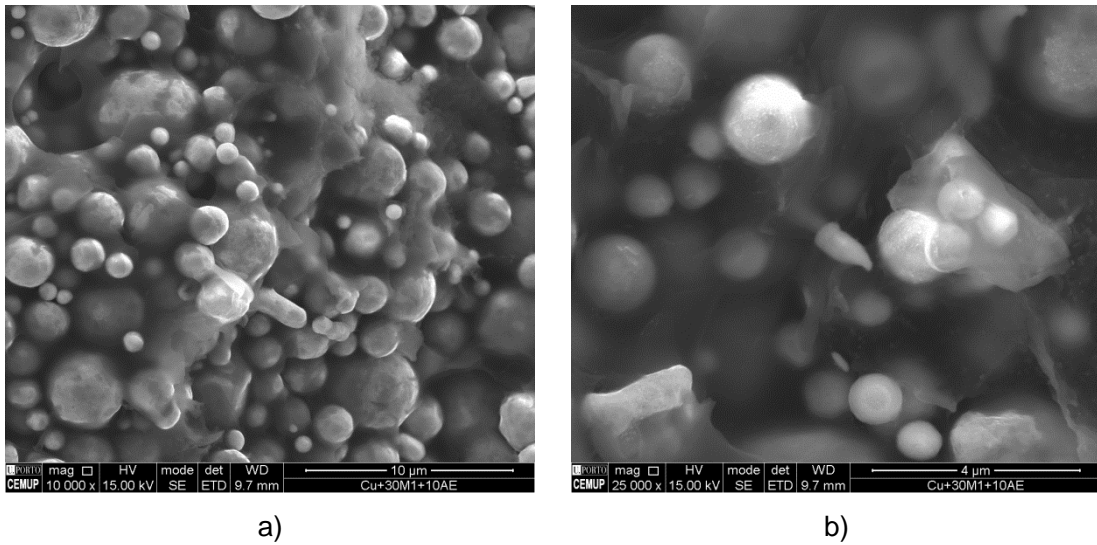
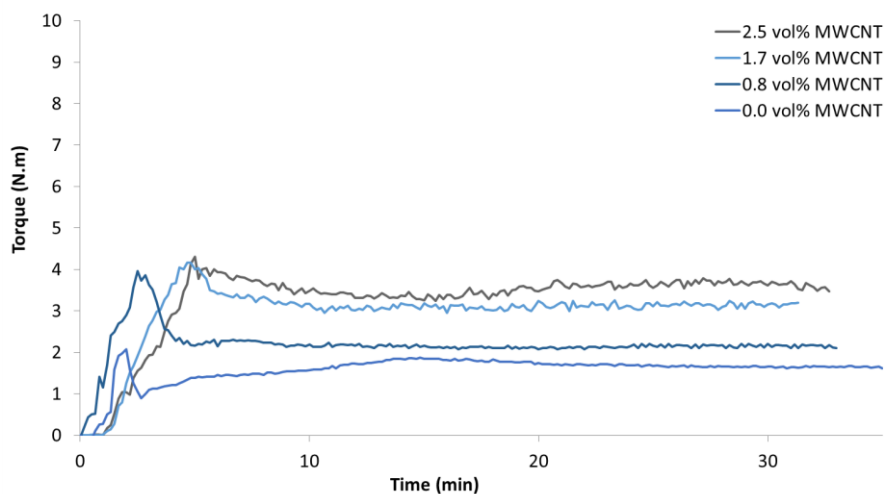


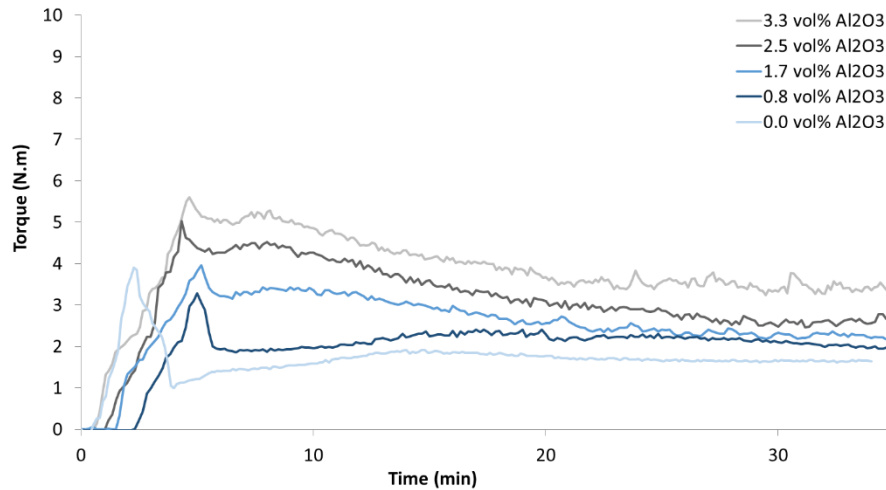
Figure A.10 – Morphological analysis of SS 316L:binder (60:(30+10) vol%) a) 10000x and b) 25000x

Henceforth, the master feedstock (MF) is constituted by 60 % of copper, 30 % of M<sub>1</sub> and 10 % of SA (vol%). And studied the effect of nanoreinforcement content in the behaviour of the feedstock (route 1 b)). The selected nanoreinforcement contents were as follows: 0.8, 1.7, 2.5 and 3.3 vol% of MWCNT or nanoalumina powders [85].

The torque values also increase with MWCNT additions (figure A.11 and table A.3), for similar compositions, the torque measured was 2.1, 3.1 and 3.6 N.m, respectively. However, when was added 3.3 vol% of MWCNT, the mixture was impossible to prepare. For alumina nanoparticles, the torque values attained for the same contents were: 2.0, 2.3, 2.6 and 3.4 N.m, respectively. In spite of the torque values be below 4 N.m, is important to select the nanoreinforcement that induces more stability along time, e. g. MWCNTs.



a) MWCNT



b) Nanoalumina

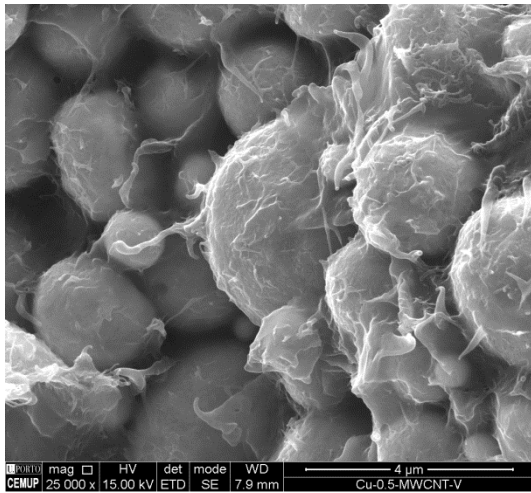
Figure A.11 – Copper composites feedstock ( $M_1+SA$ ) nanoreinforced with a) MWCNT and b) nanoalumina

Table A.3 – Torque values of copper composites feedstocks nanoreinforced with MWCNT and nanoalumina

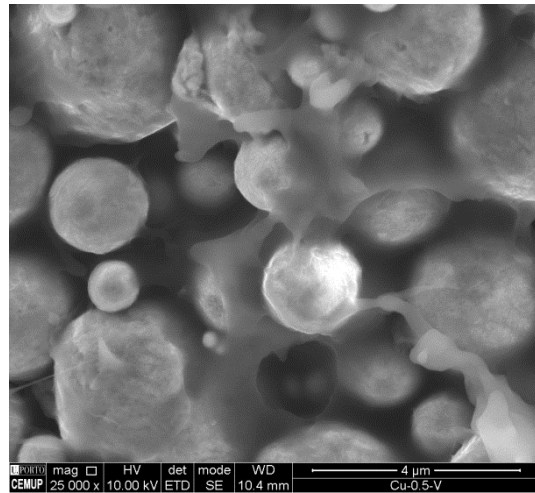
vol%	MWCNT	Nanoalumina
0.0	1.7	1.7
0.8	2.1	2.0
1.7	3.1	2.3
2.5	3.6	2.6
3.3	*	3.4

\* The mixing of copper feedstock nanoreinforced with 3.3 vol% MWCNT was impossible.

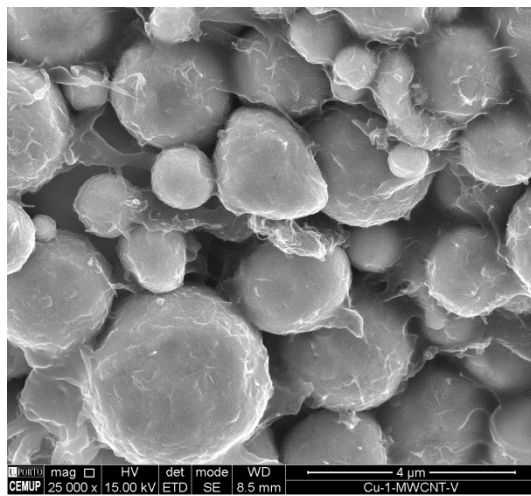
The feedstocks were analysed to assess the distribution of the various constituents in mixture. Figure A.12 shows the differences between the addition of MWCNT and nanoalumina to the copper matrix. A good distribution of powders in binder was attained, but with a different morphology depending on the type of nanoreinforcement. When the MWCNT is the nanoreinforcement, it is perceptible that binder matched to the shape of the nanotubes. In what concern to ceramic nanoparticles, the binder seems more “soft” compared with the previous case study.



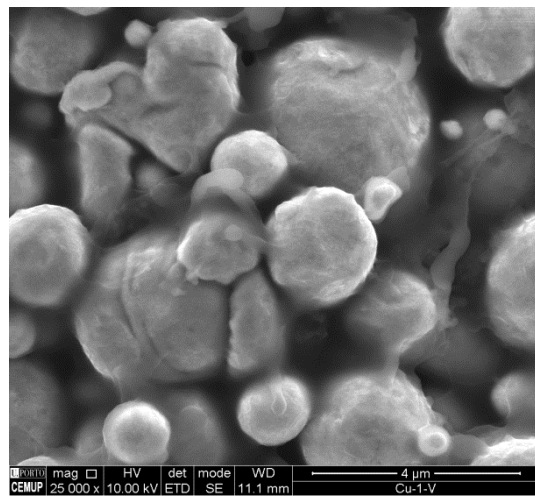
a) 0.8 vol% MWCNT



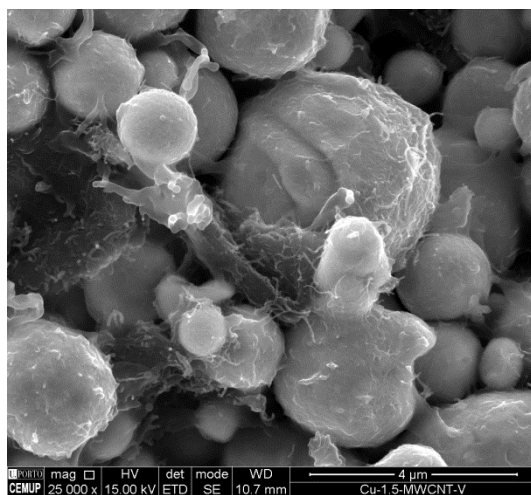
b) 0.8 vol% nanoalumina



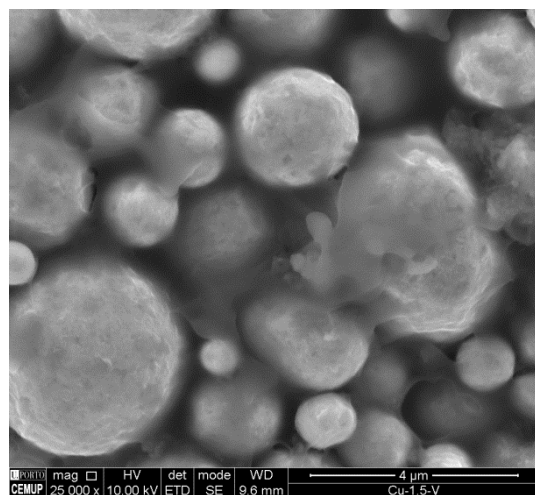
c) 1.7 vol% MWCNT



d) 1.7 vol% nanoalumina



e) 2.5 vol% MWCNT



f) 2.5 vol% nanoalumina

Figure A.12 – Morphological analysis of copper nanocomposites feedstocks with MWCNT (left) and nanoalumina (right)

Until now, the production of nanocomposites feedstocks results from the introduction of nanoreinforcement during mixing time (route 1). Previously, it was referred the problems caused by this procedure (cf. chapter 3.2 b)) and the solution was to produce the nanoreinforced composites feedstocks promoting a physical bond between powders and MWCNT by a pre-mixing, using a ball milling (figure 3.22).

Through the pre-treatment of copper powders and MWCNTs, it was possible to prevent their loss during debinding process. The morphology of pre-mixtures (copper with 3.3 vol% of MWCNT) after being milled in a planetary ball milling during 5 + 10 and 15 minutes, total 30 minutes (figure A.13). After 5 minutes, the pre-mixture presents aggregations of MWCNTs, showing not be enough to break up (figure A.13 a) and b)). However, after 30 minutes, the aggregates are fewer and the powder particles exhibit some deformation MWCNTs embedded in flatted powders (figure A.13 c) and d)). In conclusion, the mixing parameters selected were as follows: total time 30 minutes (15 minutes, with a break of 10 minutes, and more 15 minutes) and rotation speed of 200 rpm.

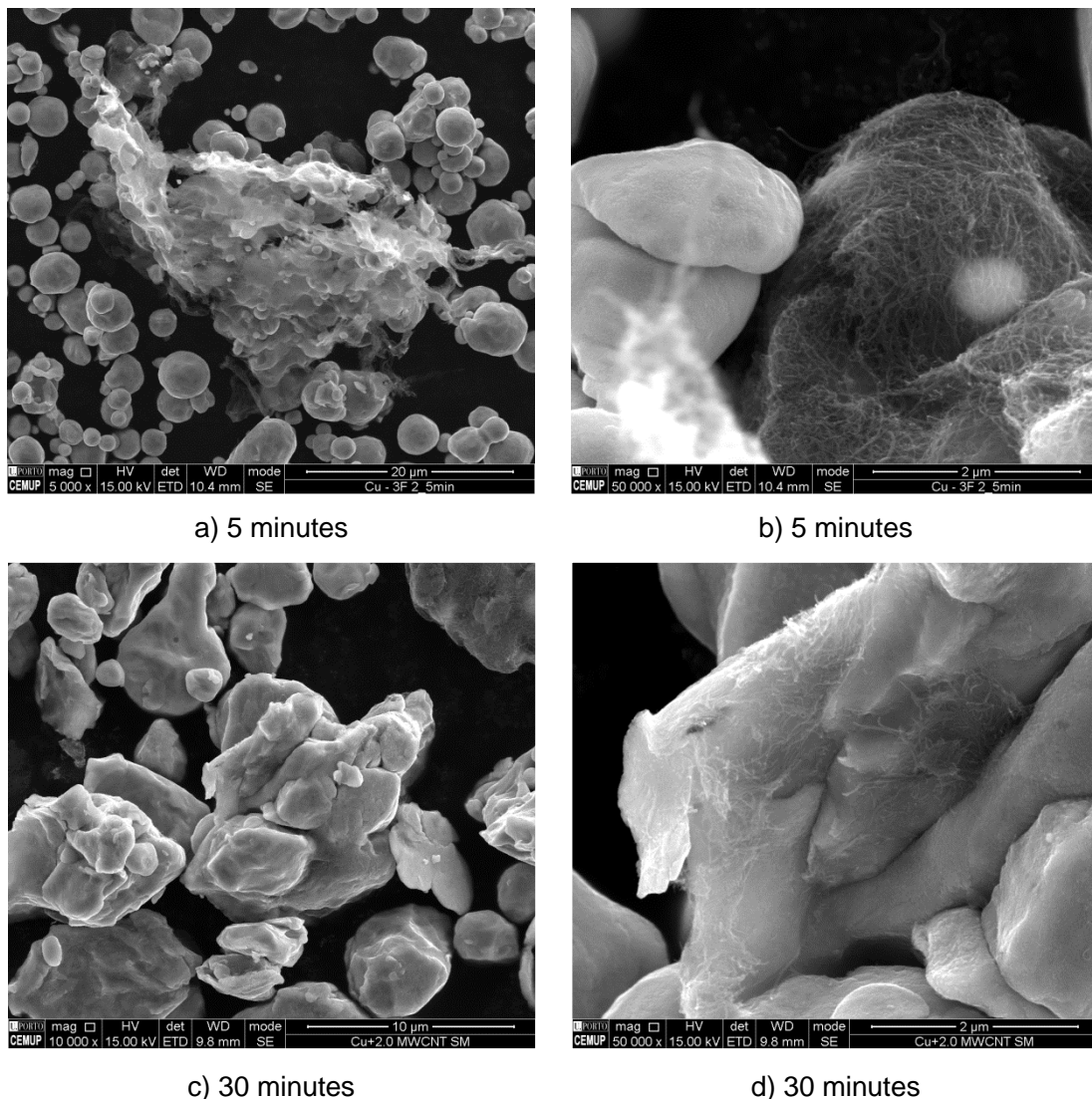


Figure A.13 – Morphological analysis of pre-mixture a) b) 5 minutes, c) d) 30 minutes

After milling optimisation, the pre-mixture (copper and MWCNT) was mixed with master binder for each composition using a Brabender Plastograph, under the same conditions that induce stable torque values (figure A.14 and table A.5). For the compositions tested, the torque values were 2.1, 2.8, 3.0, 3.7 and 4.3 N.m, respectively. This new route achieved torque values higher than the attained by the last route (route 1 b)). However, allowed the formulation of the composite feedstock with higher MWCNTs content.

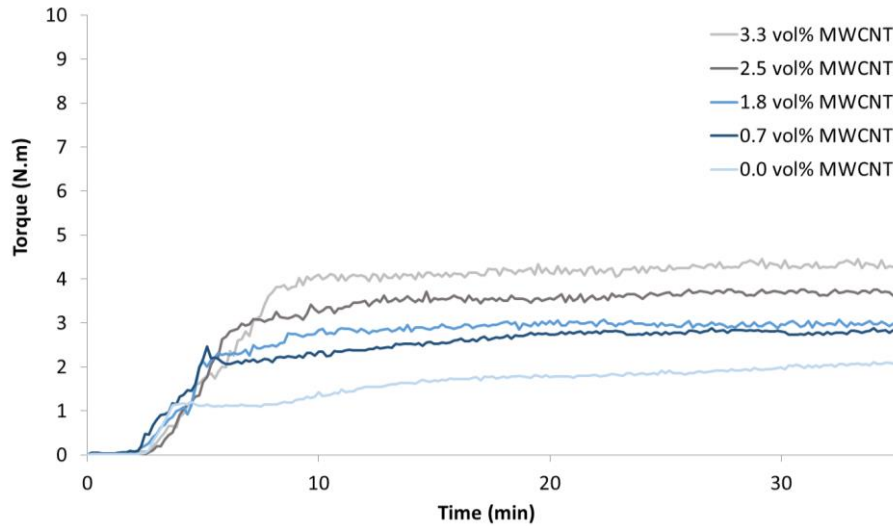


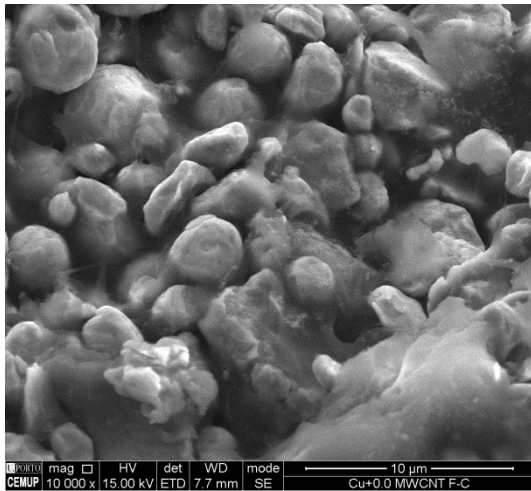
Figure A.14 – Copper nanoreinforced composite feedstock with MWCNT (pre-mixture) (route 2)

Table A.4 – Torque values of copper composites feedstocks nanoreinforced with MWCNT

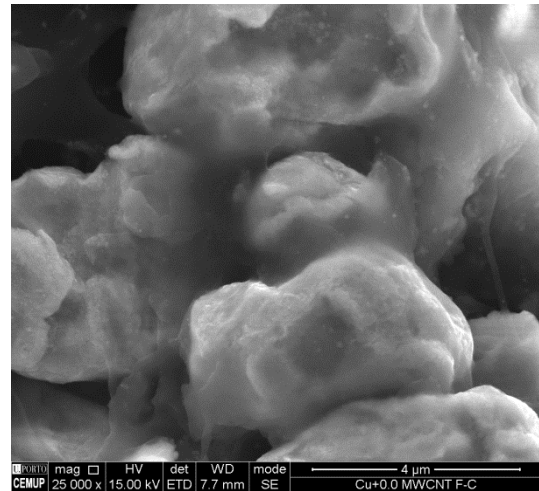
vol%	Torque (Nm)
0.0	2.1
0.8	2.8
1.7	3.0
2.5	3.7
3.3	<u>4.3</u>

The nanocomposites feedstocks were analysed by SEM, but with some limitation due to their poor electric conductivity. The pre-mixtures equally involved by binders, with the addition of nanoreinforcement is visible same differences, mainly in binder morphology (figure A.15). In addition, the shape of the copper powder is quite different due to high ductility of copper when compared to SS 316L powders.

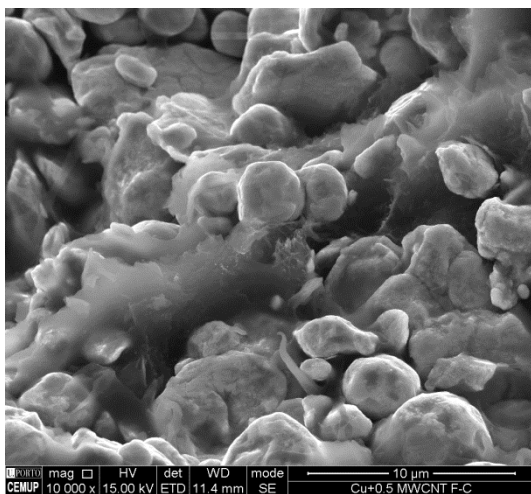




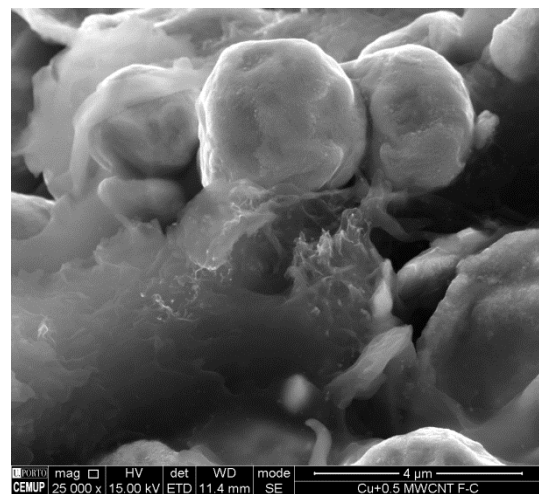
a) 0.0 vol%



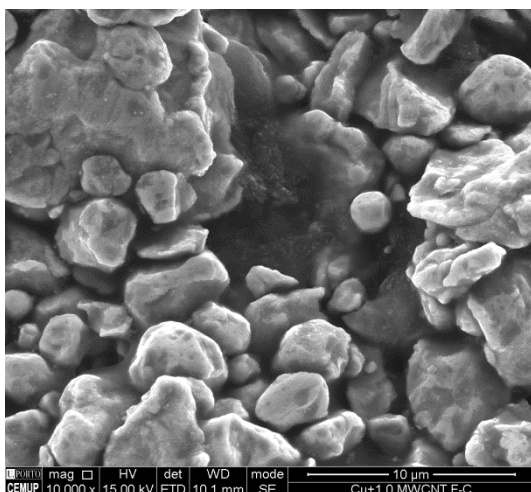
b) 0.0 vol%



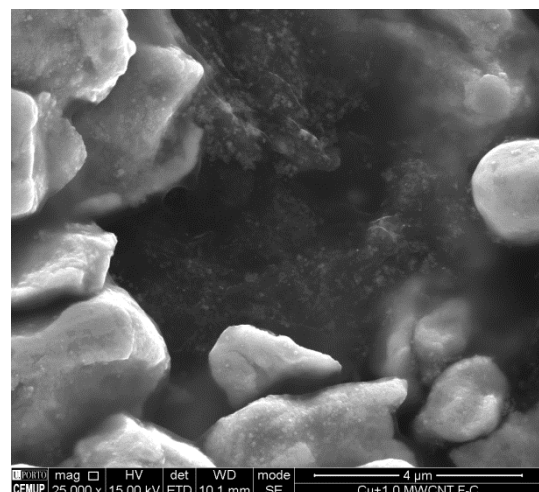
c) 0.8 vol%



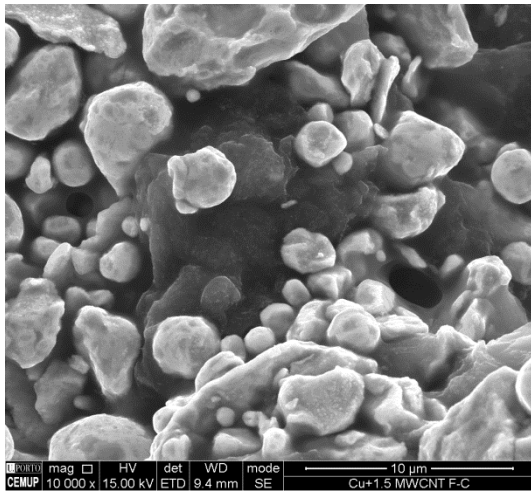
d) 0.8 vol%



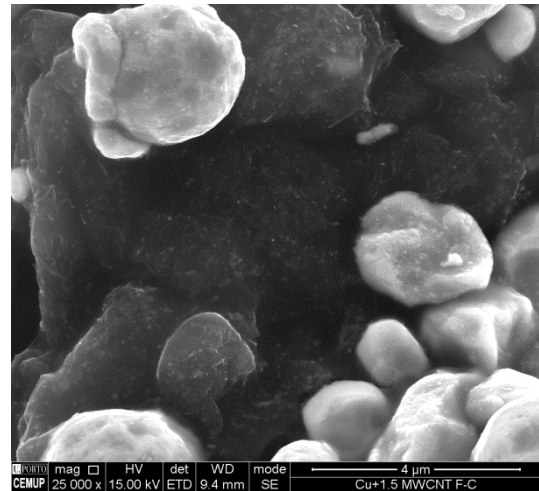
e) 1.7 vol%



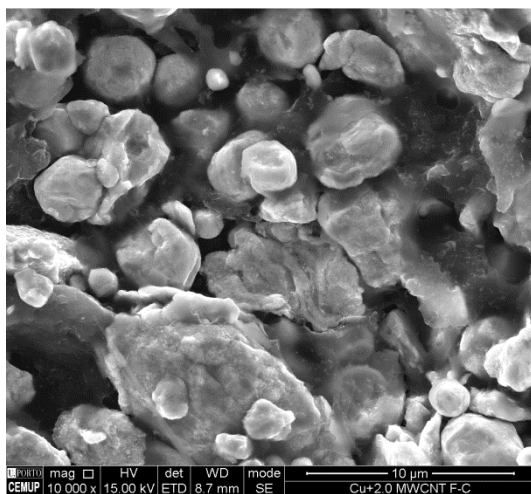
f) 1.7 vol%



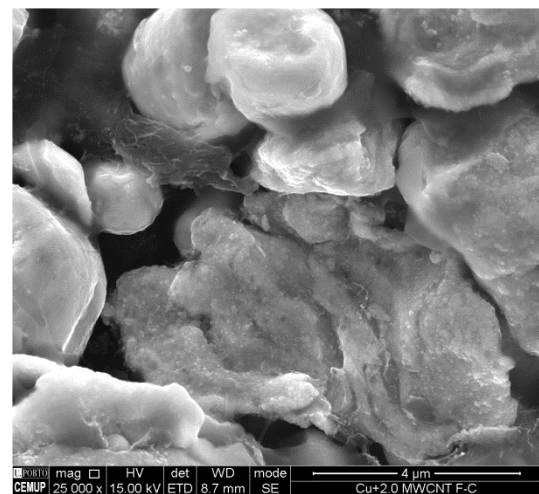
g) 2.5 vol%



h) 2.5 vol%



i) 3.3 vol%



j) 3.3 vol%

Figure A.15 – Morphological analysis of nanocomposites feedstocks different contents a), b) 0.0, c), d) 0.7, e), f) 1.8, g), h) 2.5, i), j) 3.3 of MWCNTs (vol%) 10000x (left) and 25000x (right)

Since the copper composites feedstocks produced by the route 2 attained high torque values, in opposition to the expected based on the results obtained in SS 316L.

# APPENDIX III

---

Volume and weight content conversions



Until the injection step, there are three elements to be take into account: powders, reinforcement and binder. For easy identification and calculations, the quantities added were given in volumetric percentage (vol%). Until the debinding step, the content in vol% and wt% of the several elements are in tables A.5 and A.6.

Table A.5 – Volume percentage of different elements

<b>Feedstock</b>	<b>SS 316L</b>	<b>MWCNT</b>	<b>M<sub>1</sub> (binder)</b>	<b>SA (binder)</b>
SS 316L + M <sub>1</sub>	60	-	40	-
SS 316L + M <sub>1</sub> + SA	60	-	30	10
SS 316L + MWCNT + M <sub>1</sub> + SA	59.5	0.5	30	10
	59.0	1.0	30	10
	58.5	1.5	30	10
	58.0	2.0	30	10

Table A.6 – Weight percentage of different elements

<b>Feedstock</b>	<b>SS 316L</b>	<b>MWCNT</b>	<b>M<sub>1</sub> (binder)</b>	<b>SA (binder)</b>
SS 316L + M <sub>1</sub>	92.5	-	7.5	-
SS 316L + M <sub>1</sub> + SA	92.5	-	5.6	1.9
SS 316L + MWCNT + M <sub>1</sub> + SA	92.2	0.2	5.7	1.9
	92.0	0.4	5.7	1.9
	91.7	0.6	5.7	1.9
	91.5	0.8	5.8	1.9

Table A.7. show the conversion of MWCNTs in SS 316L volume content in brown and sintered nanocomposite in weight percentage.

Table A.7 – MWCNTs contents in matrix


vol%	0.8	1.7	2.5	3.3
wt%	0.2(3)	0.4(6)	0.6(9)	0.9(2)

# ANNEX I


---

ICDD

33-0397		Wavelength= 1.78897					*
Cr0.19Fe0.7Ni0.11		2 $\theta$	Int	h	k	l	
Chromium Iron Nickel		51.072	100	1	1	1	
		59.738	45	2	0	0	
		89.576	26	2	2	0	
		111.397	30	3	1	1	
		119.250	12	2	2	2	
		170.00	3	4	0	0	
Rad.: CuK $\alpha$	$\lambda$ : 1.541880	Filter: Mono	d-sp: Diff.				
Cut off:	Int.: Diffract.	I/lor.:					
Ref: Pfoertsch, Ruud, Penn State University, University Park, Pennsylvania, USA, ICDD Grant-in-Aid, (1982)							
Sys.: Cubic		S.G.: Fm $\bar{3}m$ (225)					
a: 3.5911(1)	b:	c:	A:	C:			
$\alpha$ :	$\beta$ :	$\gamma$ :	Z: 4	mp:			
Ref: Ibid.							
Dx: 7.950	Dm:	SS/FOM: F <sub>6</sub> = 57(.0177 , 6)					
Color: Black							
Quantitative analysis by Atomic Absorption Spectroscopy: chromium 17.9%, nickel 11.4%, molybdenum <0.01%, silicon 0.88%. Austenitic Steel. Synthetic taenite is Ni-Fe rich analog. Cu type. Also called: 304-stainless steel, austenite. Silicon used as an internal stand. PSC: cF4. To replace 31-619. Mwt: 55.43. Volume[CD]: 46.31.							


 © 2000 JCPDS-International Centre for Diffraction Data. All rights reserved  
 PCPDFWIN v. 2.1

87-0722		Wavelength= 1.78897			C
Fe	2 $\theta$	Int	h	k	l
Iron	52.486	999*	1	1	0
	77.414	115	2	0	0
	99.970	175	2	1	1
Iron					
Rad.: CuK $\alpha$ 1 $\lambda$ : 1.54060 Filter: d-sp: Calculated					
Cut off: 17.7 Int.: Calculated 1/lor.: 10.76					
Ref: Calculated from ICSD using POWD-12++, (1997)					
Ref: Owen, E.A., Williams, G.I., J. Sci. Instrum., 31, 49 (1954)					
Sys.: Cubic S.G.: Im $\bar{3}$ m (229)					
a: 2.8608(4)	b:	c:	A:	C:	
$\alpha$ :	$\beta$ :	$\gamma$ :	Z: 2	mp:	
Ref: Ibid.					
Dx: 7.922 Dm: 7.870 ICSD #: 064999					
Peak height intensity. PSC: c12. Calc. density unusual but tolerable. No R value given. At least one TF missing. Mwt: 55.85. Volume[CD]: 23.41.					


 © 2000 JCPDS-International Centre for Diffraction Data. All rights reserved  
 PCPDFWIN v. 2.1

71-0552		Wavelength= 1.78897					C				
Cr23C6	2 $\theta$	Int	h	k	l	2 $\theta$	Int	h	k	l	
Chromium Carbide	16.729	12	1	1	1	90.906	134	6	6	0	
	19.341	1	2	0	0	93.332	79	7	5	1	
	27.485	7	2	2	0	94.142	4	6	6	2	
	32.349	23	3	1	1	97.392	34	8	4	0	
	33.829	16	2	2	2	99.846	41	9	1	1	
Rad.: CuK $\alpha$ 1 $\lambda$ : 1.54060 Filter:	39.261	49	4	0	0	100.667	4	8	4	2	
d-sp: Calculated	42.951	10	3	3	1	103.978	5	6	6	4	
Cut off: 17.7 Int.: Calculated I/Icor.: 2.75	44.124	228	4	2	0	106.491	17	9	3	1	
Ref: Calculated from ICSD using POWD-12++, (1997)	48.593	284	4	2	2						
Ref: Bowman, A.L et al., Acta Crystallogr., Sec. B. 28, 3102 (1972)	51.752	999*	5	1	1						
	56.734	217	4	4	0						
Sys.: Cubic S.G.: Fm $\bar{3}$ m (225)	59.588	251	5	3	1						
a: 10.65 b: c: A: C:	60.521	123	4	4	2						
	64.173	19	6	2	0						
$\alpha$ : $\beta$ : $\gamma$ : Z: 4 mp:	66.838	25	5	3	3						
Ref: Ibid.	67.714	66	6	2	2						
	71.168	2	4	4	4						
	73.711	4	7	1	1						
Dx: 6.972 Dm: ICSD #: 002837	74.552	5	6	4	0						
	77.881	1	6	4	2						
	80.352	2	5	5	3						
Peak height intensity, R-factor: 0.056. C6 Cr23 type. PSC:	84.430	30	8	0	0						
cF116. At least one TF missing. Mwt: 1267.97. Volume[CD]:	86.863	1	7	3	3						
1207.95.	87.672	38	8	2	0						



© 2000 JCPDS-International Centre for Diffraction Data. All rights reserved  
PCPDFWIN v. 2.1

36-1482

Wavelength= 1.78897


\*

Cr7C3	2 $\theta$	Int	h	k	l	2 $\theta$	Int	h	k	l
Chromium Carbide	34.235	2	0	4	0	99.299	10	5	5	1
	45.838	33	1	5	0	99.654	12	5	2	2
	46.503	3	0	0	2	99.803	12	3	9	0
	49.384	6	0	5	1	102.803	<1	1	9	2
	49.834	46	1	1	2	103.493	<1	4	1	3
Rad.: CuK $\alpha$ 1 $\lambda$ : 1.540598 Filter: Graph Mono d-sp: Diff.	51.770	100	1	5	1	104.277	1	0	0	4
Cut off: 17.7 Int.: Diffract. I/Icor.:	52.412	13	0	6	0	104.361	1	3	9	1
Ref: McMurdie, H et al., Powder Diffraction, 1, 89 (1986)	54.122	1	3	2	1	105.350	2	3	5	3
	56.081	5	2	0	2					
	57.863	11	3	3	1					
	59.011	24	2	2	2					
Sys.: Orthorhombic S.G.: Pnmm (51)	60.023	3	1	6	1					
a: 7.0149(12) b: 12.153(2) c: 4.5320(4) A: 0.5772 C: 0.3729	61.299	16	2	6	0					
$\alpha$ :	62.876	1	3	4	1					
$\beta$ :	67.397	2	3	1	2					
$\gamma$ :	72.121	2	0	8	0					
Z: 4 mp:	72.656	2	3	3	2					
Ref: Ibid.	76.779	5	0	8	1					
	78.372	1	0	3	3					
Dx: 6.877 Dm: SS/FOM: F <sub>30</sub> = 23(.0078 , 167 )	80.296	1	1	3	3					
	82.797	7	2	2	3					
Color: Greenish gray	84.327	2	2	8	1					
Peak height intensity. The mean temperature of data collection	84.674	1	1	4	3					
was 24.6 C. The sample was obtained from CERAC, Incorporated,	90.257	3	1	5	3					
Milwaukee, WI, USA. CAS #: 12075-40-0. The structure was determined	94.805	3	5	5	0					
by Rouault, M., Herpin, P., Fruchart, M., Ann. Chim. (Paris), 5 461	95.263	12	3	3	3					
(1970 $\sigma$ (l <sub>obs</sub> ) = $\pm$ 0.01. C3 Cr7 type. Also called: heptachromium	97.156	1	5	0	2					
tricarbide, Tungsten used as an internal stand. PSC: oP40. See	97.753	13	2	8	2					
11-550. Mwt: 400.00. Volume[CD]: 386.36.										



© 2000 JCPDS-International Centre for Diffraction Data. All rights reserved  
PCPDFWIN v. 2.1

85 - 1326		Wavelength= 1.78897			C
Cu	2 $\theta$	Int	h	k	l
Copper	50.754	999*	1	1	1
	59.323	427	2	0	0
Copper	88.831	171	2	2	0
	110.302	156	3	1	1
Rad.: CuK $\alpha$ 1 $\lambda$ : 1.54060 Filter: d-sp: Calculated					
Cut off: 17.7 Int.: Calculated 1/lor.: 10.76					
Ref: Calculated from ICSD using POWD-12++, (1997)					
Ref: Owen, E.A., Williams, G.I., J. Sci. Instrum., 31, 49 (1954)					
Sys.: Cubic			S.G.: Im $\bar{3}m$ (229)		
a:	3.615	b:	c:	A:	C:
$\alpha$ :	$\beta$ :	$\gamma$ :	Z:	4	mp:
Ref: Ibid.					
Dx:	8.935	Dm:	8.960	ICSD # : 064999	
Peak height intensity. PSC: cl2. Calc. density unusual but tolerable. No R value given. At least one TF missing. Mwt: 63.55					
Volume[CD]: 47.24					


 © 2000 JCPDS-International Centre for Diffraction Data. All rights reserved  
 PCPDFWIN v. 2.1

# ANNEX II

---

MatWeb: AISI 316L Stainless Steel, annealed plate



Properties of AISI 316L Stainless Steel, annealed plate (standard), used for comparisons with sintered parts produced.

Table A.8 – Properties of SS 316L annealed plate

<b>AISI SS 316L</b>	
Density (kg/m <sup>3</sup> )	7990
Hardness (HV)	152
Young's modulus (GPa)	177 - 193
YS (MPa)	235
UTS (MPa)	560
$\varepsilon$ (%)	55

